

# SYSTEM DUCTILITY AND REDUNDANCY OF FRP STRUCTURES WITH DUCTILE ADHESIVELY-BONDED JOINTS

THÈSE N° 3214 (2005)

PRÉSENTÉE À LA FACULTÉ ENVIRONNEMENT NATUREL, ARCHITECTURAL ET CONSTRUIT

Institut de structures

SECTION D'ARCHITECTURE

ÉCOLE POLYTECHNIQUE FÉDÉRALE DE LAUSANNE

POUR L'OBTENTION DU GRADE DE DOCTEUR ÈS SCIENCES

PAR

**Julia DE CASTRO SAN ROMÁN**

Ingénieur en génie civil diplômée EPF  
et de nationalité espagnole

acceptée sur proposition du jury:

Prof. Dr Th. Keller, directeur de thèse  
Prof. Dr L. Bank, rapporteur  
Prof. U. Meier, rapporteur  
Prof. Dr I. Smith, rapporteur  
Prof. Dr G. Turvey, rapporteur

Lausanne, EPFL  
2005



*Para Carmina y Julio*



# Synopsis

Summary	v
Zusammenfassung	vi
Résumé	vii
Acknowledgments	ix
Table of Contents	xi
1 Introduction	1
2 State of the Art	9
3 Ductile and Redundant Structure Concepts	49
4 Experimental Investigations	53
5 Numerical Modeling of Adhesively-bonded Double-lap Joints	89
6 Design of FRP Structures with Ductile Adhesively-bonded Joints	127
7 Conclusions and Future Work	155
References	163
List of Figures	177
List of Tables	185
Curriculum Vitae	187
Appendix	CD-ROM



---

## Summary

Fiber-reinforced polymer (FRP) composites offer several advantages in relation to traditional materials, such as high specific strength, good corrosion resistance, low thermal conductivity and rapid component installation. Despite the great potential of these materials, two major disadvantages limit their acceptance in civil engineering applications: their lack of inherent ductility and the fact that their fibrous and anisotropic character makes the joining of structural components difficult.

The purposes of this research are to develop ductile structures using brittle all-FRP materials and to provide a corresponding design method assuring robustness and structural safety.

The proposed concept for all-FRP structures incorporates system ductility through the use of ductile, adhesively-bonded joints and redundant (statically indeterminate) structural systems. The concept envisages adhesives with an initially elastic behavior sufficiently stiff to meet short- and long-term serviceability requirements. When serviceability and ultimate loads are exceeded, however, adhesive behavior should change and become plastic, or at least highly non-linear inelastic, with much lower stiffness. The ductile connections effect a favorable redistribution of internal and external forces in the redundant system in the same way as plastic hinges in statically indeterminate systems with ductile materials. In case of joint failure, the redundant system allows the creation of alternative load paths and redistribution of section forces preventing structural collapse.

Numerical and experimental investigations of adhesively-bonded double-lap joints demonstrate that using an appropriate bilinear adhesive is more advantageous than using a traditional structural and stiff epoxy adhesive. These investigations show that ductile adhesives generate a linear axial strain distribution and consequently a constant shear stress distribution along the overlap. Numerical and analytical modelings are validated with experimental results. The numerical modeling allows evaluation of the effect of ductile adhesive behavior on joint behavior and establishment of recommendations for the selection of adhesive mechanical properties, according to serviceability and failure limit state requirements. Based on numerical modeling results, joints can also be classified according to stiffness (stiff or flexible). An analytical model, based on numerical and experimental results, is developed for predicting joint stiffness when using ductile adhesives, assuming that the adhesive deforms only and uniformly in shear and that adherends deform only in tension.

The design method is developed in accordance with the new structural concept and Eurocode design philosophy. It is based on both numerical and analytical model results for adhesively-bonded double-lap joints. A case study illustrating the adhesively-bonded joint design and appropriate adhesive selection is carried out on continuous beams with adhesively-bonded joints at mid-support. Corresponding bending experiments on beams with ductile, adhesively-bonded connections demonstrate the new structural concept's feasibility and validate the proposed design method. An energy factor defined as the ultimate strength to serviceability limit state energy ratio is proposed to quantify and compare the robustness and safety of structures built from both ductile and brittle materials.

# Zusammenfassung

Faserverstärkte Kunststoffe (FRP) bieten gegenüber traditionellen Materialien mehrere Vorteile, wie zum Beispiel hohe spezifische Festigkeiten, einen guten Korrosionswiderstand, geringe Wärmeleitfähigkeit und schnelle Installation. Trotz des hohen Potentials wird die Akzeptanz des Materials durch zwei Hauptnachteile bei der Anwendung in Ingenieurtragwerken eingegrenzt: zum einen durch das Fehlen ausreichender Duktilität und zum anderen der faserhafte Aufbau und die dadurch resultierende Anisotropie, durch die sich Verbindungen von Tragkomponenten schwierig gestalten.

Ziel dieser Arbeit ist es, duktile Tragstrukturen aus spröden FRP Materialien zu entwickeln und ein entsprechendes Bemessungskonzept zu erstellen, welches Robustheit und strukturelle Sicherheit bietet.

Das vorgestellte Konzept für Tragstrukturen aus FRP erzeugt Systemduktilität durch die Verwendung von duktilen, geklebten Verbindungen und redundanten (statisch unbestimmten) Systemen. Das Konzept sieht Kleber mit zunächst elastischen Verhalten vor, die über eine ausreichende Steifigkeit im Gebrauchszustand bei Kurz- und Langzeitbeanspruchungen verfügen. Beim Überschreiten der Gebrauchslasten und Bruchlasten sollte das Verhalten des Klebers plastisch oder zumindest stark nichtlinear inelastisch mit geringerer Steifigkeit. Bei Versagen der Klebeverbindungen entstehen im redundanten System alternative Lastpfade und eine Umverteilung der inneren Kräfte, die das Versagen der Struktur verhindern sollen.

Numerische und experimentelle Untersuchungen von geklebten Doppellaschenanschlüssen zeigen, dass die Verwendung eines adäquaten Klebers mit bilinearen Werkstoffeigenschaften vorteilhafter ist als die Verwendung eines traditionellen, steifen Epoxidklebers. Die Untersuchungen zeigen, dass duktile Kleber eine lineare axiale Dehnungsverteilung und somit eine konstante Schubspannungsverteilung entlang der Überlappung erzeugen. Numerische und analytische Modelle wurden mit den Ergebnissen aus den Experimenten bestätigt. Die numerische Modellierung erlaubt eine Auswertung des Einflusses des duktilen Klebverhaltens auf das Verhalten des Anschlusses und die Angabe von Empfehlungen für die Wahl der mechanischen Eigenschaften des Klebers in Bezug auf Gebrauchslast und Anforderungen an die Bruchlast. Ausgehend von den numerischen Ergebnismodellierung können Anschlüsse nach ihrer Steifigkeit klassifiziert werden (starr oder weich). Ein analytisches Modell, basierend auf den numerischen und experimentellen Ergebnissen, wird zur Bestimmung der Anschlusssteifigkeit bei Verwendung von duktilen Klebern entwickelt, unter Annahme, dass der Kleber sich alleinig und gleichmäßig unter Schub verformt und dass die FRP Elemente nur Zugverformungen erfahren.

Das Bemessungskonzept wurde entsprechend des neuen Tragkonzeptes und der Bemessungsphilosophie nach Eurocode entwickelt. Es basiert auf den numerischen und analytischen Ergebnissen für geklebte Doppellaschenanschlüsse. Eine Fallstudie veranschaulicht die Verwendung von geklebten Anschlüssen, bei dem ein Dreifeldträger über dem Mittelaufleger unter Verwendung von angemessenen Klebern zu einem Durchlaufträger ausgebildet wird. Biegeversuche an Trägern mit duktilen geklebten Verbindungen zeigen die Machbarkeit des neuen Tragkonzeptes und bestätigen das vorgeschlagene Bemessungskonzept. Ein Energiefaktor, der sich als Verhältnis zwischen der Energie unter Bruchlast und unter Gebrauchslast definiert, wird vorgeschlagen. Er dient zur Bestimmung und zum Vergleich von Robustheit und Tragsicherheit von Tragstrukturen aus duktilen und spröden Materialien.



## Résumé

Les matériaux composites à base de polymères renforcés par des fibres (FRP) offrent de nombreux avantages par rapport aux matériaux de construction traditionnels tels qu'une haute résistance et rigidité spécifique, une bonne résistance à la corrosion et une faible conductivité thermique. Malgré leur grand potentiel, deux inconvénients majeurs limitent l'application des FRP dans le génie civil, d'une part leur manque de ductilité et d'autre part leur caractère fibreux et anisotrope qui rend difficile l'assemblage des composants structuraux.

Le but de cette recherche est de développer des structures en FRP ductiles et de fournir une méthode de dimensionnement garantissant la construction de structures robustes et sûres.

Le concept de structure proposé comprend des systèmes ductiles de part l'utilisation de joints collés ductiles et de systèmes redondants (hyperstatiques). Le concept envisage l'emploi d'adhésifs initialement rigides garantissant l'aptitude au service à long et court terme puis plastiques ou souples au-delà de l'état de service et de la sécurité structurale. Les connexions ductiles garantissent une redistribution des efforts internes et des réactions externes dans la structure de manière analogue à la redistribution créée par les rotules plastiques qui se développent dans les structures hyperstatiques en matériaux ductiles. Lorsqu'une rupture de joint survient, le système redondant permet la redistribution des forces en évitant la ruine de la structure.

Des études numériques et expérimentales de joints collés à double recouvrement ont permis de démontrer les avantages d'utiliser un adhésif bilinéaire approprié plutôt que de l'époxyde, adhésif structural et rigide traditionnellement employé. Ces études indiquent que les adhésifs ductiles génèrent dans les adhérents une distribution des déformations axiales linéaire et par conséquent une distribution des déformations de cisaillement constante le long du recouvrement. Les études numériques et analytiques sont validées par les résultats expérimentaux. Le modèle numérique permet d'évaluer l'effet des adhésifs ductiles sur le comportement des joints collés et d'établir ainsi des recommandations sur le choix des propriétés mécaniques de l'adhésif assurant l'aptitude au service et la sécurité structurale. D'après les résultats du modèle numérique, les joints peuvent être classifiés selon leur rigidité en rigide ou souple. Un modèle analytique établi d'après les résultats numériques et expérimentaux, permet de prédire la rigidité des joints collés à base d'adhésifs ductiles en supposant que l'adhésif se déforme exclusivement et uniformément en cisaillement et les adhérents uniquement en tension.

La méthode de dimensionnement se base sur la philosophie du nouveau concept structural et des Eurocodes. Elle est fondée sur les résultats numériques et analytiques des joints collés à double recouvrement. L'étude de cas d'une poutre continue sur deux travées avec des joints collés à l'appui central permet d'illustrer le dimensionnement de joints collés et la sélection de l'adhésif approprié. Par la suite, des essais de flexions sur de telles poutres ont démontré la faisabilité du nouveau concept structural et validé la méthode de dimensionnement proposée. Un facteur d'énergie, défini comme le rapport des énergies internes à l'état ultime et à l'aptitude au service, est proposé afin de quantifier et de comparer la robustesse et la sécurité de structures construites à partir de matériaux ductiles et fragiles.



---

## Acknowledgments

Over the past four years, I have received support and encouragement from many different people but here I would like to acknowledge those who have made a particularly important contribution.

First, I would like to express gratitude to my thesis director Prof. Thomas Keller for giving me the opportunity to work on this research project, his support, guidance and the rich discussions, especially those concerning the conceptual part of the thesis.

I would like to acknowledge the support of the Swiss Innovation Promotion Agency for funding this research program as well as Fiberline Composites A/S Denmark, Maagtechnic Dübendorf, Sika AG Zurich, and Scobalit AG Winterthur for funding and donating the material for the experimental program.

I wish to express my thanks to the thesis defense committee for the time and effort they put into reading and evaluating the thesis: Prof. Lawrence Bank, University of Wisconsin-Madison, USA; Prof. Urs Meier, D-MATL-ETHZ; Prof. Ian Smith, Director, IMAC-EPFL; Prof. Geoffrey Turvey, University of Lancaster, UK and Prof. Claude Morel, Director, LCC1-EPFL and President of the jury.

I also would like to thank Prof. Marie-Anne Erki, Collège militaire royal du Canada, and Dr. Toby Mottram, University of Warwick, UK, for the discussions and advice concerning pultruded-element connections and the developed structural concept.

A large part of the time devoted to preparation of the thesis was spent in the laboratory. I would like to thank the Sika AG Zurich team - Marcel Aubert, Dr. Ria de Cooman, Marcel Fleep, Roland Jäggi, Dr. Stephan Koch, Shingo Tsuno and Dr. Ambrus Zoltan - for their assistance, material testing and specimen manufacturing. Special thanks go to Victor Venetz, SIKAG AG Zurich for his assistance with the adhesively-bonded joint manufacture and the long summer days spent together preparing large-scale specimens. I would also like to thank Martin Schmid, Strength and Technology Department, EMPA, and Philippe Simonin, LMC-EPFL, for their assistance and help with material testing.

The experimental program was also made possible through the assistance of Sylvain Demierre, François Perrin, Gilbert Pidoux and Hansjakob Reist in preparing the specimens, experimental set-ups and measuring devices. The help provided by Roland Gysler, Patrice Gallay (IS-EPFL) and Laurent Gastaldo (LMR-EPFL) was also essential for this work. A particular thank-you goes to my friend and former colleague Bernard Gardel (IS-béton-EPFL) for sharing his knowledge of graphic design and advice regarding the large-scale experimental set-up.

I would like to thank my colleagues at CCLab and IS for their friendship, help and cooperation. Special thanks to Martin Schollmayer and Tommaso Tirelli for helping run tests and Florian Riebel and Aixi Zhou for assisting in the modeling investigation.

Many thanks to the those who helped prepare the thesis document: Prof. Keller (for his careful reading, valuable remarks and interesting suggestions); Margaret Howett and Craig Tracy (for converting the “French English” into American English); Dr. Etienne Fest (for his critical feedback);

Erika Schaumann (for checking figures, reading conclusions and providing the German summary) and finally Marlène Sommer (for administrative tasks).

I wish to express my sincerest thanks to my parents and friends within and without the EPFL for their unconditional support and encouragement, especially Judith Massonne for listening to my complaints when experimental investigations did not proceed as expected.

Finally, I would like to thank Etienne Fest for his help and contribution throughout these years, his critical remarks from beginning (interview preparation) to end (oral examination), including the experimental program and writing, and all his advice on becoming a good “*apprentie docteur*”.

# Table of Contents

<b>1</b>	<b>Introduction</b>	<b>1</b>
1.1	Context	1
1.2	Motivations	4
1.3	Objectives	4
1.4	Methodology	4
1.5	Thesis Organization	5
1.6	Scope and Limits	6
<b>2</b>	<b>State of the Art</b>	<b>9</b>
2.1	<b>Design Principles for all-FRP Structures</b>	<b>9</b>
2.1.1	Static System	9
2.1.2	Structural Shapes	13
2.1.2.1	Cross-section Shapes	13
2.1.2.2	Shear Deformation and Shear Coefficient	14
2.1.2.3	Local Buckling	15
2.1.3	Concluding Remarks	16
2.2	<b>Ductile and Redundant Structures</b>	<b>17</b>
2.2.1	Introduction	17
2.2.2	Ductility Theory	18
2.2.3	Ductility and Deformability Indices	20
2.2.3.1	Conventional Definition of Ductility Index	20
2.2.3.2	Ductility Index Based on Energy Considerations	20
2.2.3.3	Deformability Index	21
2.2.3.4	Overall Deformability Factor or Robustness Factor	21
2.2.4	Deformability and Robustness versus Ductility	23
2.2.5	Ductile and Pseudo-ductile Systems	24
2.2.5.1	Ductile Systems	25
2.2.5.2	Pseudo-ductile Systems	26
2.3	<b>Adhesively -bonded Joints</b>	<b>29</b>
2.3.1	Introduction	29
2.3.2	Applications	31

2.3.3	Design of Adhesively-Bonded Joints	32
2.3.4	Adhesive Characterization and Properties	34
2.3.4.1	Types of Adhesive	34
2.3.4.2	Adhesive Properties	35
2.3.4.3	Adhesive Characterization	37
2.3.5	Structural Analysis of Adhesively-bonded Joints	38
2.3.5.1	Analytical Methods	38
2.3.5.2	Numerical Finite Element Analysis (FEA)	41
2.3.6	Failure Prediction	41
2.3.6.1	Failure Modes	41
2.3.6.2	Failure Criteria and Strength Prediction	43
2.3.7	Design Manuals and Guides	45
<b>2.4</b>	<b>Concluding Remarks</b>	<b>46</b>
<b>3</b>	<b>Ductile and Redundant Structure Concepts</b>	<b>49</b>
<b>3.1</b>	<b>System Ductility and Redundancy</b>	<b>49</b>
<b>3.2</b>	<b>Concepts of Ductile and Redundant FRP Structures</b>	<b>51</b>
<b>4</b>	<b>Experimental Investigations</b>	<b>53</b>
<b>4.1</b>	<b>Adhesive Experiments</b>	<b>53</b>
4.1.1	Experiment Objectives	53
4.1.2	Specimen Description	54
4.1.2.1	Adhesives	54
4.1.2.2	Tensile Specimens	55
4.1.2.3	Compressive Specimens	56
4.1.2.4	Shear Specimens	56
4.1.3	Experimental Set-up and Instrumentation	57
4.1.3.1	Tensile Experiments	57
4.1.3.2	Compressive Experiments	58
4.1.3.3	Shear Experiments	58
4.1.4	Summary of Principal Results	59
<b>4.2</b>	<b>Double-lap Joint Experiments</b>	<b>62</b>
4.2.1	Experiment Objectives	62
4.2.2	Specimen Description	62
4.2.2.1	Dimensions	62
4.2.2.2	Materials	63
4.2.2.3	Manufacturing Process	64
4.2.3	Experimental Set-up and Instrumentation	64

---

4.2.4	Summary of Principal Results	66
4.2.4.1	Global Double-lap Joint Behavior	66
4.2.4.2	Joint Elongation and Stiffness	68
4.2.4.3	Axial Strains along Specimen and Bonded Joint	69
<b>4.3</b>	<b>Bonded Beams Experiments</b>	<b>71</b>
4.3.1	Experiment Objectives	71
4.3.2	Specimen Description	72
4.3.2.1	Dimensions	72
4.3.2.2	Materials	74
4.3.2.3	Manufacturing Process	74
4.3.3	Experimental Set-up and Instrumentation	75
4.3.4	Experimental Program	76
4.3.5	Summary of Principal Results and Discussion	77
4.3.5.1	Behavior of Simple Beams	77
4.3.5.2	Behavior of Continuous Beams	79
4.3.5.3	Behavior of Bonded Beams with 200 mm Overlap (PH1 and PH2)	79
4.3.5.4	Behavior of Bonded Beams with 300 mm Overlap (PH4)	81
4.3.5.5	Behavior of Bonded Beams with 100 mm Overlap (PH3)	81
4.3.5.6	Full-Section Elastic and Shear Moduli	82
4.3.5.7	Load-Deflection and Load-Rotation Behavior Comparisons	84
4.3.5.8	Load Transfer along the Adhesive Joint	84
4.3.5.9	Moment Redistribution and Failure Loads	85
<b>4.4</b>	<b>Concluding Remarks</b>	<b>87</b>
<b>5</b>	<b>Numerical Modeling of Adhesively-bonded Double-lap Joints</b>	<b>89</b>
<b>5.1</b>	<b>Joint FE Models</b>	<b>89</b>
5.1.1	Boundary Conditions	90
5.1.2	Geometric Considerations	90
5.1.3	Material Properties	90
5.1.4	Element Shape and Meshing	91
<b>5.2</b>	<b>Double-Lap Joint FE Model</b>	<b>92</b>
5.2.1	Description of the Model	92
5.2.1.1	Boundary Conditions and Loading	92
5.2.1.2	Geometric Considerations	93
5.2.1.3	Material Properties	93
5.2.1.4	Element Shape and Meshing	94
5.2.2	Validation of the Model	96
5.2.2.1	Specimen Load-Elongation	96
5.2.2.2	Joint Load-Elongation	96

5.2.2.3	Axial Strains Along the Specimen	100
5.2.2.4	Axial Strains in the Bonded Joint	100
5.2.2.5	Concluding Remarks	101
5.2.3	Stress Distributions	102
5.2.4	Model Sensitivity	106
5.2.4.1	Meshing Schemes	107
5.2.4.2	Adhesive-layer Geometry	107
5.2.4.3	Adhesive Material Properties	108
5.2.4.4	Laminate Material Properties	109
5.2.4.5	Geometrical Non-linearity	110
5.2.5	Strength Prediction	111
5.2.6	Analytical Method for Predicting Stiffness and Strength of ADP Joints	114
5.2.6.1	Joint Elongation and Stiffness	114
5.2.6.2	Strength Prediction	116
<b>5.3</b>	<b>Effects of Adhesive to Adherend Modulus Ratio</b>	<b>117</b>
5.3.1	Joint Stiffness	118
5.3.2	Stress Distribution	119
5.3.3	Behavior of Tailored Adhesive	121
<b>5.4</b>	<b>Concluding Remarks</b>	<b>124</b>
<b>6</b>	<b>Design of FRP Structures with Ductile Adhesively-bonded Joints</b>	<b>127</b>
<b>6.1</b>	<b>Design Philosophy</b>	<b>127</b>
<b>6.2</b>	<b>Limit States</b>	<b>129</b>
6.2.1	Serviceability Limit State (SLS)	129
6.2.2	Ultimate Limit State (ULS)	130
6.2.3	Ultimate Strength State (USS)	131
<b>6.3</b>	<b>Structural Behavior and Adhesive Choice</b>	<b>132</b>
6.3.1	Phase I - Adhesive Choice	133
6.3.2	Phase II - Adhesive Choice	135
6.3.2.1	Bending-moment Distribution	135
6.3.2.2	Structural Strength Prediction	135
6.3.2.3	Adhesive Choice	136
6.3.2.4	Robustness and Energy Factors	137
<b>6.4</b>	<b>Design Example: Bonded Pultruded Beams</b>	<b>137</b>
6.4.1	Adhesive Selection	138
6.4.1.1	Phase I	138
6.4.1.2	Phase II	140
6.4.2	Application to Experimental Beams	147



<b>6.5</b>	<b>Concluding Remarks</b>	<b>152</b>
<b>7</b>	<b>Conclusions and Future Work</b>	<b>155</b>
<b>7.1</b>	<b>Conclusions</b>	<b>155</b>
7.1.1	Structural Concept	155
7.1.2	Ductile Joints and Adhesives	156
7.1.3	Design Method	157
7.1.4	Guidelines for Ductile Adhesive Selection	157
<b>7.2</b>	<b>Future Work</b>	<b>157</b>
7.2.1	Experimental and Numerical Investigation	158
7.2.1.1	Adhesive Characterization	158
7.2.1.2	Long-term Behavior	158
7.2.1.3	Strength Prediction	159
7.2.2	Structural Concept	159
	<b>References</b>	<b>163</b>
	<b>List of Figures</b>	<b>177</b>
	<b>List of Tables</b>	<b>185</b>
	<b>Curriculum Vitae</b>	<b>187</b>
<b>Appendix</b>		<b>CD-ROM</b>
<b>A</b>	<b>Experiments on Epoxy, Polyurethane and ADP Adhesives</b>	<b>A-1</b>
<b>B</b>	<b>Experiments on Double-lap Joints with Epoxy, Polyurethane and ADP Adhesives</b>	<b>B-1</b>
<b>C</b>	<b>Experiments on Simple, Continuous and Bonded GFRP Beams</b>	<b>C-1</b>



# 1 Introduction

## 1.1 Context

The development of new materials and structural forms throughout history has been motivated by the need for improved efficiency and performance. New materials are emerging in civil engineering applications that not only offer improved performance compared to previously used materials but also overcome their weaker features. Thus, cast-iron and subsequently steel elements replaced stone and wood constructions leading to slender and lighter structures while reinforced concrete replaced cast-iron and wood constructions and led to the creation of shell structures.

When material technologies are developed, particular attention must be paid to designing appropriate structural forms, connections and manufacturing processes which take material properties into account (Keller 1999). Nevertheless, other factors such as economics and socio-politics influence structural form development (Dooley 2004). Thus, traditional steel I-shapes are more popular than closed shapes since they are simpler to roll in mild steel and easy to assemble on the building site, especially when using bolted connections. Initially concrete structures reproduced typical iron and wood frame construction since they were composed of a hierarchical structure of column, beam, floor beam and floor slab (Hennebique reinforced concrete system (Bosc et al. 2001)) but gradually they led to in-situ cast two-dimensional structures (Maillart's flat slab (Billington 1997), Isler (Chilton 2000) and Torroja (1957) shell structures). Thus, new materials were initially subjected to a substitution phase, replacing known materials, before being used in forms exploiting their material properties.

Nowadays, new materials such as high performance concrete, advanced composites and glass are appearing in the construction market. They enhance structural durability and thus reduce maintenance and rehabilitation compared with conventional materials such as steel and reinforced concrete, offering whole life cost benefits. Improvements in concrete mix design and the addition of metallic fibers have led to high performance concretes (UHPC: Ultra-High-Performance Concrete) (Habel 2004). They exhibit higher mechanical strength than reinforced concrete leading to slender elements rather than the massive elements commonly associated with concrete structures. They also display lower permeability reducing the ingress of corrosive substances. Advanced composite materials, or fiber-reinforced polymer (FRP) composites, offer several advantages over conventional

materials: high specific strength and stiffness, good resistance to corrosion and low thermal conductivity (Hollaway et al. 2001). Because of their lightness, they allow a reduction in both construction time and inconvenience in the building site environment. Contemporary architecture is increasing the demand for transparent building elements such as facade and roof structures. Traditionally glass application was concentrated on single panels with load-carrying frames (Crystal Palace (Strutt 1852)) while nowadays glazing is used as primary structural members (Laufs and Luible 2003) and thus mechanical properties and performances have been enhanced.

All these materials offer improved performances compared to conventional materials, however their costs are significantly higher. Therefore, they are employed for specific applications in aggressive environments – for UHPC and FRP – and exceptional constructions for glass. Moreover, they exhibit a brittle behavior and thus differ from conventional ductile materials. To extend their use, it is necessary to develop material-adapted structure forms, connections and construction methods that allow economic use of the material and successful integration into the construction market. Material-adapted forms mean efficient forms that exploit the material's unique properties (Keller 1998, Dooley 2004).

This thesis focuses on fiber-reinforced polymer (FRP) composites. *Composite materials* consist of at least two discrete phases, a fibrous reinforcing structure embedded in a continuous matrix which is often a resin. The reinforcement provides high strength and stiffness, while the matrix connecting the fibers assures load transfer from one fiber to another and consolidates the structure. The mechanical properties of composite materials depend on fiber and matrix properties, fiber content and fiber architecture (dimension and orientation).

Wood and bones are naturally occurring composites. Adobe (clay and organic straw fibers) was the first example of a composite material using natural substances (Mellaart 1971). Synthetic composite materials – mainly carbon (CFRP: carbon-fiber-reinforced polymer), glass (GFRP: glass-fiber-reinforced polymer) and aramid fibers (AFRP: aramid-fiber-reinforced polymer) embedded in a polymer resin – were initially developed for aeronautic, aerospace and subsequently automotive applications. Since the early 1990s they have been increasingly used in engineering structures. The first applications, concerning rehabilitation and upgrading for repair and strengthening purposes, have been accepted worldwide (Karbhari and Seible 1999, Hollaway and Head 2001, Keller et al. 2001). For new constructions, structural FRP components such as profiles and sandwiches are also starting to be used. The main applications are pedestrian bridges and bridge decks where the advantages of these materials, such as high specific strength, great insensitivity to frost and de-icing salts, and rapid component installation are appreciated (Keller et al. 2001, Bakis et al. 2002). Nevertheless, their use has been limited to a few demonstration projects. Since FRP materials were used to replace steel in construction, elements have identical cross-sections and are connected using bolts and rivets (Keller 1999, Seible et al. 1999, Mottram 1991 a). They are currently in the substitution phase. Glass fiber reinforced polymer (GFRP) members are being produced by pultrusion, an automated process used for straight profiles with a constant section and high fiber

content. This manufacturing process could become competitive since it guarantees constant quality and easy reproduction.

Despite the great potential of FRP materials, they remain largely unexploited by designers and builders due to inappropriate design codes and guidelines and certain properties that still hinder the widespread acceptance of new FRP constructions by structural engineers familiar with conventional construction materials like steel or reinforced concrete. One of these disadvantages is the lack of inherent ductility in FRP materials. Ductile materials allow redistribution of internal forces, linked with increased structural safety, dissipation of energy from impact or seismic actions as well as warning of possible structural problems thanks to large plastic or inelastic deformations before failure. A second disadvantage is the difficulty of joining structural FRP components due to the brittle fibrous and anisotropic character of the materials. The current practice of bolting is not material-adapted and in most cases leads to an over-sizing of components (Keller et al. 2001). According to Hutchinson (1997) adhesive bonding is far more appropriate for FRP materials.

The strength of well-designed adhesively-bonded joints could attain the same strength as FRP adherends while that of mechanical joints scarcely attains more than 50% of FRP adherend strength (Matthews 1987). The relatively high stiffness of brittle epoxy adhesives currently used, however, leads to high shear and through-thickness stress peaks at the edges of bonded joints (Keller et al. 2001). Furthermore, the surface preparation and adhesive application process are very demanding and simple non-destructive quality control procedures do not yet exist. Therefore, in an engineering structure composed of FRP components and adhesively-bonded joints, the unexpected failure of a bonded joint cannot be ruled out and must be considered in the structural concept.

As stress peaks at the edges of adhesively-bonded joints depend on the adhesive to adherend stiffness ratio (Renton and Vinson 1975 a), soft adhesives are preferred, although they are more affected by creep deformations and thus unfavorable for long-term serviceability requirements. Therefore, using an appropriate ductile adhesive would be more advantageous than soft adhesives and traditional brittle epoxy adhesives.

The use of adhesively-bonded joints for structural applications is not limited to FRP materials but could also be extended to other new materials such as UHPC and glass. Thus, interest in using adhesively-bonded joints in civil engineering is growing with the emergence of new materials. This method offers several advantages over more conventional methods like mechanical fastening or welding, such as the possibility of bonding dissimilar or thin adherends, making invisible connections and producing complex configurations. Furthermore, the adhesive exhibits good sealant and insulation properties. From a mechanical point of view, adhesively-bonded joints enable a more uniform load transfer and reduce stress concentrations. Despite the high potential for new types of structures offered by this method (more efficient, robust and safe), investigations in this domain are rare.

## **1.2 Motivations**

This work is motivated by several factors:

- emergence of new brittle materials such as glass, high performance concrete or advanced composites, especially fiber-reinforced polymers (FRP), in civil engineering applications;
- need to develop material-adapted structural concepts and construction methods leading to an economic use of new materials and improving their competitiveness in comparison with conventional materials – steel and reinforced concrete – in construction;
- need to overcome the drawbacks of FRP materials (brittleness, difficult joining) by developing adequate new structural concepts;
- need to develop a design philosophy and method for the new structural concept, and especially establish recommendations for the selection of the ductile adhesive, assuring robust and safe structures.

## **1.3 Objectives**

How to develop ductile structures using brittle all-FRP materials? This is the main question underlying the research presented in this thesis. In order to answer this question, the following objectives have been defined:

- develop a new structural concept that includes the use of ductile adhesively-bonded joints to provide system ductility that compensates for the lack of FRP material ductility;
- understand and characterize the structural behavior of ductile adhesives and the joints manufactured using them;
- develop a method for designing the proposed new structural concept and validate this through experimental investigation of a representative full-scale beam structure;
- provide guidelines for ductile adhesive selection.

## **1.4 Methodology**

The methodology used to attain the objectives is as follows:

- experimental characterization of brittle and ductile adhesives;
- numerical and analytical modeling and experimental investigation of lap joints using brittle and ductile adhesives;

- analytical modeling and experimental investigation of beam structures with ductile adhesively-bonded connections created using ductile adhesives;
- development of the new concept and corresponding design method;
- derivation of guidelines for adhesive selection.

## 1.5 Thesis Organization

The research presented in this thesis is divided into three parts: the first part concerns experimental investigations, the second part consists of the numerical and analytical modelings and the third part deals with the new structural concept and the design philosophy and method. The general organization of the thesis is shown in Figure 1.1.

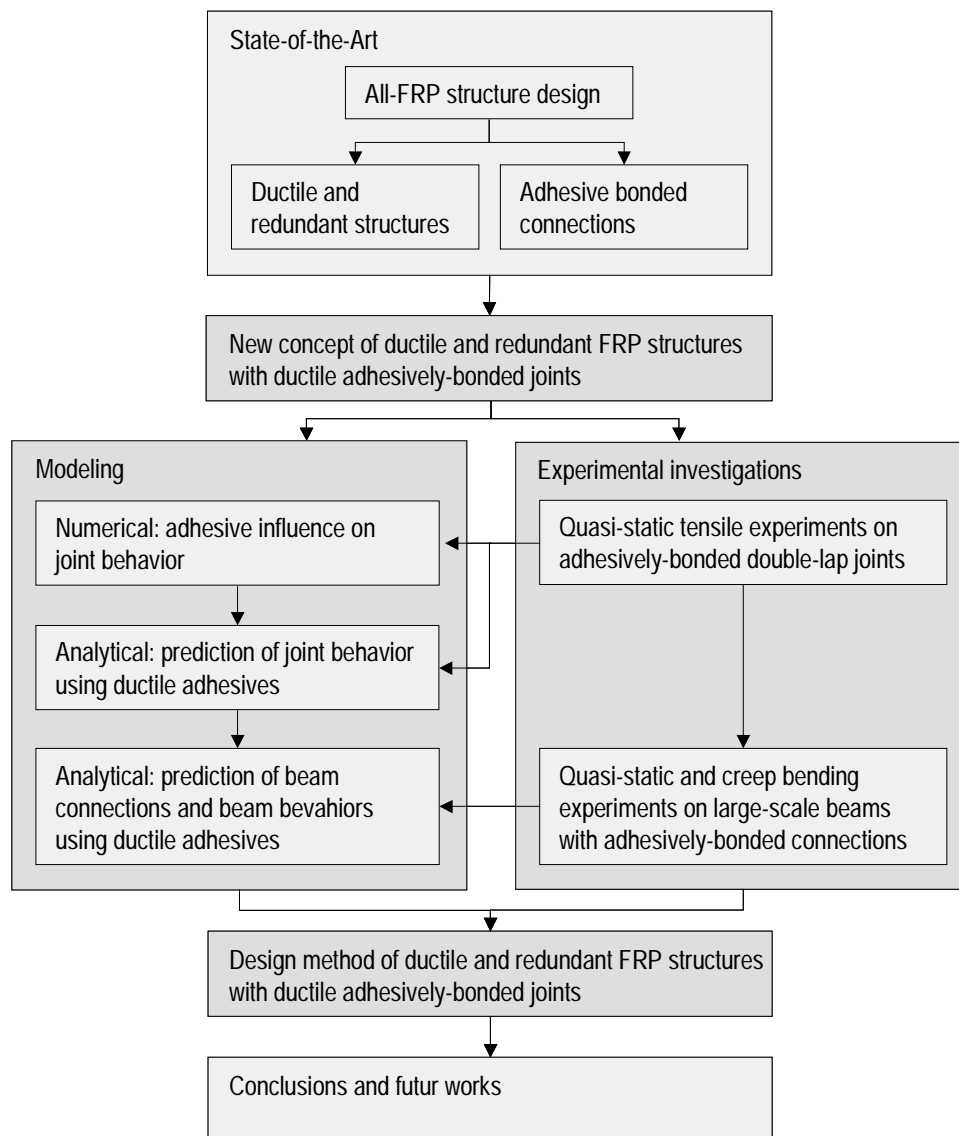


Figure 1.1: Thesis methodology and organization

The following is a summary of the chapter contents:

**Chapter 2:** The state of the art introduces the general principles of all-FRP structure design – static systems, cross-sectional shapes and connections. Concluding remarks provide justification for researching ductile and redundant structures using adhesively-bonded connections for pultruded GFRP elements. A review of ductile and redundant structures – definition, characteristics and design – and adhesively-bonded connections of composite materials follows.

**Chapter 3:** A classification of structures into ductile and redundant systems is established according to the literature survey. Then the new concept of system ductility and redundancy of FRP structures with ductile adhesive joints is described.

**Chapter 4:** Experimental investigations of adhesively-bonded double-lap joints reveal the effect of ductile adhesive behavior on joint stiffness and efficiency. Results aid adhesive selection for large-scale experiments. Subsequently, quasi-static and creep bending experiments on beams with ductile adhesively-bonded connections (large-scale) illustrate the new structural concept and demonstrate its feasibility.

**Chapter 5:** The numerical modeling of adhesively-bonded double-lap joints provides the stress distribution at the failure surface required for joint strength prediction. The modeling allows evaluation of the influence of ductile adhesive behavior on joint behavior – joint stiffness and stress distributions – and establishment of recommendations for the selection of adhesive mechanical properties according to serviceability limit state (SLS) and failure limit state (FLS) requirements. An analytical model based on experimental and numerical modeling results is developed for joint stiffness and joint strength prediction when using ductile adhesives.

**Chapter 6:** A design philosophy and design method are developed according to both numerical and analytical model results. A case study based on experimentally investigated beams with adhesively-bonded connections is carried out by way of illustration. A method for calculating bonded connection behavior is presented and validated with experimental measurements.

**Chapter 7:** Conclusions of the research and suggestions for future studies are presented. A second step in material-adapted form development is proposed consisting of elements which incorporate three different functions – load-carrying, building physics and architectural – reducing the number of building components and simplifying the construction process.

## **1.6 Scope and Limits**

This thesis limits itself to the above-mentioned tasks. The following aspects and problems require further investigations:

- practical applications of the developed structural concept;
- prediction of FRP profile's failure load caused by local buckling of the thin walls;



- 
- joint loaded in compression and bending moments;
  - fatigue behavior of adhesively-bonded joints;
  - creep behavior of adhesively-bonded joints;
  - environmental action effects and ageing of adhesively-bonded joints.

Connections were only investigated under static loads in tension. Fatigue behavior is not investigated; however fatigue studies are currently in process in the CCLab (Composite Construction Laboratory) at the EPFL (Keller and Tirelli 2003, Keller et al. 2005). Although creep behavior is not a specific subject of this thesis, one bonded beam was also subjected to a constant load for seven days – related to serviceability limit state requirements – in order to determine the magnitude of creep deformation.



---

## 2 State of the Art

The proposal of a new scientific feature requires meticulous analysis of the state of the art in the relevant field. This analysis constitutes the basis and starting point for the demonstration of the new concept. Regarding the proposal of new structures composed of brittle FRP components that include system ductility through the use of ductile adhesive joints and redundant structural systems, the following domains have to be investigated:

- Design principles for all-FRP structures focusing on static systems and structural shapes.
- Ductile and redundant structures. Concerning brittle materials, this section will describe ductility indices and provide definitions of the ductility and methods employed to deal with this specific property.
- Adhesively-bonded joints. The behavior of adhesively-bonded joints, mechanical analysis, design recommendations and strength prediction are reviewed in detail in this section.

### 2.1 Design Principles for all-FRP Structures

Aspects considered in structure design – static system, cross-sectional form of structural profiles and connection type – should integrate the main FRP properties such as anisotropic behavior, and especially the low strength in the through-thickness direction, low full-section moduli (elastic,  $E$ , and shear,  $G$ ) and material non-homogeneity and manufacturing process.

#### 2.1.1 Static System

The longitudinal Young's modulus of GFRP materials is similar to concrete stiffness (30 GPa) but since they have a much lower stiffness to strength ratio, profiles have a low flexural stiffness ( $EI$ , where  $E$  is the section flexural modulus and  $I$  is the second moment of area). The design of GFRP structures should be based on stiffness considerations (i.e. limiting deflections and preventing instabilities) and not strength considerations, as is usually the case for steel structures (Bank and Mosallam 1991, Mottram 1993, Bass and Mottram 1994). Thus, fixed connections (rigid) are preferred to hinged connections (pinned). However, these ideal connections are not easily achievable in practice and the actual connection lies between these two extremes, resulting in what is termed a "semi-rigid

connection” (partially restrained). These connections are also becoming increasingly popular in the steel industry (Chen 1987).

The action of semi-rigid connections could be demonstrated by comparing the bending moment distribution, deflections and rotations of single-span beams with different end supports. Two configurations are studied: (1) a beam with identical connections at both supports and a uniformly distributed load (Figure 2.1(a-c)) and (2) a beam with a simply-supported end and a varying end support, both beams with a concentrated load at one third of the span length (Figure 2.1(d-f)). The first case is the example traditionally described in semi-rigid connection literature due to its common use and symmetry (Bass and Mottram 1994, Mosallam 1995, Turvey 1997). The second case corresponds to the experimental investigations carried out in this study on pultruded beams (see Chapter 3). Table 2.1 summarizes the maximum moments, deflections and rotations of the three different connections for both configurations.

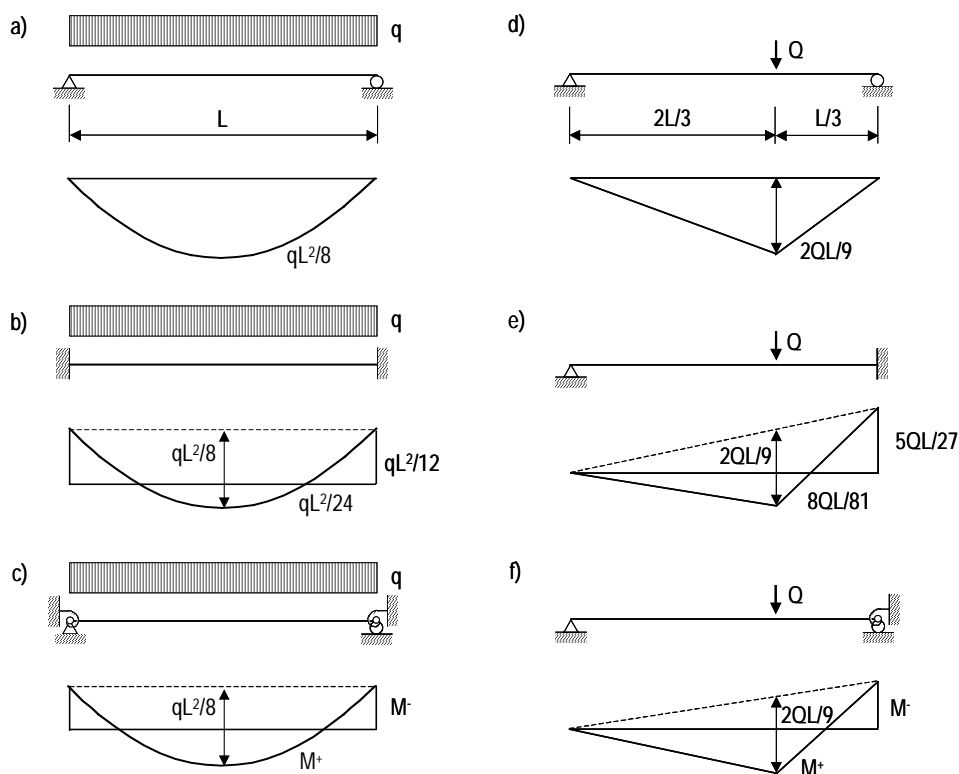


Figure 2.1: Beam with various end supports: Configuration 1 (a) simply-supported, (b) fixed, (c) semi-rigid fixed; Configuration 2 (d) simply-supported, (e) fixed, (f) semi-rigid

In a simply-supported beam the bending moment ( $qL^2/8$ ) is maximum at mid-span (Figure 2.1(a)) while in a beam with fixed supports, the maximum bending moment ( $qL^2/12$ ) occurs at the supports (Figure 2.1(b)). The hogging moment is twice the sagging moment. The deflections decrease by a factor of five and rotations at the supports became null. Figure 2.1(c) shows the beam with identical semi-rigid connections at the supports. The bending moment, deflection and rotation values lie between those corresponding to the simply-supported and fully-fixed beams. The rotational stiffness of the

connection affects the internal forces and bending moment distribution and determines whether the maximum moment will occur at the mid-span or supports. Semi-rigid connections induce a deflection reduction and failure load increase in comparison with an identical simply-supported beam. According to strength considerations, the optimum semi-rigid connection design should develop the same moment at the supports as at mid-span ( $qL^2/16$ ) for symmetrical and homogeneous sections. According to serviceability considerations, fixed end supports constitute the optimal connection design.

In the second configuration, the bending moment ( $2QL/9$ ) is maximum at the loading-point for the simply-supported beam (Figure 2.1(d)). In the beam with one fixed support, the maximum bending moment ( $5QL/27$ ) occurs at the fixed support (Figure 2.1(e)). The hogging moment is approximately 1.9 times the sagging moment. The maximum bending moment magnitude is five-sixths of that on the simply-supported beam. The loading-point flexural deflection decreases approximately by a factor of three, and the rotation at the fixed support is zero. Figure 2.1(f) shows the beam with a semi-rigid connection. As for configuration 1, bending moment, deflection and rotation values lie between those corresponding to the simply-supported and fully-fixed beams.

Table 2.1: *Moment, rotations and displacements for different end connections*

	Loading-point moment ( $M^+$ )	Connection moment ( $M^-$ )	Loading-point flexural deflection ( $w_M$ )	Connection rotation ( $\theta$ )
<b>Configuration 1</b>				
Pinned (Hinged)	$qL^2/8$	0	$5qL^4/384EI$	$qL^3/24EI$
Semi-rigid	$qL^2/24 < M^+$	$0 < M^-$	$qL^4/384EI < w_M$	$0 < \theta$
	$M^+ < qL^2/8$	$M^- < qL^2/12$	$w_M < qL^4/384EI$	$\theta < qL^3/24EI$
Rigid (Fixed)	$qL^2/24$	$qL^2/12$	$qL^4/384EI$	0
<b>Configuration 2</b>				
Pinned (Hinged)	$2QL/9$	0	$4QL^3/243EI$	$5QL^2/81EI$
Semi-rigid	$8QL/81 < M^+$	$0 < M^-$	$11QL^3/2187EI < w_M$	$0 < \theta$
	$M^+ < 2QL/9$	$M^- < 5QL/27$	$w_M < 4QL^3/243EI$	$\theta < 5QL^2/81EI$
Rigid (Fixed)	$8QL/81$	$5QL/27$	$11QL^3/2187EI$	0

q: load/unit length; Q: concentrated load; L: span; E: full-section elastic modulus; I: moment of inertia disregarding shear deformations

Connection behavior is generally characterized by the moment-rotation ( $M-\theta$ ) curve established experimentally. This curve describes the moment transmitted by the connection and the resulting relative rotation of the beam with respect to the column in a frame or of the beams with respect to the support axis in a two-span beam with a semi-rigid connection at the middle support (Figure 2.2(a)). Figure 2.2(b) shows different connection behaviors (I-VII). Curves VI and VII, close to the vertical axis ( $M$ ), represent an almost fixed connection (rigid), while curves I and II, close to the horizontal axis ( $\theta$ ), represent an almost hinged connection (pinned). The actual connection behavior is situated between these two extremes. The slope of the moment-rotation curve characterizes rotational stiffness  $k$  at a specific moment level. The inverse value  $1/k$  represents rotational flexibility.

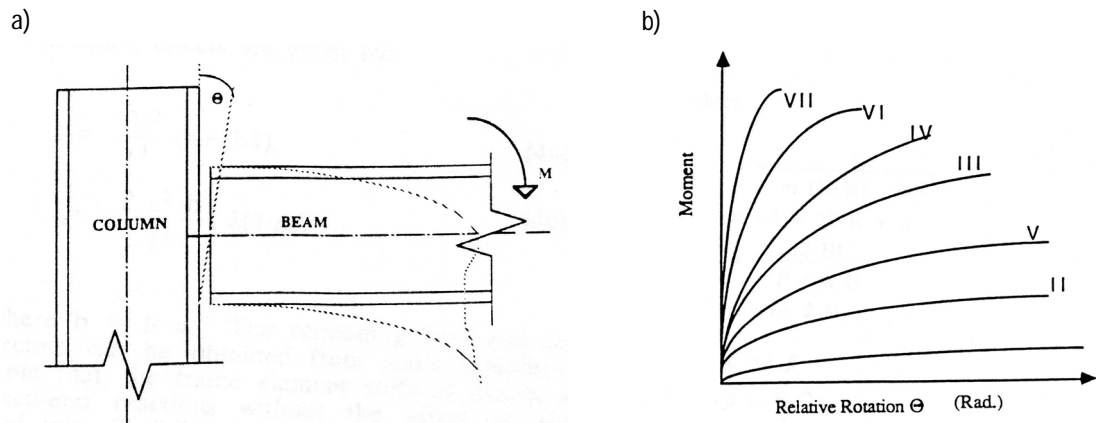


Figure 2.2: (a) Semi-rigid connection; (b) Moment-rotation curves (Mosallam 1993)

The performances of GFRP frame connections have been studied since 1988 in the form of full-scale testing and theoretical research programs on beam-to-column and column-to-base connections. Marley (1982) summarized the different connection test set-ups for steel connection characterization that were subsequently adapted for FRP connections. The first studies were performed on connections mimicking metal connection details and ignoring the material's anisotropic behavior (Bank et al. 1990, Bank et al. 1992). Connecting elements were commercially-produced FRP structural shapes not specially developed for connection purposes. The moment-rotation curves of connections were non-linear. Elastic behavior corresponded to a small portion of global capacity and full non-linear capacity was not recoverable as it was primarily due to damage in the FRP elements (Bank et al. 1990). Additionally the pultruded shapes exhibited premature failure due to local stress concentrations. Results demonstrated the inadequacy of copying metal connection details.

As mentioned, the moment-rotation curves of semi-rigid connections are non-linear. The initial rotational stiffness  $k$  is constant until the first local failure, then it generally decreases when moment is increased. The stiffness reduction is related to the progressive and irreversible damage developed in the connection and/or the beam and column sections in the vicinity of the connection (Bank et al. 1992). Failure modes are typical of pultruded materials and the result of transverse tensile failure (delamination), in-plane or through-thickness. Mosallam (1993) defined connection behavior as ductile due to its stiffness reduction caused by crack propagation while Bass and Mottram (1994) used the same term due to connected element flexibility.

In a further research stage, the test series took into account the results of past studies and the anisotropic nature of FRP materials. Research resulted in the development of a special connection element (Universal Connector, UC) (Figure 2.3). "The design criteria of the element include proper fiber orientation, ease of erection and duplication, geometrical flexibility and suitability to be used in connecting a large variety of commercially available pultruded shapes and maximizing both the overall connection stiffness and ultimate capacity" (Mosallam 1993). The connecting elements are manufactured by a molding process and fiber lay-up (Mosallam and Abdelhamid 1993). The huge increase in connection stiffness and ultimate capacity compared to initial connection details indicated the benefit of appropriate connection details. Furthermore, the connection exhibited large

deformations, providing a high energy-absorption capacity and warning before collapse, thus improving safety.

Bolted and combined (bolted and bonded) connections were analyzed in the second series. The use of combined connections increases overall stiffness and moment-transfer efficiency depending on connection design. Mosallam (1993) observed the capacity improvement, whereas Lopez-Anido et al. (1997) concluded that the application of adhesive in their studied connections did not increase ultimate load capacity in comparison with bolted connections. Mosallam (1993) designed a combined connection with the UC, achieving an initial completely fixed behavior up to 20% of the ultimate moment capacity when the adhesive failed locally. The connection then exhibited a linear behavior until it reached its ultimate capacity. The adhesive application improved serviceability and provided an additional warning before the total collapse of the mechanical connection.

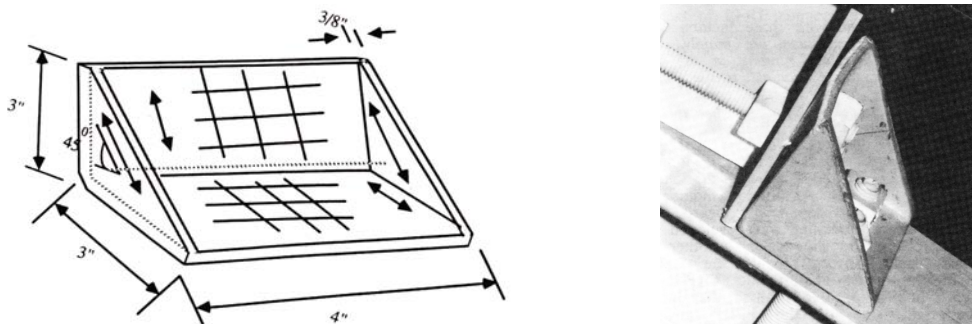


Figure 2.3: Universal Connector – UC (Mosallam 1993, Mosallam and Abdelhamid 1993)

## 2.1.2 Structural Shapes

### 2.1.2.1 Cross-section Shapes

Since FRP materials are usually used nowadays as a replacement for steel in construction, profiles have identical cross-sections (Keller 1999, Mottram 1991 a). Pultruded products are available in a variety of standard structural shapes such as I-sections, tubes and corrugated shapes (Figure 2.4(a)). The traditional use of FRP I-shapes is attributable to the common use of steel I-shapes. Steel I-shapes are more popular than closed-shapes since they are simpler to roll and easy to assemble on building sites, especially using bolted connections. However the economic considerations justifying the use of I-shape connections in steel construction are not applicable to FRP structures due to their dissimilar manufacturing process and mechanical properties. Unlike the rolling process for steel, the pultrusion manufacturing process does not favor I-shape over closed-shape elements.

Ashby (1991) described a procedure for selecting materials and section shapes for loading-bearing components. Selection of the section shape depends on the loading mode. Closed-sections and I-sections are suitable for bending, circular tubes for twisting and rectangular tubes for axial

compression leading to buckling. From the mechanical point of view, closed-sections are generally better than I-shapes because of improved local flange buckling characteristics, torsional rigidity and weak axis strength and stiffness. Smith et al. (1998) demonstrated the merit of using rectangular tubes rather than I-beams in GFRP constructions due to improved strength and stiffness of the connections. They compared the static behavior of joints used to connect I-shapes and closed-shapes (with an identical strong-axis moment of inertia) in a beam-to-column configuration. Bank et al. (1994) studied the local buckling of pultruded FRP I-shape beams and attributed the premature failure in the flange-web junction to the very small spew-fillet radii and the low torsional stiffness in the junction due to reduced continuity of fiber layers and resin-richness. This junction characteristic is unique to pultruded beams and differs from the rigid junction of steel elements. Although the flange-web junction is usually a critical point on sections, it is partially reduced in closed-sections where some fiber-layer continuity around the junction is guaranteed.

Due to the limited selection of shapes and sizes available, designers decided to make up the members from individual standard elements (I- and U-shapes) as illustrated in Figure 2.4(b). The primary load-carrying structure of the Eyecatcher building – three parallel trapezoidal frames – consists of members from assembled elements connected by means of an epoxy adhesive (Figure 2.4(b)) (Keller 1999). The two arches of the Lleida footbridge were built up in the same way (Sobrino and Pulido 2002). The rectangular tube members were made up of two U-profiles joined with flat plates using an epoxy adhesive.

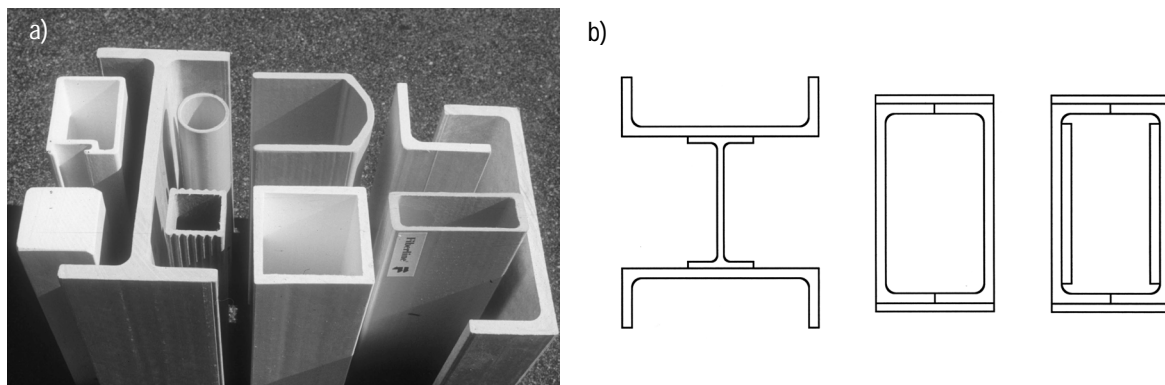


Figure 2.4: (a) Standard pultruded shapes (Fiberline Composite A/S, DK); (b) Eyecatcher building – adhesively-bonded components (CCLab)

### 2.1.2.2 Shear Deformation and Shear Coefficient

Since GFRP beams have low elastic stiffness, their design is usually governed by serviceability, deflection and buckling limitations, rather than strength limitation (Clark 1996, Chambers 1997). The exact stiffness value must be known for economic and competitive reasons. Moreover, the low shear to elastic modulus ratio ( $G/E$ ) compared to those of isotropic materials leads to significant shear deformations that cannot be disregarded and must be included in the design. In GFRP pultruded



beams, the full size beam flexural modulus is different from the flexural and longitudinal moduli of coupons (Zweben et al. 1979, Tolf and Clarin 1984). The first modulus includes structural and material mechanical properties, while the second moduli include only material properties. Thus the term “section” modulus is used to distinguish the properties measured from the “material” or “coupon” modulus. Moreover Wisnom and Atkinson (1997) observed a size effect in scaled experiments. Thus, full-size beam experiments must be carried out in order to determine beam behavior and beam mechanical characteristics.

Timoshenko (1921) extended the one-dimensional beam theory developed by Bernoulli-Euler for isotropic materials by taking shear deformations into account. He supposed that shear-strain distribution was uniform and equal to average shear stress on the cross-section, divided by the product of shear modulus  $G$  and shear coefficient  $K$ . This coefficient is a dimensionless quantity, overcoming the inability of Timoshenko’s theory to consider the real strain and stress distribution. For isotropic materials, the shear coefficient  $K$  depends on the shape of the cross-section. Cowper (1966) derived the shear coefficient for isotropic materials by integrating the equations of the three-dimensional elasticity theory. He presented a new formula for  $K$  including geometry and in-plane Poisson’s ratio  $\nu$  and indicated numerical values for commonly used solid and thin-walled beams such as thin-walled square tubes. The inclusion of a material property in  $K$  suggested that a new derivation should be performed for non-isotropic materials. Dharmarajan and McCutchen (1973) extended Cowper’s approach to orthotropic solid sections. They also indicated numerical values for certain cross-sections, rectangular for example.  $K$  depends on the geometry and mechanical properties. Bank (1987) followed Cowper’s approach to derive the shear coefficient for thin-walled cross-sections composed of orthotropic laminates. He firstly assumed that shear stress follows the contour of the cross-section and is uniform across the thickness according to the thin-walled beam theory, and secondly that the in-thickness Poisson’s ratio is zero. Formulae for rectangular and I cross-sections were developed. Omidvar (1998) modified Timoshenko’s first order beam theory to take into account actual stress distribution over the cross-section and the in-thickness Poisson’s ratio effect. He derived the shear coefficient for thin-walled cross-sections and indicated the values for rectangular, I- and T-sections. His results were identical to Cowper’s for isotropic beams and agree with Bank’s formulae.

Several methods for these moduli estimation are explained in Section 4.3.5.6 (from deflection, rotations and strains).

### **2.1.2.3 Local Buckling**

FRP beams present some disadvantages such as low resistance to concentrated loads, and weak-axis strength and stiffness (Banks and Rhodes 1980), leading to instability failure modes of GFRP, mainly local buckling of the compressive flange and lateral-torsional buckling (Barbero and Fu 1990, Barbero et al. 1991, Zureick and Shih 1998). Moreover, unlike ductile materials, the FRPs’ brittle behavior causes local damage at concentrated loads (Mottram 1991 b). From the mechanical point of view,

closed shapes are generally superior to I-shapes because of improved local flange buckling characteristics, torsional rigidity and weak-axis strength and stiffness (Smith et al. 1998).

Simplified and complex analyses have been developed for FRP orthotropic materials. Analytical solutions are based on the classical orthotropic plate buckling theory. The sections are considered as plates linked with rotationally restrained edges. The buckling load is difficult to predict due to two factors. Firstly, the large number of mechanical properties required for orthotropic materials are usually not available. Secondly, evaluation of the edge restraint provided by the web/flange junction, which differs considerably from the rigid junction of steel elements (see Section 2.1.2.1), is more complicated than for isotropic materials.

According to Bank et al. (1995) prediction of local buckling loads is influenced by several factors such as the non-linearity observed during experiments caused by the anisotropic and inhomogeneous material properties of beams. Actual material properties are required for a reliable prediction. Bank et al. (1995) demonstrated that inhomogeneity could explain discrepancies between experimental and finite element analysis results. They performed a numerical parametric study proving that in-plane shear modulus is the principal factor influencing the buckling load. Kolakowski and Kubiak (2005) analyzed the stability, post-buckling and load-carrying capacity of thin-walled composite structures and discussed the interaction between buckling modes (coupled buckling).

### **2.1.3 Concluding Remarks**

The design of FRP composite structures is governed by serviceability limit states since GFRPs present low stiffness to strength ratios. It follows that statically indeterminate systems with fixed connections (connection behavior) are more appropriate than hinged connections. Nevertheless, ideal fixed connections are not easily achievable in practice and semi-rigid connections are developed instead. The latter exhibit non-linear behavior characterized by an elastic behavior – constant stiffness – until the first local failure. Then, stiffness reduction depends on the progressive and irreversible damage propagation. Commonly used mechanical connections (joint category, see Section 2.3.1) are not appropriate to GFRP due to their brittle and anisotropic behavior and particularly their low through-thickness strength. Adhesively-bonded joints develop more uniformly distributed stresses than mechanical joints, leading to more robust joints. Moreover, relatively stiff adhesive connections create high elastic stiffness suitable to serviceability requirements. Thus the design of ductile connections (joint behavior) using ductile adhesive joints (joint category) could ameliorate structure behavior and safety.

## 2.2 Ductile and Redundant Structures

### 2.2.1 Introduction

Civil engineers regard ductility as a major safety consideration in the same way as strength when designing traditional structures in steel and reinforced and prestressed concrete. Ductility describes the ability of a material, structural element or structural system to sustain inelastic deformation prior to collapse, without significant loss of resistance and to dissipate energy during impact or reverse loading cycles (Naaman et al. 1986). Large deformations, deflections, rotations and curvatures warn of a possible structural problem before failure and can be perceived as a reliable indicator. In statically indeterminate systems, ductile materials allow redistribution of internal forces, resulting in increased structural safety.

There is no universal definition of ductility although many descriptions of quantification of material or structural member ductility are available in literature. The ductility of steel and reinforced concrete structures is traditionally expressed as the ratio of deformations at failure – deflections, rotations or curvatures – to that at the beginning of yielding. This definition is based on the steel yielding – linked with its elastoplastic behavior (Figure 2.5(a)). However, since FRP materials exhibit linear elastic behavior until brittle failure, the conventional definition is not directly applicable. Thus, a suitable ductility concept should be developed in order to quantify and compare the behavior of structures built using both brittle and ductile materials. Several studies regarding the ductility of concrete beams reinforced and prestressed with FRP bars or tendons respectively were carried out in this direction to find an appropriate ductility factor. However, few studies concerning all-FRP structures address this problem (Van Erp 2001). New concepts based on energy or deformability could also be applied to all-FRP structures.

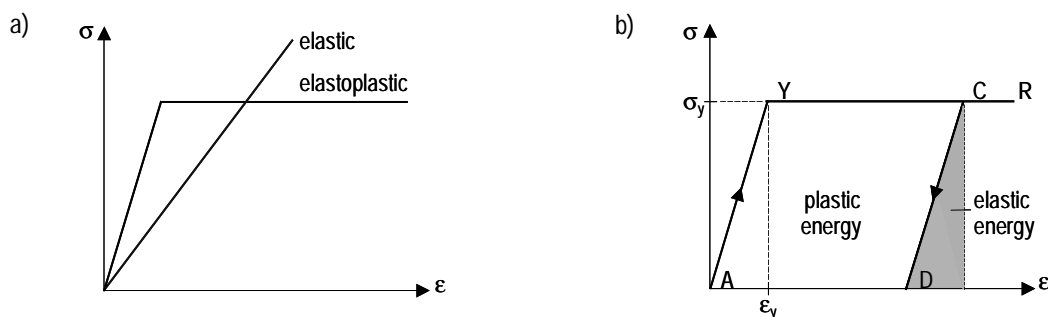


Figure 2.5: (a) Idealized elastic (GFRP) and elastoplastic (steel) models; (b) Elastoplastic model showing unloading response and energy dissipation (plastic energy)

## 2.2.2 Ductility Theory

Ductility theory has been developed since 1925 (Frey 1994) to consider the non-linear behavior of ductile materials. It is based on an idealized elastoplastic material for which the stress-strain curve consists of two straight-line segments as shown in Figure 2.5(b). As long as the stress remains below the yield stress,  $\sigma_y$ , (segment AY), the material behaves elastically and obeys Hooke's law ( $\sigma = E \cdot \varepsilon$ ). In this range, the structural member under consideration regains its initial shape after loads are removed. When stress reaches the yield stress, the material starts yielding and deforms plastically under a constant load (segment YR). If the load is removed, the unloading follows a straight-line segment parallel to the initial segment AY (segment CD). The unloading is elastic. Segment AD corresponds to the plastic – permanent – deformation resulting from the loading and unloading cycle. Figure 2.5(b) also illustrates the stored energy comprising the elastic energy, the area (DCE) located under the unloading segment, and the plastic or dissipated energy, the area (AYDC) located between the loading and unloading segments. No actual material behaves exactly as the idealized elastoplastic curve, only some steel types behaves in a similar way when hardening is disregarded. Nevertheless, the elastoplastic model is more suitable than the elastic model (Cauchy 1822) since it allows the progressive development of plastic zones to be predicted.

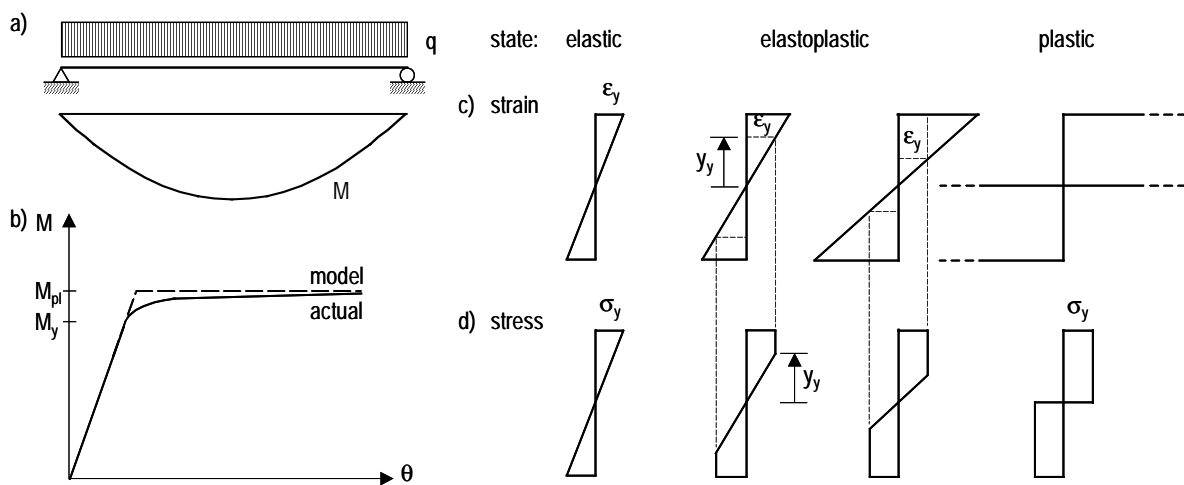


Figure 2.6: Component or material ductility – simply-supported beam subjected to uniformly distributed load (a) static system, (b) moment-curvature curve, (c) bending strain and (d) stress distributions across the mid-span section

Figure 2.6 illustrates the particular case of a simply-supported I-section beam (neutral axis coincides with the horizontal axis of symmetry) subjected to a uniformly distributed load. The axial strain and stress distributions across the mid-span section are illustrated in Figure 2.6(c-d) at different load levels indicated in the moment-rotation curve Figure 2.6(b). The first remains linear while the second varies according to load level. The axial stress distribution across the section is linear as long as maximum stresses (at the outer fibers) do not exceed the yield stress. If the bending moment is increased, the maximum stresses reach the yield stress and the outer fibers start yielding. The corresponding bending

moment,  $M_y$ , is designated the maximum elastic moment. When the bending moment increases, the plastic areas where stresses remain equal to the yield stress enlarge. The areas between plastic areas are elastic and stresses still vary linearly. The limit is reached when plastic deformations develop throughout the whole section creating a plastic hinge which leads to beam collapse (unstable structure). The corresponding bending moment,  $M_{pl}$ , is designated the plastic moment.

In statically indeterminate systems, ductility guarantees the development of plastic rotations and redistribution of internal forces from heavily loaded regions to lightly loaded regions. Figure 2.7 illustrates the case of a beam with fixed supports, a 2<sup>nd</sup> degree indeterminate structure, subjected to a uniformly distributed load. During the elastic state, the maximum bending moment ( $qL^2/12$ ) occurs at the supports and the hogging moment is twice the sagging moment (Figure 2.7(a)). The beam exhibits an elastic behavior until the hogging moment reaches the maximum elastic moment,  $M_y$  (Figure 2.7(d)). Increasing the loading leads to progressive plastification of the overall section at the supports. When the hogging moment reaches the plastic moment  $M_{pl}$  two plastic hinges develop simultaneously at the supports (Figure 2.7(b)). The structure becomes statically determinate (isostatic). If loading increases, the hogging moment at the plastic hinges remains equal to  $M_{pl}$  and the parabolic curve sinks more deeply to reach a sagging moment equal to  $M_{pl}$ . Then, a third plastic hinge develops and leads to beam collapse (unstable structure) (Figure 2.7(c)). Thus, ductility increases structural safety and assures more economical material use.

The gain in load-carrying capacity with the ductility theory rather than the elastic theory concerns both the material ductility (cross-section plastification) and system ductility (internal force redistribution).

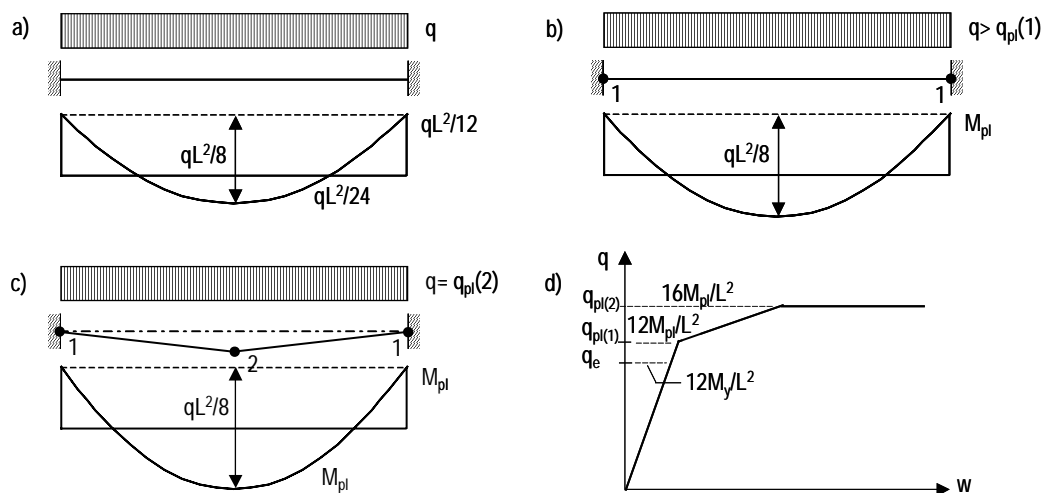


Figure 2.7: System ductility – fixed beam subjected to uniformly distributed load (a) elastic, (b) elastoplastic (two plastic hinges) and (c) plastic behavior (three plastic hinges); (d) Load-deflection curve

## 2.2.3 Ductility and Deformability Indices

### 2.2.3.1 Conventional Definition of Ductility Index

The basis for the conventional definition of ductility is an idealized load-deformation curve as shown in Figure 2.8(b), similar to the elastoplastic stress-strain curve illustrated in Figure 2.5(b). The ductility index or ductility factor is defined as the ratio of the deformation at the ultimate state to that at yield point. Conventional ductility indices are commonly expressed in terms of different parameters related to deflection, rotation or curvature as follows (Park and Paulay 1975):

$$\mu_w = \frac{w_u}{w_y} \quad \text{or} \quad \mu_\theta = \frac{\theta_u}{\theta_y} \quad \text{or} \quad \mu_\phi = \frac{\phi_u}{\phi_y} \quad (2.1)$$

where  $\mu$  is the ductility index,  $w$  the deflection,  $\theta$  the rotation and  $\phi$  the curvature. The subscript «u» symbolizes the ultimate state and «y» the yielding of reinforcements. The deflection ductility  $\mu_w$  is often used to model global ductility and is defined for a structural element or a large structure subjected to one or various loads. The rotation ductility  $\mu_\theta$  is defined for a plastic hinge subjected to a bending moment (and possibly an axial force). The curvature ductility  $\mu_\phi$  is defined for an element loaded by a bending moment. These conventional definitions are not appropriate for FRP structures since they do not yield.

### 2.2.3.2 Ductility Index Based on Energy Considerations

Another approach consists of expressing the ductility index of reinforced or prestressed concrete beams in terms of absorbed energy. Naaman and Jeong (1995) proposed that the ductility index be defined as the ratio of the total energy,  $E_{\text{total}}$ , to the elastic energy,  $E_{\text{elastic}}$ , at the ultimate state of the beam (Eq. 2.2). The total energy is the area located under the moment-curvature or the load-deflection curve at a load defined as failure load (Figure 2.8(a)). The elastic energy is the area located under the unloading curve at the same load level. Since the failure load is not easy to predict it is arbitrarily defined as the maximum load, the actual failure load or 80% of the maximum load on the unloading part of the curve.

$$\mu_{\text{energy}} = \frac{1}{2} \cdot \left( \frac{E_{\text{total}}}{E_{\text{elastic}}} + 1 \right) \quad (2.2)$$

It is observed that for an idealized elastoplastic behavior (Figure 2.8(b)), the ductility index based on energy (Eq. 2.2) is identical to that expressed with conventional rotation (Eq. 2.1). The former ductility definition provides a more general index than conventional definitions and can be used for concrete beams reinforced with either steel or FRP bars in order to compare them. Experiments carried out by Naaman and Jeong (1995) showed that the ductility index based on the energy of

concrete beams reinforced and/or prestressed with CFRP elements was lower than that of concrete beams with steel elements, which is between 4 and 4.5.

Grace and Sayed (1998) claimed that the ratio of plastic (dissipated) to total energy characterizes the ductility of concrete beams reinforced with steel and FRP bars. Both ductility definitions based on energy were developed for concrete beams reinforced and/or prestressed with FRP bars or tendons in order to compare their behavior with those reinforced and/or prestressed with steel, although they remain inappropriate for all-FRP structures.

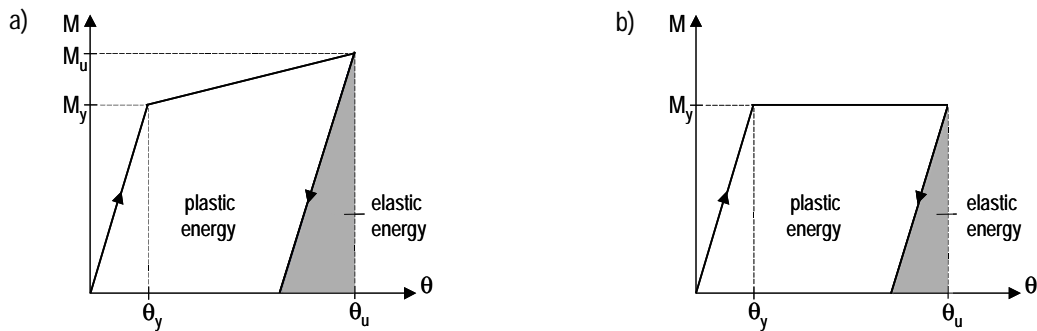


Figure 2.8: Ductility of structural members based on energy (a) general case, (b) elastoplastic case

### 2.2.3.3 Deformability Index

Abdelrahman et al. (1995) suggested using the new term “deformability” rather than the traditional term ductility for reinforced concrete beams. They proposed a deformability index as the ratio of the actual deformation,  $w_u$ , to the equivalent deformation of the uncracked section,  $w_l$ , at the ultimate state. It can be defined in terms of curvature or deflection (Eq. 2.3).

$$\mu_{\text{deformability}} = \frac{w_u}{w_l} \quad (2.3)$$

### 2.2.3.4 Overall Deformability Factor or Robustness Factor

Jaeger et al. (1995), like Abdelrahman et al. (1995), developed a new concept of deformability versus ductility and proposed a comparison method based on deformability and strength considerations instead of ductility. Since concrete beams reinforced with FRP bars are highly deformable, they recommended basing the structure design on a curvature factor, the ratio of curvature (deflection) at the ultimate state to the curvature (deflection) at a concrete strain of 0.001. This limit was chosen to represent linear stress-strain behavior in compression and defined the serviceability limit state. Moreover, they suggested considering a second factor, the strength factor, which is defined as the ratio of ultimate moment to moment at a concrete strain of 0.001. To take these two capacities into account, they defined an overall deformability factor calculated as the product of the curvature factor and strength factor (Eq. 2.4).

$$\mu_{\text{overall deformability}} = \frac{\varphi_u}{\varphi_{0.001}} \cdot \frac{M_u}{M_{0.001}} \quad (2.4)$$

The curvature factor is related to the warning of failure. Large curvatures prior to collapse indicate that the structure is overloaded and allow user evacuation. The strength factor indicates the structure's capacity to carry unexpected loads and is related to the conservative design method. Both factors indicate the structure's curvature and strength capacities and thus characterize its safety.

The overall deformability factor can be interpreted as the ratio of two energies, the energy at the ultimate state to the energy at serviceability limit state. Thus the conventional ductility index (Eq. 2.1) is a specific case of the deformability factor. Vijay et al. (1996) and Mufti et al. (1996) showed that the overall deformability factor (designated deformability factor by the former and overall factor by the latter) of an FRP-reinforced concrete beam was similar to that of a steel-reinforced concrete beam of identical strength. The curvature factor is higher for steel structures and reinforced concrete structures while the strength factor is higher for FRP structures due to their low stiffness and serviceability limit state which govern design. The overall deformability factor applies equally well to a ductile or brittle material. Mufti et al. (1996) determined that the overall deformability factor must be at least 4 for rectangular sections.

ACI440.IR-01 (2001) defines a deformability factor as the ratio of energy absorption at the ultimate strength (the area under the moment-curvature curve) to energy absorption at serviceability level. The Canadian Highway Bridge Design Code (1998) includes a section "Design for Deformability" (Bakht et al. 2000) based on Jaeger et al. (1995, 1997) and Mufti et al. (1996). Zou (2003) maintained that the sustained service load level is normally lower than or near the cracking load level and thus defined a similar deformability factor replacing the compressive concrete strain of 0.001 by first crack.

This new safety concept based on curvature and strength capacities rather than ductility could also be applied to all-FRP structures. Van Erp (2001) defined a robustness factor (Eq. 2.5) similar to the overall deformability factor (Eq. 2.5), replacing the curvature factor by a deformability factor defined as the ratio of deflection at ultimate state to deflection at serviceability limit state.

$$\mu_{\text{robustness}} = \frac{w_u}{w_s} \cdot \frac{M_u}{M_s} \quad (2.5)$$

The subscript «u» characterized the ultimate state and «s» the serviceability limit state. Van Erp (2001) provided limits for traditional reinforced concrete beams and steel beams (20) and FRP beams (16-25). Reinforced concrete and steel beams have a deflection factor of approximately 8 and strength factor of 2.5, while FRP beams have an identical deflection and strength factor of approximately 4 or 5, due to their linear-elastic behavior. The lower the structure's deformability, the greater the strength required to obtain similar safety levels.



## 2.2.4 Deformability and Robustness versus Ductility

Traditionally, a moment-rotation curve exhibiting a plateau or stiffness reduction is associated with ductile behavior. Engineers regard them as a “good thing” (Burgoyne 2001). Nevertheless, stiffness reduction and ductility are not necessarily related. Figure 2.9(a) shows the moment-rotation response of a concrete beam prestressed with unbonded low-friction steel strands (Burgoyne 2001) where the initial stiff behavior is followed by a zone of concrete continuously cracking up to failure without the steel yielding. The unloading curve is similar to the loading curve since prestress closes up the cracks. Most of the energy is elastic except for the small part dissipated via the original cracks. A similar behavior is observed for an under-reinforced beam where the FRP tendon reaches its maximum capacity before concrete failure occurs (Morais and Burgoyne 2001). Only a small part of the concrete’s plasticity develops and thus the plastic energy is small.

Figure 2.9(b) illustrates an extreme case of non-linear brittle behavior where loading and unloading curves are superimposed. Thus, stiffness reduction leads to deformability – the ability to be deformed – but not necessarily ductility. Nevertheless in both cases the stiffness reduction leads to force redistribution from the more to the less heavily loaded areas. The unloading curve before failure indicates the stored plastic or inelastic energy and thus characterizes the ductility.

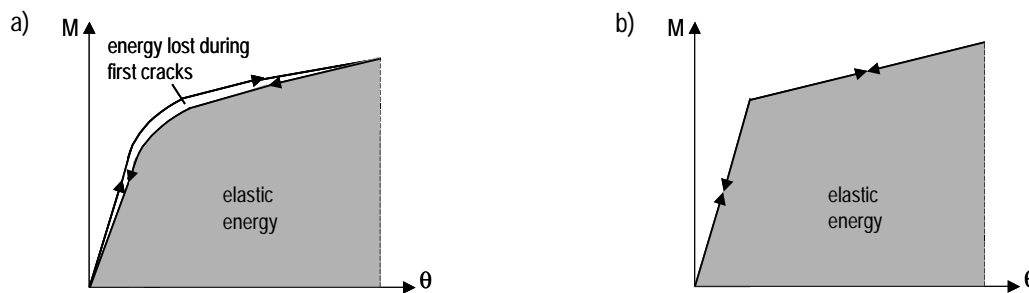


Figure 2.9: Moment-rotation curve for (a) unbonded prestressed slab (example from Burgoyne 2001), (b) non-linear brittle behavior

Real structures are usually subjected to loads and not displacements as in experimental investigations. Thus a load increase could lead to structure collapse without large deformation development and warning of failure. Figure 2.10(a) illustrates this phenomenon where an unexpected load  $\Delta Q$  increases load level from  $Q_1$  to  $Q_2$ . The structure’s behavior considered as ductile by most engineers does not warn of failure. A stiffness reduction is therefore, much more favorable for structural safety than a plateau (Figure 2.10(b)).

Only buildings in seismically active regions require energy dissipation under cyclic loading while for others structures it is only necessary to ensure deformability and stiffness reduction leading to internal force redistribution and thus strength increase. The deformability indicates the ability to give warning of collapse and the internal force redistribution the capacity to carry unexpected loads.

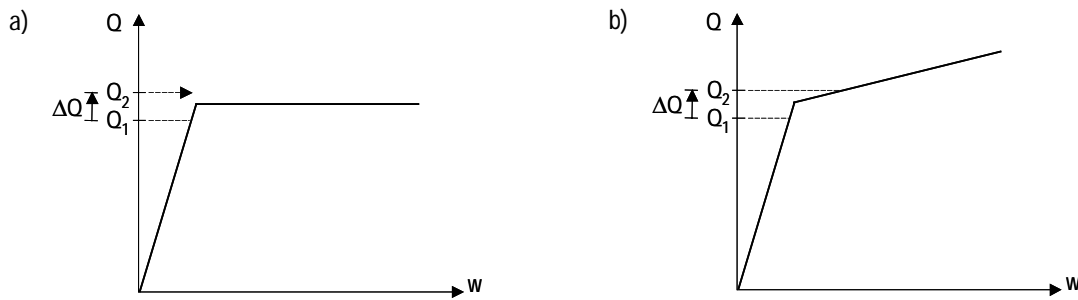


Figure 2.10: Load-deflection curve (a) idealized ductility, (b) appropriate ductility

Since the 1950s, design methods have been based on ductility theory. Reinforced concrete and steel codes establish the geometrical properties of cross-sections in order to assure plastic hinge development (Eurocodes 2 and 3 (2002)). These design methods are not appropriate for FRP structures and limit their application. However, a hundred years ago, before ductile materials were in use, structures were built using brittle materials such as wood, stone, brick and cast iron and some still remain standing. Thus, design philosophy depends on material properties; ductile materials require ductility while brittle materials require robustness, “the ability of a structure to deal with unexpected loads caused by events such as explosions, overloading, impact, abuse etc.” (van Erp 2001). It is nonetheless necessary to compare the efficiency of structures built from different materials. As previously mentioned, van Erp (2001) suggested a robustness factor independent of material properties. This factor is defined as the product of a deformability factor, related to warning of failure, and a strength factor, related to the capacity to carry unexpected loads. A trade-off between deformability and strength should be defined - the lower the structure’s deformability, the greater the strength required (FRP) and vice versa (steel and reinforced concrete).

### 2.2.5 Ductile and Pseudo-ductile Systems

Structures with the ability to deform before failure, absorb energy and allow internal force redistribution are desirable, although these three characteristics are not always required. To develop all or some of these features, researchers suggest joining dissimilar material components (members) to form hybrid structures, also called composite structures, where materials will be used to their best advantage (Hollaway and Head 2001). Thus, the following safety systems have been developed:

- ductile systems with hybrid beams combining FRP and ductile material (concrete or steel) components;
- “pseudo-ductile” systems with hybrid beams combining different FRP components.

### 2.2.5.1 Ductile Systems

#### Hybrid beams with FRP and concrete components

Several research developments have focused upon structures combining FRP and ductile materials, in particular concrete. Developments have been made in two main directions, mimicking conventional material structures: reinforced and prestressed concrete beams with FRP tendons and/or bars and composite beams with a hybrid section combining GFRP pultruded sections with a concrete layer or decks. The (low) plasticity of the compressed concrete is used to guarantee a ductile failure.

Concrete beams reinforced and prestressed with FRP bars and tendons respectively offer advantages compared to conventional concrete beams: corrosion resistance and electromagnetic transparency. As mentioned in 2.2.4, extensive experimental and analytical investigations are being performed in this field all over the world. Most concern simply-supported beams and develop material ductility – large deformations and energy dissipation – (see Section 2.2.2) Naaman and Jeong 1995, Mufti et al. 1996, Vijay et al. 1996, Grace and Sayed 1998). Morais and Burgoyne (2001) suggested supplementing the FRP member's lack of ductility by increasing the plasticity of concrete (confining, adding steel fibers).

Maissen (1997, 2000) observed the development of quasi-elastic hinges in his study of continuous concrete beams prestressed with carbon (CFRP) strands. The quasi-elastic hinges prevented collapse immediately after formation of the first hinge and allowed increased resistance and deformation of the structure. He showed that the behavior and failure mechanism of beams prestressed with carbon strands were similar to those of beams prestressed with steel strands. Continuous beams allowed internal force redistribution due to the relatively low post-tensioning level (50%) which resulted in a large strain reserve in the CFRP strands. They developed system ductility (see Section 2.2.2).

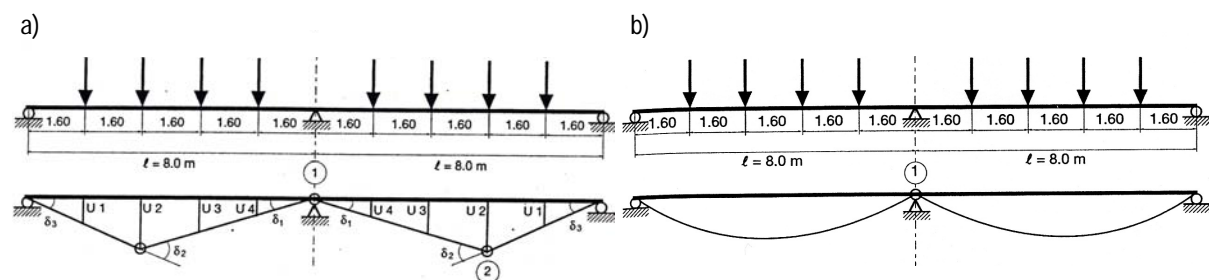


Figure 2.11: Static system and failure mechanism of concrete beams with (a) steel strands: first plastic hinge forms over the mid-support and second in the right-hand span, (b) CFRP strands: an elastic hinge forms over the mid-support (Maissen 2000)

One of the first hybrid beams comprised concrete cast into FRP boxes (Fardis and Khalili 1981). The FRP's mechanical role was to carry tensile force in the tension zone and shear force through the webs. The concrete's role was to provide compressive strength, rigidity to prevent local buckling of the top FRP flange and ductility. Thus both materials are used to their best advantage. Triantafillou and Meier (1992) and Deskovic et al. (1995) improved the concept by reducing the concrete area and presented an innovative hybrid box section for simply-supported beams (see Figure 2.15(a) page 28).

This concept had been transformed into a real beam structure (van Erp 2002). Canning et al. (1999) and Hulatt et al. (2003) detailed the development of a composite/concrete duplex beam for rectangular- and T-sections following an optimization study of different configurations.

Designing hybrid structures correctly leads to the crushing failure of concrete and develops material ductility. Nevertheless, the use of low-weight FRPs does not result in a significant reduction in structure self weight. Hybrid beam efficiency also requires composite action and thus the appropriate connection system – water-based adhesive and mechanical connectors (Deskovic et al. 1995, Canning et al. 1999, Hulatt et al. 2003).

### Hybrid beams with FRP and steel components

FRP bridge decks connected to steel girders are an example of hybrid beams with FRP and steel components. Research is being conducted on connection methods – mechanical (Solomon and Godwin 2002, Park et al. 2004, Stiller et al. 2004) and adhesively-bonded (Keller and Gürtler under review) – to assure composite action between all components. Keller and Gürtler (in press, a) reported on ductile failures of hybrid GFRP and steel girders (Figure 2.12). Brittle GFRP bridge decks failed during yielding of the bottom steel flanges.

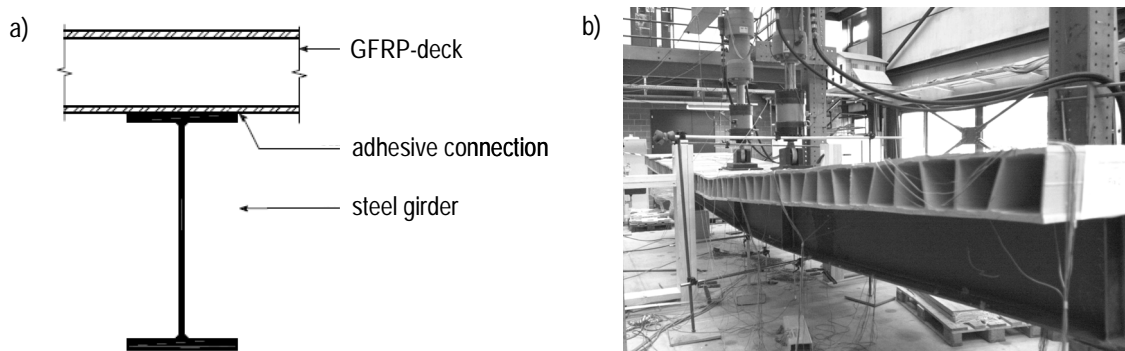


Figure 2.12: Hybrid GFRP and steel girder (a) cross-section, (b) deflection at the onset of failure, plastic hinge between the jacks (CCLab)

### 2.2.5.2 Pseudo-ductile Systems

Non-linear inelastic load-deformation behavior, showing decreasing stiffness with increasing load similar to the behavior of ductile structures, can be achieved by progressive failure of brittle components or connections (Figure 2.13). To prevent structural collapse, however, structural redundancy is required. In contrast to ductile structures, however, pseudo-ductile structures can dissipate energy only within a limited number of loading cycles, depending on the degree of static indeterminacy. With a statically determinate system, after a certain number of failures, further failure would lead to a brittle collapse of the structure. Figure 2.13 illustrates the pseudo-ductile behavior of

a redundant structure composed of three components. The failure of components 1 and 2 produces energy dissipation and the failure of component 3 leads to the structural collapse.

The redundancy is a requirement for pseudo-ductile systems and could be realized through statically indeterminate systems and cross-sectional redundancy.

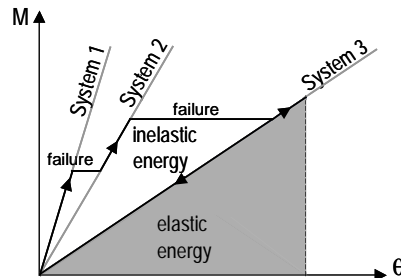


Figure 2.13: Pseudo-ductile behavior

### Structural redundancy (statically indeterminate system)

Statically indeterminate systems provide alternative load paths in case of failure of a component or connection. An example is the truss structure of the Pontresina pedestrian bridge with adhesively-bonded joints in one span (Keller 1999) (Figure 2.14). The crossed diagonals offer alternative load paths in case of failure of one or several of the components or bonded joints. Furthermore, the addition of bolts in the adhesive joints provides a mechanical back-up system. Other pedestrian bridges – Technics bridges as Antioch bridge, Homestead bridge – present the same redundant structure (Keller et al. 2001).



Figure 2.14: Redundant system – structural redundancy: Pontresina bridge (CCLab)

### Cross-sectional redundancy

Cross-sectional redundancy is provided in multi-component cross-sections. Combinations of rigid carbon fiber laminates and flexible glass fiber sections (two components) were proposed by Triantafillou and Meier (1992) (Figure 2.15(a)). The carbon fiber laminates are used to increase

stiffness in the serviceability limit state while the glass fiber sections increase deformations before failure (and assure the strength). Failure of the first material is interpreted as warning of future collapse. A similar concept was developed for a modular bridge system incorporating GFRP/CFRP girders (two components) and a fiber-reinforced concrete deck (Karbhari and Seible 1999) (Figure 2.15(b)). In both examples a concrete layer was added on the top flange providing compressive strength and rigidity to prevent local buckling of top FRP component flange (see Section 2.2.5.1). Based on a similar concept, Razaqpur and Ali (1996) developed concrete beams reinforced externally by bonded carbon fiber sheets and internally by a low modulus polypropylene fiber grid.

The sandwich girders with adhesively-bonded flanges (Keller et al. 2004) illustrated in Figure 2.15(c) and the built-up sections of the “Eyecatcher” building (Keller 1999) are further examples. The former girder web is composed of two GFRP sandwich elements and the flanges consist of four GFRP pultruded profiles (square hollow-, L- and flat-shape). Single cross-sectional components, or the adhesive bond between single components, can fail without failure of the whole section, avoiding brittle failure and providing warning of structure collapse. Internal stress redistribution operates in the cross-section like internal force redistribution in ductile statically indeterminate systems.

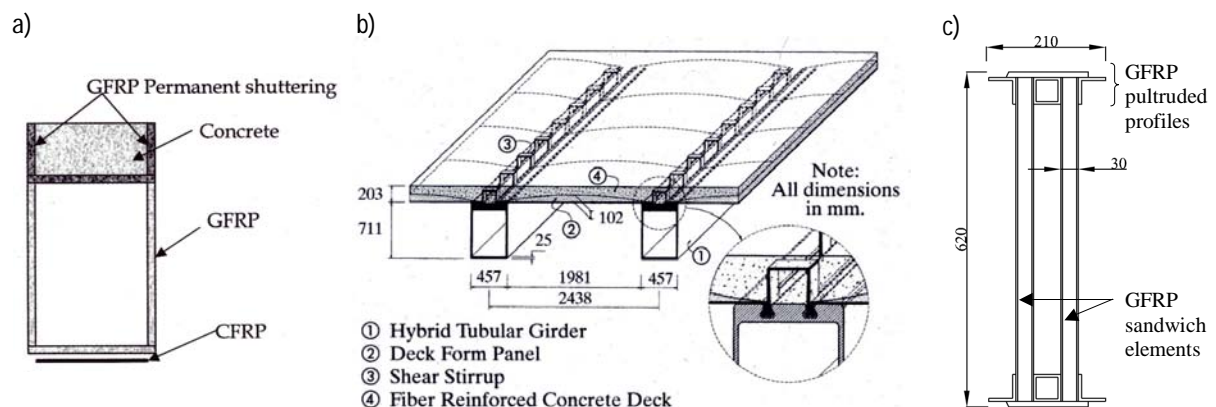


Figure 2.15: Redundant system – cross-sectional redundancy: (a) hybrid GFRP/CFRP and concrete section (Triantafyllou and Meier 1992), (b) modular bridge system incorporating GFRP/CFRP girders and fiber-reinforced concrete deck (Karbhari and Seible 1999), (c) hybrid girder with GFRP sandwich panels and pultruded profiles adhesively-bonded (Keller et al. 2004)

A pseudo-ductile behavior can also be developed at the component level. The non-linear inelastic increase in deformation due to stiffness loss in the brittle FRP components is caused by progressive internal failures. Keller and Gürtler (in press, b) reported on experiments on bridge deck specimens subjected to in-plane shear loading. Transverse bending in the deck webs led to progressive local delamination failures and non-linear inelastic behavior, similar to the behavior of a ductile material. Thornton and Edwards (1982) and Farley (1986) studied the effect of geometry (thickness to diameter ratio) and fiber architecture (lay-up) on energy absorption when tubular specimens are subjected to axial loading. Karbhari and Haller (1998) showed the increased energy absorption of braided tubes when size and fiber types are hybridized. Harris et al. (1998) developed an FRP bar

combining different reinforcing fibers – with different fiber architecture and fiber content – with a bilinear stress-strain and a Young's modulus approaching that of steel. The bar failed in a gradual manner. Bakis et al. (2001) followed the same approach for FRP bar design.

## **2.3 Adhesively-bonded Joints**

### **2.3.1 Introduction**

Structures are built from linear or surface components and connections, which should assure continuity and internal force transfer between components. Thus, connections enable large structures to be built, new forms to be developed and different materials to be combined. However, connections are critical points since they usually weaken the structure and thus proper design is crucial to maintaining the structure's load-carrying capacity. Connections in FRP structures are weaker due to the material's anisotropic and brittle properties. The former lead to stress concentrations and the latter do not allow stress redistribution. Connections used on FRP structures are classified into the following categories (Hutchinson 1999, Tierney et al. 2000):

- mechanical connection;
- bonded connection;
- mixed connection;
- interlocking connection;
- welded connection.

“The use of appropriate joining techniques and the satisfactory fabrication of joints is fundamental to the successful exploitation and use of FRP materials” (Hutchinson 1997). As the anisotropic and brittle behavior of FRP is totally different from that of isotropic steel, the use of mechanical connections is not appropriate and leads, in most cases, to over-sizing of the components (Keller et al. 2001) (Figures 2.14 and 2.16(a-c)).

Adhesive bonding is far more appropriate for FRP materials (Hutchinson 1997). The strength of well-designed adhesively-bonded joints could reach FRP adherend strengths while that of mechanical joints scarcely attains more than 50% of FRP adherend resistance (Matthews 1987). Moreover adhesively-bonded joints are stiffer than mechanical fasteners. From a material point of view, the adhesive seems to be very suitable since it is a polymer, like the resin composing the matrix of FRP materials, with similar chemical composition and mechanical properties (Hutchinson 1999).

Mixed connections, combining bolts and adhesive or rivets and adhesive, guarantee the most rigid and resistant connections. In a serviceability state, the adhesive transmits most of the force while the bolts or rivets ensure a certain pressure during the joining process.

Maunsells Structural Plastics Ltd. (Beckenham, Kent, UK) developed interlocking connectors for the Advanced Composite Construction System (ACCS) shown in Figure 2.16(d)). Plank units (multi-cell box sections) can be assembled into a large variety of different structures – buildings, pedestrian and road bridges (Aberfeldy bridge, Scotland (1992), Bonds Mill Lift bridge, Gloucestershire (1994) UK) – by sliding a toggle section into the groove of each panel where an adhesive layer had been previously applied (Hollaway and Head 2001).

Welded joints could guarantee performance and economic advantages but are restricted to materials containing thermoplastic resins (Tierney et al. 2000). This connection seems the most appropriate to composite materials.

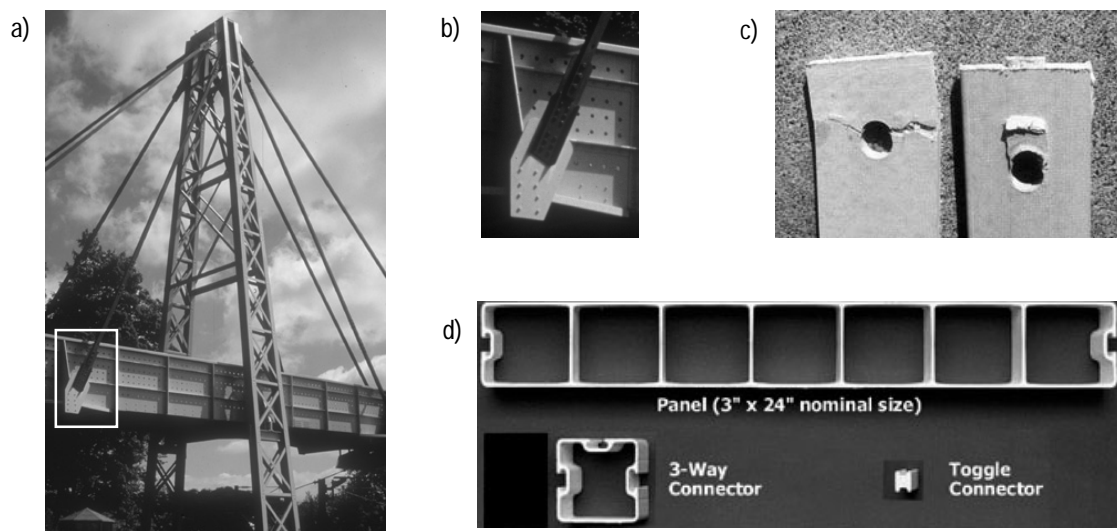


Figure 2.16: Mechanical connection (a) partial view and (b) detail of pedestrian bridge in Strandhude, DK (Braestrup 1999), (c) failure modes (CCLab); (d) Advanced Composite Construction System (Maunsell Structural Plastics, UK)

In order to clarify terms used in the study, their definitions, according to the Institution of Structural Engineers (1999), are presented. An extended glossary concerning adhesive technology is presented in ASTM D907-96a (1996) and EN 923 (1998). Figure 2.17 shows the adhesive joint components and geometrical characteristics.

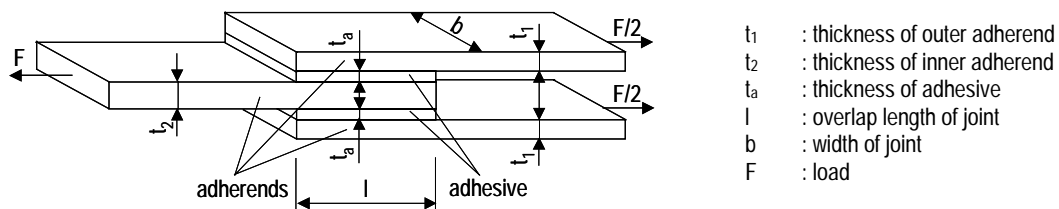


Figure 2.17: Parameters of adhesively-bonded double-lap joints



*Adherend* – A member of a bonded joint (also designated substrate).

*Adhesion* – The attraction between surfaces whereby, when they are brought into contact, work must be done to separate them.

*Adhesive* – A polymeric material capable of holding two materials together by surface attachment.

*Bond* – The adhesion of one surface to another, with the use of an adhesive or bonding agent.

Table 2.2 summarizes the advantages, disadvantages and limitations of adhesively-bonded joints.

Table 2.2: *Advantages and disadvantages of adhesively-bonded joints (Hutchinson 1999, The Institution of Structural Engineers 1999)*

Advantages	Disadvantages/Limitations
Ability to bond dissimilar adherends	Complexity of manufacturing process, especially the surface treatment required
Ability to bond thin adherends	Curing time to achieve full load-carrying capacity
Ability to make invisible connections (aesthetically good)	Carefully controlled environmental conditions during assembly and curing
Ability to produce complex configurations	Adhesive's properties are time-dependent
Better control of tolerances	Sensitivity to effect of environmental agents (temperature and moisture) on durability
Good sealing properties of adhesive against gases, moisture, chemicals	Adhesive's properties affected by temperature; strength reduction at high temperature and brittle failure at low temperature
Good insulating properties of adhesive layer against electricity, heat, sound	Possible toxicity
Lightness	Difficulty of inspection
Increased stiffness	Difficulty of dismantling
Increased dynamic damping	Lack of recognised design guide (only for some materials)
Reduced sensitivity to fatigue (reduced stress concentrations)	Lack of long-term experience in some applications

### 2.3.2 Applications

Bonding technology has a long history dating back to 3000 BC. Adhesives were initially based on plant and animal substances and were used by the Egyptians, Romans and Chinese to bond paper, stone and wood (Schindel-Bidinelli and Gutherz 1988). During industrialization, in the 19<sup>th</sup> century, natural adhesives were synthetically modified, increasing their performances. The real evolution came during the Second World War, when the first fully synthetic adhesives were developed. Improved adhesive properties increased their use for structural applications in many sectors, firstly in the aerospace industry and then in land transport, infrastructures and naval applications. Structural adhesives were initially used in the aerospace domain for wooden structures – the "Mosquito" aircraft was one of the most successful wooden structures bonded with epoxy adhesive (de Bruyne, 1957) – then for metals and finally for composite materials. Nowadays engineering adhesives are based on synthetic polymers such as epoxy, urethane, acrylic and phenolic (Kinloch, 1987).

Adhesively-bonded joints are seldom employed in the construction industry due to lack of knowledge in the field of civil engineering and the absence of dimensioning standards. According to the

Institution of Structural Engineers (1999), the greatest use of structural adhesives in civil engineering, more than 75%, is estimated to be in repairs (Hollaway and Head 2001, Meier 1987). As for construction materials, the greatest use of adhesives is with timber, in the form of fabricated products – plywood and glued laminated timber (glulam) – and for member connections (Davis 1997). Adhesives are also extensively used for glazing (Laufs and Luible 2003) and in connections between concrete precast units such as in glued segmental bridges or the segments of the Sydney Opera House). Further information on adhesive joint applications is presented in the Guide to The Structural Use of Adhesives (The Institution of Structural Engineers 1999) and Mays and Hutchinson (1992).

The pedestrian bridge in Pontresina (CH, 1997) illustrates the use of adhesively-bonded joints combined with mechanical connections in GFRP structures (Figure 2.14) (Keller 1999). The truss bridge has two spans; one comprises mechanical connections while the other has connections adhesively-bonded with an epoxy resin. For safety reasons, since the bridge is a public structure and the use of adhesive joints is not yet standardized, the adhesively-bonded joints were also bolted.

The Eyecatcher building (CH, 1998) consists of columns and beams assembled from standard sections to obtain higher and more complex sections than those currently available (Figure 2.4(b)) (Keller 1999). Figure 2.18 shows the (a) open cross-section and (b) manufacturing process of closed cross-section. Components were connected with an epoxy resin. The load-carrying elements were mechanically connected however since the building was dismantled and rebuilt after its first use. This technique was subsequently applied for the construction of a GFRP footbridge near Lleida (2001) in Spain (Sobrino and Pulido 2002).

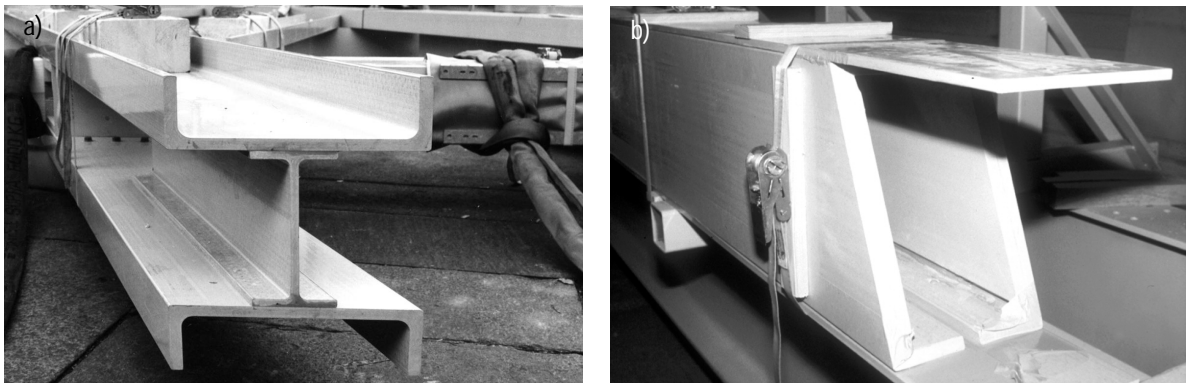


Figure 2.18: Eyecatcher building (a) open cross-section, (b) closed cross-section manufacture (CCLab)

### 2.3.3 Design of Adhesively-Bonded Joints

Several aspects must be considered in the design of adhesively-bonded joints: bonded area geometry, selection of a suitable adhesive with the appropriate properties and consideration of stress distribution in the adhesive and adherends while in service. Mays and Hutchinson (1992) have identified some general principles for designing adhesively-bonded joints:

- provide the maximum bond area;
- stress the adhesive in the direction of the adherend's maximum strength;
- avoid stress concentrations;
- make the adhesive layer as uniform as possible to avoid stress concentrations;
- maintain a continuous bond line.

The joint should be designed to transfer the load in the direction of the adherend's maximum strength and avoid or minimize loading in the weak direction (through-thickness). Thus, joints loaded in shear and compression are preferred to joints loaded in tension and through-thickness (also designated normal, out-of-plane and peel). The latter two loading modes should be minimized since they are dominated by high tensile stresses. Figure 2.19 shows typical adhesive joint configurations. The single-lap joint is one of the most common joints used in the industry since it is cheap and easy to manufacture.

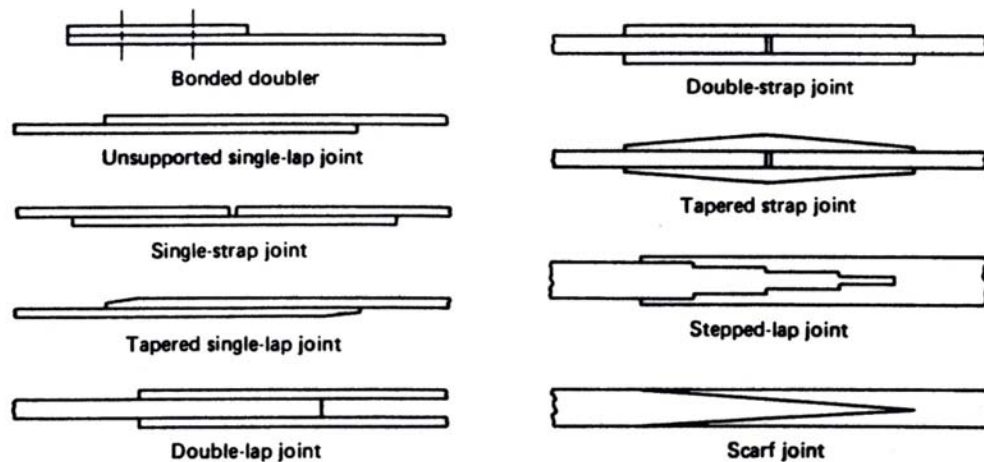


Figure 2.19: Typical structural adhesive joint configurations (Hart-Smith 1987)

The eccentricity of the forces induces through-thickness stresses in the adhesive and adherends. Its effects are greatest in lap- and strap-joints. They must be reduced as much as possible but stress peaks still exist in all adhesive joints, at the end of the adhesive layer, and depend on the adhesive to adherend stiffness ratio (Renton and Vinson 1975a). Stiffer adhesives cause higher shear and through-thickness stress concentrations than soft adhesives. Figure 2.20 shows the (a) shear and (b) through-thickness stress distributions in a single-lap joint along the overlap length, at bondline, using stiff and soft adhesives. Both stresses reach their maximal values at overlap ends.

Hutchinson (1999) has defined two principal requirements for structural adhesives:

- relative ductility;
- resistance to creep effects and environmental conditions (high temperature and moisture).

The use of relatively ductile adhesives (Hart-Smith 1987) and modification of joint geometry – adhesive spew-fillets, adherend scarfing and tapering – even out load transfer and reduce stress concentrations (Adams and Peppiatt 1974, Adams and Harris 1987, Tsai and Morton 1995, Lang and Mallick 1998).

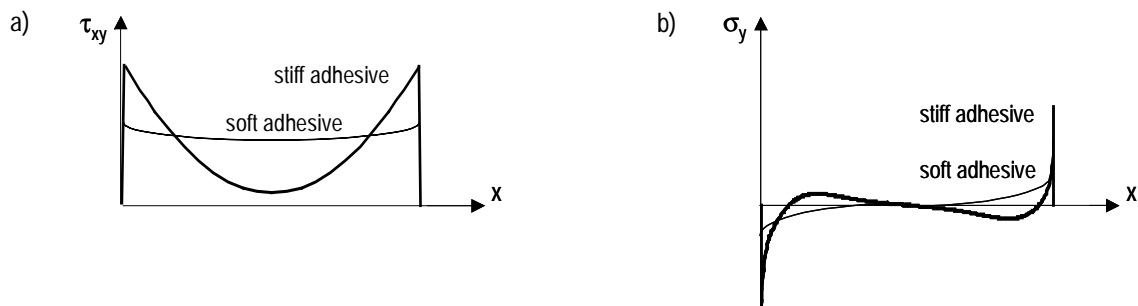


Figure 2.20: Typical elastic stress distribution along the overlap length at the adhesive centerline in a single-lap joint, made with adhesives with low and high modulus (a) shear, (b) through-thickness

## 2.3.4 Adhesive Characterization and Properties

### 2.3.4.1 Types of Adhesive

Adhesives are polymers such as the resin (matrix) included in composite materials. They are classified as thermoplastic or thermoset, depending on their molecular structure (cross-linking process) and the effect of temperature on their hardening state. A thermoplastic is “capable of being repeatedly softened by an increase of temperature and hardened by a decrease in temperature” while a thermoset “is cured by heat and pressure or with a catalyst into an infusible and insoluble material; once cured, a thermoset cannot be returned to the uncured state” (Hollaway and Head 2001). Adhesives are available in a wide variety of forms including liquids, thin-films, or pastes and as one or two components. In the latter, a hardener, or catalyst, is mixed with the resin to promote polymerization (curing). Heat could be required.

Engineering adhesives suitable for FRP materials are epoxies, thermosetting polyurethanes and acrylics. Table 2.3 summarizes the principal properties and characteristics of these adhesive families. High strength is usually linked to low ductility and toughness. Epoxy resin adhesives are strong and durable. They generally exhibit low creep and resist environmental effects well. Polyurethane adhesives are slightly weaker than epoxies and more susceptible to creep and moisture effects. Acrylics are softer and more ductile than epoxies. Toughened acrylic adhesives are generally used for structural applications. Thermoplastic acrylics exhibit significant creep, particularly at high temperature. Additional explanations concerning adhesive use in engineering applications are found in Mays and Hutchinson (1992) and Lees (1989).

Table 2.3: Typical properties and characteristics of some structural adhesives (The Institution of Structural Engineers 1999)

Property (at 20°)	Epoxy	Polyurethane	Acrylic
Shear strength [MPa]	15-35	15-25	15-25
Shear modulus [GPa]	0.5-2	0.1-0.2	0.01-0.02
Shear failure strain [%]	5-50	50-200	50-200
Tensile strength [MPa]	20-40	15-25	15-35
Tensile modulus [GPa]	1-10	≤ 0.5	≤ 0.5
Tensile failure strain [%]	1-4	10	50
Glass transition [°C]	30-70	40	50
Poisson's ratio [-]	0.3-0.4	0.4	0.43
Thermal expansion [ $10^{-6}/^{\circ}\text{C}$ ]	15-35	15-25	15-25
Characteristics			
Creep resistance	Excellent	Poor	Poor
Moisture resistance	Excellent	Fair	Good
Heat resistance	Good	Fair	Fair
Cold or hot cure	Both	Cold	Cold
Cure time	Medium/long	Medium/short	Short

### 2.3.4.2 Adhesive Properties

The stress-strain curve for an adhesive varies according to the operating environment, i.e. both temperature and loading rate. In general, an increased loading rate has an effect equivalent to temperature reduction upon properties such as the elastic modulus ( $E_c$ ) and stress ( $\tau_c$ ) (Figure 2.21(a)). This increases the adhesive's stiffness and reduces its ductility. Nonetheless, the strain energy, proportional to the area under each stress-strain curve, remains similar (Hart-Smith 1990). The dependence of properties upon loading rate and temperature characterizes visco-elastoplastic materials. Thus, estimations made with bulk properties could differ from adhesive joint behavior because of differences in operating environment.

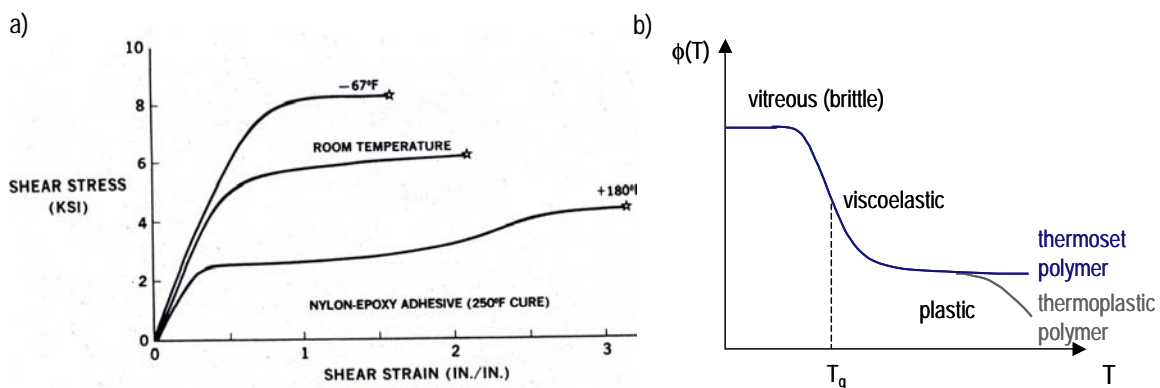


Figure 2.21: (a) Effect of temperature on adhesive behavior (Hart-Smith 1987); (b) Polymer state dependency on temperature

The glass transition temperature ( $T_g$ ) is the approximate mid-point of the temperature range over which a polymeric material changes from a relatively stiff and brittle material to a viscous material

(The Institution of Structural Engineers 1999). Figure 2.21(b) illustrates the phenomenon, where  $\phi(T)$  is a material's mechanical property.

In contrast to metal joints, GFRP joints usually fail in the adherends rather than in the adhesive layer (see Section 2.3.6). Nevertheless, adhesive behavior must be characterized since it influences load transfer in the joint, and then ultimate failure in the adherends. The adhesive layer is subjected to a complex stress state (Figure 2.20). This can be related to available stress-strain data by the evaluation of an "effective" uniaxial tensile stress equivalent to the combined stress state. The state of stress may be obtained by superimposing the hydrostatic and deviatoric stresses (Figure 2.22) (Adams and Coppedale 1979). The hydrostatic stress component, also called second stress invariant, is the mean of the three normal stresses, while the deviatoric stress component, also called first stress invariant, is the normal stress reduced by the value of the hydrostatic stress component. The hydrostatic stress component tends to change the material's volume, but not its shape, since all the faces of the element are subjected to the same stress. The deviatoric stress component tends to change the shape of the material element, or distort it, but not its volume. For ductile isotropic materials, the "effective stress" depends on the deviatoric component of stresses. This is the case for the commonly known yield functions postulated by Tresca and von-Mises. However, for adhesives and all polymers, it has been found that the effective stress depends on the deviatoric and hydrostatic components of stresses. This is due to a significant difference between the stress-strain curves and yield stress level under uniaxial tension and uniaxial compression loading (Ikegami et al. 1979).

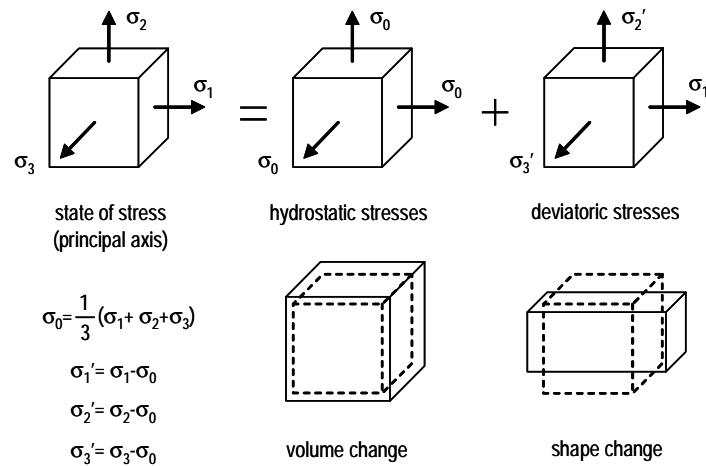


Figure 2.22: Hydrostatic and deviatoric stress components and associated material changes

Various von-Mises modified functions have been developed: the first one was adapted from Raghava and Caddell (1973) by Peppiatt (1976) and another one has been presented by Gali et al. (1981). Both include the ratio between the compressive and tensile yield stress or strength values. Nevertheless, Jeandreau (1991) disregarded the volumetric component of stress and used the von-Mises criterion which gives the following relationships:

$$\sigma_t = \sigma_c = \sqrt{3} \cdot \tau \quad (2.6)$$

$$\varepsilon_t = \varepsilon_c = \frac{\sqrt{3}}{2 \cdot (1 + \nu)} \cdot \gamma \quad (2.7)$$

where  $\sigma_t$ ,  $\sigma_c$ ,  $\tau$  are the tensile, compressive and shear stresses,  $\varepsilon_t$ ,  $\varepsilon_c$ ,  $\gamma$  are the tensile, compressive and shear strains and  $\nu$  is the Poisson's ratio.

### 2.3.4.3 Adhesive Characterization

An understanding of adhesive behavior is essential for predicting joint deformation and strength. Unfortunately however there is a lack of reliable data concerning the mechanical properties of adhesives. Since few adhesive manufacturers are currently able to supply the appropriate adhesive mechanical properties of interest to designers, mechanical testing has to be carried out. Industrial, governmental and research groups have developed an extensive variety of standard test methods, which are updated and revised. The most commonly used standards are the ASTM (American Society for Testing and Materials), ES (European Standards) and ISO (International Standards Organisation). Adams et al. (1997) present a brief overview. Intrinsic mechanical characteristics can be measured in two ways:

- on the bulk adhesive material;
- on adhesively-bonded joints, in the thin layer form;

using a static or dynamic testing method. The testing of bulk specimens determines adhesive properties without influence from the adherends. These properties are obtained under a uniform and uniaxial state of stress – tension, compression, flexiure and torsion. Testing of bulk specimens is easier than that of adhesive layers since the elastic deformations are larger and can therefore be measured more accurately using standard extensometers or strain gages. The most difficult part is to manufacture specimens without defects such as voids and porosity, since air bubbles trapped during mixing are difficult to remove if the adhesive is very viscous or has a short pot-life. The testing of adhesively-bonded joints must be correctly designed to ensure a uniform and uniaxial state of stress in the adhesive layer. Specimens are usually in the form of a cylindrical butt joint to which an axial load or a torque is applied, or in the form of a thick adherend joint loaded in tension. The main difficulty is the accurate measurement of the small displacements across the adhesive. Available tensile, compressive and shear tests are illustrated and commented on Appendix A (see Sections 2.1, 3.1 and 4.1).

For a long time, researchers thought that the bulk adhesive properties were different from adhesive properties in the joint. It was believed that elastic modulus increased with reduction of adhesive thickness but this was due to incorrect interpretation of experiments (Adams et al. 1997). Nevertheless, Adams and Coppendale (1977) showed that the layer and bulk mechanical properties are similar under the same curing conditions. The difficulty is in providing the same curing conditions for bulk and layer materials because of runaway exothermic reactions in bulk forms, which can explain the discrepancies. In his study of five epoxy adhesives, Jeandrau (1986, 1991) confirmed

that good correlation exists between the properties of the adhesive in bulk forms and those of the adhesive layer between the adherends. This conclusion had already been reached by Althof and Brockmann (1976), Dolev and Ishai (1981) and Ishai and Dolev (1981). It should be borne in mind that correlation between bulk and layer properties depends on the quality of bulk specimens without defects, such as voids and porosity, since the contents and size of defects are generally smaller in layer than in bulk specimens (Tong and Steven 1999).

### **2.3.5 Structural Analysis of Adhesively-bonded Joints**

The theoretical analysis of bonded joints in metals, based on the classical analytical methods of continuum mechanics, was developed in the 40s and 50s. This consists of setting up a series of differential equations describing stress and strain states in a joint and then, obtaining algebraic solutions for given boundary conditions. The solutions become more difficult when including non-linearity and complex geometry and boundary conditions. Thus, depending on the complexity of the solution, equations could be solved analytically or numerically using methods such as finite differences (FD) or finite elements (FE). The latter facilitates parametric studies. Basic theories have been modified for composite materials in order to consider their anisotropic properties. A review of published work, mainly theoretical, derived from analytical and FE methods, relating to adhesively-bonded joints in composite materials is given in Matthews et al. (1982).

#### **2.3.5.1 Analytical Methods**

##### **Linear analysis**

Analyses are usually related to large width joints where the stress distribution is assumed to be constant across the width and edge effects can be ignored. Plane-stress or plane-strain analyses are performed. The first theories were developed for single-lap joints. The simplest approach consists of assuming the adherends to be rigid and that the adhesive will deform in shear. Thus, the shear distribution remains constant along the overlap length and axial stress decreases linearly from the maximum value in the adherend to zero at the joint's free end (Figure 2.23(a)). Volkersen (1938) developed the "shear lag" analysis. It is assumed that adhesive deforms only in shear while the adherends deform only in tension (Figure 2.23(b)). He described the shear stress distribution along the overlap length where the maximum shear stresses occurred at the overlap's ends and depend on the adhesive shear modulus to adherend Young's modulus ratio. Nevertheless, he neglected two important factors: the eccentricity of the tensile load, which creates bending moments in the joint and the bending of the adherend, allowing joint rotation (Figure 2.23(c)).

Goland and Reissner (1944) took into account the bending effects and then defined the through-thickness (peel) stresses in the bondline (Figure 2.23(c)). They assumed a constant stress distribution across adhesive thickness since the latter is assumed to be small compared to the adherend



thickness. Both shear and through-thickness stress distributions reach maximum values at the joint ends. Non-zero shear stress at the ends violates the stress-free boundary conditions and is the consequence of neglecting through-thickness adhesive stress variation. The location of the maximum shear stress moves from joint ends by the equivalent of approximately one adherend thickness when considering this variation (Matthews et al. 1982). Although double-lap joints are symmetric and do not exhibit load eccentricity like single-lap joints, they are subjected to internal bending moments as shown in Figure 2.23(d). The internal adherend is loaded in tension while external adherends are also subjected to bending. The latter develop through-thickness compressive stresses across the adhesive layer at the loaded overlap end and through-thickness tensile stresses in the unloaded end.

Several authors (Renton and Vinson 1975 a, Kadioglu et al. 2003) carried out parametric studies to identify the factors most influencing stress distributions in order to establish recommendations for maximum stress reduction. It was concluded that using identical adherends (identical stiffness), high adherend stiffness, low adhesive stiffness and high overlap length reduces stress peaks. Analysis of adhesively-bonded joints between composite adherends is more complicated due to the anisotropic properties of the adherends. Parametric studies led to the same recommendations as for isotropic adherends (Renton and Vinson 1975 b).

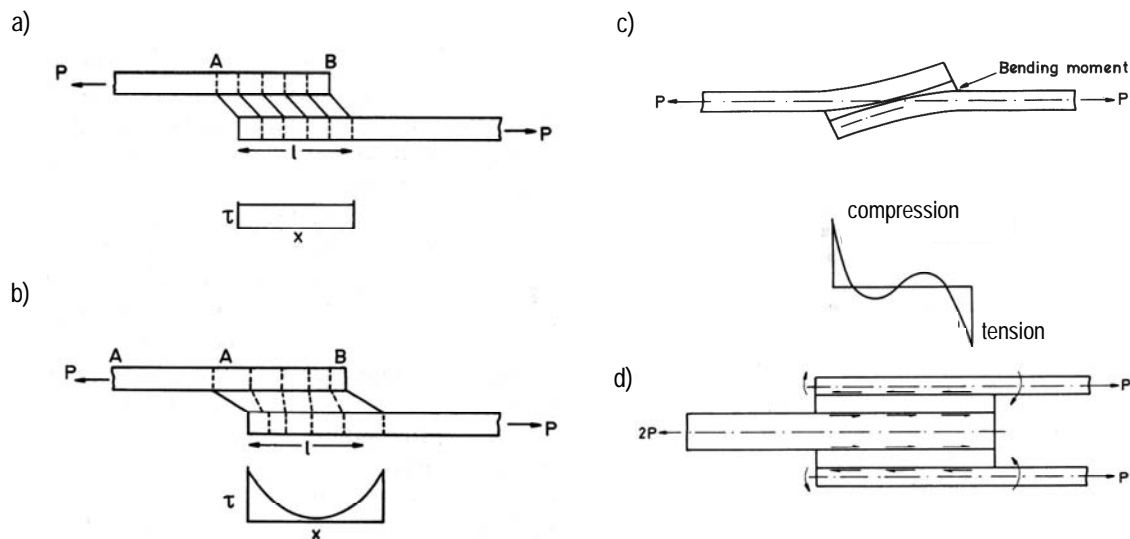


Figure 2.23: Single-lap joint (a) rigid adherends and shear stress distribution, (b) elastic adherends and shear stress distribution (Volkersen 1938), (c) Goland and Reissner's bending moment and through-thickness stress distribution (1944); (d) Double-lap joint

### Non-linear analysis

Hart-Smith (1973) performed a detailed non-linear analysis of double-lap joints, single-lap joints and scarf and stepped joints. It shows that for double-lap joints, the adhesive shear-strain energy is the only significant factor affecting joint strength. Thus, a ductile adhesive with a large area under the stress-strain curve will generate higher joint strength than a stronger brittle adhesive with a small area

under the stress-strain curve. The measured shear stress-strain curve could be characterized with different mathematical models. Hart-Smith used two models (Figure 2.24(a)):

- idealized elastoplastic model

$$\tau = \begin{cases} G \cdot \gamma & \gamma \leq \gamma_e \\ \tau_p & \gamma_e \leq \gamma \leq \gamma_p \end{cases} \quad (2.8)$$

where the elastic strain,  $\gamma_e$ , and shear modulus  $G$  are chosen in such a way that the strain energy using the idealized elastoplastic model and the measured curve are identical. The plastic strain,  $\gamma_p$ , remains the same.

- bilinear model

$$\tau = \begin{cases} G_e \cdot \gamma & \gamma \leq \gamma_e \\ \tau_e + G_p \cdot (\gamma - \gamma_e) & \gamma_e \leq \gamma \leq \gamma_p \end{cases} \quad (2.9)$$

where the elastic strain,  $\gamma_e$ , and shear moduli,  $G_e$  and  $G_p$ , are chosen in the same way as for the idealized elastoplastic model. The plastic strain,  $\gamma_p$ , remains the same. The bilinear model is closer to measured behavior over the entire strain range.

Figure 2.24(b) illustrates shear stress and strain distribution in the adhesive bondline, assuming an idealized elastoplastic adhesive model, when the applied load is progressively increased. The shear stress distribution is proportional to the loading level as long as the maximum shear strains at the edges of the adhesive layer do not exceed elastic strain. When the load level increases, the shear stress reaches the maximum value and the adhesive's plastification starts. Increasing the load leads to an enlargement of plastic areas from the edges to the middle of the adhesive layer. Thus, the elastoplastic adhesive allows a higher load-carrying capacity and larger deformations than elastic adhesives.

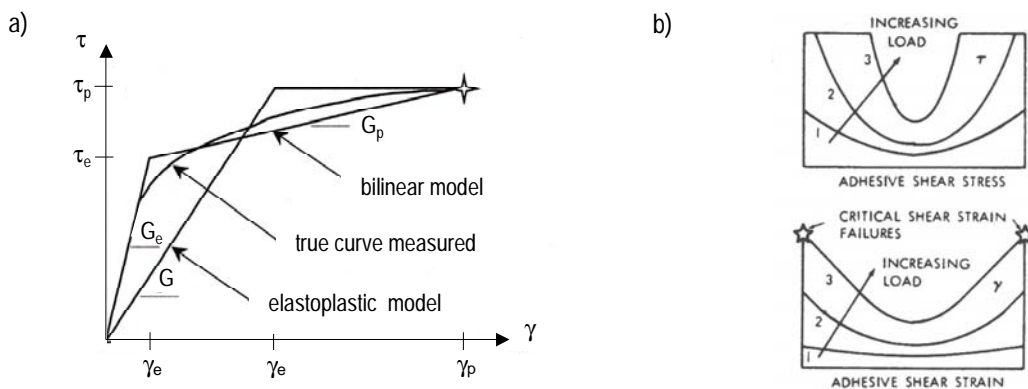


Figure 2.24: (a) Adhesive non-linear behavior; (b) Shear stress distribution at the bondline (Hart-Smith 1973)

### 2.3.5.2 Numerical Finite Element Analysis (FEA)

As previously mentioned, non-linearity and complex geometry and boundary condition configurations require FE analysis. Moreover, adhesively-bonded joints with FRP adherends usually exhibit interlaminar failure and thus the critical stress distribution is located inside the adherend and not at the bondline as assumed in classical analytical models. Information concerning the characteristics of joint FEA models is summarized in Chapter 4, particularly in Section 4.1.

Richardson et al. (1993) compared results from two- (2D) and three-dimensional (3D) finite element analyses of adhesively-bonded joints. The 3D analysis showed that the adhesive remains in a state of plane strain over approximately 80% of joint width and stresses decrease towards the edges. Thus, the commonly used FEA 2D analysis assuming a state of plane strain is often satisfactory. Andruet et al. (2001) developed special 2D and 3D adhesive elements for adhesively-bonded single-lap joint analyses and observed higher 3D effects on through-thickness than shear stress distribution (Figure 2.25). Through-thickness stresses are greater at the center of the joint than at the edges due to the Poisson's ratio.

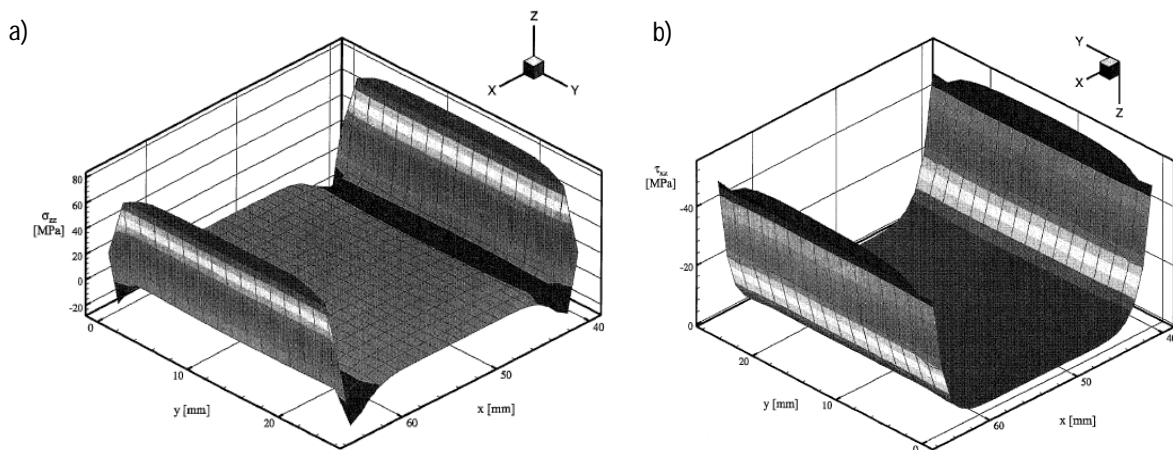


Figure 2.25: 3D FEM analysis of single-lap joint (a) through-thickness, (b) shear stress distributions (Andruet et al. 2001).

## 2.3.6 Failure Prediction

### 2.3.6.1 Failure Modes

Adhesively-bonded joints are subjected to mechanical loads (short- and long-term static load, fatigue load, impact load) as well as to environmental actions which affect joint performance. Water, high humidity and ultraviolet radiation have a long-term effect on joint performance and lead to joint degradation and strength reduction (Adams et al. 1997). A high temperature normally reduces

adhesive strength and stiffness and a low temperature reduces ductility. The combination of these actions could lead to joint failure. The possible failure modes of adhesively-bonded FRP joints are (Figure 2.26(a)):

- adhesive (cohesive) failure caused by shear and through-thickness stresses;
- interlaminar adherend failure due to delamination caused by shear and through-thickness stresses;
- tensile adherend failure as a result of axial (in-plane) tensile, compressive or bending stresses;
- transverse adherend failure as the result of Poisson's ratio contraction (mainly observed in composites rich in loading-direction fibers);
- adhesion failure between adhesive and adherend caused by shear and through-thickness stresses.

When the adhesive joint fails cohesively, cracks develop locally at high stress concentration points and progressively grow and spread leading to the final adhesive crack. Interlaminar failure occurs inside the adherends since composites have anisotropic properties mainly characterized by weak through-thickness properties. The failure surface is located in the matrix layer or at the fiber/matrix interface and is initiated at the joint's free edge where through-thickness and shear stresses reach their maximum values (Figure 2.20). Figure 2.26(b) illustrates the progression of interlaminar delamination (Heslehurst and Hart-Smith 2002). Adhesion failure at the adherends/adhesive interface indicates inadequate surface treatment of adherends or inappropriate material combination and should be avoided by suitable preparation. It is noted that failure modes of bonded joints between composite materials are more diverse and complex than those between isotropic materials such as steel. The latter usually exhibit cohesive failure (in adhesive layer), while composite materials exhibit interlaminar failure (in matrix layer or at fiber-matrix interface).

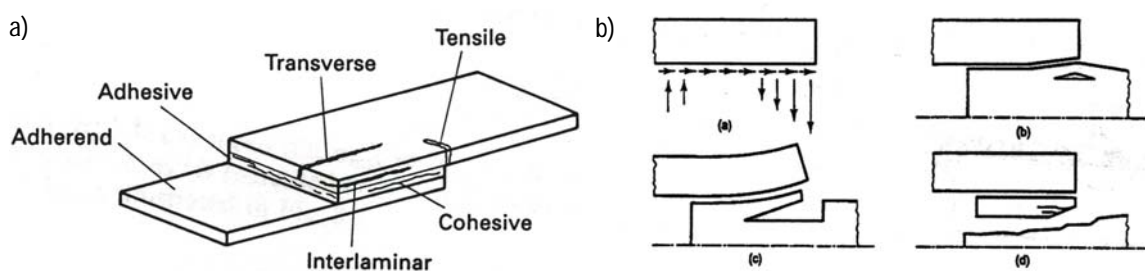


Figure 2.26: (a) Possible failure modes of adhesively-bonded joints with composite materials loaded in shear (Hollaway 1994); (b) Interlaminar tensile mode of failure (Heslehurst and Hart-Smith 2002)

Figure 2.27 shows the extended classification of FRP joint failure modes from ASTM D5573-99. Two kinds of interlaminar delaminations are distinguished, “fiber-tear” and “light-fiber-tear” failure depending on failure surface depth. The former occurs within the FRP matrix and the latter within the FRP adherend, near the surface, characterized by a thin layer of FRP matrix on the adhesive with few or no fibers. Concerning the adhesive failure, the standard differentiates between proper “adhesive

failure” – at the adhesive/adherend interface – the “adhesive to adhesion promoter” failure and “adhesion promoter to substrate” failure. The promoter is an additional product applied to adherends during surface preparation to improve adhesion (primer and/or activator see Section 4.2.2).

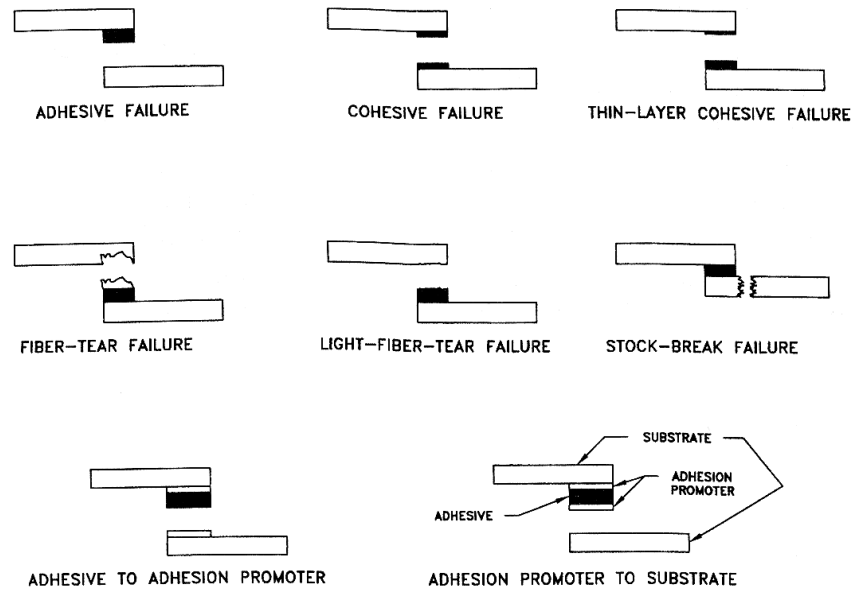


Figure 2.27: Failure modes of adhesively-bonded joints in composite materials according to ASTM D5573-99 classification

### 2.3.6.2 Failure Criteria and Strength Prediction

There are two approaches to predicting joint failure: one based on material strength and one on fracture mechanics. In the first, the design stress is compared to material strength and the material is selected if its strength is greater than the estimated stress level. In the second, three variables – applied stress, flaw size and fracture toughness – and the critical combinations of these three variables are quantified using fracture mechanics to define a structure’s strength and service life. The material strength-based approach will be used in the present study since a failure criterion had been developed in the CCLab for similar adhesively-bonded joints between GFPR adherends (Vallée 2004).

As mentioned in the previous section, joints can fail in several failure modes and locations depending on many factors such as geometrical configuration, material combinations and manufacturing process and quality. Interlaminar delamination usually occurs in adhesive joints between FRP adherends because of their weakness in the through-thickness direction. Thus, only interlaminar failure criteria are dealt with and adhesion and cohesive failure modes are assumed as having been avoided. These could be classified into maximum criteria and interactive criteria. In both, failure is described in terms of a limiting condition being reached at a specific point in the fracture surface.

### Maximum criteria

A maximum stress criterion is a limiting criterion. It is assumed that interlaminar failure occurs when shear stress,  $\tau_{xy}$ , or through-thickness tensile stress,  $\sigma_y$ , at the failure surface exceed their ultimate strength  $\tau_{xy,u}$  or  $\sigma_{y,u}$ . The failure surface is usually assumed to be a matrix layer. The two criteria are described by the following equations:

$$\frac{\sigma_y}{\sigma_{y,u}} \leq 1 \quad (2.10)$$

$$\frac{\tau_{xy}}{\tau_{xy,u}} \leq 1 \quad (2.11)$$

### Interactive criteria

Long (1991) and Tong (1997) developed interlaminar failure criteria for adhesively-bonded joints between traditional composite materials. Some are derived from the well-known Tsai criterion and Norris criterion applied to composite material laminates (Nahas 1986). Long (1991) developed a failure criterion, based on experimental investigations, which considered the interaction of through-thickness tensile and shear stresses at the failure location,  $\sigma_y$ - $\tau_{xy}$ . Experimental investigations were conducted on ARALL (Aramid-Aluminum-Composites) single- and double-lap joints. Long developed a “flatwise tension” device to measure (pure) through-thickness tensile strength. The (pure) shear strength was obtained from the 0°-Iosipescu test on prepreg samples. Nevertheless, no shear-tensile interaction strength values were obtained. Long performed FE calculations to determine stresses at the failure location and subsequently developed two interactive criteria (Eq. 2.12 and 2.13) where  $\sigma_y$  and  $\tau_{xy}$  are interlaminar through-thickness tensile and shear stresses respectively. Tong (1997) established six criteria including the axial stress in the interaction failure criterion.

$$\frac{\sigma_y}{\sigma_{y,u}} + \left( \frac{\tau_{xy}}{\tau_{xy,u}} \right)^2 \leq 1 \quad (2.12)$$

$$\left( \frac{\sigma_y}{\sigma_{y,u}} \right)^2 + \left( \frac{\tau_{xy}}{\tau_{xy,u}} \right)^2 \leq 1 \quad (2.13)$$

Vallée (2004) followed a similar approach to Long. He developed a failure criterion for joints with pultruded GFRP laminates taking into account the interaction of through-thickness tensile and shear stresses at the failure location. Vallée designed a shear-tensile-interaction device (STI-device) able to independently measure shear strength,  $\tau_{xy}$ , and through-thickness strength,  $\sigma_y$ , on 50x50mm coupons and determine the GFRP failure criterion for any combination of shear and through-thickness stresses (Figure 2.28). Vallée tested laminates identical to those used in the present study (5 mm and 10 mm thick). The failure in the coupons occurs, as for adhesively-bonded joints, at a depth of approximately 0.5 mm. The shear and through-thickness stresses developed with the STI-device were uniformly distributed (according to Vallée’s FE model), unlike the stress state in the joint where high stress

gradients were observed at the edges. Thus the related failure criterion function,  $f_{\text{device}}$  (Eq. 2.14), was not adapted to actual joint stress conditions and two correction factors ( $\kappa_{\tau}$ ,  $\kappa_{\sigma}$ ), one for each kind of stress, were added taking stress distribution shape and stress peaks into account. Keller and Vallée (2005) maintained that material strength depended on expansion of the stressed surface. Resistance to local high stresses should be much greater than to uniformly distributed stresses.

$$f_{\text{device}} = \left( \frac{\tau_{xy}}{\tau_{xy,u}} \right)^2 + \left( \frac{\sigma_y}{\sigma_{y,u}} \right)^2 \quad (2.14)$$

The joint failure criterion function,  $f_{\text{joint}}$ , was defined in (Eq. 2.15). The shear and through-thickness stresses are the result of FEA calculations for the arbitrary load of 100 kN. The maximum value of the function,  $\eta$ , along the overlap length defines the critical stress interaction point (Eq. 2.16). Subsequently the failure load could be predicted with (Eq. 2.17).

$$f_{\text{joint}} = \left( \frac{\tau_{xy}}{\kappa_{\tau} \cdot \tau_{xy,u}} \right)^2 + \left( \frac{\sigma_y}{\kappa_{\sigma} \cdot \sigma_{y,u}} \right)^2 \quad (2.15)$$

$$\eta = \max (f_{\text{joint}}) \quad (2.16)$$

$$F_{u,\text{calc}} = \frac{100 \text{ kN}}{\sqrt{\eta}} \quad (2.17)$$

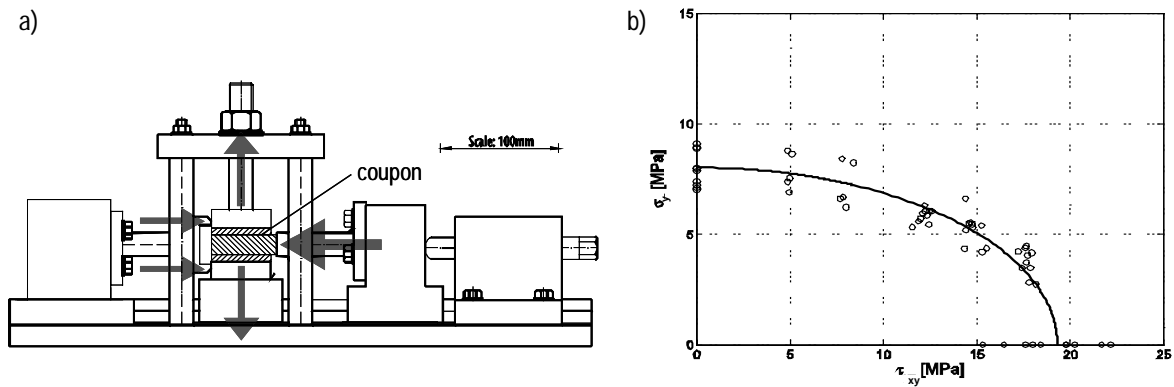


Figure 2.28: (a) Longitudinal section through STI-device; (b) Shear-tensile criterion for 10 mm thick coupons (Vallée 2004)

The correction factors were calibrated using experimental results from double-lap joint specimens with an epoxy adhesive and different overlap lengths and chamfering levels (no, slight and full chamfering). Factor  $\kappa_{\tau}$  depends on the overlap and varies between 1 (short,  $l=50$  mm) and 4 (long,  $l=200$  mm) and factor  $\kappa_{\sigma}$  depends on chamfering level and varies between 2 (full) and 4 (none).

### 2.3.7 Design Manuals and Guides

There is no code currently available for the dimensioning of FRP structures and particularly of adhesively-bonded connections. Design guidelines are supplied by pultruders (Anon 2000 a, 2000 b

and 2003) and organizations or associations such as the Structural Plastics Design Manual (Heger et al. 1984) from the American Society of Civil Engineers and the Eurocomp project (Clarke 1996) – an engineering consortium in collaboration with European partners.

Morrison Molded Fiber Glass Co. drew up the first design manual for pultruded structural profiles in 1971. The current manual was published in 1989 and is periodically updated (Anon 2000 a). Mechanical connections – mechanical fastenings – are dealt with but not adhesive connections. The Pultex Pultrusion Global Design Manual from Creative Pultrusions (Anon 2000 b) gives an overview of connection configurations and mechanical fastening assembly techniques. Fiberline Composite A/S prepared their design manual in 1995; an updated version appeared in 2003 (Anon 2003). The manual covers the assembly methods and dimensioning of bolted connections but gives no information about concerning adhesive connections. The Structural Plastics Design Manual (Heger et al. 1984) introduces adhesively-bonded joint configurations and general principles and recommendations although no dimensioning methods are included.

The Eurocomp Design Code and Handbook (Clarke 1996) is the first independent guide to structural FRP connections. It provides a “simplified” and a “rigorous” analytical design procedure for lap- and strap-joints (plate-to-plate connections loaded in tension). These procedures are summarized by Hutchinson (1997) and Mottram and Turvey (1998). The simplified design procedure should be used for the preliminary sizing of tensile loaded joints. Experimental data from lap shear joints is required to define the ultimate load per unit width of joint, which is divided by a partial material safety factor to obtain joint resistance. Then the design tensile load is derived from joint strength. Joint overlap length should be twice that of the test specimen or at least 50 mm. The rigorous design procedure should be used for the final design of structural connections with lap- and strap-joints. The procedure is based on elastic adhesive behavior and closed-form analytical models and is thus usually too conservative for elastoplastic adhesives. It is important to note the large number of material properties required for stress analysis. Moreover, the suggested failure criteria are not appropriate for FRP materials since they assume cohesive failure or interlaminar failure characterized by a maximum stress criterion rather than an interaction criterion.

## **2.4 Concluding Remarks**

The detailed literature review shows that research on all-FRP structures has been concentrated on experimental and numerical studies of frame connections (beam-to-column) largely influenced by steel technology, mimicking mechanical connections and using open sections (I- and U-shapes). The first studies taking into account certain inherent FRP properties (anisotropic nature and low full-section stiffnesses) led to combined connections (bolting and bonding) and closed sections (rectangular shapes). Material-adapted sections and construction methods are still lacking however. Moreover, the lack of ductility of FRP materials still limits their acceptance for construction purposes.



Ductility is a basic requirement in the design approach for conventional materials such as steel and reinforced concrete and is considered a safety characteristic by civil engineers. Based on a ductility literature review, safety structures can be classified into ductile and deformable structures. To prevent a brittle structural collapse of the latter, a redundant structure is required. A definition of terms should be made and a classification of structures is required (Section 3.1). Consequently, new concepts of FRP structures consisting of system ductility and redundancy should be developed (Section 3.2).

Efficient material use requires an appropriate design philosophy which takes the inherent properties of materials into account (Section 6.1). Nevertheless, one single approach for comparing the efficiency of structures built with brittle and ductile materials should be established. New concepts have been developed for quantifying structure safety based mainly on stored energy, rather than the conventional ductility factors based on idealized elastoplastic materials. The “overall deformability” and “robustness” factors include the deformability of the structure and its capacity to carry excess load and allow a material-independent comparison of structure robustness and safety. The behavior of structures designed according to the new concept should be evaluated according to these factors (Section 6.4.1).

Adhesive bonding results in more rigid connections and more uniform load transfer than bolting. Moreover, the use of ductile adhesives leads to large deformations above the ultimate limit state, energy dissipation and stress concentration reduction. Research on adhesively-bonded joints for aeronautical applications has been carried out, firstly with metal adherends (isotropic materials) and subsequently traditional composites, consisting of a succession of laminae (anisotropic adherends). However, the behavior of joints with pultruded FRP adherends for construction purposes was insufficiently investigated (Sections 4.2, 5.2.3). Since these adhesive joints differ significantly from previously studied joints, the effect of material mechanical properties and geometrical parameters should be evaluated (Section 5.2.4).

Analytical methods for adhesively-bonded joints have been developed since the 40s and 50s at different levels of complexity and include simplification assumptions. FE analyses take into account joints' actual geometry (spew-fillets), material properties (orthotropic FRP and non-linear adhesive behavior) and geometrical non-linearities (Section 5.2). Moreover stress distributions have been calculated analytically in the bondline, while composite adherends exhibit an interlaminar failure and thus the determinant position is located inside the adherends.

Several strength-prediction criteria have been developed for bonded joints with traditional composite adherends but only a few are applicable to the studied joints. Failure criteria are determined by through-thickness and shear stresses at the failure surface. An interaction criterion has been developed for adhesively-bonded joints with GFRP pultruded adherends and an epoxy adhesive, a stiff adhesive displaying high stress peaks. Its use in joints with lower adhesive stiffness should be validated (Section 5.2.5).

The effect of adhesive stiffness (high and low) on stress distributions is known while no limits have been established based on serviceability limit state or failure requirements (Section 5.3.1 and 5.3.2). The analysis of joints using ductile adhesives (idealized elastoplastic and bilinear models) has been studied theoretically while a design method defining the appropriate adhesive behavior (selection or design of adhesive behavior) for a previously defined structure behavior (Section 5.3.3 and 6.3.2) is required for extending bonded joint applications.

An understanding of adhesive behavior is essential for predicting joint deformation and strength but is limited by the lack of reliable data concerning the mechanical properties of adhesives. Since adhesives behave differently in tension and compression, different material tests should be performed (Section 4.1) and a modified von Mises criterion applied. In practice, when bonded joints are designed, the required adhesive properties included in the modified von Mises criteria are not available and thus assumptions must be made and simplified criteria used (Section 5.2.4 and 6.3.2).

---

## 3 Ductile and Redundant Structure Concepts

As mentioned in the previous chapter, FRP materials present two major disadvantages limiting their acceptance in civil engineering applications: lack of inherent ductility and difficulty in joining structural components due to their fibrous and anisotropic character. These two drawbacks should be overcome by the appropriate design of FRP structures.

This chapter presents a classification of structures into ductile and redundant systems according to the literature survey (see Section 2.2.5). Subsequently, two new system concepts which take FRP material properties into account are introduced. Only the first is dealt with in the present thesis; an overview of the second is given in Section 7.2.2 concerning future work. The proposed concept for structures composed of brittle FRP components achieves system ductility through the use of ductile adhesive joints and redundant (statically indeterminate) structural systems.

### 3.1 System Ductility and Redundancy

Ductility is a basic requirement in the design approach for conventional materials such as steel and reinforced concrete and is considered a structure safety characteristic by civil engineers. Ductility (A) indicates structure failure by means of large deformations (deformability), (B) assures energy dissipation during impact, reverse loading cycles and seismic loading (C) allows internal force redistribution. The analysis of conventional ductile structures (see Section 2.2.2) differentiates between component ductility inherent to the material (A and B) and system ductility (A to B) inherent to the material and statically indeterminate system. When brittle materials such as FRP are used, component (material) ductility cannot be developed and only system ductility can be created.

Nevertheless, all system-ductility features are not required for every structure; the failure warning and internal force redistribution (A and C) are essential for most structures, while energy dissipation is only required for those potentially sensitive to impact and seismic loading (A to C). In some cases structures only exhibit large deformations due to their low stiffness (A) or stiffness reduction which leads to internal load redistribution (A and C), characterizing deformability. The choice of the required features depends on the structure's function and the loads to which it will be subjected. Figure 3.1 illustrates these different structural behaviors and Figure 3.2 summarizes the features linked to component ductility, system ductility and deformability.

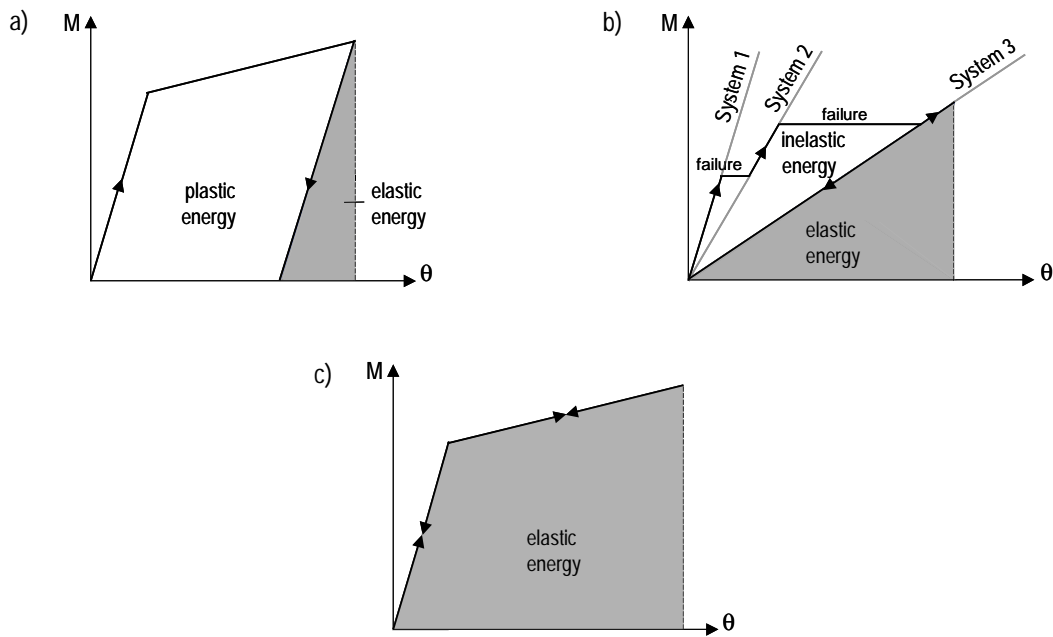


Figure 3.1: System ductility: (a) ductility, (b) pseudo-ductility; (c) Deformability

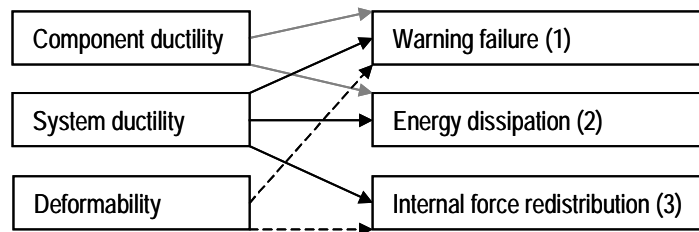


Figure 3.2: Ductility and deformability features

System ductility can comprise several distinct “sub-concepts” developed in earlier works by different researchers. Table 3.1 summarizes and classifies these sub-concepts into ductility and pseudo-ductility concepts. Ductility concepts include combinations of “brittle” and “ductile” components or connections at system level (see Section 2.2.5.1). Ductile adhesively-bonded joints, as described in Section 3.2, can form plastic hinges and are classified under ductile concepts. Pseudo-ductility concepts include combinations of “brittle” and “brittle” components or connections at system level (see Section 2.2.5.2). Non-linear, inelastic behavior, exhibiting decreasing stiffness with increasing load similar to the behavior of ductile structures, can be achieved by the progressive failure of brittle components or connections at system level. To prevent structural collapse, however, system redundancy is required. In contrast to ductile structures, pseudo-ductile structures can dissipate energy only within a limited number of loading cycles, depending on the degree of static indeterminacy. Thus, ductile structures allow full energy dissipation while pseudo-ductile structures allow only partial energy dissipation. A comparable pseudo-ductile behavior can occur at the component level through a non-linear, inelastic deformation increase caused by progressive internal

failures (see Section 2.2.5.2). Analogous to system ductility at the system level, the term system redundancy is proposed as a requirement for pseudo-ductile behavior. Table 3.1 also gives an overview of possible system redundancy “sub-concepts” classified into structural redundancy (statically indeterminate system) and cross-sectional redundancy. Structural redundancy provides alternative load paths in case of failure of a component or connection. Cross-sectional redundancy is provided in multi-component cross-sections. Single cross-sectional components or connections between single components can fail without failure of the whole section.

Table 3.1: System Ductility and Redundancy - Overview

System ductility		System redundancy	
Concepts	Description	Concepts	Description
Ductility	Combinations of brittle/ ductile components or connections (system level)	Structural redundancy (statically indeterminate)	Systems with alternative load paths, back-up systems
Pseudo-ductility	Combinations of brittle/ brittle components or connections (system level)	Cross-sectional redundancy	Multi-component cross-sections
	Brittle components: progressive loss of stiffness (component level)		

### 3.2 Concepts of Ductile and Redundant FRP Structures

A new concept for structures composed of brittle FRP components is proposed which achieves system ductility through the use of ductile adhesive joints and redundant structural systems (statically indeterminate). The proposed concept envisages adhesives with an initially elastic behavior that is sufficiently stiff to meet short- and long-term serviceability requirements. However, when serviceability (SLS) and ultimate (ULS) loads are exceeded, the adhesive behavior should change and become plastic, or at least highly non-linear/inelastic, with much lower stiffness. The ductile joints can compensate for the lack of material ductility of FRP components by providing ductility in the structural system - system ductility - which also offers the aforementioned advantages of ductile materials. In the case of unexpected joint failure, the redundant system provides alternative load paths and redistribution of the section forces, thus preventing structural collapse.

The first concept-development stage consists of creating system ductility through ductile connections (at system level) and structural redundancy (see Sections 4.3 and 6.1) and the second consists of creating component ductility through ductile connections (at system level) and cross-sectional redundancy (see Section 7.2.2). Only the first stage will be studied in the present thesis. Figure 3.3 shows examples illustrating both steps.

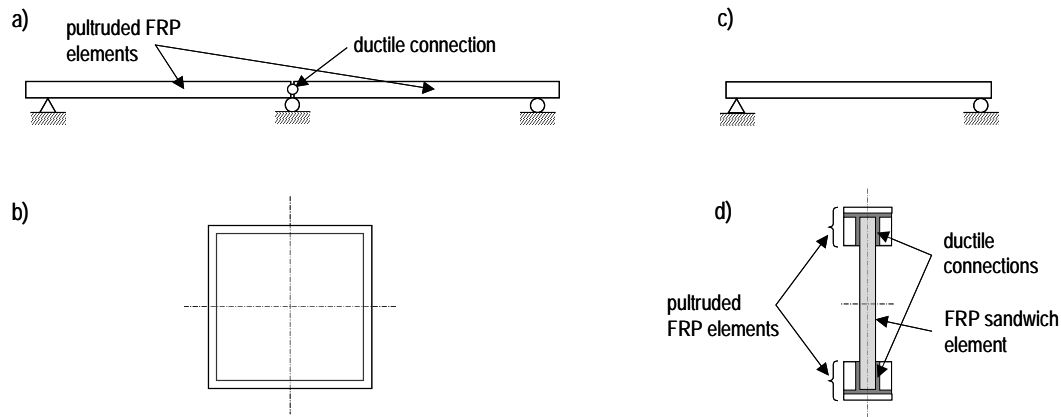


Figure 3.3: *New ductile and redundant FRP structure concept, stage 1: statically indeterminate structure with ductile connections (a) static system, (b) cross-section; stage 2: statically determinate hybrid structure with ductile connections (c) static system, (d) cross-section*

Figure 3.3(a-b) illustrates an FRP continuous beam over two spans with a ductile adhesively-bonded connection at mid-support. The use of ductile adhesives leads to favorable redistribution of internal and external forces in the redundant system, thereby increasing load-carrying capacity and structural safety compared to traditional systems such as simple and continuous beams. In case of unexpected joint failure, the redundant system allows creation of alternative load paths and redistribution of section forces. The static-system modification and structure-stiffness reduction lead to increased deflections and rotations, thus preventing structural collapse.

Figure 3.3(c-d) illustrates a sandwich girder with adhesively-bonded flanges. The hybrid girder web is composed of an FRP sandwich element and the flanges consist of pultruded FRP profiles. The use of ductile adhesives limits stress transfer from low-stressed to high-stressed components, consequently leading to favorable stress distribution across the redundant cross-section and increasing load-carrying capacity and structural safety. Single cross-sectional components, or the adhesive bond between single components, can fail without failure of the whole section, avoiding brittle failure and warning of structural collapse. Internal stress redistribution operates in the cross-section in the same way as internal force redistribution in ductile, statically indeterminate structures.

---

## 4 Experimental Investigations

This chapter demonstrates the feasibility of the proposed concept of FRP structures with system ductility and demonstrates its performance in comparison with traditional static systems such as simple and continuous beams. It also gives experimental results used to validate a numerical FE model developed for adhesive double-lap joints and an analytical model developed for ductile adhesively-bonded double-lap joints (see Chapter 5) and beam connections (see Chapter 6).

The chapter summarizes the main results of experimental investigations carried out for the development of system ductility. Experimental investigations were made on: adhesives (see Section 4.1), adhesively-bonded double-lap joints (see Section 4.2) and adhesively-connected beams (see Section 4.3). Details of these experimental investigations are given in Appendices A-C. Three different adhesives were selected to observe and quantify the effect of ductile adhesive behavior on FRP double-lap joints under quasi-static tensile loading. The main aims were to measure joint elongation and strains along the overlap length to derive joint stiffness and quantify load transfer respectively. The results were used to select the appropriate adhesive behavior for the development of ductile joints and validate a numerical FE model. Subsequently, bending experiments were performed on continuous FRP beams with adhesive joints at the mid-support manufactured with the selected adhesive. Additional bending experiments were carried out on simple beams and continuous beams without joints in order to compare and evaluate bonded beam performances. The main aims were to measure support reactions and rotations in order to derive the connection rotational stiffness, bending moment redistribution and strains along the overlap length to quantify load transfer.

### 4.1 Adhesive Experiments

#### 4.1.1 Experiment Objectives

To determine the mechanical properties of adhesives used in the investigation of joints comprising pultruded GFRP elements (see Section 4.2), tensile and compressive tests in accordance with EN ISO 527-1 and EN ISO 527-2 (1996) and ASTM D 695-96 (1996) respectively and shear tests designed at the EMPA, similar to the former EN ISO 11003-1 (1993), were carried out. The experimental series have three main objectives:

- determination of stress-strain curves in tension, compression and shear, for use in the analytical and FEA models;
- comparison of adhesive mechanical properties;
- determination of the adhesive suitable for development of ductile joints.

A summary of the experimental report (Appendix A) is presented in this section.

## 4.1.2 Specimen Description

### 4.1.2.1 Adhesives

Three adhesives were considered in the research program: the epoxy resin SD 330, the polyurethane adhesive S-Force 7851 and the acrylic adhesive SikaFast 5221. The three adhesives are resins rather than adhesive films since the adhesive thickness can vary and thus compensate for the lack of flatness of adherends. An appropriate viscosity is required to guarantee easy application. They are produced by SIKA AG. The reasons for their choice are explained in Section 4.2.1. The SD 330 (designated EP in the research program) is a resin developed for impregnation of carbon-fiber fabrics used for strengthening purposes. It offers high strength and stiffness but presents brittle failure. As epoxies are commonly used for structural bonding, it seems worthwhile to compare their behavior with new adhesives chosen for the same application. Since the aim of the project is to create ductile joints that develop larger deformations and increase joint strength, adhesives with non-linear behavior are preferred. The S-Force 7851 was developed for structural bonding of car-body parts made from carbon-fiber reinforced epoxy resins. It is more flexible and ductile than the epoxy. The SikaFast 5221 adhesive, based on ADP (Acrylic Double Performance) technology, was developed specially for structural bonding. ADP technology offers a new generation of fast-curing soft adhesives designed to replace welding and mechanical-fastening techniques. It is very flexible and ductile. Table 4.1 presents the adhesive technical data.

Table 4.1: Adhesive technical characteristics

Property	SD 330 (EP)	S-Force 7851 (PU)	SikaFast 5221 (ADP)
Chemical base	two-component epoxy resin	two-component polyurethane adhesive	two-component acrylic adhesive
Supplier	Sika	Sika	Sika
Glass transition temperature $T_g$ <sup>1</sup>	+45°C (23°, 7 days cured)	+40 °C	+52°C (23°, 1 day cured)
Consistency	thixotropic	thixotropic	thixotropic
Cure	ambient temperature	ambient temperature	ambient temperature
Working time <sup>2</sup>	40 min at +23°C	15 min at +25°C	9 min at +23°C
Application temperature (environment and supports)	+10°C to +25°C	+15°C to +100°C	+10°C to +40°C

<sup>1</sup> supplier data

<sup>2</sup> maximum allowable period after mixing of components in which joint must be assembled



### 4.1.2.2 Tensile Specimens

For each of the three adhesives, five tensile test specimens were prepared according to EN ISO 527-2 (1996) and tested. The EP and PU specimens were manufactured according to type 1A (Figure 4.1(a)) and the ADP specimens according to type 5A (Figure 4.1(b)). The choice of specimen type depends on adhesive stiffness; larger specimens are required for stiff adhesives due to their low deformations and the manufacturing process (see Section 2.2.2 Appendix A). The specimens have a prismatic form with reinforcement at the ends to avoid grip failure. The transition is made with a constant radius of 25 mm for specimens 1A and two successive constant radii, 12.5 mm and 8 mm, for specimens 5A. Additional tensile tests with loading-unloading-reload cycles were carried out on the ADP adhesive to quantify visco-elastoplastic behavior. Tensile load-unload-reload test specimens had a rectangular form without reinforcement at the ends. Thus, failure occurred at the grips and the strength was lower than for the tensile test specimens but this did not affect the load-unload-reload cycles.

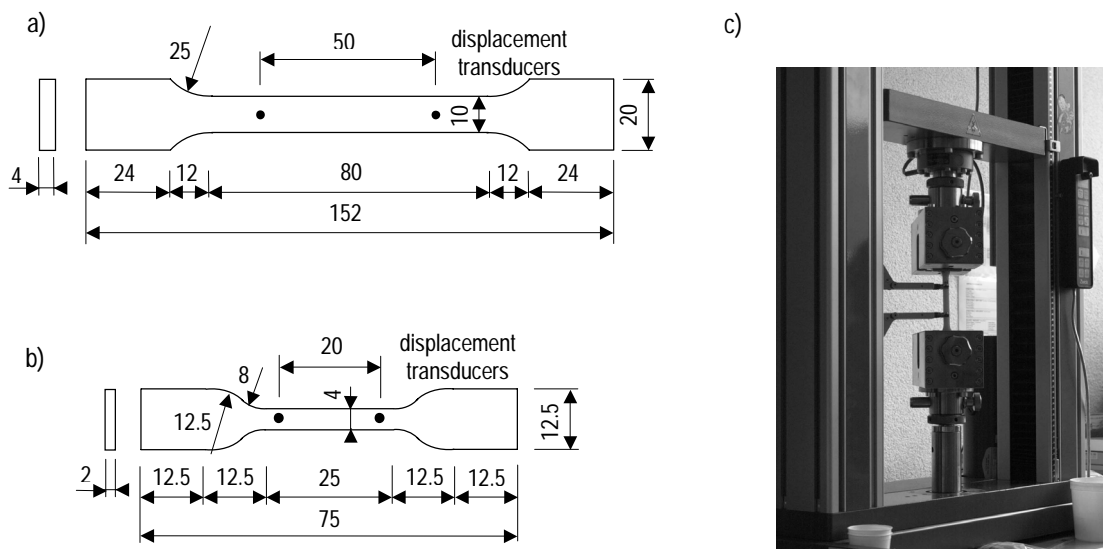


Figure 4.1: Dimensions of tensile test specimen according to EN ISO 527-2 (1996) (a) specimen 1A (EP, PU), (b) specimen 5A (ADP) (dimensions in mm); (c) Tensile testing device (Sika)

The specimens were made of bulk adhesives and prepared according to the supplier's specifications. After mixing the two components, the EP and PU adhesives were poured into a casting mold of appropriate dimensions. The ADP adhesive was added in a large plate mold. The specimens were cured under ambient laboratory conditions,  $23 \pm 1^\circ\text{C}$  and  $50 \pm 5\%$  relative humidity, for one week. Subsequently, EP and PU specimens were removed from the casting molds and ADP specimens were manufactured by machining the plate to the required dimensions. The specimens were stored under ambient laboratory conditions for four weeks for EP and PU series and one week for the ADP series.

### 4.1.2.3 Compressive Specimens

Five and four compressive test specimens were prepared and tested for the EP adhesive and the PU and ADP adhesives respectively. Specimens had a parallelepiped form with a square section according to ASTM D 695M-96 (1996) (Figure 4.2(a)). The specimens were made from bulk adhesives, molded and cured as the tensile specimens, according to the supplier's specifications.

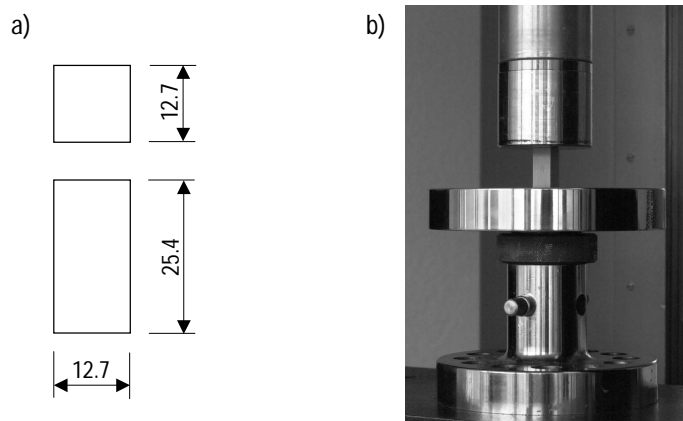


Figure 4.2: (a) Dimensions of compression test specimen according to ASTM D 695M-96 (1996) (dimensions in mm); (b) Compression testing device (Sika)

### 4.1.2.4 Shear Specimens

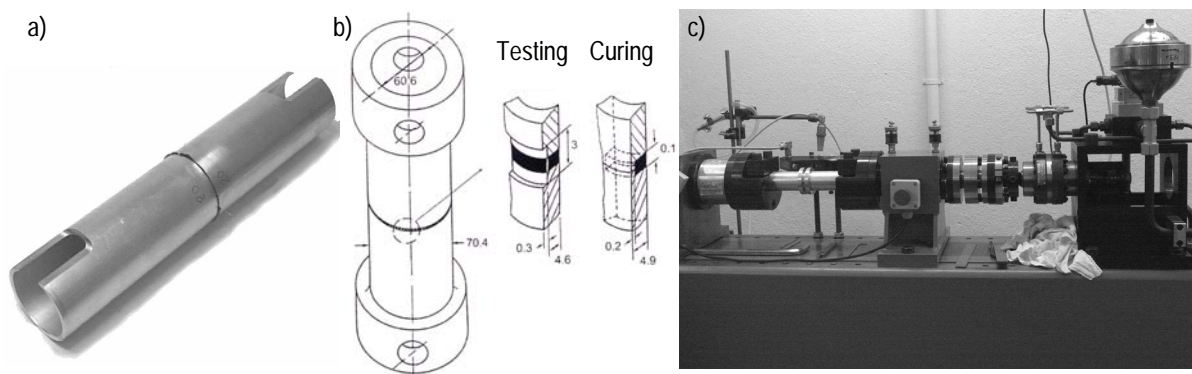


Figure 4.3: (a) Napkin-ring specimen (Schmid and Kieselbach 2003); (b) Napkin-ring specimen dimensions (mm) (Bassetti 2001); (c) Shear testing device (Department of Strength and Technology, EMPA)

For the three adhesives, four napkin-ring specimens in accordance with Figure 4.3(a) were prepared and tested. Specimens are in the form of two thin-walled cylinders bonded together, as described by Schmid and Kieselbach (2003). The cylinders have a 50 mm diameter and 3 mm thickness and are made of an AA6082 aluminum alloy. Bondline thickness is 0.1 mm and is guaranteed by a rim during curing (Figure 4.3(b)). Before bonding, adherend surfaces were sanded and degreased. The

adhesives were prepared according to the supplier's specifications. After mixing the two adhesive components, the uncured adhesive was applied to the bottom cylinder.

The cylinders were then bonded. The specimens were stored in a support and cured under ambient laboratory conditions,  $23\pm 1^\circ\text{C}$  and  $50\pm 5\%$ , for one week. Before testing, the rim was removed with a lathe. The turning process certainly had a negative influence on parameters tested, but since any kind of spacer element has some influence on the bondline, the 0.1 mm rim was adopted for the tested specimens (Figure 4.3(b)).

### 4.1.3 Experimental Set-up and Instrumentation

The tensile and compressive experiments were carried out in the laboratory of SIKA AG in Zurich and shear tests were carried out in the Strength and Technology Department at the EMPA, Dübendorf.

#### 4.1.3.1 Tensile Experiments

The specimens were loaded into a tensile testing machine, Zwick Z005, with grips (Figure 4.1(a)). The fixation procedure induces a pre-stress load of 3 N in the EP and PU specimens and 1 N in ADP specimens. The tests were conducted under ambient laboratory conditions,  $23\pm 1^\circ\text{C}$  and  $50\pm 5\%$  relative humidity. According to EN ISO 527-1 (1996) and the specified specimen geometry (specimen 1A according to EN ISO 527-2 (1996)), the Young's modulus should be determined at a constant displacement rate of 0.5 mm/min and the strength at a constant displacement rate of 5 mm/min. Thus, tests started at a constant displacement rate of 0.5 mm/min, were changed after 0.25% of specimen deformation to 5 mm/min until failure. Additional tests were performed on ADP specimens with various loading rates: 10/50/100 mm/min in order to examine their visco-elastoplastic behavior. The machine's load cell measurements and displacement over the joint height, measured with two transducers, were recorded. These measurements allow calculation of the nominal axial stress, dividing the force by the initial cross-section area; axial strain, dividing the extension by the initial length of 50 mm, and tensile elastic modulus (0.5-1.0% strain interval).

The load-unload-reload test specimens were loaded into a tensile testing machine, Instron 1185, with grips. Tests began with loading at a displacement rate of 5 mm/min until approximately 50% of the specimen strength (approximately 4-5 MPa), followed by unloading at 1.3 MPa/min, similar to the initial displacement rate, until 0 MPa. The specimens remained unloaded during a period of time (0-5-30 min and 12 hours, one specimen per period). The test finished with a second loading at a displacement rate of 5 mm/min until failure. The machine's load and displacement cell measurements were recorded.

### 4.1.3.2 Compressive Experiments

The specimens were loaded into a compression testing machine, Instron 5500R 1185, which was formed by two plates. The bottom plate was fixed and the top plate mobile (Figure 4.2(b)). The tests were conducted under ambient laboratory conditions,  $23\pm 1^\circ\text{C}$  and  $50\pm 5\%$  relative humidity. The load was applied at a constant displacement rate of 1.3 mm/min up to a nominal strain of 5% for the EP, 60% for the PU and ADP adhesives according to ASTM D 695-96 (1996). Different maximum strains were designated for each adhesive because of their very different stiffness and deformability.

The machine's load cell measurements and the displacement of the mobile plate were recorded. These measurements allow calculation of the nominal axial stress, dividing the force by the initial cross-section area and axial strain, dividing the change in length by the initial height and compressive elastic modulus (0.5-1.0% strain interval).

### 4.1.3.3 Shear Experiments

The specimens were twisted in a testing machine with grips (Figure 4.3(c)). The tests were conducted under ambient laboratory conditions,  $23\pm 1^\circ\text{C}$  and  $50\pm 5\%$  relative humidity. The load was applied at a constant displacement rate to produce specimen failure in approximately 1 min. The machine's torque cell measurements,  $T$ , and displacement between two points on each adherend,  $v_m$ , measured with a laser, were recorded. This displacement  $v_m$  consists of displacement of the adhesive,  $v_a$ , and displacement caused by the twisting of adherends,  $v_t$  (Figure 4.4(a)). The measurements allow calculation of the shear stress,  $\tau$ , shear strain,  $\gamma$ , and shear modulus,  $G$ . The torque  $T$  can be expressed as (Figure 4.4(b)):

$$T = \int_A r \cdot \tau \, dA = \int_{r_i}^{r_o} \int_0^{2\pi} r^2 \cdot \tau(r) \cdot dr \cdot d\phi = \frac{\pi}{2} \cdot \frac{\tau_o}{r_o} \cdot (r_o^4 - r_i^4) \quad (4.1)$$

with:

$$\tau(r) = \frac{\tau_o}{r_o} \cdot r \quad (4.2)$$

The shear stress at the median radius is determined with:

$$\tau = \frac{T}{\pi} \cdot \frac{1}{(r_o^2 + r_i^2) \cdot (r_o - r_i)} \quad (4.3)$$

The shear strain is calculated as follows:

$$\gamma = \frac{v_a}{d} = \frac{v_m - v_t}{d} \quad (4.4)$$

where  $v_t$  is calculated from the shear stress in the adherends and the known shear modulus of aluminum. For the specimen dimensions ( $r_i=44$  mm,  $r_o=50$  mm), the difference between shear stress on the outer and median radius is 6% and thus negligible.

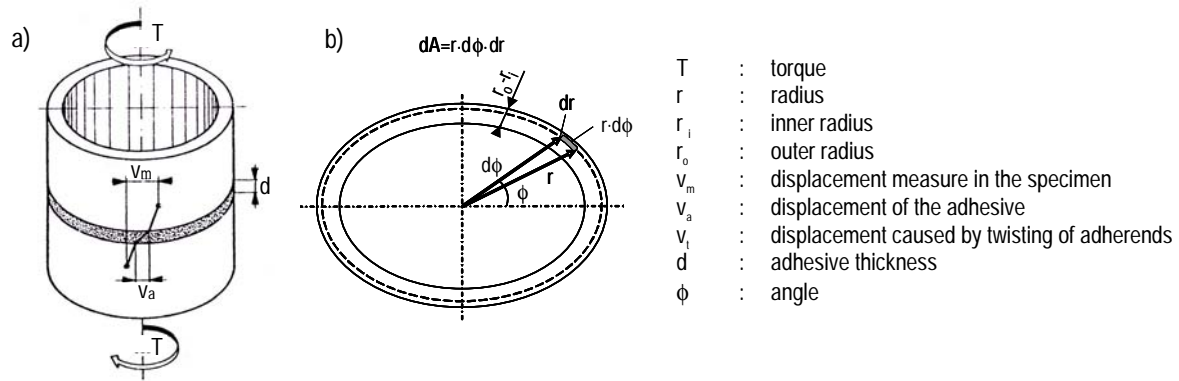


Figure 4.4: (a) Displacements on surface of bonded cylinders (Fischer and Pasquier 1989); (b) Area parameters for torque calculation

#### 4.1.4 Summary of Principal Results

The nominal tensile and compressive stress-strain curves for the three adhesives are given in Appendix A. Air inclusions were observed in the failure surfaces, which might have influenced the failure load. Nevertheless, it is assumed that the determined stress-strain curves were representative of the adhesives. The nominal stress-strain curves are based on undeformed geometry. While adhesives, especially the PU and ADP, exhibited large deformations, since the length and cross-section during the test differed significantly from the initial values, instantaneous dimensions must be considered. Thus, the average nominal stress and strain must be converted into the true stress and strain. Only tensile and compressive stress-strain curves are given for adhesive EP since shear tests did not provide conclusive results due to high adhesive to adherend modulus ratio.

The EP adhesive exhibits brittle behavior while the PU and ADP exhibit a ductile (highly non-linear) behavior (stress-strain curve shapes). The EP and PU are stiff adhesives while the ADP is a flexible adhesive.

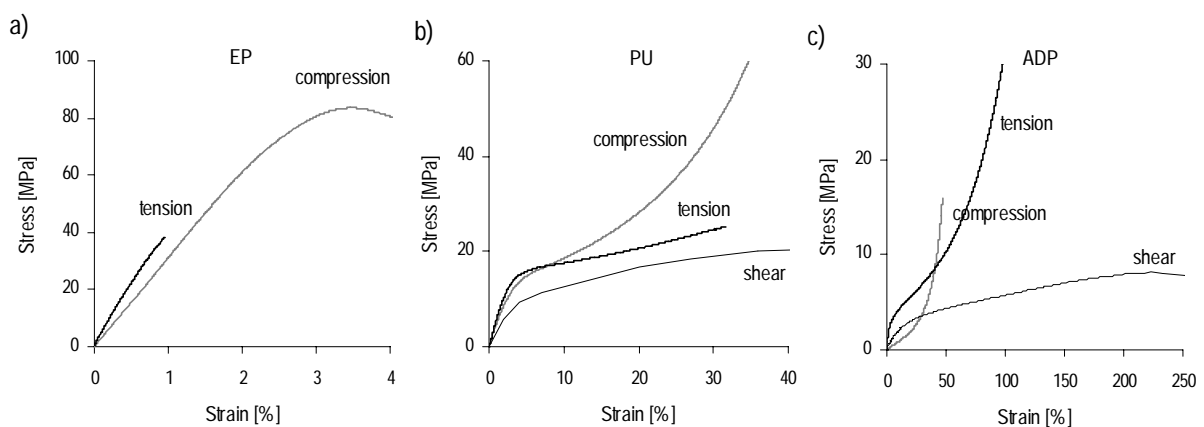


Figure 4.5: True average stress-strain curves for (a) EP, (b) PU and (c) ADP adhesives

Tables 4.2 and 4.3 list the tensile and compressive properties and the shear properties of the EP, PU and ADP adhesives respectively based on the experimental results. The elastic modulus in tension and compression,  $E_{t,e}$  and  $E_{c,e}$ , and the shear elastic modulus,  $G_e$ , were estimated on the basis of true stress-strain curves (Figure 4.5) from the secant through the 0.5-1.0% strain interval. The tensile plastic modulus,  $E_{t,p}$ , compressive plastic modulus,  $E_{c,p}$ , and shear modulus,  $G_p$ , of PU and ADP adhesives were calculated from the secant through the 10-20% (PU) and the 30-50% (ADP) strain interval respectively. The interval choice depended on curve shape. The tensile and compressive elastic stresses,  $f_{t,e}$  and  $f_{c,e}$ , and shear elastic stress,  $\tau_e$ , designate the elastic to plastic modulus transition. The ultimate stress and ultimate strain correspond to the ultimate strength or maximum measured values (for the compressive tests on the PU and ADP adhesives). The Poisson's ratio was not calculated from measurements as thickness contraction could not be measured due to lack of appropriate instrumentation. Schmid (2002) indicated values for the EP and PU adhesives and Venetz (2004) gave values for the ADP adhesive (see Section 2.4.3 Appendix A). It can be seen that the elastic modulus based on tensile results is higher than that based on compression results. Elastic moduli of the PU and ADP adhesives showed a larger standard deviation than that of the EP adhesive (see Section 2.4 Appendix A).

Table 4.2: Tensile and compressive mechanical properties of adhesives EP, PU and ADP

Adhesive	$E_{t,e}$ [MPa]	$E_{t,p}$ [MPa]	$f_{t,e}$ [MPa]	$f_{t,u}$ [MPa]	$\epsilon_{t,u}$ [%]	$E_{c,e}$ [MPa]	$E_{c,p}$ [MPa]	$f_{c,e}$ [MPa]	$f_{c,u}$ [MPa]	$\epsilon_{c,p}$ [%]	$\nu$ [-]
EP <sup>1</sup>	4563	-	-	39	1	3064	-	-	84	3	0.37
PU <sup>1</sup>	586	31	15	25	32	433	79	13	-	60	0.42
ADP <sup>1</sup>	101	14	3	29	97	10	-	-	-	60	0.40
ADP <sup>2</sup>	136	14	4	27	91						
ADP <sup>3</sup>	216	14	5	31	93						
ADP <sup>4</sup>	230	15	7	30	91						

Tensile load applied at a displacement rate of <sup>1</sup>5 mm/min, <sup>2</sup>10 mm/min, <sup>3</sup>50 mm/min, <sup>4</sup>100 mm/min

Table 4.3: Shear mechanical properties of adhesives PU and ADP

Adhesive	$G_e$ [MPa]	$G_p$ [MPa]	$\tau_e$ [MPa]	$\tau_u$ [MPa]	$\gamma_u$ [%]
PU	355	42	10	20.8	40
ADP	33	3	3	8.3	230

The experimental mechanical properties will be used for validation of the FE model developed for double-lap joints and the analytical model of joints made with ADP adhesive. The tensile properties of the adhesive ADP at the lower loading rate, 5 mm/min, will be considered.

Figure 4.6(a) focuses on the ADP tensile test series (5/10/50/100 mm/min). The ADP adhesive exhibited visco-elastoplastic behavior as observed comparing the four series loaded at different displacement rates. Generally, higher strength and lower failure strain are expected when testing at higher displacement rates (Hart-Smith 1990) but this was not observed in the test since failure strain increased slightly at the high rate. This discrepancy should indicate better quality of specimen tested at a higher rate. As for displacement rate, it must be noted that the shear tests were performed at a

higher displacement rate than uniaxial tests, thus the moduli and elastic and ultimate stresses should be higher than those for axial test displacement rates.

Tensile nominal stress-strain curves for the ADP specimens loading-unloading-reloading at 5 mm/min are illustrated in Figure 4.6(b-c). Specimens exhibited premature failure compared to the specimens only loaded in tension up to failure since failure occurred at the grips. Nevertheless, the curve shapes are similar. The loading and unloading behaviors were different due to adhesive visco-elasticity while loading and reloading behaviors were similar. The reeep strain, at 0 MPa, increased as the recovery period lengthened (Figure 4.6(d)). The greatest increases in reeep to instantaneous (just after unloading) strain ratio occurred within the first 30 min.

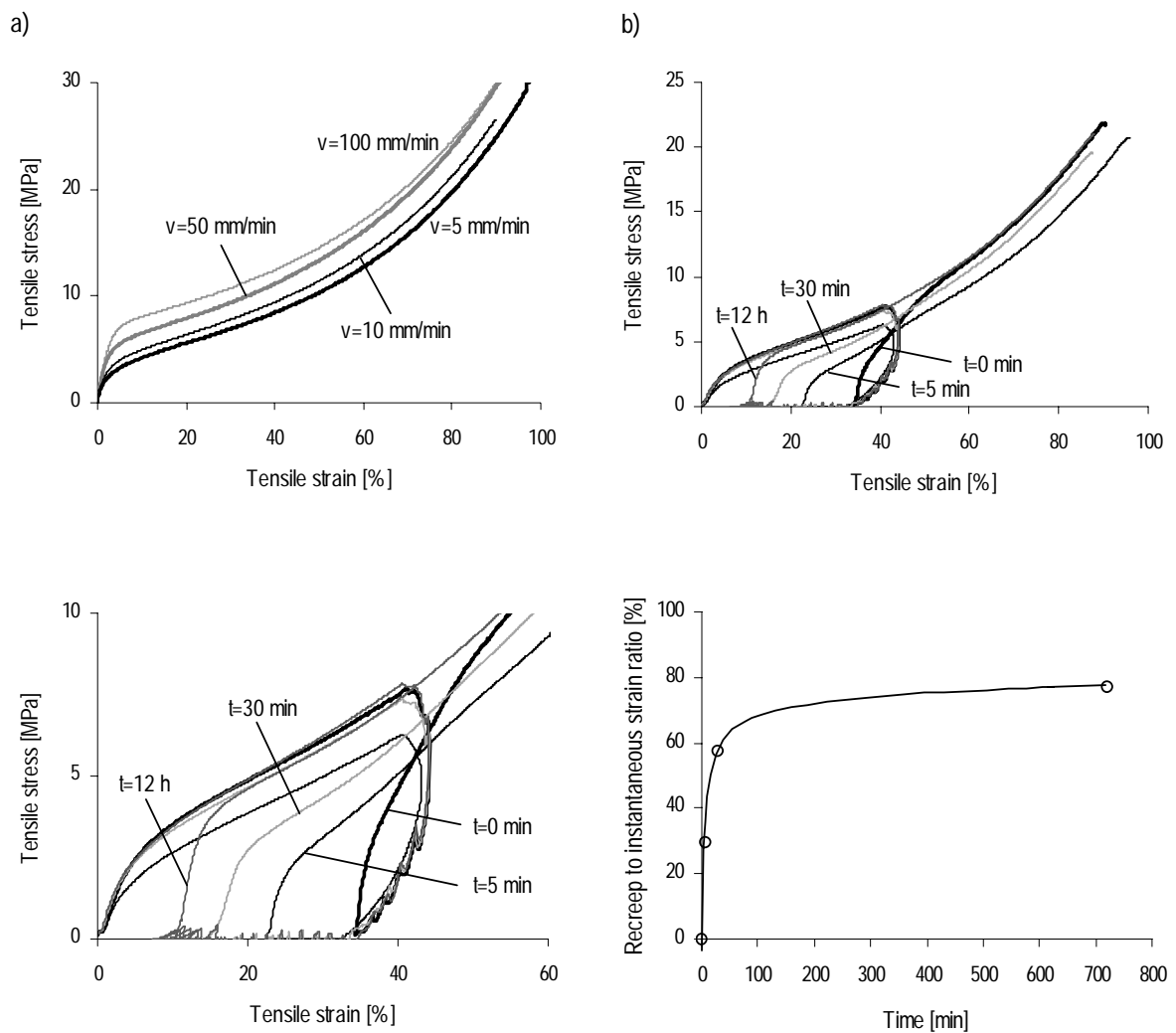


Figure 4.6: (a) Tensile true average stress-strain curves for ADP (5,10,50,100 mm/min); (b) and (c) Tensile nominal load-unload-reload stress-strain curves for ADP (0,5,30 min and 12 h); (d) Time-dependent reeep to instantaneous strain ratio

## 4.2 Double-lap Joint Experiments

### 4.2.1 Experiment Objectives

The experimental program consists of testing bonded double-lap joints in GFRP elements using different adhesives (brittle and ductile, stiff and soft). The experimental series focus on three objectives:

- investigation of the effect of adhesive behavior on joint stiffness, load transfer along the overlap and joint strength;
- selection of the most appropriate adhesive for the development of ductile joints;
- acquisition of experimental data for validation of the FE and analytical models.

A summary of the experimental report (Appendix B) is presented in this section.

### 4.2.2 Specimen Description

#### 4.2.2.1 Dimensions

The dimensions of specimens with a 100 mm overlap length are shown in Figure 4.7(a). The double-lap specimens consist of three laminates of 500 mm length and 100 mm width. The outer laminates were 5 mm thick and the inner laminate was 10 mm thick, twice that of the outer laminates in order to guarantee a constant section area and consequently constant axial stress.

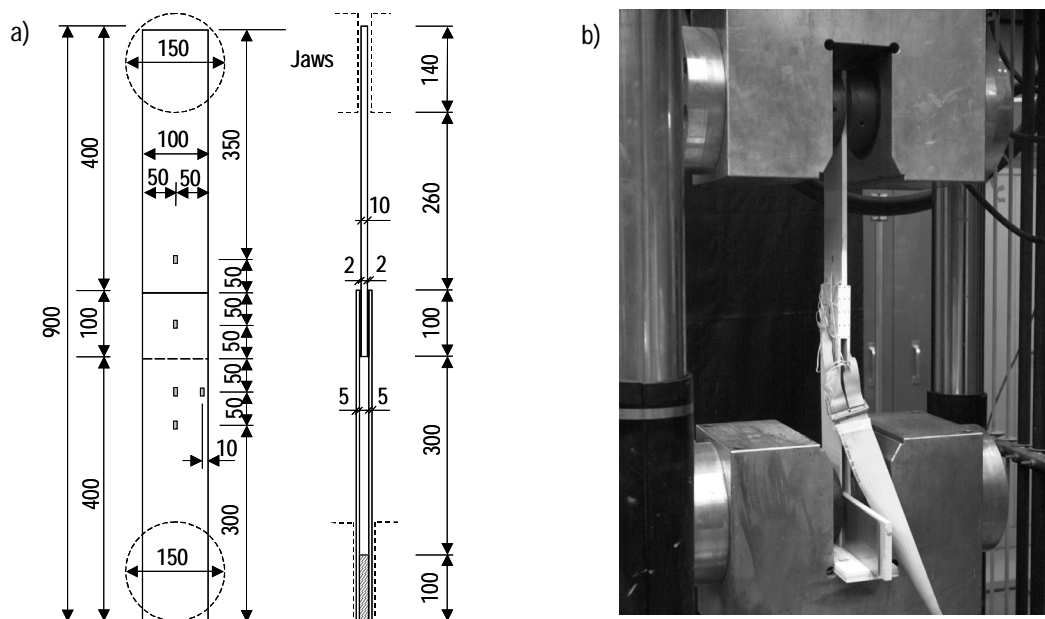


Figure 4.7: (a) Specimen with 100 mm overlap length and gage positioning; (b) Tensile testing device



Two overlap lengths were studied, 100/200 mm. The chosen adhesive thickness was 2 mm due to the tolerances of the sections and the wires of the strain gages bonded onto the 10 mm thick laminate (see Section 4.2.3). The double-lap configuration is easy to manufacture and minimizes bending moments due to load eccentricity, unlike single-lap joints. The laminate length guarantees sufficient distance between the grip and joint areas (260/160 mm), thus the joint area is not influenced by load introduction.

#### 4.2.2.2 Materials

The 5 mm and 10 mm laminates were composed of approximately 47% and 46% E-glass fibers by volume respectively and an isophthalic polyester resin (Tirelli 2003). The 5 mm laminate architecture consisted of approximately 79% UD-rovings and one outer and one inner combined mat (CSM and  $0^\circ/90^\circ$  fabrics stitched together) whereas the 10 mm laminate architecture consisted of approximately 70% UD-rovings and two outer and two inner combined mats. A polyester surface veil ( $40\text{g/m}^2$ ) covered the outsides. Figure 4.8(a) illustrates the fiber architecture of a 10 mm laminate after resin burn-off and Figure 4.8(b) shows fibers were well embedded (no voids) through the thickness by means of a microscope (Tirelli 2003). The corresponding longitudinal Young's moduli were determined experimentally from measured strains. Figure 4.9 indicates (a) local axis and (b) the succession of layer composing the laminate.

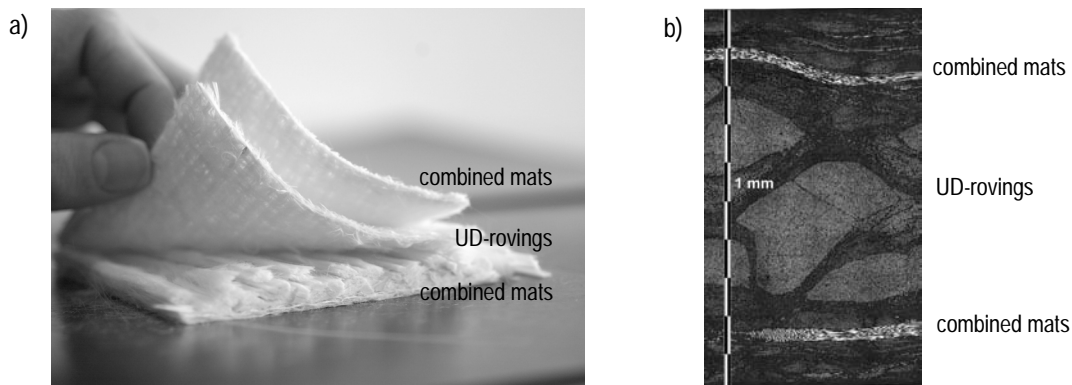


Figure 4.8: 10 mm GFRP laminate (a) fiber architecture after resin burn-off (without surface veil), (b) microscopic section through thickness (Tirelli 2003)

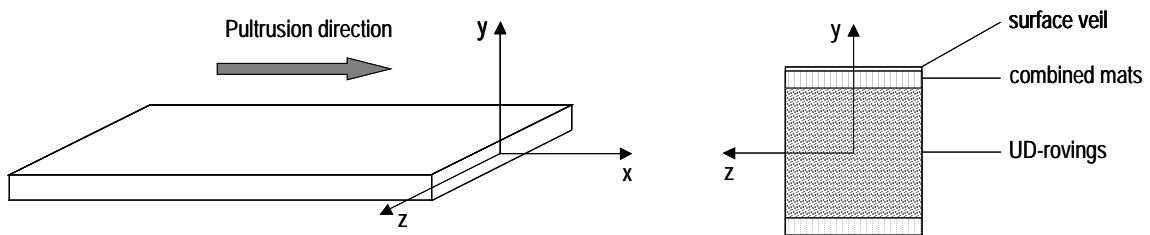


Figure 4.9: (a) Local axis; (b) Schematic drawing of laminate section (not to scale)

The adhesives used were the two-component epoxy resin SD 330, (designated EP), the two-component polyurethane adhesive S-Force 7851(PU) and the acrylic-based two-component SikaFast 5221 structural adhesive (ADP) (see Section 4.1). Adhesive behaviors are shown in Figure 4.5. The EP adhesive exhibits almost linear-elastic behavior and brittle failure while the PU and ADP adhesives exhibit highly non-linear behavior. The EP adhesive is stronger and stiffer than the PU and ADP adhesives.

### **4.2.2.3 Manufacturing Process**

The joints were manufactured in three main steps: surface treatment, bonding and cure. Surface treatment of the GFRP laminates started with degreasing, sanding (removal of polyester and surface veil until the mat appeared at approximately 0.1 mm depth) and cleaning the bonded area. The EP specimens were then ready for adhesive application. PU and ADP specimens required the application of two products: an activator and a primer, according to the specifications of the supplier, who carried out some preliminary tests to check the effect of the activator and four primers (Tsuno 2003). Primers 206 G+P and 215 were selected. Table 1 in Appendix B shows the test series and their corresponding manufacturing processes (1-8). The two components were mixed using the appropriate static mixer tube according to the supplier's specifications and the uncured adhesive was then spread onto one outer laminate. Four glass balls of 2 mm diameter were placed on the bonding area to guarantee adequate adhesive-layer thickness. The inner laminate was then laid and pressed. The laminates were aligned with a rule. Weights were placed on the top of the joint to provide pressure during the curing time. After one day of cure, the second outer laminate was bonded following the same process. The specimens were cured under ambient laboratory conditions,  $23\pm 2^\circ\text{C}$ , for one to five weeks, depending on the test series.

### **4.2.3 Experimental Set-up and Instrumentation**

Specimens were subjected to an axial tensile quasi-static loading via a Schenk Hydropuls-Zylinder Typ PL testing machine with a capacity of 1000 kN in static loading (tension as well as compression) and possible displacements up to  $\pm 250$  mm (Figure 4.7(b)). The diameter of the horizontal hydraulically-controlled circular jaws was 150 mm. Grip lengths were 140 mm and 100 mm for the 10 mm and 5mm laminate respectively; thus specimen lengths between grips were 660 mm and 560 mm for the 100 and 200 mm overlap lengths respectively. A 14 mm thick spacer block was placed between the 5 mm laminates at the grip area to ensure in-plane loading. The tests were conducted in a laboratory environment at room temperature. The load was applied at a constant displacement rate of 0.6 mm/min until specimen failure. Experiments were carried out in the laboratory of the Structural Engineering Institute at the EPFL.

The load and displacement were measured by transducers within the testing machine. Some specimens were also instrumented with strain gages (up to 10) at different cross-sections and strain

gages in the bonded joints (up to 10) (Figure 4.11(b)). The strain gages along the specimen were used to measure axial strain distributions through the length and width of the specimen and indicated load eccentricities in width (transversal) or thickness (out-of-plane) directions (Figure 4.7(a)).

In addition, strain gages were installed in the bonded joints on the 10 mm laminate according to two configurations (Figure 4.10). Configuration 1 consisted of eight gages placed along three sections, indicating strain distribution across the joint width and thus indicating the 2- or 3-dimensional effect of the joint. Configuration 2 consisted of ten gages placed along nine different sections, giving more accurate information about strain distribution along the overlap length. As strains greatly increase at the ends compared to the middle area of the joint, most of the gages were placed between 5 and 20 mm from the ends. Gages on the middle section of the bonded area indicated any loading eccentricity in the width (transverse) direction. Test results for joints with and without internal gages were compared, leading to the conclusion that gages did not affect joint behavior.

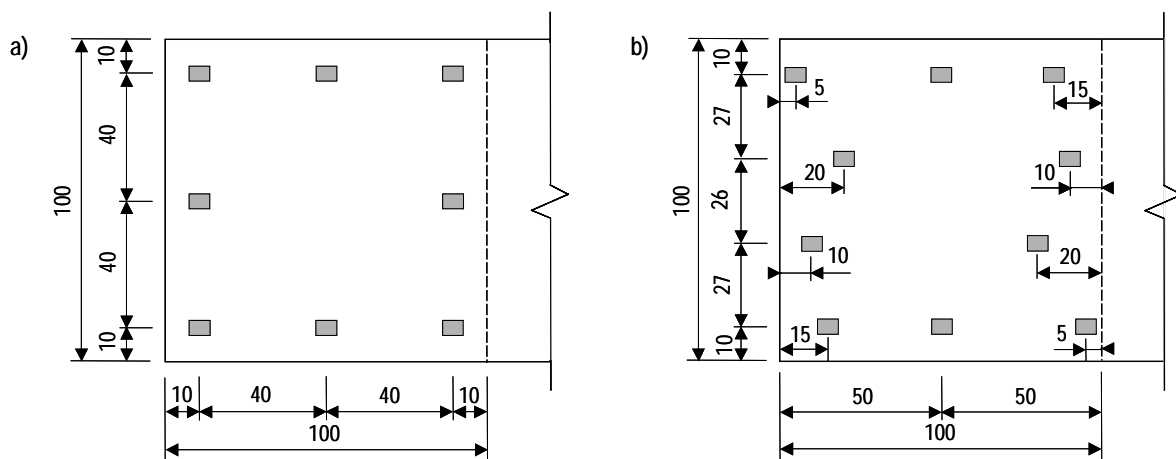


Figure 4.10: Internal strain gage positioning: (a) configuration 1 and (b) configuration 2

A video-extensometer followed the position of fifteen points in the joint area, five points on each axial line with a distance of 22 or 25 mm between them (Figure 4.11(a)). Joint elongation and stiffness were estimated from the measured relative elongation of the laminates in the axial direction (Figure 4.11(a)).

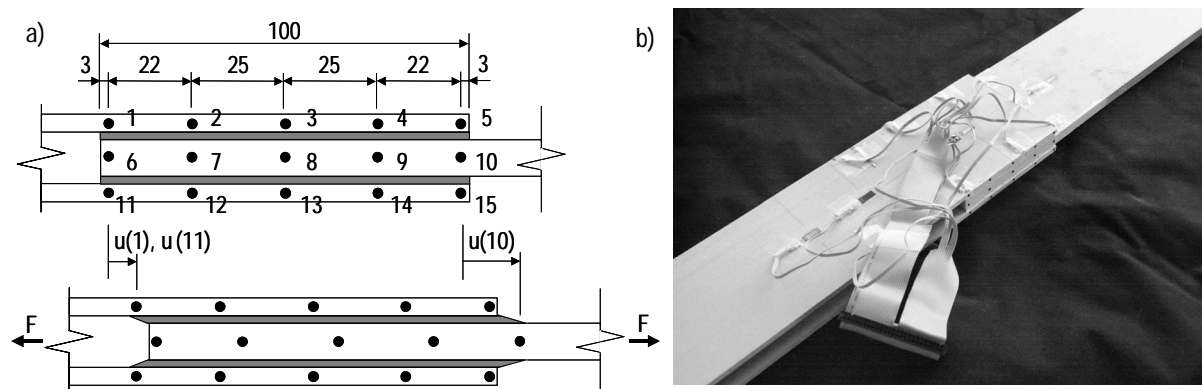


Figure 4.11: (a) Positioning of video-extensometer measurement points; (b) Fully-instrumented specimen

## 4.2.4 Summary of Principal Results

### 4.2.4.1 Global Double-lap Joint Behavior

Table 4.4 summarizes the experimental double-lap joint results (failure load and failure mode). The average shear stress is calculated by dividing the load by the two bonded areas. The joint efficiency is defined as the ratio of joint strength to ultimate material strength (Sotiropoulos et al. 1994). The latter is 332 kN and corresponds to the 10 mm laminate strength, which is lower than that of the 5 mm laminate, 2x215 kN (see Table 3 Appendix B). The ultimate load in brackets corresponds to the maximum strength of the series.

Table 4.4: Overview: experimental double-lap joints and results at failure (see Appendix B)

Series	Number of specimens	Overlap [mm]	Ultimate load [kN]	Ultimate elongation [mm]	Ultimate average shear stress [MPa]	Joint efficiency [%]	Failure mode
EP-A	9	100	141±11	4.1±0.4	7.1±0.6	43± 3	fiber-tear
EP-D	3	200	182±14	4.7±0.6	4.6±0.3	55± 4	fiber-tear
PU-A	2	100	160±16 (171 <sup>2</sup> )	4.8±0.6	8.0±0.8	48± 5	mixed <sup>1</sup>
PU-B	7	100	140±13 (157 <sup>2</sup> )	3.9±0.3	7.0±0.7	42± 4	light-fiber-tear/mixed <sup>1</sup>
PU-C	1	100	173	4.6	8.7	52	mixed <sup>1</sup>
ADP-A	3	100	130±7	6.7±0.4	6.5±0.3	39±2	mixed <sup>1</sup>
ADP-B1	1	100	64	2.4	3.2	19	mixed <sup>1</sup>
ADP-B2	1	100	202	9.2	10.1	61	mixed <sup>1</sup>
ADP-B3	2	100	150±33 (173 <sup>2</sup> )	6.6±1.4	7.5±1.6	45±10	mixed <sup>1</sup>
ADP-B4	3	100	154±22 (173 <sup>2</sup> )	7.3±1.2	7.7±1.1	46±7	mixed <sup>1</sup>
ADP-C	9	100	119±12	6.0±0.5	6.0±0.6	36± 4	mixed <sup>1</sup>
ADP-D	3	200	253±8	8.7±0.6	6.3±0.2	76± 3	mixed <sup>1</sup>

<sup>1</sup> maximum strength of the series

<sup>2</sup> mixed failure: adhesion promoter to substrate failure and light-fiber-tear and/or fiber-tear failure

The global load-elongation curve of representative specimens of series EP.A, PU.B and ADP.C (l=100 mm) are shown in Figure 4.12(a). Behavior of specimens EP.A and PU.B was almost identical: linear-elastic up to approximately 70 kN (50% of ultimate failure load for both series). At this load level, a slight decrease in specimen stiffness was observed. Joint stiffness remained constant as shown in the next section and axial strain measurements along the specimen indicated no stiffness reduction in the laminates (see Sections 4.1.3, 4.2.3, 4.3.3 Appendix B). Thus, part of the displacement could be due to local deformations or the specimen sliding in the machine grips and did not indicate a specimen stiffness reduction. Specimens ADP.C exhibited bilinear behavior as for the ADP adhesive, with a stiffness reduction at approximately 30 kN (25% of ultimate failure load). Figure 4.12(b) shows the global load-elongation curves for representative specimens of series EP.D and ADP.D (l=200 mm). Specimens EP.D were linear-elastic up to approximately 70 kN (38% of ultimate failure load), as for specimens with a 100 mm overlap (EP.A). Specimens ADP.D exhibited bilinear behavior with a stiffness reduction at approximately 70 kN (28% of ultimate failure load).

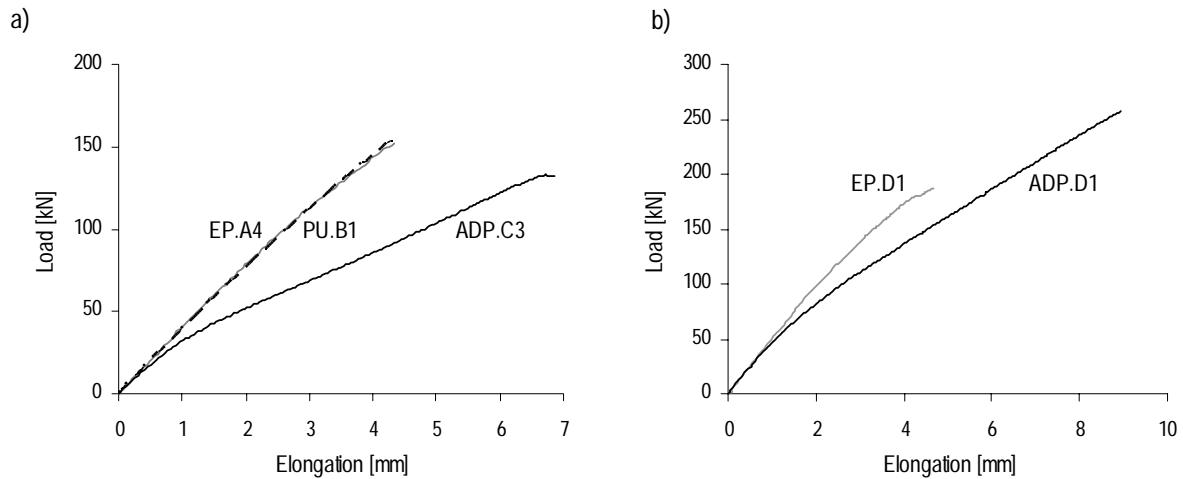


Figure 4.12: Load-elongation curves for specimens (a) EP.A4, PU.B1 and ADP.C3 ( $l=100$  mm), (b) EP.D1 and ADP.D1 ( $l=200$  mm)

Failure of specimens EP.A and EP.D occurred in the 5 and 10 mm laminates between the two outer fiber layers, the combined mat and UD-roving for the 5 mm laminates and two combined mats for the 10 mm laminates, or inside the first combined mat (Figure 4.13(a-b)). According to the failure-mode classification described in ASTM D 5573-99 (1999), it was a “fiber-tear” failure, commonly designated interlaminar adherend failure, due to the weak through-thickness properties of pultruded GFRP materials, mainly influenced by matrix properties (Hart-Smith 1987). This could be caused by combined through-thickness tension and shear stresses. Failures occurred in a brittle manner without the previous appearance of cracks in the joint area. Because of the brittle failure and large dissipation of energy leading to extensive secondary damage, it is difficult to define where failure really started. In order to investigate the crack initiation and failure process, Vallée (2004) carried out similar EP specimen tests involving a high-speed camera. He concluded that failure was initiated in the inner, 10 mm, laminate and demonstrated that the cracks in the 5 mm laminate occurred due to dynamic effects. The main failure surfaces are inside the 10 mm laminates at approximately 0.5 mm depth. The depth varies slightly due to variability of fiber-layer position (Figure 4.8(b)).

Specimens PU.A-C exhibited two kinds of failure modes, a “light-fiber-tear” failure or a mixed failure combining “adhesion promoter to substrate” and “light-fiber-tear” failure (according to ASTM D 5573-99 (1999)). Adhesion promoter to substrate failure occurred in the interface between the primer and activator layers or between the primer and laminate (for series without activator) and revealed inappropriate surface treatment (physical or chemical incompatibility). Light-fiber-tear failure occurred in the laminate, near the surface, and was characterized by a thin layer of matrix on the adhesive with few or no fibers (Figure 4.13(c)).

Specimens ADP.A-D exhibited a mixed failure combining “adhesion promoter to substrate” and “fiber-tear” and/or “light-fiber-tear failure” (according to ASTM D 5573-99 (1999)). The bad-adhesion areas were related to quality of surface treatment and failure load. Stronger specimens revealed smaller bad-adhesion areas. The adhesion failure mode explains the large scatter of the

ultimate failure load. Specimen ADP.B2.1, related to manufacturing process 7 (with primer 1 and 5 weeks of cure), exhibited the maximum failure load (202 kN) and showed a mixed failure combining the previously mentioned failure modes and cohesive failure (see Figure 36 Appendix B). Thus manufacturing process 7 (with primer 1 and 5 weeks of cure) was the most appropriate to the ADP adhesive and GFRP laminate combination but still caused low adhesion problems.

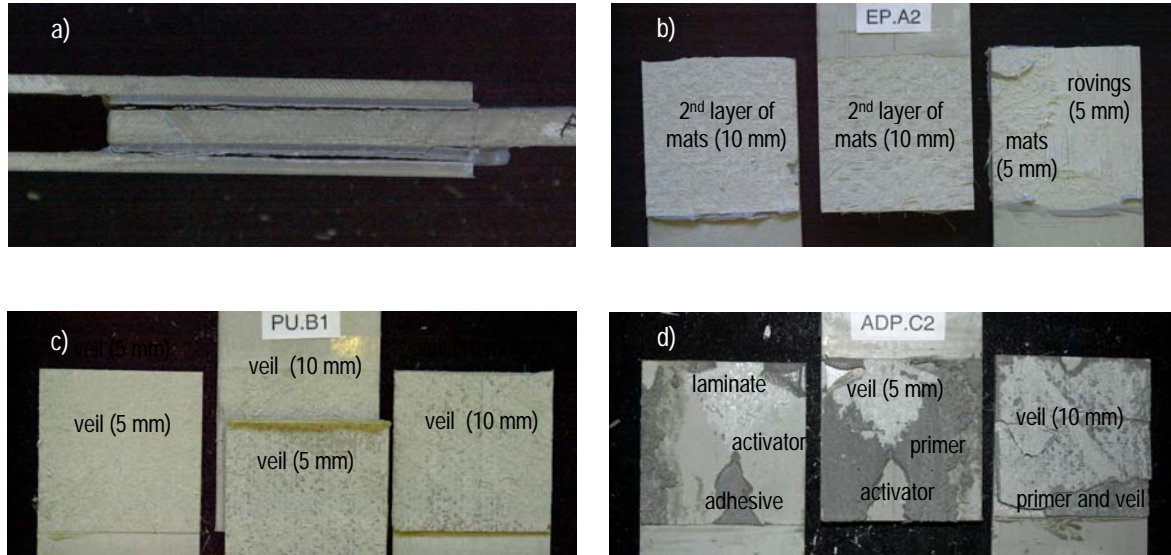


Figure 4.13: Failure modes (a) and (b) EP specimens: fiber-tear, (c) PU specimens: light-fiber-tear, (d) ADP specimens: adhesion promoter to substrate failure and light-fiber-tear failure (mixed), surface failure indication

#### 4.2.4.2 Joint Elongation and Stiffness

Load-joint elongation curves for representative specimens of series EP.A, PU.B and ADP.C, with an overlap length of 100 mm, are illustrated in Figure 4.14(a). Joint elongation,  $u_{\text{joint}}$ , was estimated from the relative elongation of the laminates in the axial direction, from video-extensometer measurements, as follows:

$$u_{\text{joint}} = u(10) - 0.5 \cdot (u(1) + u(11)) \quad (4.5)$$

where  $u(i)$  is the displacement of points  $i=1,10,11$  as indicated in Figure 4.11(a). Joint load-elongation curves for EP and PU joints were linear and demonstrated that specimen stiffness reduction (see previous section) was not due to joint stiffness decrease. ADP joints exhibited bilinear behavior as for the ADP adhesive. Joint stiffness,  $k_{\text{joint}}$ , was calculated from the axial force,  $F$ , and the joint elongation,  $u_{\text{joint}}$ , according to Eq. 4.6. When joint stiffness varies as in ADP joints, it is calculated from increments ( $\Delta F$  and  $\Delta u_{\text{joint}}$ ) at the related interval.

$$k_{\text{joint}} = \frac{F}{u_{\text{joint}}} \quad (4.6)$$

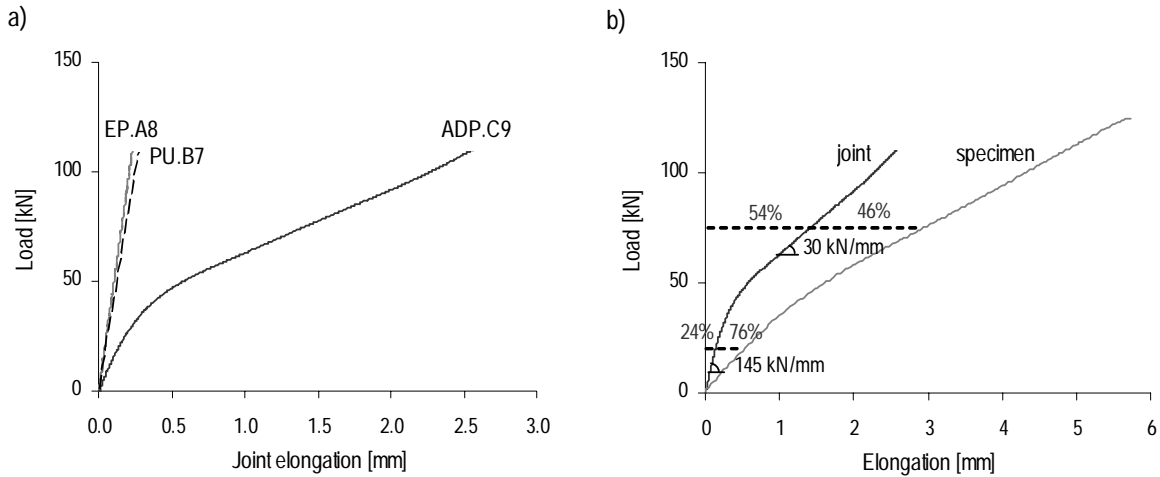


Figure 4.14: (a) Load-joint elongation of specimens EP.A8, PU.B7 and ADP.C9; (b) Load-elongation of global specimen and joint of specimen ADP.C9

Table 4.5 shows the joint stiffness and the joint elongation to specimen elongation ratio of series EP.A, PU.B and ADP.C (three specimens per series). The joint stiffness of EP the and PU specimens remained almost constant but that of ADP specimens changed significantly. EP joints were approximately 23% stiffer than PU joints while the average value of the Young's moduli in tension and compression was approximately 7.5 times higher. For ADP specimens, joint stiffness was defined at two loading levels, 20 kN and 100 kN, both characterizing almost constant curve slopes. Initial the ADP joint stiffness (20 kN) was approximately 3.5 lower than the EP joint stiffness and decreased by a factor of 4 when becoming plastic (100 kN). The joint to specimen elongation ratio indicates joint influence on specimen behavior.

Table 4.5: Measured joint stiffness and joint elongation to specimen elongation ratio of joint series EP.A, PU.B and ADP.C (three specimens per series)

Joint characteristics	EP.A (50 kN)	PU.B (50 kN)	ADP.C (20 kN)	ADP.C (100 kN)
Joint stiffness (kN/mm)	474±4	385±22	135±31	33±6
Joint/specimen elongation (%)	8±1	9±1	24±5	51±2

#### 4.2.4.3 Axial Strains along Specimen and Bonded Joint

The Young's modulus,  $E_x$ , of the 5 mm and 10 mm thick laminates was estimated from strain gage measurements. Average values were 32 GPa and 28 GPa for the 5 mm and 10 mm laminates respectively (see Sections 4.1.3, 4.2.3, 4.3.3 Appendix B). Significant variability in the laminates Young's moduli was observed during the experiments, with scatter reaching 10% of mean values. It is important to note that both laminates were loaded in tension but the 5 mm thick laminates were also subjected to bending. The FE model of the double-lap joints (see Section 5.2.2.3) demonstrates that calculated strains at the gage locations were 3-4% lower than those assuming only tension. Thus the Young's modulus of the 5 mm thick laminates is slightly overestimated.

Load-axial strain curves of gages in the bonded area were linear until the gage no longer worked or the ultimate load and indicated that the axial strain distribution remained constant during the loading, even for ADP joints (see Section 4.3.4 Appendix B). The axial strain distribution in the ADP joints was not influenced by adhesive bilinear behavior since both moduli were low compared to those of laminates (see Section 5.3.2). Identical behavior and failure load of specimens with and without internal gages proved that gages did not affect load transfer and measured actual strain distribution in the joint.

Configuration 1 showed that strains close to the edge were usually higher than in the middle as shown in Figure 4.15 for EP joints. Measured axial strain distributions (symbols) were approximated by a parabolic fit curve. An identical distribution was observed in the ADP joints. The non-uniform load transfer across the width is in agreement with Richardson et al. (1993). Figure 4.15 also indicates a uniform distribution; the maximum deviation between measurements and the average value reached 13%. Thus a uniform approximation of transverse strain distribution is acceptable since deviations are not significant and a 2D model, rather than a more complex 3D model, could be developed for joint analyses.

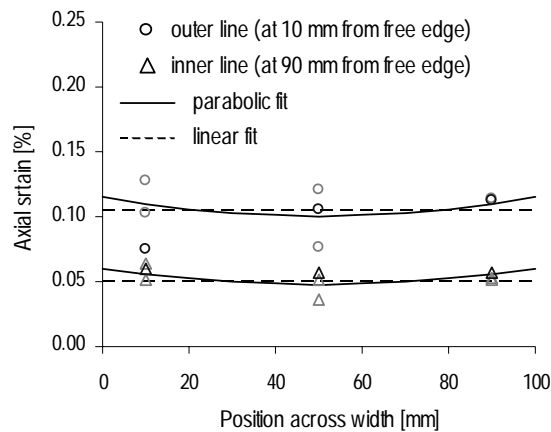


Figure 4.15: Axial strain distribution across joint width of series EP.A at 50 kN, measurements and parabolic and linear fit curves

Figure 4.16 (a-c) shows axial strain distribution along the overlap length in the 10 mm laminate interface at a load of 50 kN. Measured axial strain distributions (symbols) were approximated by a linear regression. The strains greatly increased in the first and last 10 mm. Figure 4.16(d) compares the three linear regressions. Curve slopes increased with adhesive stiffness decrease. Axial strains were more uniformly distributed in ADP joints than in EP and PU joints, proving more uniform load transfer along the joint.



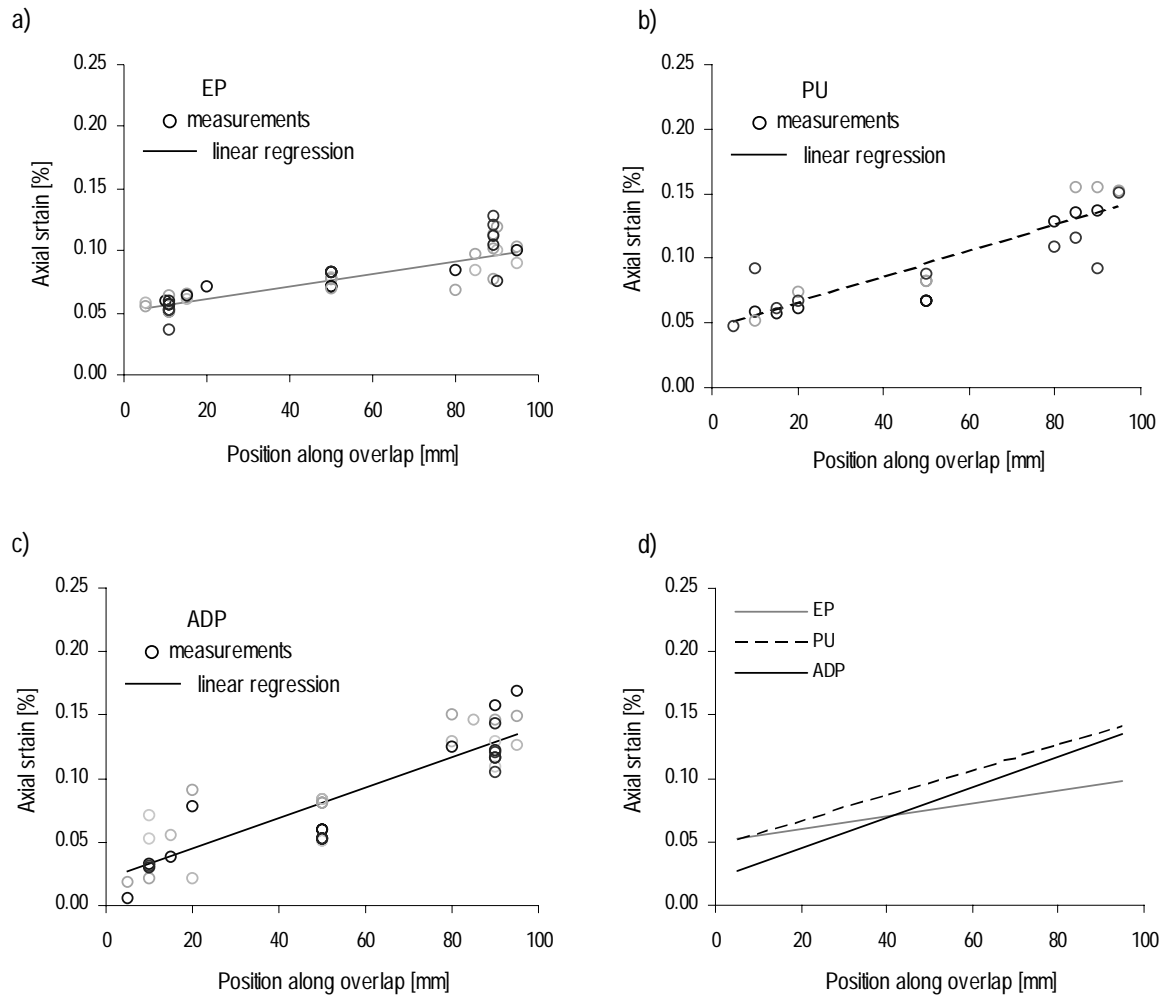


Figure 4.16: Axial strain distribution along overlap length at 50 kN for series (a) EP.A, (b) PU.B, (c) ADP.C, measurements and linear regression, (d) linear regression comparison

## 4.3 Bonded Beams Experiments

### 4.3.1 Experiment Objectives

Bending experiments were performed on GFRP continuous beams over two spans with a highly non-linear (almost bilinear) adhesively-bonded connection at mid-support. The experimental series has three main objectives:

- validate the structural system, verifying its improved performance compared to conventional static systems such as the simple and continuous beam over three supports;
- investigate the structural system behavior;

- compare the experimentally-observed behavior of the structural system with that predicted using an analytical model based on GFRP orthotropic and adhesive properties in order to validate the model.

A summary of the experimental report (Appendix C) is presented in this section.

## 4.3.2 Specimen Description

### 4.3.2.1 Dimensions

Experiments were carried out on GFRP beams with ductile and flexible adhesive joints (see Section 3.1.4) as seen in Figure 4.17(a). Four two-span beams, designated PH1-4, were tested. The beams were built from two single-span beams. Beam spans were 3.60 m. Pultruded beams with square box cross-sections of 240x240 mm and 12 mm wall thickness were used (Figure 4.18(e)). The depth/span-ratio was 1/15. The beam flanges were connected with adhesive strap joints (see Figure 2.19 page 33) at mid-support, the location of the maximum negative bending moment, as shown in Figure 4.17(b). The strap joints had different overlap lengths, 1: 2x100 mm (PH3), 2x200 mm (PH1 and PH2) and 2x300 mm (PH4), as listed in Table 4.6. Due to the size of the support surface required at mid-support, the beam with upper overlaps of 2x100 mm (PH3) had lower overlaps of 2x200 mm. The flanges were connected with cover plates of the same thickness (12 mm) and width (240 mm), as shown in Figure 4.17(b) and 4.18(f). The cover plates were cut from identical beam sections. The average gap between connected beams,  $e$ , ranged from 12 to 16 mm. The beam webs were not connected. The bonded joints were thus able to transfer bending moments over mid-support but not vertical shear forces. The chosen adhesive thickness was 2 mm due to the tolerances of the sections and wires of the strain gages bonded onto the flanges in the joints.

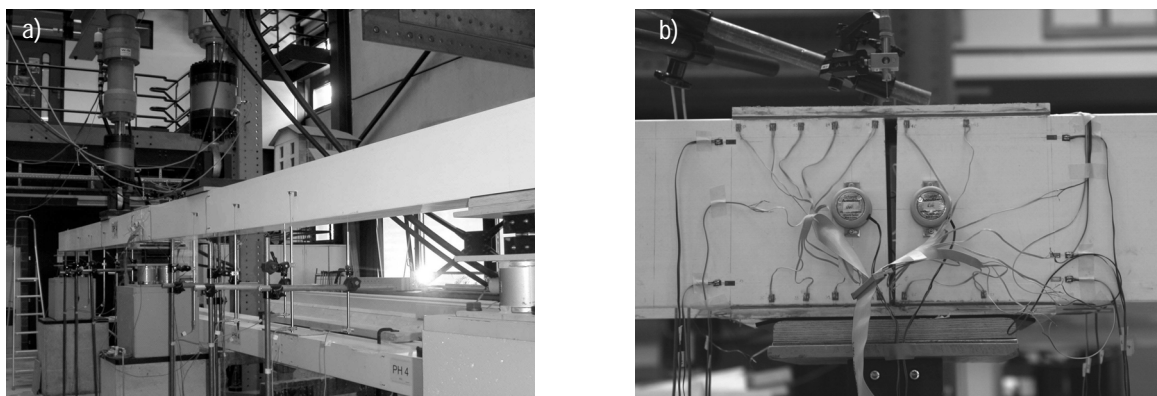


Figure 4.17: (a) Loading test set-up for bonded beam PH2; (b) Bonded joint over mid-support of beam PH1 with strain gages and clinometers

The bonded beam configuration and experimental set-up were chosen primarily from a scientific and practical point of view to demonstrate the feasibility of the general structural concept developed. The

practical application of this layout with the bonded joints over the supports was not the main concern. In order to compare the behavior of the 4 bonded beams, PH1-4, 3 simple (single-span) beams, PS1-3, with 3.60 m span and 3 continuous two-span beams, PC1-3, without bonded joints over the mid-support, were also tested. Table 4.6 shows beam details and test results at failure.

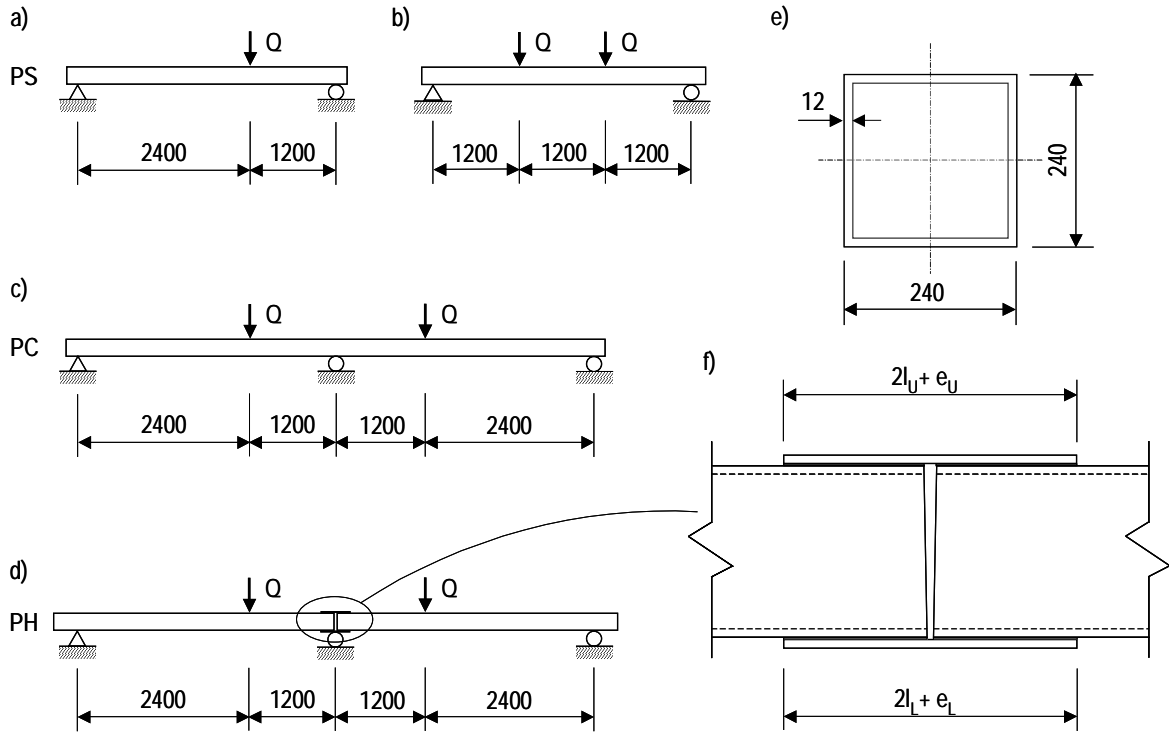


Figure 4.18: Loading positions: (a) and (b) simple beams PS, (c) continuous beams PC, (d) bonded beams PH (dimensions in mm); (e) Idealized beam section; (f) Joint detail

Table 4.6: Overview: experimental beams and results at failure

Beam	Specification	Ultimate load per jack [kN]	Deflection loading section [mm]	Rotation middle support [°]	Reaction middle support [kN]	Moment middle support [kNm]	Moment at jack location [kNm]	Failure location
PS1-3	Simple	155±5	66±3	2.9±0.1	103±3	0	125±4	Loading section
PC1-3	Continuous	146±11	32±6	0	242±17	-86±7	60±5	Mid-support
PH1	Adhesive joint overlap 2x200 mm	180	45	1.6	278	-67	99	Loading section
PH2	Adhesive joint overlap 2x200 mm	178	50	1.8	267	-53	107	Loading section
PH3	Adhesive joint 2x100 mm (top) 2x200 mm (bottom)	1) 135 2) 154	1) 38 2) 55	1) 1.5 2) 2.2	200 206	1) -36 2) 0	1) 84 2) 122	1) Adhesive joint 2) Loading section
PH4	Adhesive joint overlap 2x300 mm	178	47	1.4	274	-66	98	Loading section

<sup>1</sup> first failure: at the adhesively-bonded joint, <sup>2</sup> second failure (leading to structural collapse): at the loading section

### 4.3.2.2 Materials

The beams were composed of approximately 45% E-glass fibers by volume and an isophthalic polyester resin. The architecture consisted of approximately 67% UD-rovings and two outer and inner combined mats (CSM and 0°/90° fabrics stitched together). The edges of the overlaps of combined mats were visible on the outer surfaces at approximately 30 mm from section edges (Figure 4.19). A polyester surface veil (40g/m<sup>2</sup>) covered the outsides. Stiffness properties of the beams were determined experimentally on the simple beams (PS1-3) by three-point and four-point bending tests and compared to the pultruder's design values (Anon 2003). Table 4.7 gives an overview of the results. The values used to predict beams behavior were 30 GPa for the elastic modulus and 3 GPa for the shear modulus.

The adhesive used was the acrylic-based two-component SikaFast 5221 (ADP) structural adhesive (see Section 4.1.2.1 and 4.1.4). Adhesive choice was based on the preceding experiments on bonded GFRP double-lap joints using epoxy, polyurethane and acrylic adhesives (see Section 4.2.4). The behavior was highly non-linear, almost bilinear, and the elastic modulus was lower than the traditional structural and stiff epoxy adhesive (Figure 4.5(a) and 4.5(c)). The adhesive allows good load transfer in joints, increasing the failure load, and the development of large deformations.

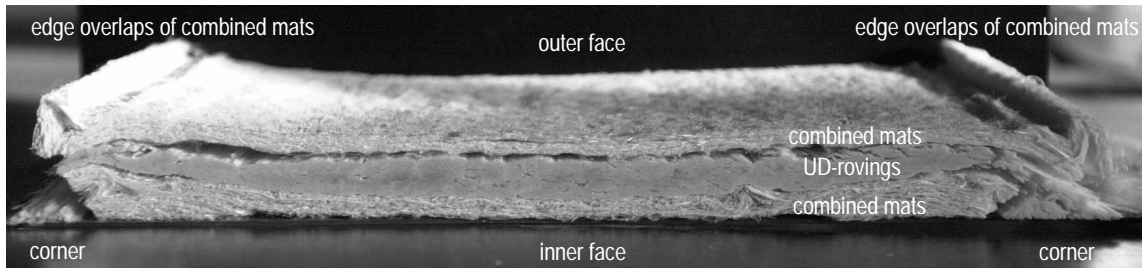


Figure 4.19: Fiber architecture of a 240x240x12 mm profile after resin burn-off test

Table 4.7: Material Properties of GFRP Beams

Data origin	Failure strength ( $f_u$ ) [MPa]	Elastic Modulus (E) [GPa]	Shear Modulus (G) [GPa]
Design Manual	240	23.0	3.0
Obtained from beams PS1-3:	tension and compression 153 (buckling)		
- from deflections		32.1±1.8	2.1±0.5
- from rotations (E) and deflections (G)		29.8±0.2	3.3±0.2
- from strain gages 0° (E) and 45° (G)		30.3±0.4	4.3±0.1
Used for calculations		30.0	3.0

### 4.3.2.3 Manufacturing Process

The joints were manufactured in three main stages: surface treatment, bonding and cure, as explained in Section 4.2.2.3. Bonding was prepared according to the supplier's specifications (Sika) and manufacturing process (see Section 2.3 Appendix B). Four glass balls of 2 mm diameter were placed

on each bonding area to guarantee the adequate adhesive-layer thickness. The laminates were then laid and pressed. After one day of cure, the beam was delicately turned over and the second laminates were bonded following the same process. The beams were cured under ambient laboratory conditions, nine weeks at  $22\pm 2^\circ$  for PH1 and five weeks at  $26\pm 2^\circ$  for PH2-4 (variations during the summer).

### 4.3.3 Experimental Set-up and Instrumentation

The experimental set-up can be seen in Figures 4.17(a) and 4.18(a-d). The two-span beams were loaded by one hydraulic jack of 500 kN capacity per span. The jacks were located at one third of the span on the mid-support side. Load-application points were determined in such a way that, for the continuous beam configuration, the hogging (maximum negative) moment over the support,  $M^-$ , to the sagging (maximum positive) moment in the span,  $M^+$ , ratio was a maximum in order to clearly demonstrate the effect of the flexible joints in the bonded beams. On the other hand, this ratio was chosen as being close to the uniform load distribution ratio, which is  $M^-/M^+=1.79$  (disregarding shear deformations). Given these considerations, a load-application point at one third of the span on the support side of each span resulted in a ratio of  $M^-/M^+=1.88$  (ignoring shear deformations). For the simple beams, in addition to the three-point configuration, a four-point load-configuration was used to determine beam properties (Figures 4.18(a-b)).

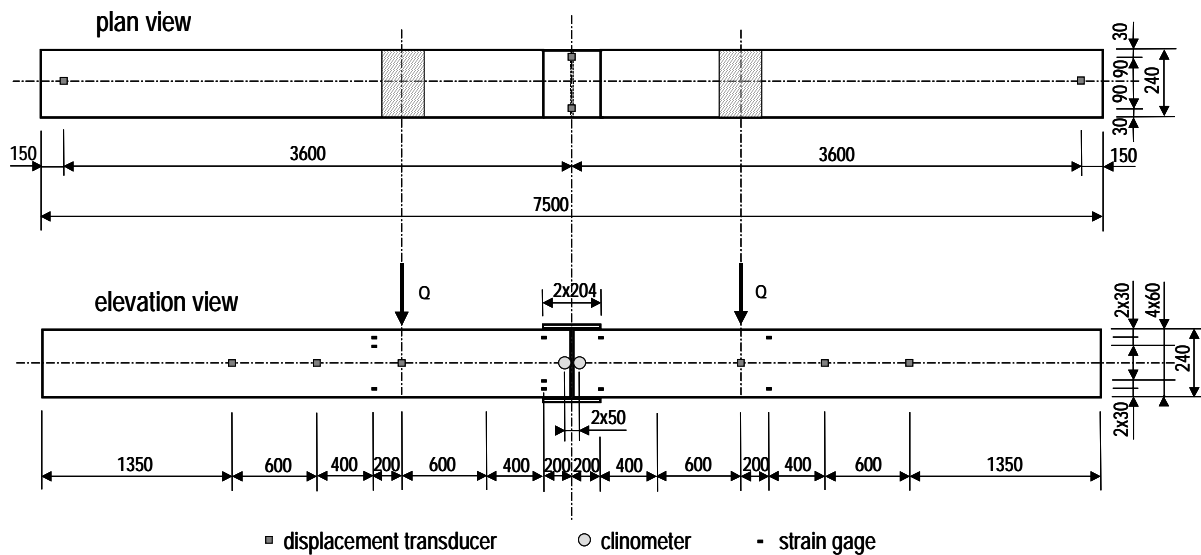


Figure 4.20: Arrangement of displacement transducers, clinometers and strain gages in beam PH2 (dimensions in mm)

Timber plates and 5 mm thick neoprene pads were placed at the loading and support points. Timber plate dimensions for the most critical mid-support were 300 mm long by 260 mm wide by 27 mm thick. In addition, plate edges were chamfered to a 10 mm radius to relieve stress concentrations.

The vertical load and displacement at the jacks were measured by transducers within the machine. In addition, load sensors were placed at each support, as well as vertical displacement transducers (up

to 12), electronic clinometers at the supports (4), and strain gages (up to 20) at different cross-sections (Figure 4.20). The strain gages were used to measure axial strain distributions through the depth and across the width of the beams. In addition, strain gages were placed in the bonded joints of beams PH1-4 on the top and bottom flanges (40 gages in each connection). Except for PH1, which had twenty gages on each joint, twenty-four gauges were installed in the tensile joint, i.e. the upper joint, and sixteen in the compressive joint, i.e. the lower joint. Gages were arranged on three (lower flange) or five (upper flange) sections along the overlap length and on three lines across the beam width. The strain gage arrangement in both joints of beam PH2 with 2x200 mm overlap length is shown in Figure 4.21. On beam PH3, because of the short overlap length, gages at the edges were not aligned (Figure 4.29).

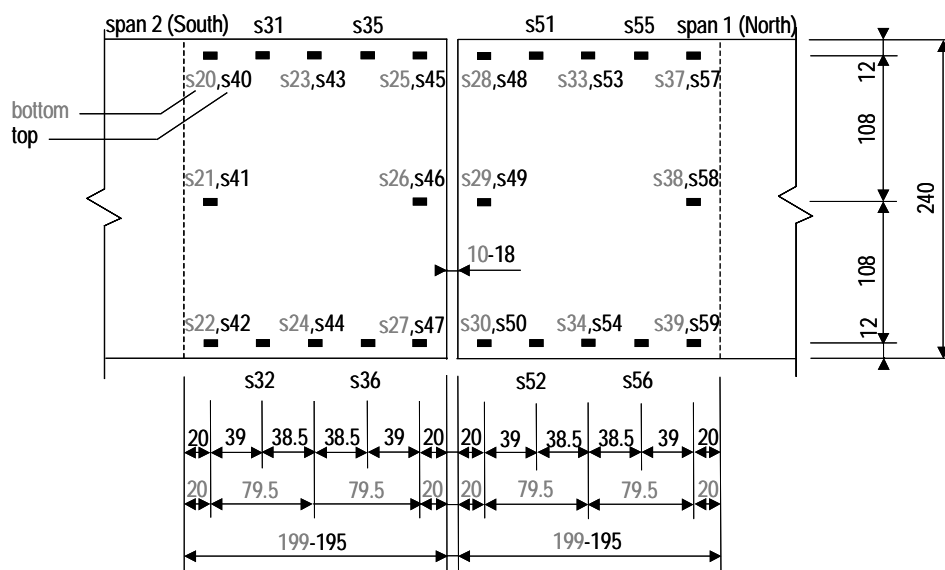


Figure 4.21: Strain gage arrangement in upper and lower adhesive joints of beam PH2 with 200 mm overlap (grey label: lower flange; black label: upper flange)

#### 4.3.4 Experimental Program

In the first phase of the experimental program, each beam was subjected to several load cycles at different load levels to observe the behavior of the beams and the instrumentation. These cycles were carried out under load-control at a rate of 5 kN/min. In the second phase, the beams were loaded up to failure under displacement-control at rates of 1.2-2.3 mm/min. These rates were calibrated in such a way that they corresponded to the load-control rate of the first phase. The single beams were loaded in the three-point configuration up to failure with the load at the one-third span position. With regard to the flexible adhesive used, a creep experiment was performed on the bonded beam PH2 between the first and second phases of the experimental program. The beam was subjected to a load of 40 kN per jack for a period of 7 days. The immediate deflection-to-span ratio of 1/400 was approximately equal to the admissible deflection ratio at the serviceability limit state in building construction. Figure 4.22 shows the loading procedure for beam PH2.

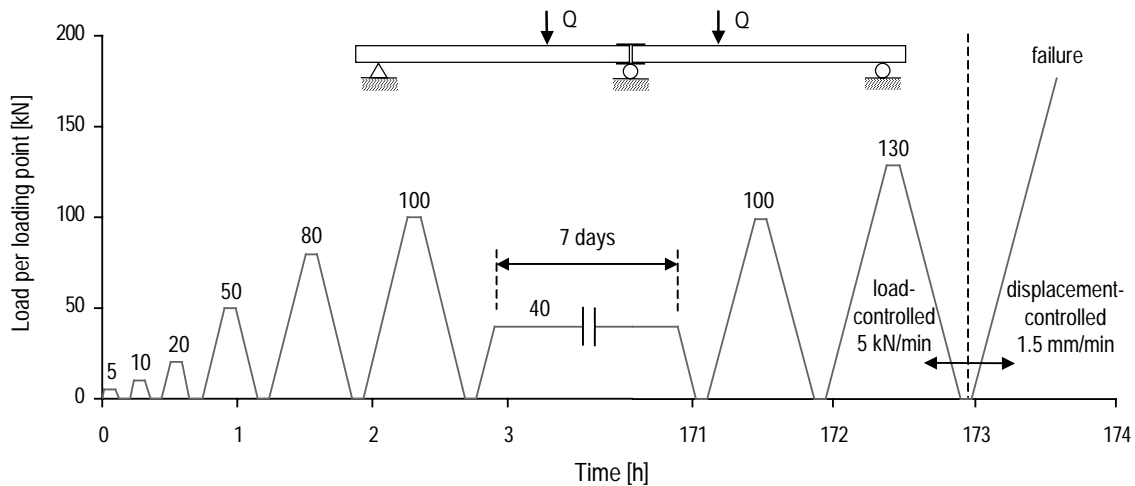


Figure 4.22: Loading procedure for beam PH2

### 4.3.5 Summary of Principal Results and Discussion

#### 4.3.5.1 Behavior of Simple Beams

Results of the first phase of the experimental program showed that axial strains through the depth of all beams remained linear. The neutral axis was approximately 2 mm below the centerline in the spans due to the slightly different elastic tensile and compression moduli. Compression strains were slightly higher than tensile strains. Furthermore, strains across the flange width remained constant. No reductions due to shear lag were observed.

The load-deflection curves for the three simple beams, PS1-3, are shown in Figure 4.23. Beam behavior was identical and linear-elastic up to a load of approximately 100 kN per jack (approximately 65% of ultimate failure load). At this load level, a slight decrease in stiffness was observed. The stiffness decrease coincided with the onset of buckling of the compression (top) flange of the beams, indicated by the strain gages distributed across the width of the top flanges. Figure 4.24(a) shows strain measurements across the top and bottom flanges of beam PS2, 50 mm from the edge of the patch loading. The strains in the tension (bottom) flange increased linearly up to failure, whereas strains in the compression (top) flange began to decrease non-linearly as the load exceeded approximately 65% of the ultimate failure load. Subsequent to the onset of buckling, the stiffness of the beams continued to decrease slightly up to failure (Figure 4.23). The top flange failed in beams PS1 and PS3, as shown in Figure 4.24(b). At the same time, horizontal cracks formed in the webs at the locations of the overlap ends of the combined fiber mats. In beam PS2, only the webs failed and two horizontal cracks formed on each side, one of them also at the locations of the overlap ends of the combined mats.

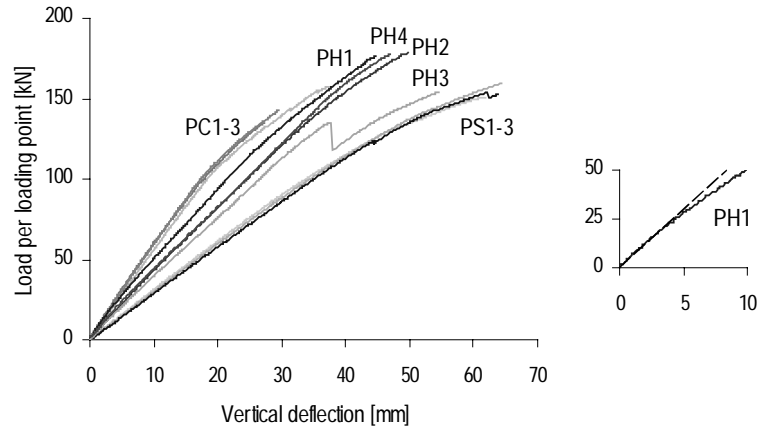


Figure 4.23: Load-deflection curves at loading section

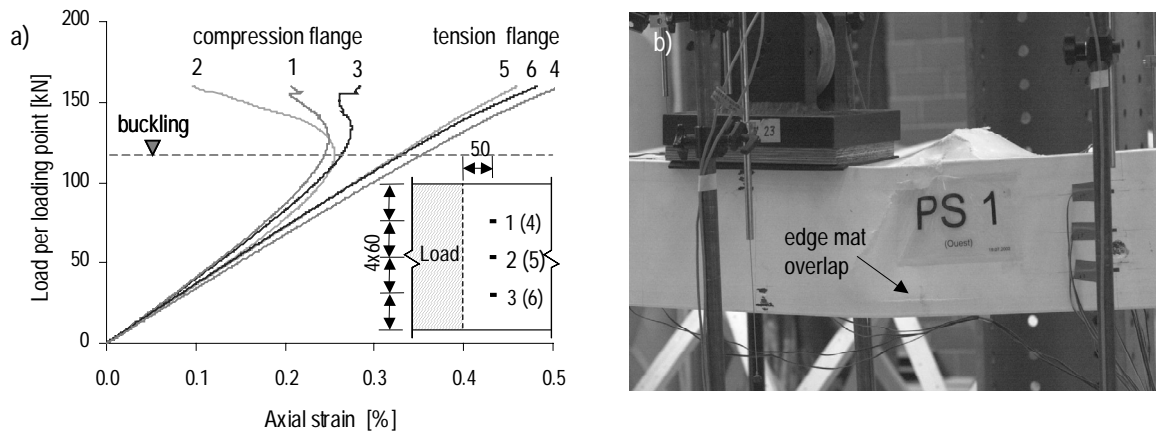


Figure 4.24: (a) Strain distribution across tension and compression flanges of beam PS2 (dimensions in mm); (b) Failure of beam PS1 near patch load

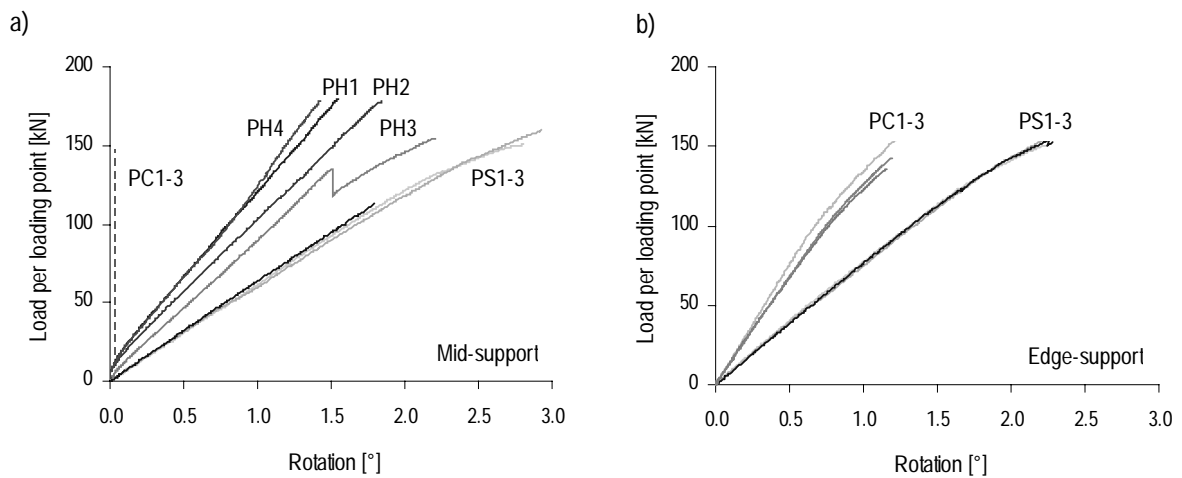


Figure 4.25: Load-rotation curves at (a) mid-support for beams PS1-3, PC1-3 (not measured) and PH1-4, (b) edge-support for beams PS1-3 and PC1-3



Figure 4.25(a) shows the measured load-rotation behavior of beams at the support closer to the jack in the three-point bending tests. The rotation curves showed the same elastic/non-linear behavior as the deflection curves. The measured ultimate failure loads, maximum deflections at the loading section and maximum rotations at the support closer to the jack (mid-support for the continuous beams) are listed in Table 4.6 (average values and standard deviations).

#### 4.3.5.2 Behavior of Continuous Beams

The load-deflection curves for the three continuous beams, PC1-3, are shown in Figure 4.23. Average values of the two jack loads and deflections at the two loading sections are indicated. Beam behavior was identical and linear-elastic up to a load of approximately 100 kN per jack (approximately 70% of ultimate failure load). As for the simple beams, stiffness began to decrease at this point due to the onset of buckling of the compression flange and particularly of the webs (Figure 4.26(a)). In the continuous beam configuration, the most highly compressed flange and webs were the bottom flange and webs at mid-support. Ultimate failure occurred in the webs at mid-support. Horizontal cracks formed 30 mm above the lower edges in the region where the overlaps of the combined fiber mats ended. The support plate crushed the beam, as can be seen in Figure 4.26(b) for beam PC3. Furthermore, two longitudinal cracks, at the location of the overlap ends of the combined mats, formed in the lower flange of all three beams 30 mm from the edges.

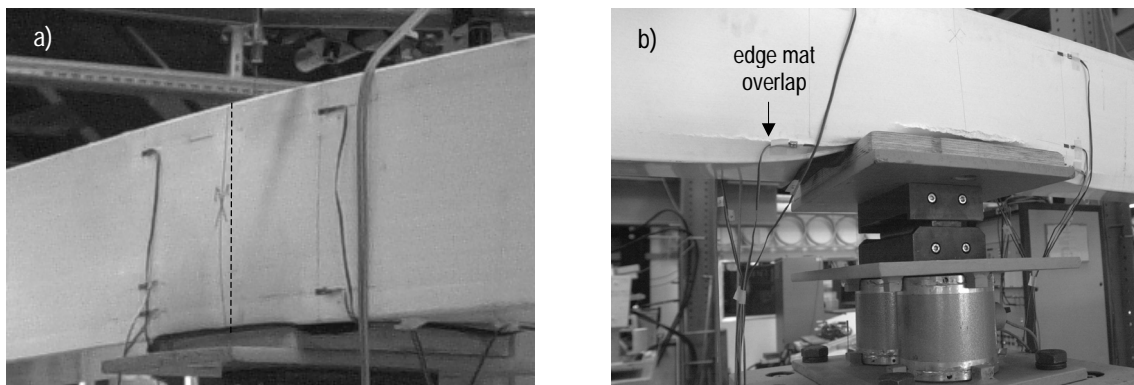


Figure 4.26: (a) Buckling of beam PC2 at mid-support; (b) Failure of beam PC3 at mid-support

No rotations occurred over the mid-support. The principal experimental results are listed in Table 4.6. The ultimate failure loads were slightly lower than those of the simple beams. Maximum deflections at the loading section varied between 27 and 38 mm (approximately span/110) and reached approximately 50% of simple beam values.

#### 4.3.5.3 Behavior of Bonded Beams with 200 mm Overlap (PH1 and PH2)

The load-deflection responses of bonded beams PH1 and PH2 with 2x200 mm joint overlap are shown in Figure 4.23. The beams showed trilinear behavior. In a first phase up to approximately

125 kN (70% of ultimate failure load), behavior was bilinear, as for the ADP adhesive. In the load range up to approximately 20 kN load per jack, the initial stiffness decreased to 73% and 78% respectively, and subsequently remained constant. In the second phase, exceeding 125 kN, the stiffness began to decrease further, coinciding firstly with the onset of buckling of the top flanges and webs below the patch load and then the bottom flanges and webs at mid-support. Beam PH1 was slightly stiffer than beam PH2, which could be explained by the different temperature in the laboratory during experiments (PH1 22°, PH2 28°). Figure 4.27(a) shows the deformed beam PH1 at the onset of failure. The negative curvature over the mid-support due to the continuity effect resulting from the bonded joint is clearly visible. Below the left jack, the buckling of the web is also visible. Beam failures occurred in the webs below one of the jacks as had been observed for the simple beams, in the area of the end of the mat overlap Figure 4.27(b). No damage or failure was observed in the bonded joint.

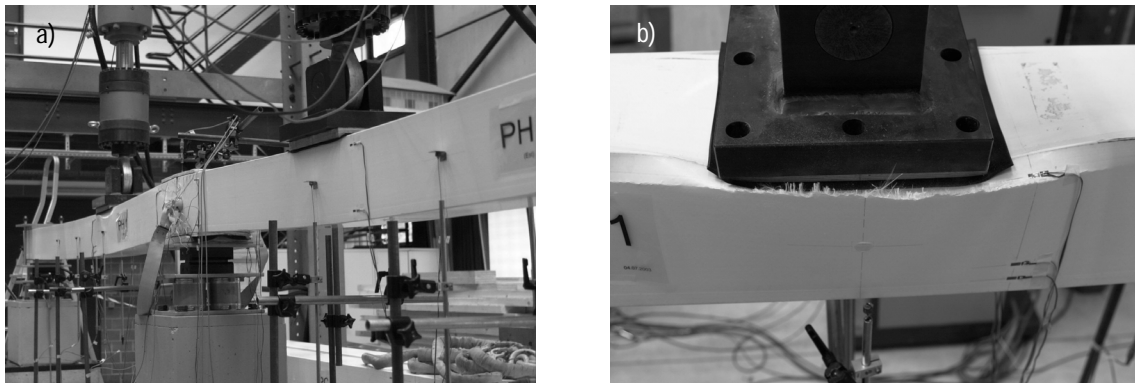


Figure 4.27: (a) Deformation of bonded beam PH1 at onset of failure; (b) Failure of beam PH1 below patching load

Figure 4.25 shows the measured load-rotation behavior of the beams at mid-support. The rotation curves showed the same bilinear behavior as the deflection curves in the first phase of the experiments. However, the stiffness decrease in the second phase, due to buckling, could not be detected. The main experimental results are listed in Table 4.6.

Beam PH2 was subjected to 7 days of creep loading as already mentioned (Figure 4.22). The first hour of the measured deflection-time curve is shown in Figure 4.28. The loading curve up to 9 mm deflection is not totally linear due to the manually-driven loading. Subjected to constant loads, the maximum deflection increased from 9.1 mm to 11.6 mm (approximately 25%) during the 7 days (see Section 4.3.5 Appendix C). 70% of the increase occurred within the first 5 minutes.

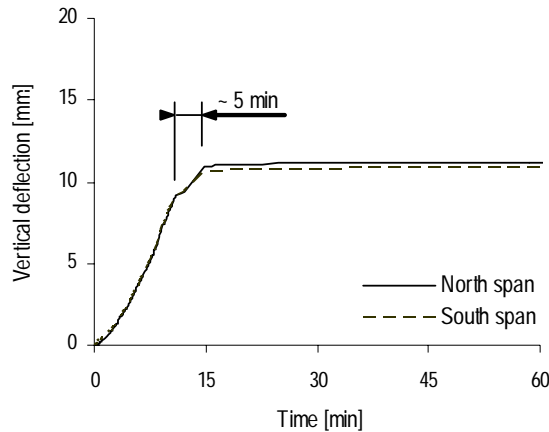


Figure 4.28: Creep deformation of bonded beam PH2 during first hour

#### 4.3.5.4 Behavior of Bonded Beams with 300 mm Overlap (PH4)

The bonded beam with 2x300 mm overlap lengths, PH4, showed almost the same load-deflection and load-rotation behavior as beams PH1 and PH2 with 200 mm overlaps, as shown in Figures 4.23 and 4.25. In the first phase, the deflections matched those of beam PH2, while the rotations matched those of beam PH1. In the load range up to approximately 25 kN load per jack, the initial stiffness decreased to 78%. In the buckling phase (above 155 kN per jack), stiffness loss was less pronounced than in beams PH1 and PH2. Failure occurred through buckling of the webs below the North jack and was similar to the failures of beams PH1 and PH2, in the area of the end of the mat overlap. The bonded joint remained undamaged.

The principle experimental results are listed in Table 4.6. The ultimate failure load was 178 kN per jack and the maximum deflection at the loading section amounted to 47 mm. Both values matched those of beam PH2. The maximum rotations at mid-support were 1.4°, which is approximately 12% less than beam PH1 and 23% less than beam PH2.

#### 4.3.5.5 Behavior of Bonded Beams with 100 mm Overlap (PH3)

The bonded beam with 2x100-mm top overlap lengths, PH3, showed load-deflection and load-rotation responses analogous to beams PH1, PH2 and PH4 in the first bilinear part up to approximately 120 kN. The stiffness was slightly lower than that of the other beams, as shown in Figure 4.23. In the load range up to approximately 10 kN load per jack, the initial stiffness decreased to 75%. Exceeding 120 kN, the stiffness also began to decrease due to the onset of buckling in the compressed flanges and webs firstly below the jacks and then at mid-support. At a load of 135 kN, however, this beam's behavior was distinctly different from that of the others. One part of the adhesive joint in the upper flange failed, as can be seen in Figure 4.29(a). Failure occurred partially in the outer mat of the pultruded beam ("light-fiber-tear" failure according to ASTM D 5573-99

(1999)) and partially in the interface (“adhesion promoter to substrate” failure). A small area failed in the interface between cover plate and adhesive (“adhesion promoter to substrate” failure). The load decreased slightly after this first failure due to the displacement-controlled driving. Subsequently, however, the load increased again with increasing deflection. The load-deflection path then progressed in parallel with the simple beams up to an ultimate failure load of 154 kN. Ultimate failure occurred below the North jacks, as was observed for the simple and other bonded beams. The webs buckled and the same horizontal cracks formed, as already described. The principal experimental results are listed in Table 4.6.

Figure 4.29(b-c) shows the widening of the upper gap in the joint between the two beam parts: a) 20 mm at the beginning of loading and b) 27 mm at 118 kN load per jack. The shear deformation of the adhesive edges of the overlap can be seen. The visible shear angle is approximately  $50^\circ$  at 118 kN; a proportional increase up to the failure load of 135 kN gives an angle of  $57^\circ$ .

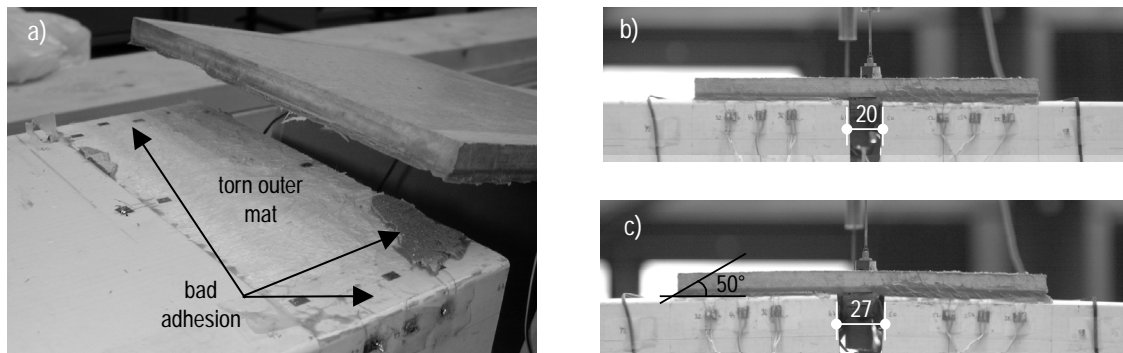


Figure 4.29: (a) First failure of bonded beam PH3 at mid-support (strain gages staggered in the 100 mm overlap); Widening of upper part of bonded joint of beam PH3 (b) initial position, (c) deformation at 118 kN

#### 4.3.5.6 Full-Section Elastic and Shear Moduli

The stiffness properties of the beams were determined experimentally on the simple beams (PS1-3) by three- and four-point bending tests and compared to the pultruder’s values (Anon 2003). Table 4.7 gives an overview of the results. The full-section elastic and shear moduli,  $E$  and  $G$ , were calculated by three different methods from measured the deflections, rotations and strains.

**Method 1.** The elastic and shear moduli were calculated by conducting four-point bending tests and measuring loads and deflections at mid-span and third-points. The flexural and shear moduli were computed from these deflections. Zureick et al. (1994) pointed out that estimated moduli are very sensitive to experimental values of mid-span and third-point deflections, which are very close to each other. The shear stiffness includes the shear coefficient (synonymous with shear correction factor),  $K$ , which was estimated ( $K=0.38$ ) according to Bank (1987) and Omidvar (1998) and taking into account the thin-walled correction factor (Young 1989). More information concerning the shear coefficient is given below.

**Method 2.** The elastic and shear moduli were computed by conducting four-point bending tests and measuring loads and deflections at mid-span and rotations at supports. The elastic modulus was calculated from the rotation. Replacing the elastic modulus in the mid-span deflection equation gave the shear modulus.

**Method 3.** The elastic and shear moduli were calculated from strain measurements recorded during the three- and four-point bending tests. In the four-point bending experiments, the beam part located between the two loading points was in pure bending state. Thus, axial strains (in the 0° direction) measured at mid-span were free of shear influence and could be used to compute the elastic modulus. In the three-point bending experiments, the mid-span was subjected to a bending and shear load. Since the axial strain at the centerline was nearly zero, the strain in the 45° direction was affected only by shear deformations and could be used to compute the shear modulus.

Finally, the values used to predict beam behavior were 30 GPa for the elastic modulus and 3 GPa for the shear modulus. The full-section elastic and shear moduli calculations demonstrated that approximately 83% of vertical deflections were due to bending and 17% due to shear on beams PS1-3.

Table 4.8 summarizes shear coefficient  $K$  with Bank's and Odmivar's approaches (see Section 2.1.2.2). As previously mentioned, the formulae depend on the geometry and mechanical properties. It was assumed from the range indicated in the pultruder's design manual (Anon 2003) and from experiments performed on similar GFRP profiles (Tirelli 2003) that  $E_x=30$  GPa,  $E_z=8.5$  GPa,  $G_{zx}=3$  GPa,  $\nu_{zx}=0.26$  and  $\nu_{yx}=0.09$  (axis defined in Figure 4.9, page 63). The shear coefficient  $K$  with Cowper's formula for an isotropic material was also estimated.  $K$  values according to Bank and Odmivar are observed to be the same and are quite similar to the value for an isotropic material. Thus, the beam shear stiffness is not really affected by the material's orthotropic behavior due to the pultruded GFRP material's low orthotropic characteristics in comparison with other composites, whose elastic to shear modulus ratio is 10 to 30 times higher than that of isotropic materials (Bank 1987). Mottram (1991), in his study of pultruded box beams, employed Bank's formula for estimating the shear modulus of thick-walled square tubes and corrected it to take into account actual non-uniform shear distribution across the wall thickness. Applying the appropriate Roark's formula (Young 1989), the shear coefficient was reduced by the thick-walled correction factor. In the present case the correction factor is 0.91 and the actual shear coefficient  $K$  is 0.38.

Table 4.8: Beam shear coefficient  $K$  determined with different approaches

Approach	Cowper	Bank	Odmivar	Odmivar + thick-walled correction factor
Formula	$\frac{20(1+\nu)}{48+39\nu}$	$20$	$20$	$0.91 \cdot \frac{20}{48 - \frac{G_{zx}}{E_x}(\nu_{zx} + 5\nu_{yx})}$
		$48 - 3 \frac{G_{zx}}{E_x} \nu_{zx}$	$48 - \frac{G_{zx}}{E_x} (\nu_{zx} + 5\nu_{yx})$	
Value	0.43	0.42	0.42	0.38

### 4.3.5.7 Load-Deflection and Load-Rotation Behavior Comparisons

As expected, deflections of the bonded beams were between the values of the simple (28% smaller on average) and continuous beams (49% higher on average), as shown in Table 4.9. The bonded beams showed trilinear behavior with an initial stiffness loss due to the bilinear behavior of the adhesive and a subsequent loss due to the onset of buckling deformations in the compressed regions. Beam PH3 showed an additional stiffness loss due to failure of the bonded joint. Therefore, the bonded beams exhibited system ductility with ductile behavior in the first part (ductile joint). However, the effect was quite small because the adhesive was initially too flexible. Ideally, the adhesive should be much stiffer at the beginning (comparable to EP or PU adhesives, see Section 4.1.4) and then should behave more plastically. Subsequently, bonded beams exhibited deformability in the second part (local buckling). Loss of stiffness due to local buckling is an elastic and reversible deformation. The additional stiffness loss due to failure of the bonded joint of beam PH3 can, however, be considered an additional pseudo-ductility given by the statically indeterminate system configuration.

Table 4.9: Comparison of beams with adhesive joints and simple/continuous beams

Beams with adhesive joints	Ultimate failure load		Maximum deflection at failure	
	Simple beam (reference)	Continuous beam (reference)	Simple beam (reference)	Continuous beam (reference)
PH1 (200 mm)	+16%	+23%	-32%	+42%
PH2 (200 mm)	+15%	+22%	-24%	+58%
PH3 (100 mm)	-1%	+5%	-17%	+74%
PH4 (300 mm)	+15%	+22%	-29%	+48%
Average (PH3 excluded)	+15.3±0.6%	+22.3±0.6%	-28.3±4.0%	+49.3±8.1%

The creep experiment showed that, although a very flexible adhesive was used, creep deformation was kept within admissible values due to the design-governing deflection limit for the GFRP beams and associated low shear stresses of approximately 1.1 MPa in the adhesive joint. The shear stress was calculated according to Eq. 6.16 on page 141.

### 4.3.5.8 Load Transfer along the Adhesive Joint

Load-axial strain curves of gages in the bonded area were almost linear until the gage no longer worked or the ultimate load. They indicated that axial strain distribution remained constant during the loading (see Section 4.3.4 Appendix C). Figure 4.30 shows the measured axial strains along the upper strap joints at a load of 50 kN for bonded beams. Symbols represent average values from 4 strain-gage readings at symmetrically equal positions in the joint. Measured axial strain distributions were approximated by a linear regression.

The measured axial strains of the flanges in the joints showed a linear distribution, with the exception of small regions at the beginning and end (each approximately 5% of joint length). Therefore, shear stresses in the adhesive layer must be constant in the region of linear strain distribution, which is

approximately 90% of the overlap length. Hence, the magnitude of constant shear stress is proportional to the slope of the straight line fit to the axial strains. Only beam PH4, which had the longest overlap lengths of 2x300 mm, deviated slightly from this conclusion. The slope of the straight-line fit was quite small and therefore a considerable part of the shear stresses had to be transmitted towards overlap edges.

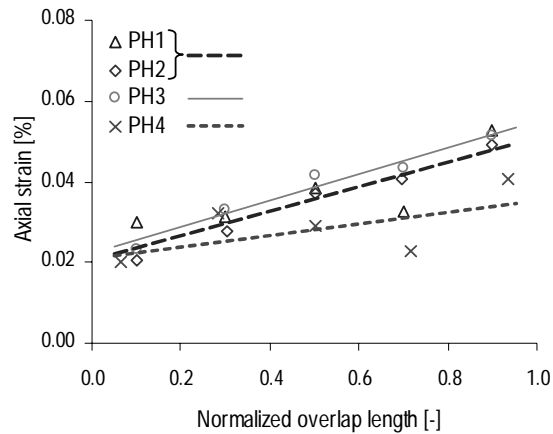


Figure 4.30: Axial strain distribution (symbols) on upper flanges in adhesive joints of beams PH1-4 at load of 50 kN per jack and linear regression (line)

#### 4.3.5.9 Moment Redistribution and Failure Loads

Figure 4.31 shows the bending moment diagrams for all of the beams at 136 kN per jack, corresponding to the lowest failure load (beam PC2). The moments were calculated from the measured support reactions (Table 4.6). Compared to the simple and continuous beams, the flexible adhesive joints led to a better distribution of the moments and support reactions. The maximum moments and the support reactions at the mid-support were reduced in comparison to the continuous beam, which failed at this location. On the other hand, the sections below the jacks were more lightly loaded due to the partial fixity at mid-support so that loads could be increased beyond the failure loads of the simple and continuous beams. As listed in Table 4.9, ultimate failure loads were increased by 15% compared to simple beams and 22 % compared to continuous beams (average values without PH3). In this respect, however, a direct comparison of the beams is not possible since the bottom cover plate reinforced the support region of bonded beams.

In the beams with 200 and 300 mm overlaps, failures occurred in the spans below the hydraulic jacks. The adhesively-bonded joints remained undamaged. Only in beam PH3, with the shortest overlaps of 2x100 mm, did premature failure occur in the adhesive joint. This beam showed a redundant behavior however, due to the statically indeterminate system. The load could be increased again by 14% up to ultimate failure.

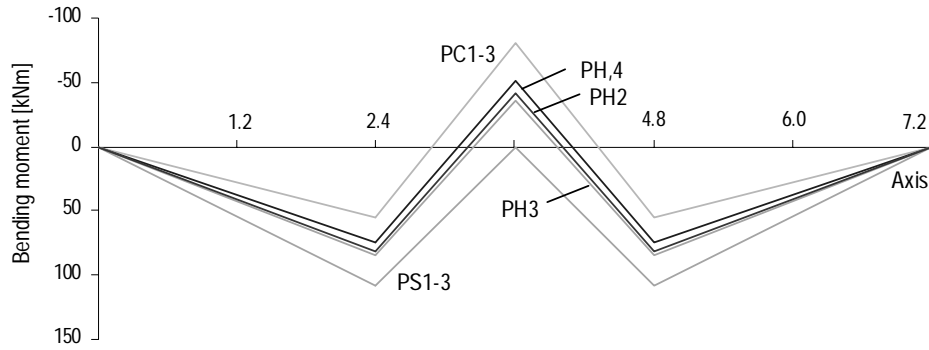


Figure 4.31: Bending moment distributions (at 136 kN load per jack)

Figure 4.32 shows that a redistribution of the moments from the support ( $M^-$ ) to the loading point regions ( $M^+$ ) occurred in the PH beams. The reason for this redistribution is the non-linear behavior of the adhesive joint. Again, the effect was smaller than expected because the initial stiffness of the adhesive was too low. In an ideal case, the moment ratio should be constant up to the ultimate-limit-state load (approximately  $1.5 \times 40 \text{ kN} = 60 \text{ kN}$ , serviceability-limit-state load:  $40 \text{ kN}$  (load level corresponding to an admissible deflection to span ratio of  $1/400$ , defined in Section 6. 4.1)), and then start to decrease.

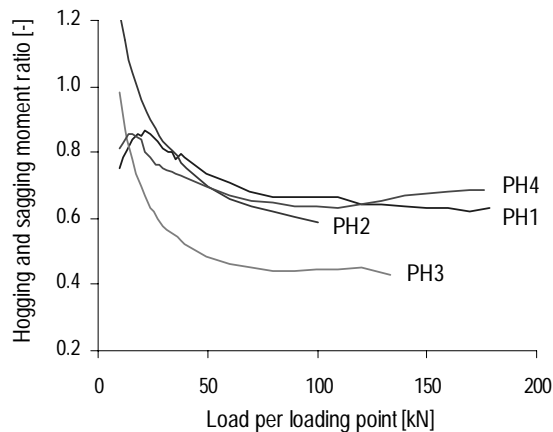


Figure 4.32: Redistribution of bending moments from mid-support ( $M^-$ ) to loading point sections ( $M^+$ )

The demonstration of the proposed new concept's full potential by means of the experiments performed was partially affected by two factors. Firstly, the local buckling failures of the compressed flanges or webs in the loading or support sections were expected, but at higher loads. Failure in compressed flanges or webs at load-introduction points is the normally observed failure mode of pultruded thin-walled sections (Barbero et al. 1991, Zureick and Shih 1998). However, the maximum compressive stresses at failure were only approximately  $153 \text{ N/mm}^2$  (see Table 4.7) and therefore far below the  $240 \text{ N/mm}^2$  indicated in the pultruder's design manual. The short overlap of the combined fiber mats,  $2 \times 30 \text{ mm}$  from section edges, proved to be a weak area in the beams. As a result of the experiments, the fiber architecture was improved by the pultruder. Secondly, the



adhesive available did not behave exactly as desired. An ideal adhesive should be stiffer initially (comparable to EP and PU adhesives, see Section 4.1.4) and should then behave more plastically. With the improved beams and a tailored adhesive, the enhanced load-carrying behavior should be much more pronounced in comparison to the single and continuous beams.

## 4.4 Concluding Remarks

This chapter presents the description and results of experimental investigations carried out on adhesives, adhesively-bonded double-lap joints and adhesively-connected beams. The conclusions of these investigations are presented in two parts: from the double-lap joint experiments and the beam experiments.

Quasi-static tensile experiments on adhesively-bonded double-lap joints with different adhesives were performed in order to quantify the effect of adhesive behavior. The conclusions from the adhesively-bonded double-lap joints are:

- The epoxy (EP) and polyurethane (PU) joints exhibited linear behavior up to the brittle failure and thus constant stiffness. The PU adhesive remained elastic and did not reach plastic deformations as the elastic strain was too high. Comparing both joints indicates that reducing the adhesive Young's modulus by a factor of approximately 7.5 has a minor effect on joint stiffness whilst increasing joint strength.
- The acrylic (ADP) joints exhibited bilinear behavior as for the ADP adhesive, with a joint stiffness reduction of approximately 75% when reaching plastic deformations in 100 mm overlap length joints.
- The EP and PU joint failure occurred in the laminates by fiber-tear or light- fiber-tear failure (commonly called interlaminar failure), while ADP joints exhibited a mixed failure including adhesion failure and fiber-tear or light-fiber-tear failure. The adhesion failure led to a lower strength than expected, which was related to the dimension of the bad adhesion areas (adhesion promoter to substrate failure). ADP joints with the large overlap length (200 mm) were 40 % stronger than EP joints. Nevertheless, a few joints with the short overlap length (100 mm) showed a higher strength than the EP and PU series. Thus, applying the appropriate surface treatment will improve performance of the ADP joints. The supplier must carry out research to solve the adhesion problem.
- The ADP joints with highly non-linear adhesive characteristics allowed large elongation deformations and provided a more uniform load transfer. Nevertheless, adhesion problems (inappropriate surface treatment, physical/chemical incompatibility) induced a premature failure.
- Ductile adhesively-bonded joint efficiency (76% for ADP joints with 200 mm overlap length) was greater than mechanical joint efficiency (50% according to Matthews (1987))

and stiff and brittle adhesively-bonded joint efficiency (~50% for EP joints). Thus ductile adhesive-bonded joints are more appropriate to FRP materials than mechanical joints.

- The use of an appropriate ductile adhesive (ADP) creates ductile joint behavior, while that of an inappropriate ductile adhesive (PU) results in joint failure before plastic deformations develop.
- Ductile and flexible adhesives exhibit a linear axial strain distribution and therefore constant shear stress distribution along the overlap.
- The axial strain distribution across the joint width indicated higher strains at the edge than in the middle. The deviations reached 13% when compared to a uniform transverse distribution. Thus, a uniform approximation could be assumed for numerical and analytical analyses leading to 2D rather than 3D models.

Quasi-static and creep experiments on brittle GFRP beams connected with ductile and flexible adhesive joints were carried out and compared to quasi-static experiments on simple and continuous beams. Conclusions from the adhesively-connected beams are as follows:

- The flexible adhesively-bonded joints with ductile adhesive provided a favorable redistribution of the internal and external forces in the redundant system (statically indeterminate structure).
- The redistribution effect was smaller than expected because the ADP adhesive was initially too flexible. Ideally, the moment ratio should be constant up to the ULS load and then start to decrease.
- In the case of adhesively-bonded joint failure, a structural collapse could be prevented due to the redundancy of the statically indeterminate system. After joint failure, the load could be increased up to the ultimate load.
- The low stiffness of the ADP adhesive led to an almost constant load transfer along the joint and thus constant shear stress distribution.
- Due to the stiffness-governed design of GFRP beams, stresses in flexible adhesively-bonded joints were small and creep deformation in the joints could be controlled.
- The results of this research confirmed the feasibility of the proposed concept for structures composed of brittle FRP components. The concept includes the use of redundant structural systems and ductile or flexible adhesively-bonded joints to provide system ductility that compensates for the lack of material ductility inherent to FRP structures.

---

## 5 Numerical Modeling of Adhesively-bonded Double-lap Joints

The double-lap joint experimental investigation described in the previous chapter resulted in the determination of joint elongation and axial strain distribution in the adherends, inside and outside the bonded area. The effect of adhesive behavior on joint stiffness and load transfer inside the joint could be seen. However, no information was obtained directly concerning stress distribution at the failure surface. Thus, an FE model was developed and validated by comparison with the experimental measurements to determine stress distributions in the joint area, at the interface and failure surface. The latter were integrated in a failure criterion for predicting joint strength. Based on the stress distributions, a simplified analytical model was developed to predict joint elongation and failure load using ductile adhesives.

The FE model was developed for studying the behavior of a double-lap joint specimen loaded in tension. Joint stiffness, axial strain and stress distributions along the overlap length were investigated. A study of the adhesive to adherend modulus ratio was conducted in order to define the appropriate adhesive behavior for a predefined structural behavior. The results determine the bilinear adhesive selection. Elastic modulus is based on the required joint stiffness at the serviceability limit state, assuring low deformations. The Plastic modulus is based on the development of large deformations up to failure. A constant shear distribution and low through-thickness peak values are also required. Suggestions concerning adhesive selection are given and certain limits established.

### 5.1 Joint FE Models

Analytical models have been developed for metal adherends where cohesive failure occurred in the adhesive layer; for this reason analytical stress distributions were established in the adhesive bondline. As joints with FRP adherends exhibit interlaminar failure, the determining stress distribution is located inside the adherend, at the failure surface. Moreover, analytical models were intended for perfect joint geometries (idealized configuration). Thus, the adhesive spew-fillets could not be considered and their positive influence on maximum stresses and peak stress reductions (Adams and Peppiatt 1974, Adams and Harris 1987) was ignored. In addition, traditional analytical models were developed for linear or elasto-plastic adhesive behaviors and not for common highly non-linear behavior. All these reasons were catalysts for the present FE analysis. The FE model is characterized by

the following aspects: boundary conditions, geometric considerations, material properties and element type and element selection.

### **5.1.1 Boundary Conditions**

In actual applications, the joint is part of a larger structure. Stress analysis is usually carried out using a model of the isolated joint rather than modeling the whole structure. The challenge consists of defining the boundary conditions (adjacent to the attached elements) and the loads adequately. The boundary conditions must be sufficiently distant from the joint area to avoid influencing local boundary stresses. Penado and Dropek (1990) recommend a distance of ten times the adherend thickness, which is larger than the distance according to Saint-Venant's principle (two to three times). The entire specimen is usually modeled when it has a simple geometry such as single-lap or double-lap joints. Symmetry conditions could be taken into account to reduce joint configuration dimensions and decrease the number of elements and calculation time.

### **5.1.2 Geometric Considerations**

Joint geometry is characterized by the geometry of both the adherends and the adhesive layer. The pultruded adherend geometry is relatively easy to define since the manufacturing process guarantees fairly constant properties and tolerance limits have been established by the manufacturer. The adhesive-layer geometry is more complex due to the application method and in-situ curing. A spew-fillet can form even if not planned in the design due to adhesive overflow during the curing process. The shape and size of the spew-fillet depend on such elements of the manufacturing procedure as pressure, curing temperature and amount of adhesive applied between the two adherends (Tong and Steven 1999). Two types of model are usually considered, one with an ideal adhesive layer, and no spew-fillets, and a real model with spew-fillets of different shapes and sizes. The spew-fillets influence the stress distribution along the joint and especially at the edges, where maximum stresses are located (Adams and Peppiatt 1974, Belingardi et al. 2002). Joints are three-dimensional (3D) structures but in many cases a two-dimensional (2D) plane-strain or plane-stress analysis is adequate (see Section 2.3.5.2). The latter (justified by Richardson et al. 1993) is usually carried out.

Geometric non-linear conditions could exist in common joints such as single-lap joints. The large deformations are due to bending effects caused by loading eccentricities. The frequently used solution is to apply the load or displacement on the FE model in an incremental way. Thus the geometric stiffness matrix is recalculated for each incremental loading or displacement step and the resulting incremental deformations are added to the deformations from previous steps.

### **5.1.3 Material Properties**

The material properties considered in joint analysis must include environmental effects to which the joint will be exposed. The most important environmental factors include moisture, temperature,

chemicals, thermal and mechanical fatigue. They affect the stiffness and strength of the adhesive and adherends. For comparison with laboratory experimental results, environmental effects will be disregarded. Material tests must be conducted on the adhesive and adherends to define the material properties (stiffness and strength). When the material exhibits linear behavior, the Young's modulus or shear modulus can be adequately represented by a single value. If the material exhibits non-linear behavior, curves relating stress to strain are required.

FRP materials are generally composed of two orientated layers of fibers without reinforcements in the thickness direction. This induces delamination failure between the plies adjacent to the adhesive layer, in the thin resin layer (the weak layer). A first approach consists of modeling each ply of the composite adherends as a different layer and inserting resin plies between them. The ply properties of composites consisting of superposed laminae could be determined experimentally whereas the ply properties of pultruded laminates are difficult to identify. They are predicted with micromechanical models (Reinhart 1987) based on the proportion and properties of the matrix and reinforcements as well as the reinforcement architecture (Osnes and Andersen 2003). A second approach consists of modeling the adherends as orthotropic homogeneous materials with global material properties.

#### 5.1.4 Element Shape and Meshing

The model's accuracy depends on the element selection and meshing scheme. No established limits are available in literature concerning the element size through the adhesive thickness. Nevertheless, only one row of elements leads to a constant stress distribution through the adhesive thickness as assumed in analytical solutions (Volkersen 1938, Goland and Reissner 1944). Adams et al. (1997) suggested three or four eight-node quadrilateral elements across the thickness at the ends of the adhesive layer. Penado and Dropek (1990) recommended at least three elements through the adhesive thickness and four-node quadrilateral isoparametric elements in plane-stress or plane-strain 2D analyses and eight-node solid isoparametric elements in 3D analyses. Element size is related to element type, especially the number of nodes per side. The number of elements through the adhesive thickness varies from two, using eight-node elements (Li and Lee-Sullivan 2001), to five, using four-node elements (Zetterberg et al. 2001, Baylor and Sancaktar 1995). Smaller sizes are recommended with four-node elements than with eight-node elements. A refinement is required in areas of high stress variations such as geometrical singularity areas (sharp edges) and at material interfaces.

Joints made of isotropic adherends usually fail in the adhesive bondline (cohesive failure). Thus, the stress distribution on the adhesive bondline determines joint strength. The maximum adhesive stresses occur at points A and G (Figure 5.1). However, stress singularities exist at these locations, with geometrical and material changes complicating the interpretation of results. Reducing element size will not lead to the convergence of stresses and generates higher peaks; the maximum values are meshing- dependent (Tong and Steven 1999). For these reasons it is usual to determine adhesive stress distribution at the centerline of the adhesive layer (line B-F), the average stress location. In the case of joints made of composite adherends, failure usually occurs in the adherends (interlaminar

failure). Therefore, stress distribution at the failure line (D-H) is less affected by singularities than at the interface lines (Figure 5.1). Nevertheless, it is recommended that stresses be determined at a small distance from the singularity to avoid influence from the singularity stress field. The nearest Gauss point or third node point from the singularity is used (Sancaktar and Narayan 1999).

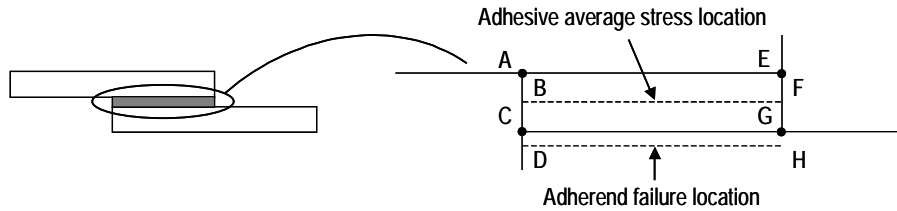


Figure 5.1: Singularity points (A, C, E and G), average stress location in the adhesive (line BF), and failure location (line DH)

## 5.2 Double-Lap Joint FE Model

### 5.2.1 Description of the Model

#### 5.2.1.1 Boundary Conditions and Loading

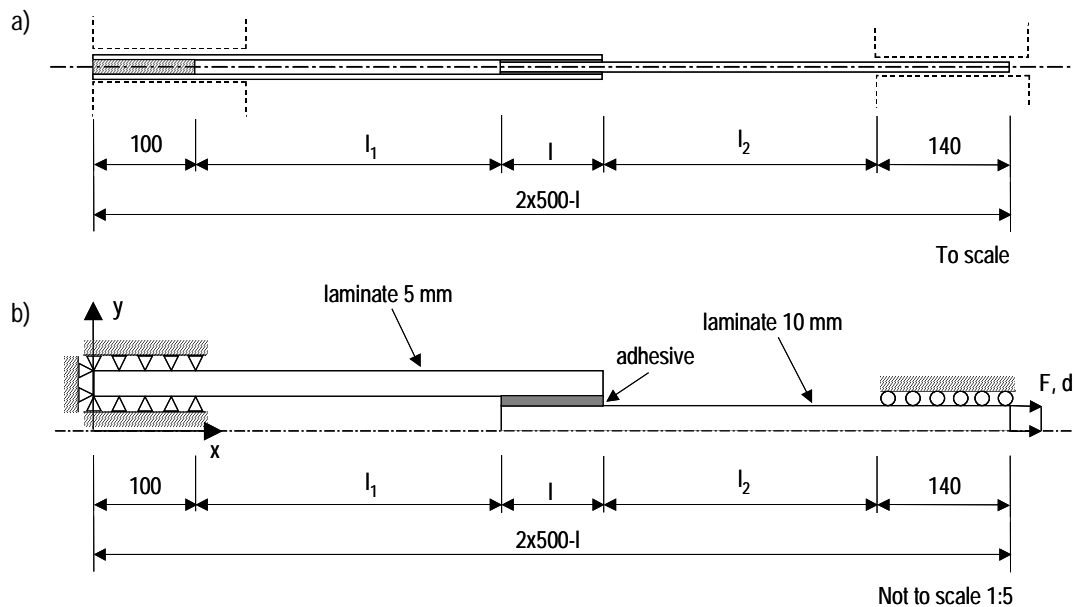


Figure 5.2: (a) Specimen and machine loading-grips; (b) 2D double-lap joint geometry, materials and boundary conditions

Figure 5.2 shows the double-lap joint dimensions, materials and boundary conditions. The longitudinal symmetry axis allows modeling of half the entire specimen. The  $y=0$  line (middle axis of the 10 mm thick laminate) is prevented from moving in direction  $x$ . The boundary conditions represent the machine loading-grips. The left end was constrained from movement in directions  $x$  and

y while the right end was constrained in direction y. The prescribed load or displacement is applied uniformly by the grips of the machine at the right end of the specimen.

### 5.2.1.2 Geometric Considerations

The joint model is composed of two 5 mm thick adherends of different materials. The adhesive is uniformly distributed along the overlap length and has a constant thickness of 2 mm. The overlap length is 100 or 200 mm. The study included no spew-fillet (ideal joint), a curved spew-fillet with 1 mm and 2 mm radius and a 45° spew-fillet conditions, as schematically shown in Figure 5.3. The specimen width (100 mm) is large compared to adherend thickness (5 mm), thus plane strain is assumed and the model is reduced to a 2D analysis.

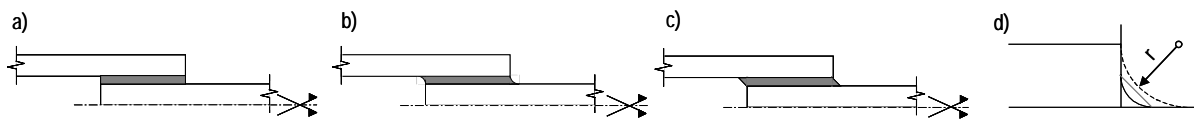


Figure 5.3: Adhesive spew-fillet geometry (a) no spew-fillet (ideal), (b) a curved spew-fillet with 2 mm radius, (c) a 45° spew-fillet; (d) Studied spew-fillet geometries: 1mm radius, half of adhesive thickness, 2 mm radius and a 45° spew-fillet in half of adhesive thickness

### 5.2.1.3 Material Properties

The pultruded GFRP laminates are modeled as homogeneous and orthotropic materials with global material properties. Longitudinal tensile experiments on adherend material were carried out on similar laminates by Tirelli (2003) and through-thickness tensile experiments by Vallée (2004). The laminates exhibited linear-elastic behavior up to failure that is characterized by the Young's moduli. Moreover, the outside of the 5 mm and the 10 mm thickness laminates that made up the double-lap joint specimens were instrumented with strain gages to measure the axial strain. The actual longitudinal Young's modulus of the laminates could be estimated from these measurements. The 10 mm thick laminates were loaded in tension while the 5 mm thick laminates were also subjected to bending due to the eccentricity. The FE model demonstrated that strains at gage locations were slightly influenced by the bending - they corresponded to only 3-4% of the tensile strain (see Section 5.2.2.3), so the bending effect could be disregarded in the modulus calculation. Both (5 mm and 10 mm) longitudinal Young's moduli,  $E_x$ , were calculated from axial strain measurements (see Section 4.2.4.3). Through-thickness Young's moduli,  $E_y$ , were provided by Vallée (2004), Poisson's ratio,  $\nu$ , by Tirelli (2003) and shear moduli,  $G_{xy}$ , by Anon (2003). The laminate mechanical properties introduced in the FE model are listed in Table 5.1.

Table 5.1: GFRP laminate mechanical properties for FE model

Laminate	$E_x$ [GPa]	$E_y$ [GPa]	$G_{xy}$ [GPa]	$\nu_{xy}$ [-]
5 mm	32.0	3.5	3.0	0.27
10 mm	28.0	3.5	3.0	0.27

Adhesives are isotropic materials exhibiting significantly different behavior under uniaxial tension and compression loading. Tensile, compressive and shear tests were carried out on EP (SD 330), PU (S-Force 5871) and ADP (SikaFast 5221) adhesives, but only tensile and compressive properties were inserted into the FE model (see Section 4.1.4). The *Anisotropic Plastic Material* model (Ansys 2004) was used for this purpose assuming the same behavior in all directions. The adhesive EP is modeled with a linear behavior in tension and compression while the adhesive PU is modeled with a bilinear behavior and the ADP is modeled with a bilinear behavior in tension and a linear behavior in compression. Figure 5.4 shows the tensile and compressive model stress-strain curves for the three adhesives and Table 5.2 lists the tensile and compressive mechanical properties for the adhesive models where  $E_{t,e}$  and  $E_{c,e}$  are the tensile and compressive elastic moduli respectively,  $E_{t,p}$  and  $E_{c,p}$  are the tensile and compressive plastic moduli, and  $f_{t,e}$  and  $f_{c,e}$  are the tensile and compressive yield stresses. Their determination is extensively defined in Appendix A. Adhesive viscosity was not included in the study. Large deformations were anticipated for soft adhesives and high load levels. Geometrically and materially non-linear FE models were developed.

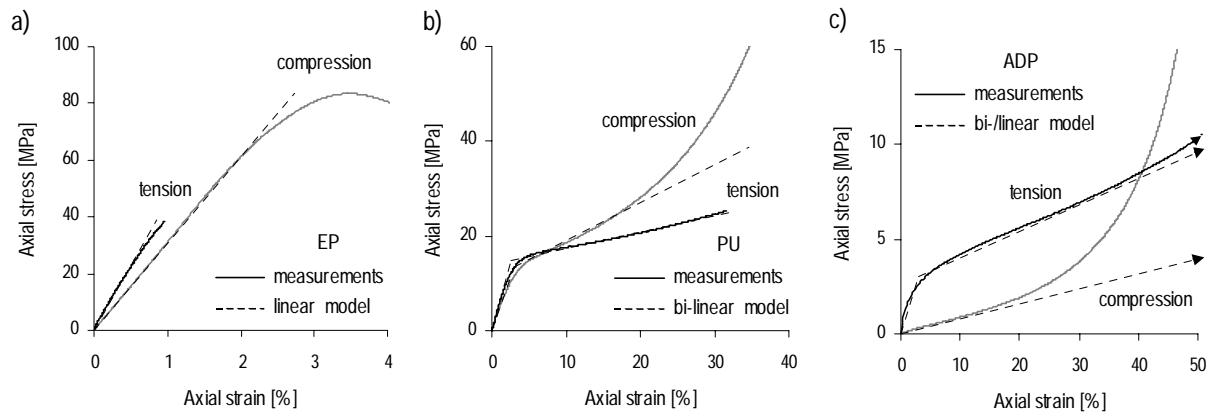


Figure 5.4: Tensile and compressive model stress-strain curves (a) EP, (b) PU, (c) ADP (partially see page 59)

Table 5.2: Adhesive mechanical properties for FE model

Adhesive	$E_{t,e}$ [MPa]	$E_{t,p}$ [MPa]	$f_{t,e}$ [MPa]	$E_{c,e}$ [MPa]	$E_{c,p}$ [MPa]	$f_{c,e}$ [MPa]	$\nu$ [-]
EP	4560	-	-	3060	-	-	0.37
PU	590	30	15	430	80	13	0.42
ADP	100	15	3	10	-	-	0.40

### 5.2.1.4 Element Shape and Meshing

The joint model was developed using the ANSYS code version 7.1. The element used is the Plane183, 2D eight-node isoparametric quadrilateral plane element shown in Figure 5.5 (Ansys 2004). For each node there are two degrees of freedom: nodal translations in directions  $x$  and  $y$ . Degenerated triangular shapes could be formed by defining three nodes as the same point. Because of the curved element sides and high-order node displacement fields, this element can tolerate irregular shapes and curved boundaries without too much loss of accuracy. The element has the ability to model



orthotropic material properties (adherends). The orthotropic material directions correspond to the element coordinate directions. The element also models non-linear material properties (PU and ADP adhesives). The element Plane183 has the same properties as the element Plane82 used by Li and Lee-Sullivan (2001) and Vallée (2004) but offers additional capabilities such as modeling different behavior in tension and compression (adhesives).

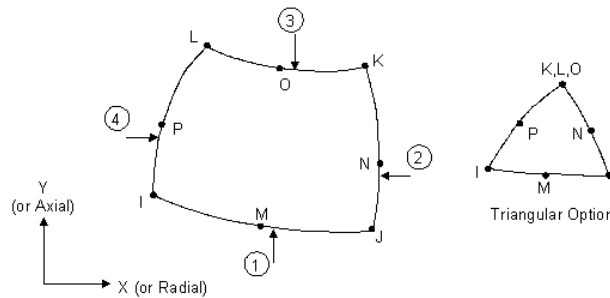


Figure 5.5: Element Plane183 and its variation (Ansys 2004)

The accuracy of the stress distribution at the failure line is essential for estimating joint strength. In order to avoid the influence of the singularity points, the failure line should coincide with the third node point from the interface (Sancaktar and Narayan 1999). Two rows of elements should be placed between the interface and the failure line. As observed in the experimental investigations and confirmed by Vallée (2004), the interlaminar failure occurred in the 10 mm laminates at a depth of approximately 0.5 mm. Thus, element size in the vicinity of the overlap edges was at the most 0.25 mm. The mesh was refined at overlap edges and in the spew- fillet.

Different mesh sizes (two, four and eight elements through the adhesive thickness) were evaluated in preliminary studies to observe the convergence of stresses at the overlap edges. Subsequently, the most convenient mesh scheme was applied in the main study. Figure 5.6 shows the FE mesh in detail. The mesh was refined at overlap edges and in the spew-fillets.

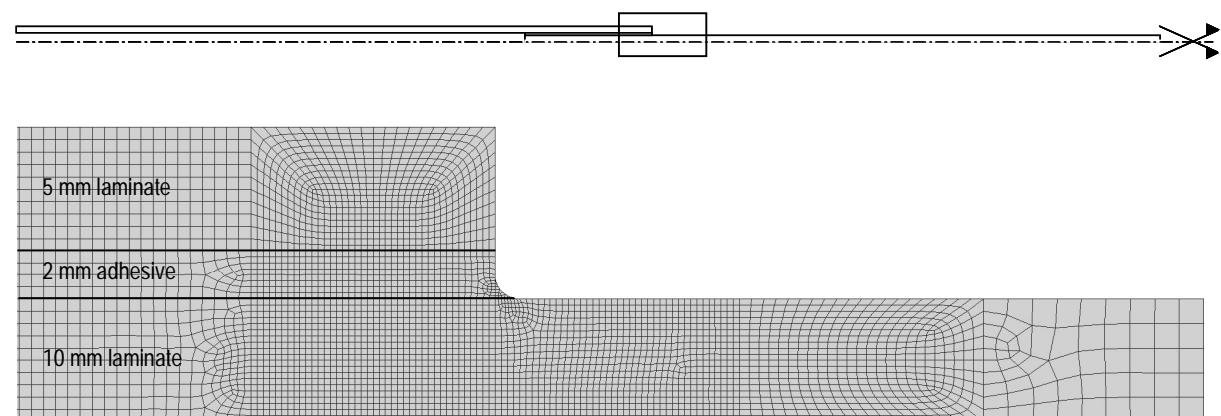


Figure 5.6: Mesh used in FE model of double-lap joint

## 5.2.2 Validation of the Model

Model validation consists of comparing the calculated values with experimental measurements of the following characteristics: global specimen elongation, joint elongation, axial strain in some sections of the specimen and axial strain on the overlap length, at the interface of the 10 mm thick laminate. Non-linear analyses were carried out on double-lap joints including rounded spew-fillets with a 1 mm radius. The adhesive material model took both tensile and compressive behaviors into account.

### 5.2.2.1 Specimen Load-Elongation

The specimen load-elongation curves for series EP.A, PU.B, ADP.C, with an overlap length of 100 mm, and series EP.D, ADP.D, with an overlap length of 200 mm, are illustrated in Figure 5.7. The continuous lines represent experimental measurements and the dashed line corresponds to FE model calculation. The corresponding failure loads are estimated in Section 5.2.5. The two kinds of curves matched well. The joint models with EP and PU adhesives exhibit linear behavior (Figure 5.7(a-c)). Calculated and measured initial global stiffness matched well. Deviations were observed at high loading levels. These were not due to the actual non-linearity of the adhesives, as explained in the following section, but were probably caused by geometrical non-linearity. The joint models with ADP adhesive exhibited bilinear behavior with a stiffness reduction at approximately 35 kN and 77 kN (15% and 26% of the estimated failure load (see Section 5.2.5) for the 100 mm and 200 mm overlap lengths respectively. Figure 5.7(d-e) show the agreement between measurements and calculations with the ADP adhesive. The calculated stiffness reduction occurred at a 10-15% higher load level than the measured stiffness reduction (see Section 4.2.4.2).

### 5.2.2.2 Joint Load-Elongation

The joint load-elongation curves for three specimens of series EP.A, PU.B and ADP.C, with an overlap length of 100 mm, are illustrated in Figure 5.8(a-c). Three specimens per experimental series were subjected to the joint displacement measurements (by videoextensometer see Section 4.2.3). The continuous lines represent experimental measurements and the dashed line corresponds to the model calculation. The joint elongation is estimated with the relative displacement of the laminates in the axis direction as indicated in Figure 4.11(a) (page 65). The failure load is predicted in Section 5.2.5. Table 5.3 compares the joint stiffnesses and the ratio of the joint elongation to the global specimen elongation of the calculations and the experiments. The joint stiffness was calculated as the load per joint elongation (Eq. 4.6 page 68). Both properties remained almost constant for EP and PU joints but changed significantly on ADP joints. For the latter, the properties are defined at two loading levels, 20 kN and 100 kN, characterizing both almost constant curve slopes.

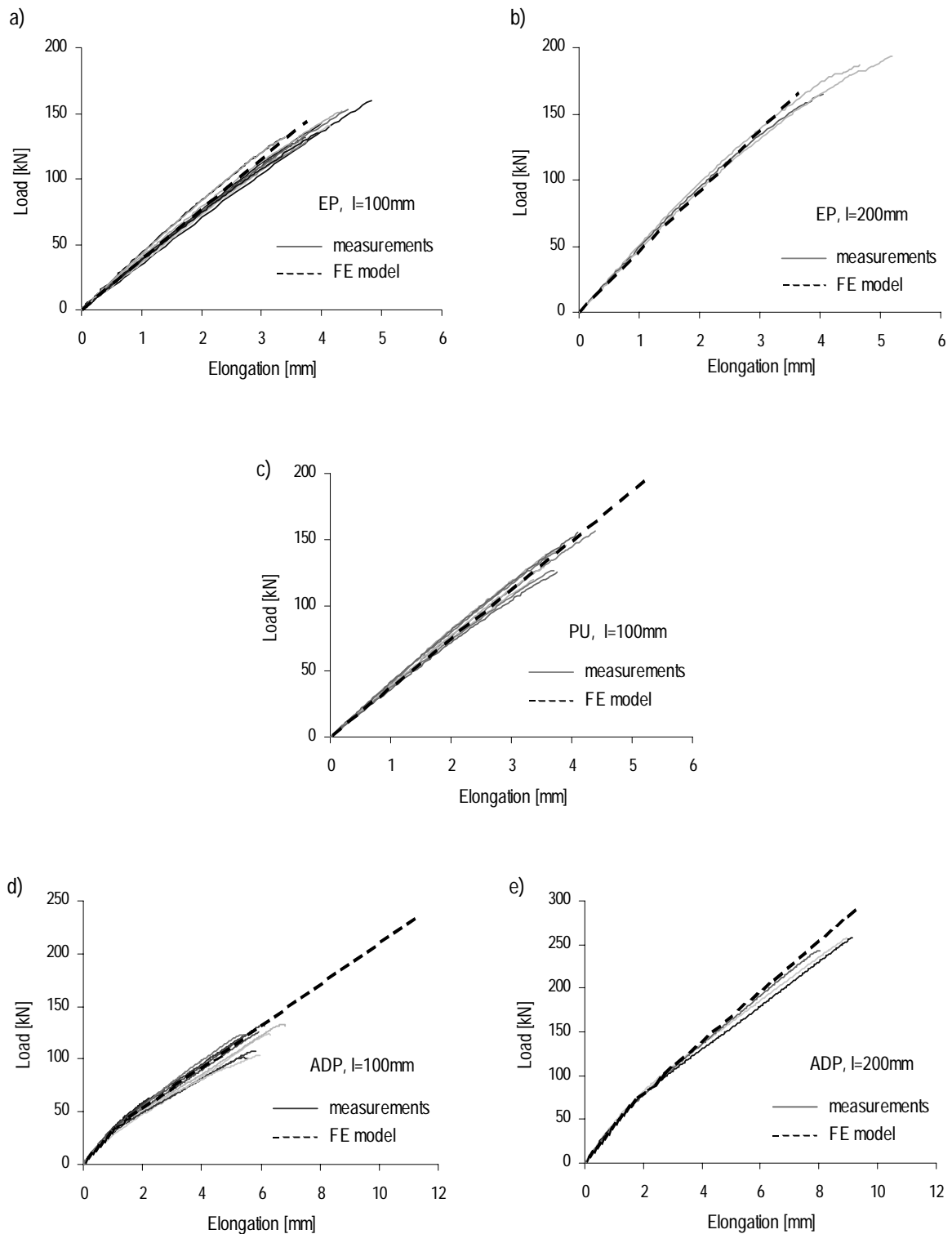


Figure 5.7: Load-elongation curves of global specimen for series (a) EP.A ( $l=100$  mm), (b) EP.D ( $l=200$  mm); (c) PU.B ( $l=100$  mm), (d) ADP.C ( $l=100$  mm), (e) ADP.D ( $l=200$  mm), comparison of FE calculations and measurements

The measured joint load-elongation curves with EP and PU adhesives were linear (Figure 5.8(a-b)). They demonstrated that specimen stiffness reduction (see Section 5.2.2.1) was not caused by a decrease in joint stiffness. Calculations indicated, in agreement with experiments, that PU joints

exhibited linear behavior up to failure. The adhesive remained linear-elastic and stresses did not reach the second phase of bilinear behavior where large deformations develop. The calculated and measured curves matched well. Joint stiffness deviations were zero for EP and 5% for PU joints. The calculated joint elongations represented 8% and 9% of global specimen elongation for EP and PU joints respectively and matched those which occurred in experiments.

The ADP joint model exhibited bilinear behavior with a stiffness reduction at approximately 35 kN (15% of the estimated failure load as previously noted) (Figure 5.8(c)). Calculated and measured curves did not match as well as for the other adhesive joints, which could be a consequence of the greater variability in ADP adhesive in-situ behavior observed in experiments. The load level at which the calculated stiffness change occurred agreed with two of the measured curves and the calculated stiffness decrease (curve slope) agreed with the third curve. The joint stiffness differences were 2% at 20 kN and 12% at 100 kN.

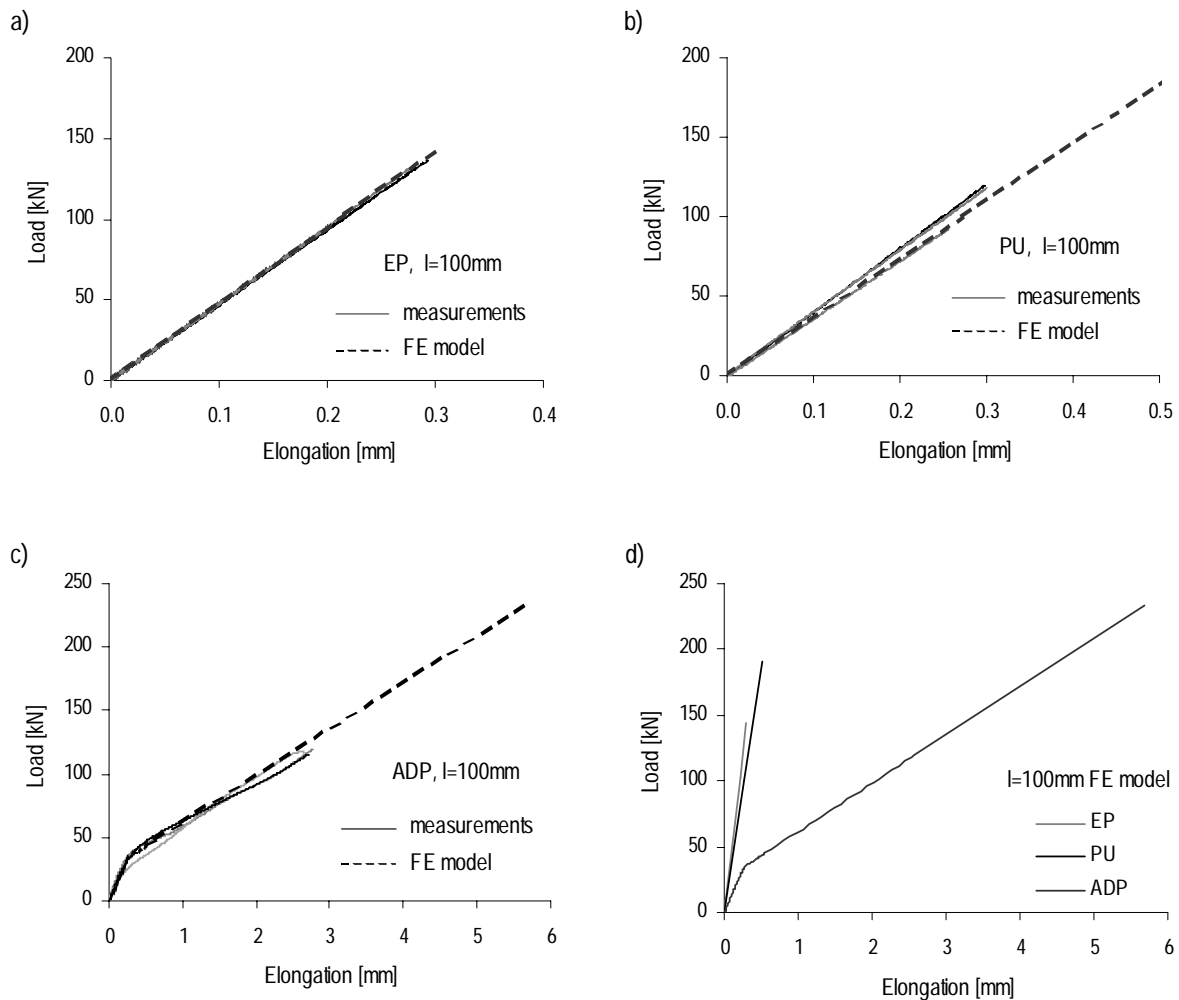


Figure 5.8: Load-elongation curves for joint of series ( $l=100$  mm) (a) EP.A, (b) PU.B, (c) ADP, comparison of FE calculations and measurements, (d) FE calculations

Figure 5.8(d) shows the calculated load-elongation curves for the three joints. Reducing the adhesive elastic modulus by a factor of 7 (with an average value of elastic moduli in tension and compression)

(EP/PU) leads to a joint stiffness decrease of 20% and reducing it by a factor of 70 (EP/ADP) leads to a 250% decrease. Thus, the joint stiffness varied non-linearly with the adhesive elastic modulus (Figure 5.24 (b) page 119).

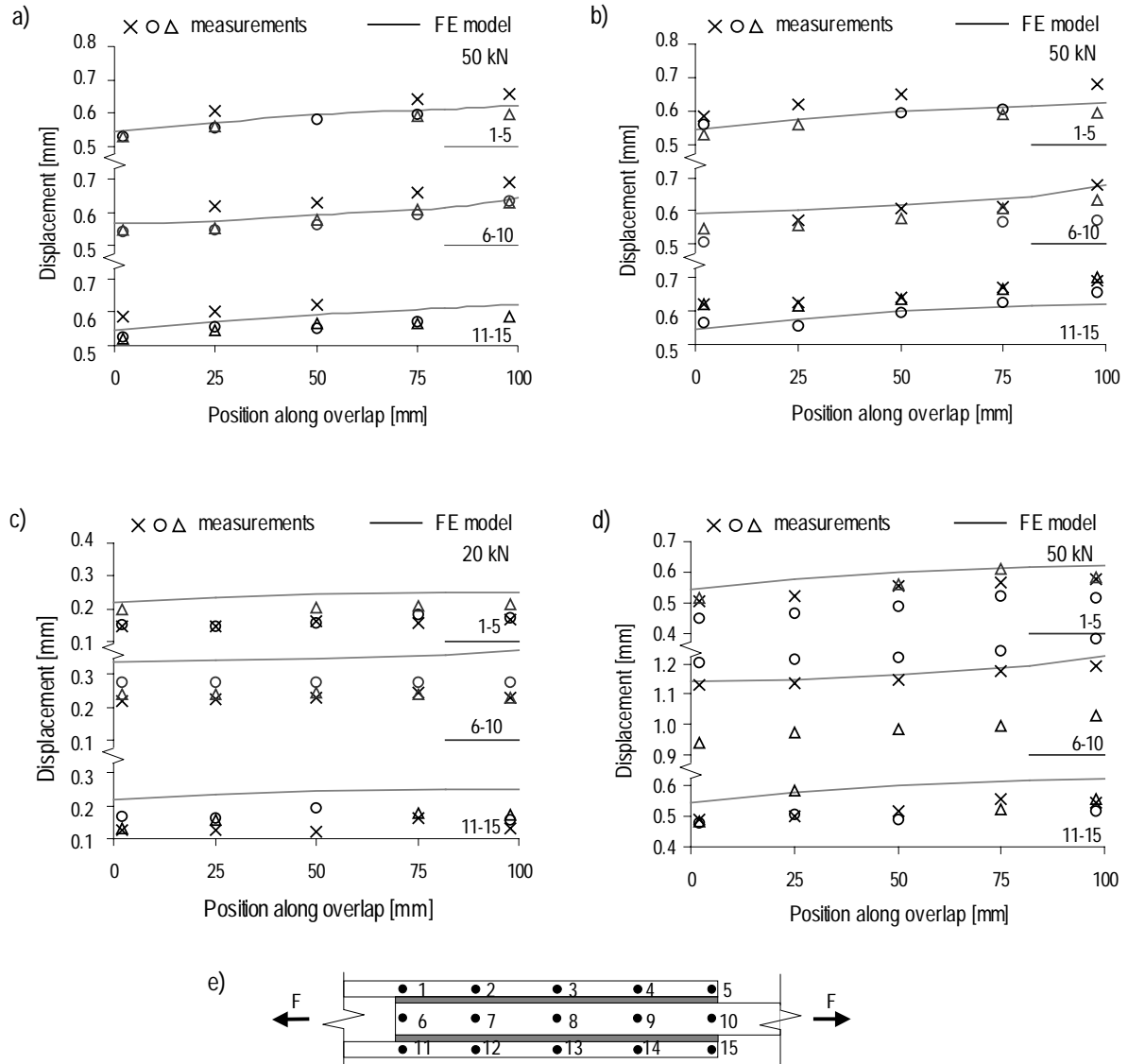


Figure 5.9: Displacement-position curves along the joint for series ( $l=100$  mm) (a) EP.A at 50 kN, (b) PU.B at 50 kN, ADP.C (c) at 20 kN and (d) at 50 kN, comparison of FE calculations and measurements; (e) Point positioning in the joint

Table 5.3: Joint stiffness and ratio of joint elongation to specimen elongation of series EP.A, PU.B and ADP.C

Joint characteristics	EP (50 kN)		PU (50 kN)		ADP (20 kN)		ADP (100 kN)	
	model	measurement	model	measurement	model	measurement	model	measurement
Joint stiffness (kN/mm)	475	474±4	367	385±22	132	135±31	37	33±6
Joint/specimen elongation (%)	8	8±1	10	9±1	24	24±5	46	51±2

Distributions of laminate elongations in the axial direction are illustrated in Figure 5.9(a-d). The ordinate in figures indicates the displacement of each point designated in Figure 5.9(e). The abscissa

indicates point position along the overlap length. The numbers above the lines on the right side of the curves designate the related points and thus the related laminate. The symbols correspond to the measurements (three specimens) and the lines characterize the model calculation. The distributions at 50 kN on EP and PU joints and at 20 kN and 50 kN on ADP joints are represented. The shape of the calculated curves matches the shape of the measured curves. Calculated and measured distributions of the EP and PU joints matched well; differences were lower than 8% and 9% for EP and PU joints respectively. The comparison of calculated and measured distributions on 5 mm laminates (upper and lower curves) of ADP joints reveals that the actual laminates are stiffer than the value used in the FE model, which corresponds to the average value of all the experiments (Figure 5.9(c-d)). This is confirmed by the Young's moduli estimated from the strain measurements on the three specimens (see Section 4.3.3 Appendix B). The differences in the measured displacements of the 10 mm laminates (middle curve), including adhesive deformation and laminate elongation, at 50 kN indicate greater variability in the in-situ ADP adhesive behavior.

### 5.2.2.3 Axial Strains along the Specimen

The Young's moduli of the 5 mm and 10 mm thick laminates were estimated from the strain gage measurements, assuming that both laminates were loaded in tension (see Section 4.2.4.3). Nevertheless, the 5 mm thick laminates were also subjected to bending. The FE model demonstrates that the strains at the gage locations were only slightly influenced by bending; the calculated strain was 3% (for EP) and 4% (for ADP) lower than assuming only tension. Thus, the Young's modulus of the 5 mm thick laminates was slightly overestimated but remains approximately the same as the modulus scatter from the experiments (10% of mean value).

### 5.2.2.4 Axial Strains in the Bonded Joint

Figure 5.10(a-c) shows axial strain distribution at the 10 mm laminate interface of the double-lap joints subjected to a tensile load of 50 kN. The ordinate in figures indicates axial strain and the abscissa indicates position along the overlap length (Figure 5.10(e)). The measured load-axial strain curves for the three joints were linear, thus the axial strain distribution remained constant and independent of loading level (see Section 4.2.4.3). The axial strain distribution in ADP joints was scarcely influenced by adhesive bilinear behavior and tensile modulus decrease since both elastic and plastic moduli are low in comparison with the laminate Young's moduli (see Section 4.3.4 Appendix B). The reason is explained in Section 5.3.2. Calculated and measured strain distributions in the EP and PU joints showed relatively good agreement while greater differences were observed in ADP joints. Figure 5.10(d) compares the calculated axial strain distribution of all the adhesives. The shape of the strain distribution curves in the PU and ADP joints was similar and the slopes were constant over most of the interface. The slope of axial distribution in EP joint was lower along the whole length of the interface, except at the ends. The axial strain distribution is related to axial stress distribution and therefore load transfer. Thus, the load is transferred mostly at the edges of the

overlap in EP joints, while it is more uniformly transferred when softer adhesives such as PU and ADP are used.

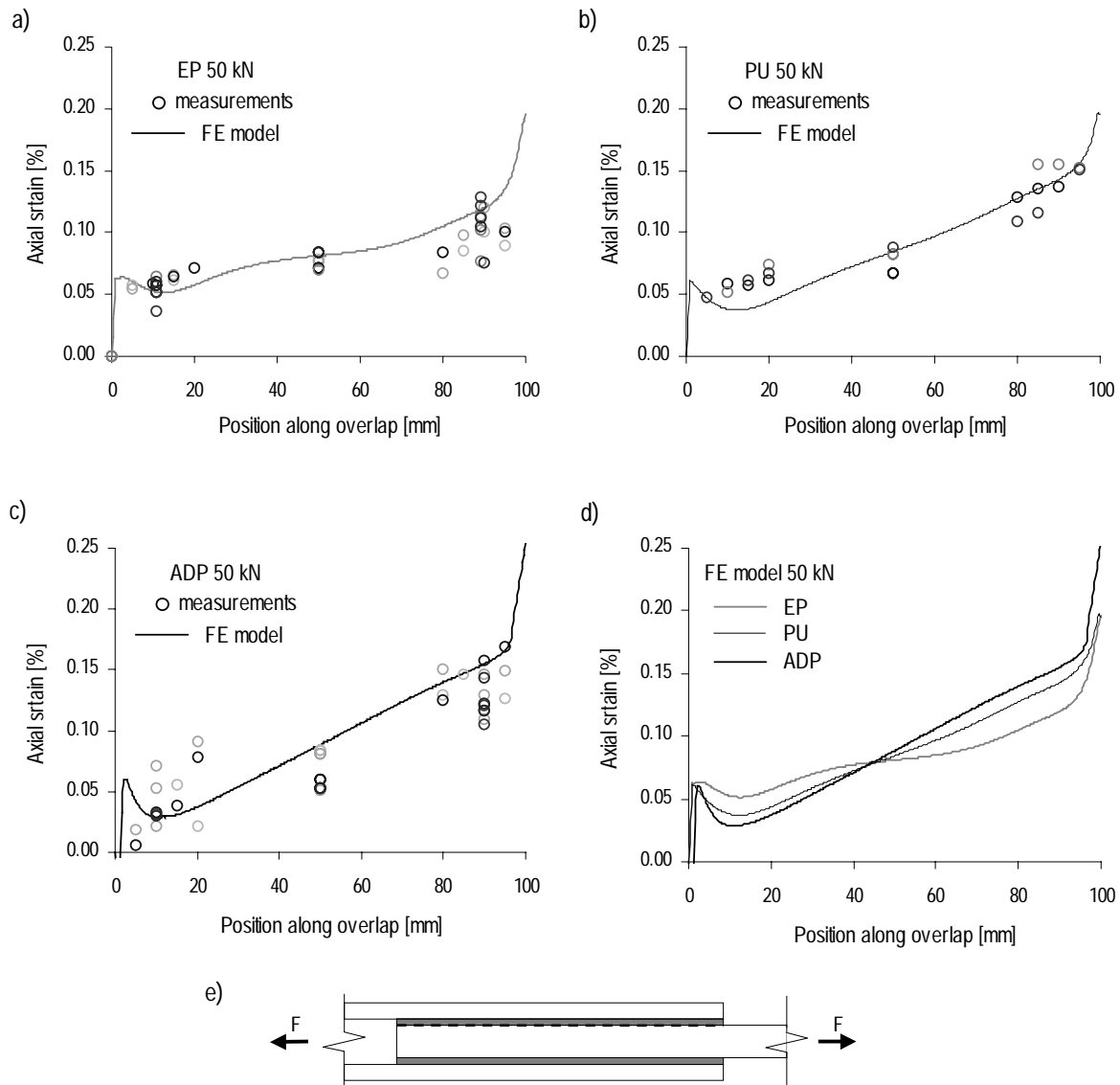


Figure 5.10: Axial strain distribution along overlap length at 50 kN for series (a) EP.A, (b) PU.B, (c) ADP.C, comparison of FE calculations and measurements, (d) FE calculations; (e) 10 mm laminate interface (dotted line)

### 5.2.2.5 Concluding Remarks

The FE model was validated by comparison between the calculated results and the experimental measurements of the specimen and joint elongations, axial strains on laminate cross-sections and along overlap length. The EP and PU joints exhibited good agreement (joint stiffness deviation: 0% and 5% respectively) while slight discrepancies were observed for ADP joints (joint stiffness deviation: 12% at 100 kN), which could be caused by adhesive property variations observed during

adhesive bulk and double-lap joint experiments, especially concerning stiffness and the load level corresponding to the stiffness decrease in the latter.

### 5.2.3 Stress Distributions

The FE joint model was validated in Section 5.2.2. It was then used for investigation of stress distributions along two paths, the interface and failure line (surface of actual joint). Stress distribution at the interface indicated load transfer, while stress distribution at the failure line, at 0.5 mm depth, was used to predict joint strength. The shape of stress distribution at the failure line defines the two correction factors included in the failure criterion (see Section 5.2.5) involving the shear and through-thickness stresses. Consequently, these two stress components were investigated in the following.

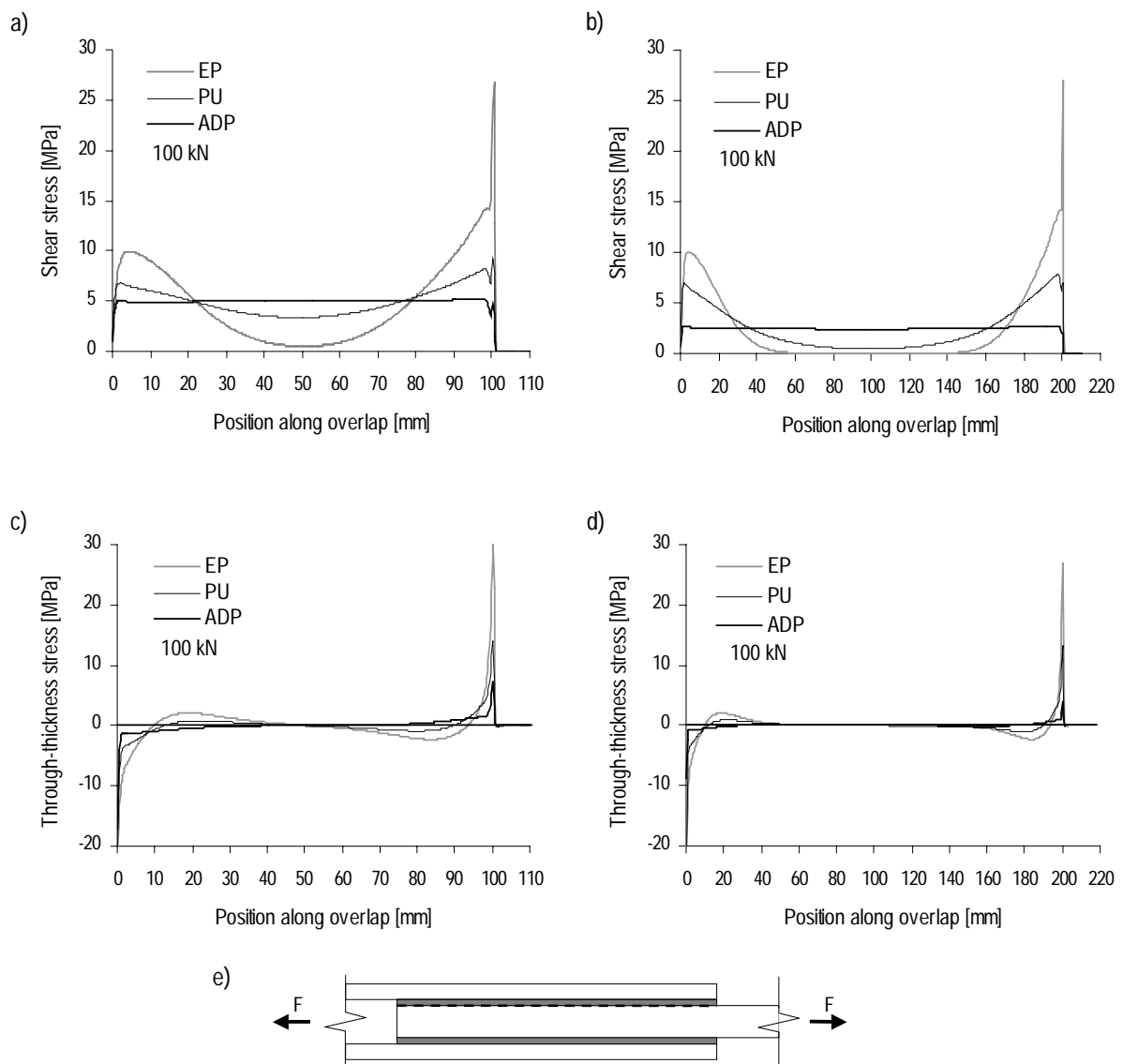


Figure 5.11: Shear stress distribution (a)  $l=100$  mm, (b)  $l=200$  mm and through-thickness stress distribution (c)  $l=100$  mm, (d)  $l=200$  mm along overlap length at 10 mm laminate interface at 100 kN; (e) 10 mm laminate interface (dotted line)



Figures 5.11 and 5.12 show the distribution of the through-thickness shear stress (hereafter referred to as shear stress),  $\tau_{xy}$ , and through-thickness normal stress (hereafter referred to as through-thickness stress),  $\sigma_y$ , at the interface and failure line respectively (0.5 mm depth in the 10 mm laminate) for a tensile load of 100 kN. The ordinate in figures indicates the corresponding stress component and the abscissa indicates position along overlap length. Stress distributions were calculated for EP, PU and ADP joints with an overlap length of 100 and 200 mm.

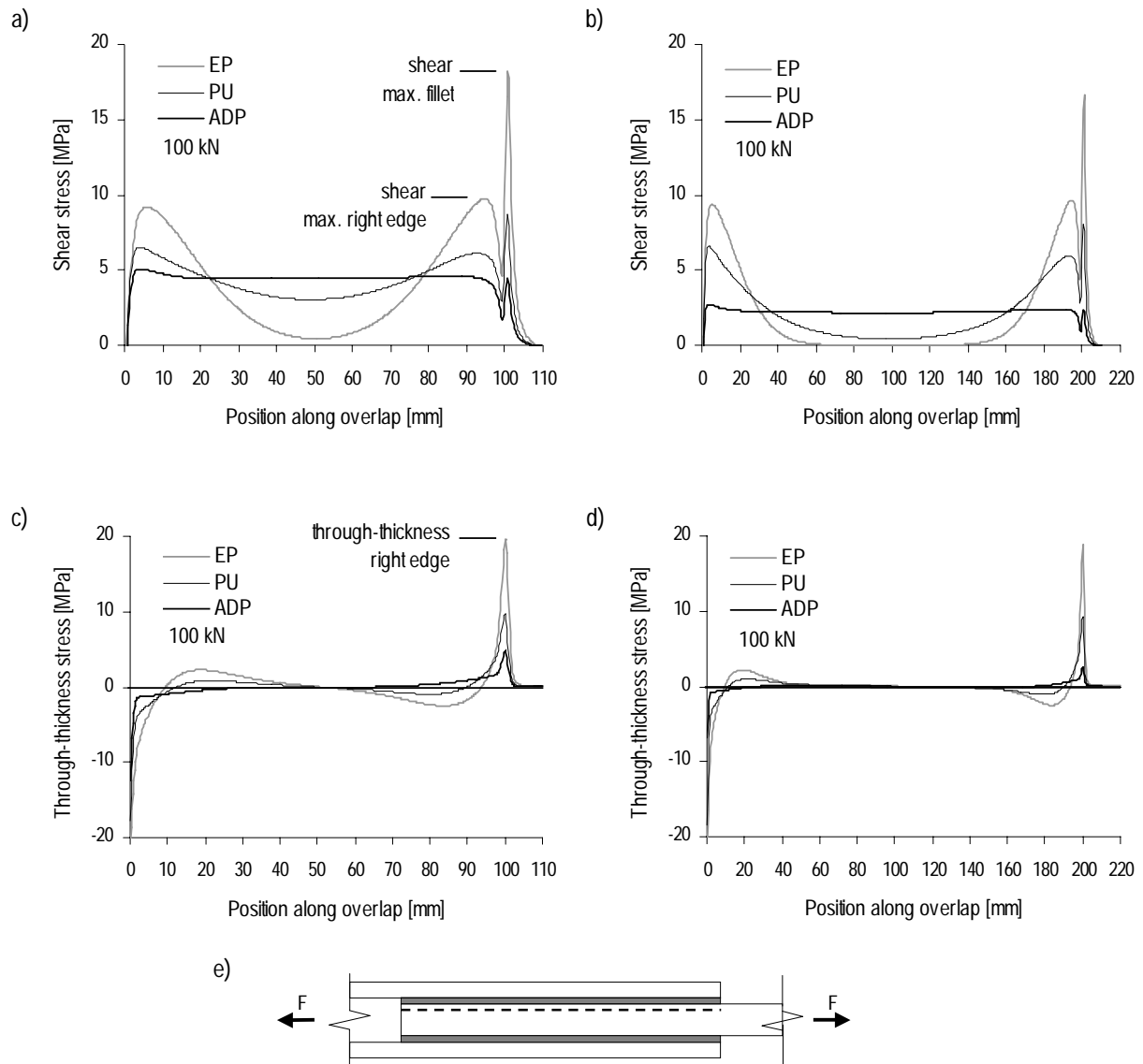


Figure 5.12: Shear stress distribution (a)  $l=100\text{mm}$ , (b)  $l=200\text{ mm}$  and through-thickness stress distribution, (c)  $l=100\text{mm}$ , (d)  $l=200\text{ mm}$  along overlap length at failure line at 100 kN; (e) 10 mm laminate failure line (0.5 mm depth) (dotted line)

The stress distributions along both paths were similar. However, the high peaks observed at the interface on EP joints, caused by geometrical singularities, were softened at 0.5 mm depth. Shear stress distributions on joints with a 100 mm overlap were quite different depending on the adhesive. The EP adhesive produces the distribution typical of stiff adhesives with maximum stresses at the

edges and low stresses in the central part of the joint, while the ADP adhesive allows almost constant shear stress distribution. The PU joint exhibits a shear distribution between the two. The maximum stresses are developed in EP joint.

Figure 5.12(a) shows that the maximum shear stress in the *spew-fillet* on the EP joint, at the failure line, was 2 and 4 times higher than those on the PU and ADP joints respectively and the maximum shear stress at the *right edge* was 1.5 and 2 times higher. The maximum stresses at the *spew-fillet* and *right edge* were approximately 3.5 and 2 times higher than the average shear stress (5 MPa). In the EP joint, approximately 75% of the shear was transferred in the first and last 20 mm of the overlap, which represented 40% of the overlap length, and the rest was transferred in the middle part. In the PU joint, approximately 60% of the shear was transferred in the first and last 20 mm of the overlap. Thus, from an efficiency point of view, the ADP adhesive was preferable since it allowed uniform load transfer and utilized the entire overlap length. These differences were more noticeable in the joints with the 200 mm overlap where the shear stress was almost zero in 40% of the EP joint overlap length and approximately 90% of transfer occurred in the first and last 20 mm, corresponding to 20% of overlap length.

Through-thickness stress distributions of the three joints are different. The maximum values were attained in the EP joints, as for shear stresses. Figure 5.12(c) shows that the maximum through-thickness stress at the *right edge* on the EP joint is approximately 2 and 4 times higher than those in the PU and ADP joints respectively. The right edge was determinant because it was loaded in tension in the adherend's weak direction. The EP joint with 100 mm overlap exhibited through-thickness stresses along the whole overlap length while the EP joints with 200 mm overlap had none in the middle part, corresponding to approximately 40% of the overlap, as for shear stresses. The two ADP joints had no through-thickness stresses in the middle part, 30 mm from the edges.

Comparing the results for the EP joints with different overlap lengths, it was noticed that increasing the overlap length slightly reduces the peaks in shear and through-thickness stresses. Nevertheless, beyond a certain overlap length the "diminishing return" was reached (Renton and Vinson, 1975 a). This does not happen on ADP joints where shear stresses are inversely proportional to overlap length since it is almost constant. To conclude, the ADP adhesive allows more uniform load transfer into the joint and considerably reduces the shear and through-thickness stress peaks observed in EP joints.

Previous stress distributions corresponded to a 100 kN load level and remained constant in the EP and PU joints due to their linear adhesive behavior. Nevertheless, in the case of ADP joints, with bilinear adhesive behavior, the distribution could vary due to the adhesive modulus reduction. Figure 5.13 shows the stress distribution at the failure line (at 0.5 mm depth) at two load levels, 20 kN and 100 kN, characterizing both behaviors. To facilitate comparison, shear and through-thickness stresses were divided by their corresponding average shear stress,  $\tau_{avg}$ , (1 MPa and 5 MPa respectively) calculated from the axial force,  $F$ , joint width,  $b=100$  mm, and overlap length,  $l=100$  mm, as follows:

$$\tau_{\text{avg}} = \frac{F}{2 \cdot b \cdot l} \quad (5.1)$$

Slight variations were observed which agreed with imperceptible variations in the measured axial strain along the overlap (see Section 4.2.4.3).

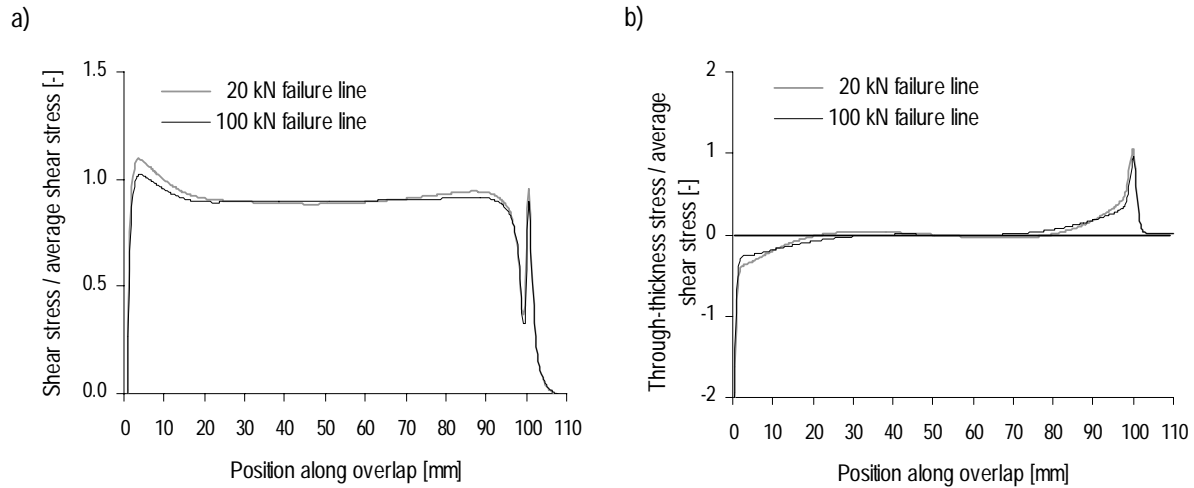


Figure 5.13: (a) Shear stress to average shear stress distribution and (b) through-thickness to average shear stress distribution along overlap length at failure line at 20 kN and 100 kN

As previously noted, stresses at the failure line were lower than those at the interface. However, the stress decrease through the laminate thickness depended on the adhesive elastic modulus. Figure 5.14(a-d) shows the shear stress and through-thickness stress distributions through the joint thickness of the EP and ADP joints with a 100 mm overlap along six paths, 0/0.5/1/2/5/25 mm from the right edge as indicated in Figure 5.14(e), at 100 kN. The two vertical dashed lines represent both joint interfaces (10 mm laminate-adhesive, 5 mm laminate-adhesive). The evolution of the stresses from the interface to the inner 10 mm laminate was examined. The shear stress distributions of the EP and ADP joints were parabolic and the latter distribution became almost linear towards the center of the joint. Except in the first 1 mm from the edge, the through-thickness stress distributions of both joints were almost constant through the 10 mm laminate. The joints with a 200 mm overlap developed identical stress distributions.

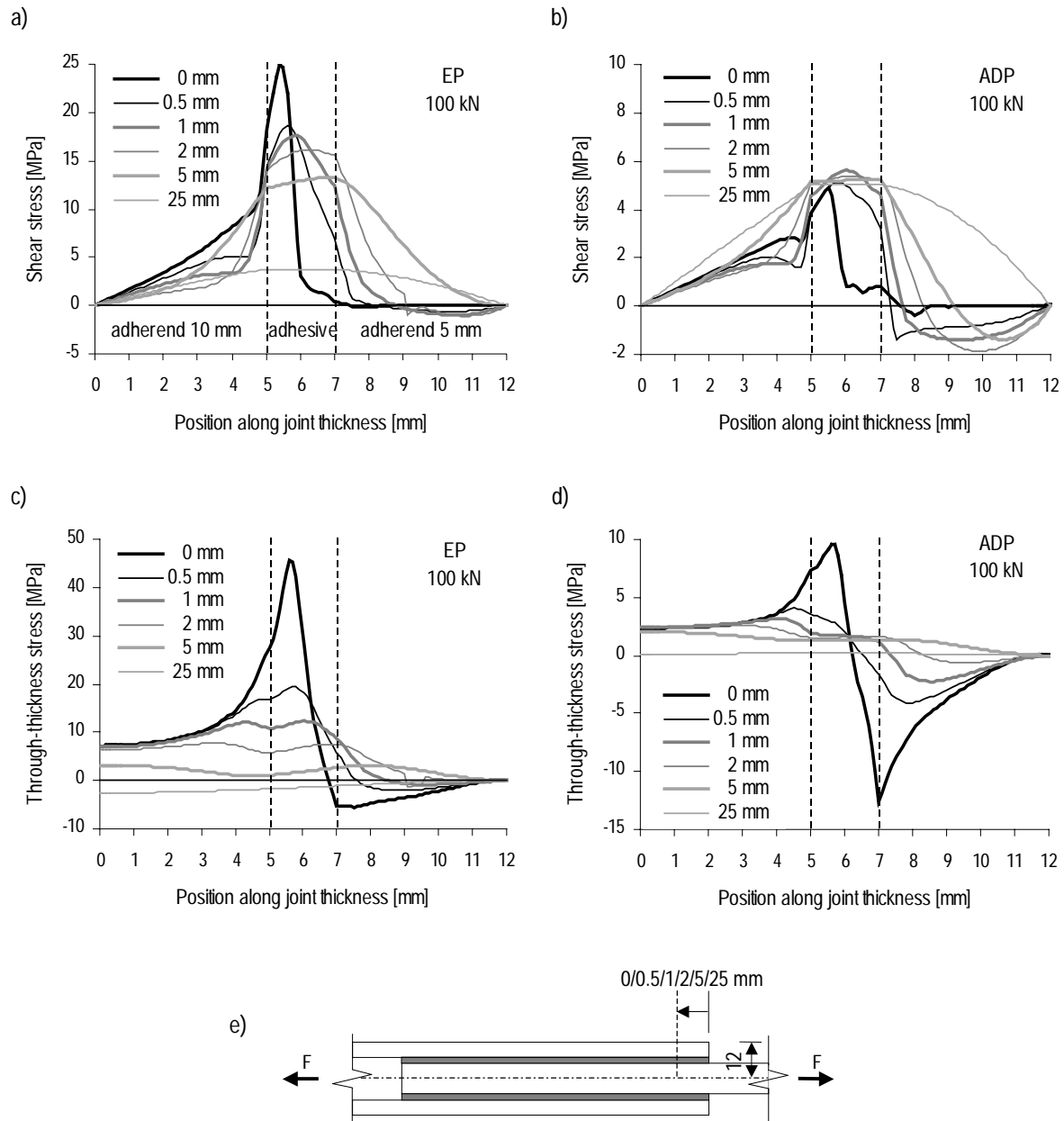


Figure 5.14: (a) EP, (b) ADP shear stress distribution and (c) EP, (d) ADP through-thickness stress distribution along joint thickness at six distances from right edge (0/0.5/1/2/5/25) for joints with 100 mm overlap length at 100 kN; (e) Path position

## 5.2.4 Model Sensitivity

The aim of this study is to investigate the FE model's sensitivity to the following aspects: meshing schemes, adhesive-layer geometry (spew-fillets), adhesive and laminate material properties and geometrical non-linearity. The first two aspects had an effect on the stress distribution along the overlap length and the others also affected the joint stiffness. Analyses were performed on double-lap joints with a 100 mm overlap length.

### 5.2.4.1 Meshing Schemes

As mentioned in Section 5.2.1.4, the meshing schema influences model accuracy. A refinement is usually provided in areas of high stress gradient such as joint edges. Three analyses were carried out with different meshing schemes; the first scheme included two elements through the adhesive thickness (1 mm per side,  $t_a/2$ ), the second analysis included four elements (0.5 mm,  $t_a/4$ ) and the third analysis included eight elements (0.25 mm,  $t_a/8$ ). The analyses were performed on idealized joints, without spew-fillets, using the EP adhesive, the stiffer adhesive, which leads to higher stress peaks.

Figure 5.15 shows the shear and through-thickness stress distributions along the overlap at the failure line (0.5 mm inside the 10 mm laminate) at 100 kN. The shear stress peaks fluctuated and tended to a value located between those calculated with the two- and eight-element through-adhesive-thickness models. The four- and eight-element through-adhesive-thickness models generated almost identical through-thickness stress peaks. The element dimension limit (eight-element through-adhesive-thickness) for accurate stress prediction was attained. The meshing effects were greatest at the interface due to stress concentrations at joint edges. However, the position of the actual failure, inside the laminate and distant from the edges, was less influenced by discontinuity effects.

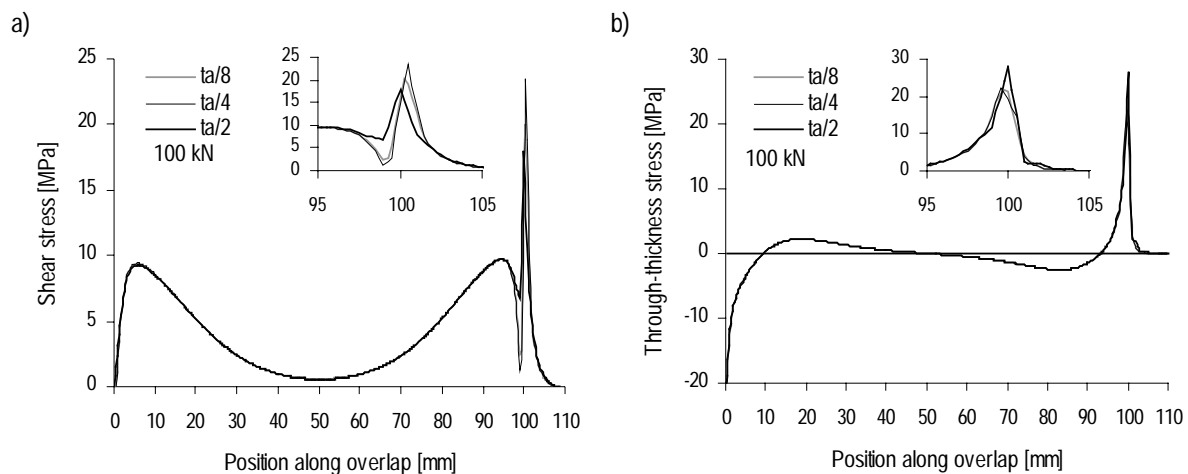


Figure 5.15: Effect of meshing (number of elements through adhesive layer) on stress distribution at 0.5 mm inside the 10 mm laminate of EP joint at 100 kN (a) shear stress, (b) through-thickness stress

### 5.2.4.2 Adhesive-layer Geometry

The effect of the adhesive spew-fillet on the stress distributions has been widely demonstrated for metal and traditional composite joints. Nevertheless, the effect on the studied joints, with their specific dimensions and materials properties, should be investigated. Therefore, three analyses were carried out with different spew-fillet shapes and sizes and were compared with the idealized adhesive-layer analysis, without spew-fillets. The first and second analyses included curved spew-fillets with a 1 mm radius (half of adhesive thickness) and 2 mm radius (adhesive thickness) respectively

(Figure 5.3). The third analysis included a 45° spew-fillet over half of the adhesive thickness. The analyses were performed on joints with EP adhesive, the stiffer adhesive, which leads to higher stress peaks. A mesh refinement on spew-fillet areas was provided.

The spew-fillets did not influence joint elongation. Figure 5.16 shows the shear and through-thickness stress distributions along the overlap of the curved spew-fillets and the idealized joint at the failure line at 100 kN. As expected, the spew-fillets reduce peaks but the effect was much less than referred to in literature (Adams and Peppiatt 1974). This is caused by several factors: joint material properties (higher adhesive to adherend stiffness ratio than traditional composite joints with CFRP); dimensions (higher adhesive to adherend thickness ratio than traditional composite joints) and the small size of spew-fillets (formed during the manufacturing process and not designed for study purposes). It can be noticed that the stress reduction was more pronounced for through-thickness stresses than shear stresses. The rounding of sharp edges eliminates the geometrical singularity. The third analysis including the 45° spew-fillet over half of the adhesive thickness exhibited the same behavior as the spew-fillets with a 1 mm radius.

All joint analyses, except those in the previous and present sections (meshing schemes and adhesive-layer geometry), included the curved spew-fillets with a 1 mm radius which were similar to actual conditions.

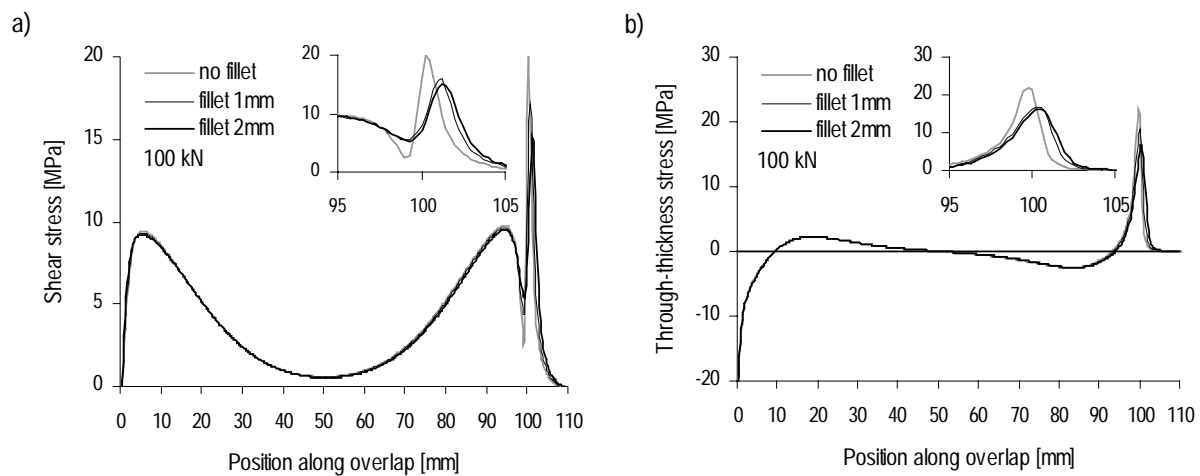


Figure 5.16: Effect of adhesive-layer geometry on stress distribution at 0.5 mm inside 10 mm laminate of EP joint at 100 kN, (a) shear stress, (b) through-thickness stress

### 5.2.4.3 Adhesive Material Properties

As previously mentioned, adhesives exhibit different behavior in tension and compression which should be included in the FE model. Nevertheless, a simplified model including an identical behavior in tension and compression could be developed, reducing considerably the number of loading steps and calculation time. Two additional analyses were performed with the simplified adhesive behavior and compared with results from the reference behavior, with different tensile and compressive behaviors. In the first analysis the single tensile behavior ( $E_{t,c}=4560$  MPa see Table 5.2 page 94) was

maintained because joint failure initiated near the adhesive-layer region loaded in shear and tension (positive through-thickness stresses). In the second analysis an average of the tensile and compressive curves was defined ( $E_{avg}=3810$  MPa). Tensile elastic modulus,  $E_{t,c}$ , was approximately 20% higher than average elastic modulus,  $E_{avg}$ . Figure 5.17 shows the shear stress and through-thickness stress variations along the overlap at the failure line at 100 kN. Models including tensile behavior and tensile and compressive behaviors exhibited almost identical stress peaks at the right edge, with positive through-thickness stresses, while the model with the average behavior slightly underestimated these stresses (4%). A joint elongation increase was observed with the second model (6%) while no variation was perceived with the first model in comparison to the reference model. Thus, it is recommended to introduce tensile behavior instead of average behavior because the former governs failure but the differences are not significant. The influence of adhesive model on joint behavior increases with adhesive stiffness.

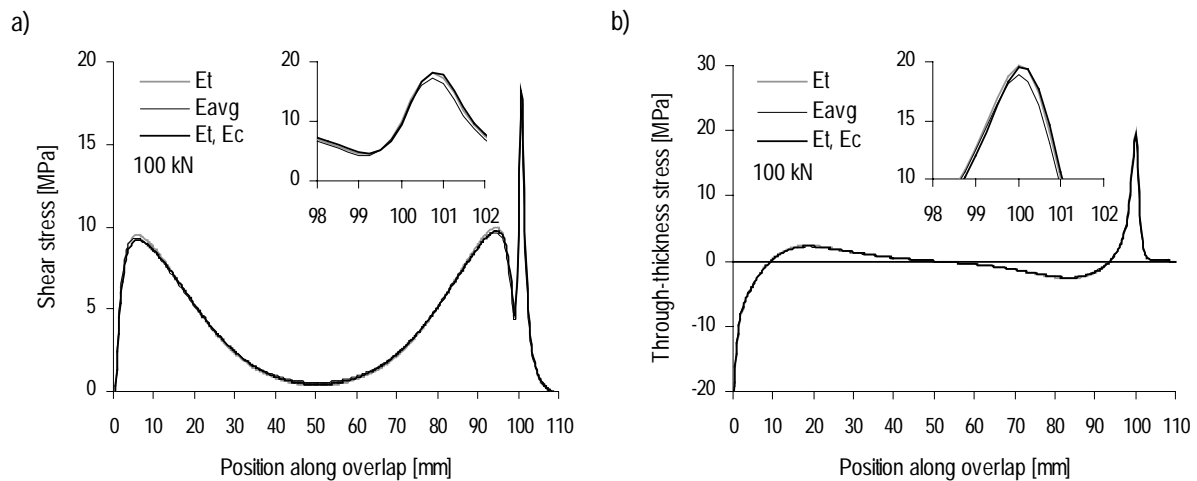


Figure 5.17: Effect of EP adhesive model on stress distribution at 0.5 mm inside 10 mm laminate at 100 kN (a) shear stress, (b) through-thickness stress

#### 5.2.4.4 Laminate Material Properties

Significant variability in the laminates Young's moduli was observed during the experiments, with scatter reaching 10% of mean values (see Section 4.2.4.3). Therefore, the effects of Young's moduli on joint model behavior were investigated. Two models were developed; the first with a 10% reduction in the mean values of both laminates (28.8 GPa for 5 mm, 25.2 GPa for 10 mm) and the second with a 10% increase (35.2 GPa for 5 mm, 30.8 GPa for 10 mm). Both models are compared with the reference model characterized by the mean values summarized in Table 5.1. The other laminate properties included in the numerical model ( $E_y$ ,  $G_{xy}$  and  $\nu$ ) had a negligible influence on the behavior of joints loaded in tension which are governed by longitudinal mechanical properties.

Figure 5.18 shows shear and through-thickness stress distributions along the overlap at the failure line at a load of 100 kN. As expected, the decrease in the laminate's Young's moduli led to an increase in peak stresses. A variation of  $\pm 10\%$  in the laminate Young's moduli led to a variation of  $\pm 5\%$  in the

maximum shear and through-thickness stress, which was negligible. An increase of 11% on joint elongation was observed with the first model and a reduction of 9% with the second model in comparison to the reference model. The opposite effects were observed on joint stiffness. As demonstrated in the study of the effects of the adhesive to adherend modulus ratio (see Section 5.3), variations in the laminate Young's moduli have a greater influence on joint stiffness and stress distributions when a flexible adhesive is used. This could explain the greater differences between the FE calculations and measurements on ADP joints than on EP and PU joints.

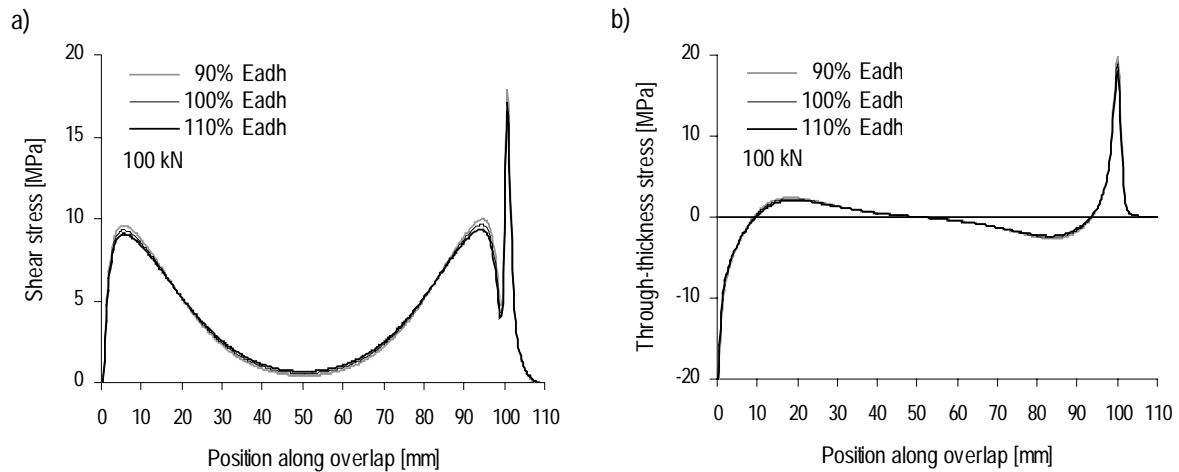


Figure 5.18: Effect of laminate Young's moduli on stress distribution at 0.5 mm inside 10 mm laminate of EP joint at 100 kN (a) shear stress, (b) through-thickness stress

### 5.2.4.5 Geometrical Non-linearity

Large deformations were expected with high load levels and soft adhesives. Geometrical non-linear FE analysis should be carried out and compared with linear analysis in order to quantify the geometrical non-linear effects due to the eccentricity of the 5 mm laminates. In the case of negligible effects, linear analysis could be performed, reducing considerably the number of loading steps and calculation time of non-linear analysis. In the present study, using EP, PU and ADP adhesives, the corresponding adhesive material models required non-linear analysis which takes material and geometrical non-linearities into account. Nevertheless, comparison of both analyses is recommended when modeling identical linear behavior in tension and compression. The parametric study performed on adhesive to adherend Young's modulus ratio (see Section 5.3), assuming identical linear behavior in tension and compression, indicated that geometrical non-linear effects are not significant. Joint elongation increases only 1.5% and maximum stresses decrease approximately 5% with an adhesive elastic modulus of 40 MPa (adhesive to adherend modulus ratio of 0.13%).



## 5.2.5 Strength Prediction

Experimental investigations indicated an interlaminar (fiber-tear) failure in EP and PU joints and an adhesion (adhesion promoter to substrate) failure on ADP joints due to inappropriate surface treatment. The interlaminar failure occurred inside the 10 mm laminate, at 0.5 mm depth. When predicting joint strength, it was assumed that failure takes place as a result of interlaminar failure in the laminates and that adhesion problems and cohesive failure were avoided (Vallée 2004). The failure may be described in terms of a limiting condition being reached at a specific point in the fracture line. The failure criterion based on limiting values of the shear and through-thickness stress interaction,  $\tau_{xy}-\sigma_y$ , on the laminates was considered. Joint strength was predicted by applying the failure criterion to the FE results for the 10 mm laminate, at 0.5 mm depth, and considering the laminate shear strength,  $\tau_{xy,u}$ , and through-thickness strength,  $\sigma_{y,u}$ . Long (1991) and Tong (1997) developed several interlaminar failure criteria for traditional composite materials. Some are derived from the well-known Tsai criterion and the Norris criterion (Nahas 1986). Vallée (2004) developed a failure criterion according to Long's for interlaminar failure in joints made of pultruded laminates. He designed a shear-tensile-interaction device (STI-device) to measure shear strength and through-thickness strength independently on 50x50 mm coupons and determine the GFRP failure criterion for any combination of shear and through-thickness stresses. He tested the same 5 mm and 10 mm laminates used in the present study. The failure in the coupons occurs, as for adhesively-bonded joints, at approximately 0.5 mm depth. Laminate shear and through-thickness strengths are listed in Table 5.4. They are similar in both laminates since they are mainly characterized by the matrix (weak layer) strengths and slightly influenced by fiber architecture. Fibers interlocked in the matrix layer create a favorable effect on its strength.

Table 5.4: Shear and through-thickness strengths of GFRP laminate coupons (Keller and Vallée 2005)

Laminate	$\tau_{xy,u}$ [MPa]	$\sigma_{y,u}$ [MPa]
5 mm	22.6	9.4
10 mm	19.3	8.0

The shear and through-thickness stresses developed with STI-device are uniformly distributed, unlike the stress state in the joint where high stress gradients were observed at the edges. Thus, the related failure-criterion,  $f_{device}$ , (Eq. 2.14 page 45), was not adapted to actual joint stress conditions and two correction factors ( $\kappa_\tau$ ,  $\kappa_\sigma$ ), one for each kind of stress, were added to take the stress distribution into account. The joint-failure criterion function,  $f_{joint}$ , was defined in Eq. 2.15 (page 45). Shear and through-thickness stresses were obtained from the FE calculations for an arbitrary load of 100 kN. The maximum value of the function along the overlap length,  $\eta$ , defines the critical stress interaction point (Eq. 2.16 page 45). Since EP and PU joints exhibited linear behavior, the load reaching the failure limits could be predicted with Eq. 2.17 (page 45). The ADP joints exhibited bilinear behavior but the shear stress and through-thickness stress distributions were slightly influenced by the adhesive modulus decrease since both adhesive (elastic and plastic) moduli were low compared to the adherend Young's modulus (see Section 5.3.2). Thus, the ADP joint strength could also be predicted.

The correction factors were calibrated using the experimental results of two double-lap joint specimens with EP adhesive and different overlap lengths and chamfering levels. Factor  $\kappa_\tau$  depends on the overlap and varies between 1 (short,  $l=50$  mm) and 4 (long,  $l=200$  mm) and factor  $\kappa_\sigma$  depends on the chamfering level and varies between 2 (full) and 4 (none).

Figure 5.19 shows the shear and through-thickness stress distributions at failure line and the related correction factors of the STI-device and the joints with a 100 mm overlap length. The correction factors for the EP joints are well defined because the specimens are similar to those tested by Vallée (2004). The ADP joints provide almost constant shear distribution, similar to that developed with the STI-device, thus no correction factor is applied to the corresponding strength ( $\kappa_\tau=1$ ). The almost linear through-thickness distribution and low peak stresses lead to a factor close to 1 (two assumptions  $\kappa_\sigma=1.0-1.5$  for both overlap lengths). As for PU joints, the correction factors lie between those of previous joints. The stress distributions in PU joints are located between those of EP and ADP joints and the stress peaks are half as high as those observed in EP joints. Two assumptions are made concerning the through-thickness correction factor ( $\kappa_\sigma=2.0-2.5$ ).

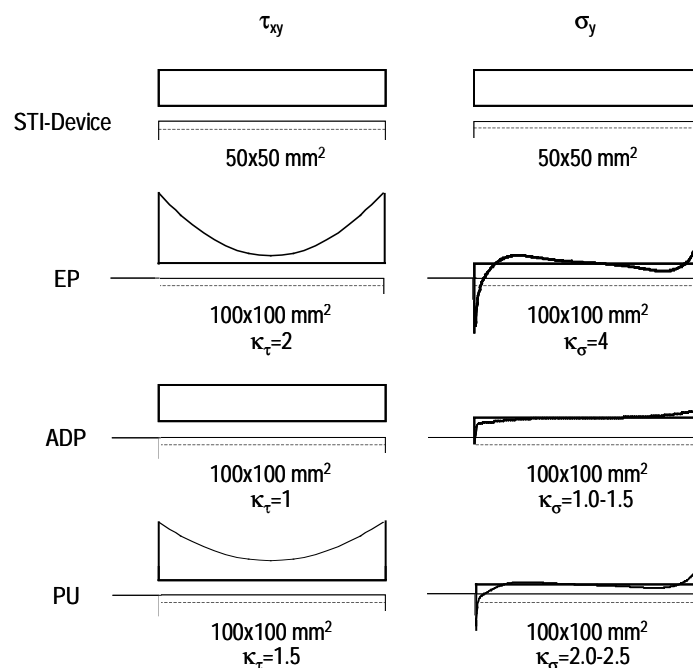


Figure 5.19: Shear and through-thickness stress distributions at failure line and related correction factors of STI-device and EP, ADP, and PU series ( $l=100$  mm)

Table 5.5 lists the correction factors,  $\kappa_\tau$  and  $\kappa_\sigma$ , the maximum value of the failure-criterion function (at 100 kN),  $\eta$ , predicted strength,  $F_{u,calc}$ , measured strength,  $F_{u,meas}$ , and predicted (average value) to measured strength ratio for each adhesive and overlap length. The comparison of predicted strength in the 5 mm and 10 mm laminates, both at 0.5 mm depth (resin layer: weak layer), indicates that failure always initiated in the 10 mm laminate. The predicted strength for EP joints with 100 mm overlap matched well with experimental results while that for the 200 mm overlap was underestimated. The two predicted strengths for the PU joint, calculated with two different  $\kappa_\sigma$  factors,

approach the experimental measurements. They are slightly higher than the average measured value and maximum failure load of all the series with 100 mm overlap <sup>(1)</sup> (173 kN). Both predicted strengths are higher than that for EP joint, which agrees with some experimental results (see Section 4.2.1 Appendix B).

Table 5.5: Correction factors, maximum value of failure-criterion function, calculated and measured failure loads and calculated and measured failure load ratio of EP.A, PU.B, ADP.C, EP.D, ADP.D series

Series	Adhesive	l [mm]	$\kappa_\tau$ [-]	$\kappa_\sigma$ [-]	$\eta$ [-]	$F_{u,calc}$ [kN]	$F_{u,meas}$ [kN]	$F_{u,calc}/F_{u,meas}$ [-]
EP.A	EP	100	2.0	4.0	0.48	144	141±11	1.02
PU.B	PU	100	1.5	2.0-2.5	0.41-0.27	156-192	140±13 (173 <sup>1</sup> )	1.12-1.37
ADP.C	ADP	100	1.0	1.0-1.5	0.36-0.18	167-236	119±12 (202 <sup>2</sup> )	1.40-1.98
EP.D	EP	200	4.0	4.0	0.38	162	182±14	0.89
ADP.D	ADP	200	1.0	1.0-1.5	0.11-0.05	302-447	253±8	1.19-1.77

<sup>1</sup> maximum strength of series with PU adhesive and 100 mm overlap length (specimen PU.C1)

<sup>2</sup> maximum strength of series with ADP adhesive and 100 mm overlap length (specimen ADP.B2.1)

Predicted strengths for ADP joints were much higher than measured strengths due to premature adhesion failure. In the case of the 100 mm overlap length, the predicted strength with  $\kappa_\sigma=1.5$  was still higher than the maximum measured strength of all the series <sup>(2)</sup> reached by specimen ADP.B2.1 (202 kN). Its failure surface showed smaller adhesion areas, located at one edge, than the other specimens (Figure 5.20). The prediction with  $\kappa_\sigma=1.0$  underestimated the joint strength; this correction factor is too restrictive.

The predicted strengths for the 200 mm overlap joint were closer to the average measured value because the specimens exhibited fewer adhesion problems than 100 mm overlap specimens. The predicted strengths assumed interlaminar failure and not the actual failure that should be avoided with an appropriate surface treatment. Thus, comparison of predicted and measured strengths was not really appropriate. Nevertheless, comparison of predicted strength with the processed strength based on measured strength and assuming no adhesion problems seemed more appropriate. A variation of shear and through-thickness stress distributions and maximum values proportional to the effective bonded area was assumed. The processed strength,  $F'_{u,meas}$ , was derived from measured strength, taking into account the actual *good adhesion* area,  $A_{good\ adhesion}$ , instead of the bonded area,  $A$ , as indicated in Eq. 5.2.

$$F'_{u,meas} = F_{u,meas} \cdot \frac{A}{A_{good\ adhesion}} \quad (5.2)$$

The *good adhesion* area presents no adhesion problems. The three specimens with highest measured strength were considered (ADP.B2.1, ADP.B3.1 and ADP.B4.2). Table 5.6 summarizes the *good adhesion* area to bonded area ratio, measured strength,  $F_{u,meas}$ , processed strength,  $F'_{u,meas}$ , predicted strength,  $F_{u,calc}$ , and predicted to processed strength ratio,  $F_{u,calc}/F'_{u,meas}$ . Differences in processed strength could be caused by *bad adhesion* area location; positioned in the center of the overlap (ADP.B3.1 and ADP.B4.2), it had a more unfavorable effect on strength than when located at the

edges (ADP.B2.1). The assumption the concerning stress variation proportional to the effective bonded area was certainly adequate for shear stresses, which were uniformly distributed along the overlap length, but not for through-thickness stresses. The predicted ( $\kappa_{\sigma} = 1.5$ ) to processed strength ratio was 1.09 for ADP.B2.1 and reached 1.27 for the other two. In the first case, the predicted strength calculated with the FE results matched well with the processed strength based on measured strength and assuming no adhesion failure. Thus, solving the adhesion problem will lead to a joint strength increase of 40-97% ( $\kappa_{\sigma} = 1.0-1.5$ ) for the 100 mm overlap length and 19-77% ( $\kappa_{\sigma} = 1.0-1.5$ ) for the 200 mm.

Table 5.6: Strength of specimens ADP.B2.1, ADP.B3.1 and ADP.B4.2, measured, processed, predicted and predicted to processed strength ratio

Specimen	$A_{\text{good adhesion}}/A$ [-]	$F_{u,\text{meas}}$ [kN]	$F'_{u,\text{meas}}$ [kN]	$F_{u,\text{calc}}$ [kN]	$F_{u,\text{calc}}/F'_{u,\text{meas}}$ [-]
ADP.B2.1	14/15	202	216	236	1.09
ADP. B3.1	13/14	173	186	236	1.27
ADP. B4.2	13/14	173	186	236	1.27

The EP and ADP joint failures were mainly governed by through-thickness stresses while the PU joint failure was governed by shear stresses. The through-thickness stress contribution to the failure-criterion function,  $f_{\text{joint}}$ , was 76-95% ( $l=100/200\text{mm}$ ) for EP, 50-28% ( $\kappa_{\sigma}=2.0-2.5$ ) for PU and 94-88% ( $\kappa_{\sigma}=1.0-1.5$ ) for both ADP joints.

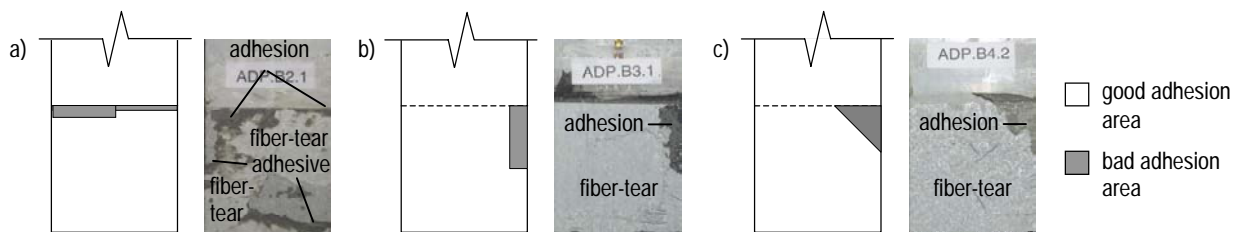


Figure 5.20: Failure surface of specimens and types of failure (a) ADP.B2.1, (b) ADP.B3.1, (c) ADP.B4.2

## 5.2.6 Analytical Method for Predicting Stiffness and Strength of ADP Joints

### 5.2.6.1 Joint Elongation and Stiffness

As previously noted, the shear stress distribution is almost uniform at the interface line in ADP joints. Assuming a constant shear stress distribution in the adhesive bond, an estimate of the resulting adhesive shear could be made for every load level. The constant shear stress,  $\tau_{xy}$ , was calculated from the axial force,  $F$ , joint width,  $b=100$  mm, and overlap length,  $l=100/200$  mm, as follows:

$$\tau_{xy}(\text{adhesive}) = \frac{F}{2 \cdot l \cdot b} \quad (5.3)$$

Joint elongation,  $\Delta l$ , consists of shear deformations of the adhesive layer,  $\Delta l_1$ , and axial elongation of the 5 mm and 10 mm laminates,  $\Delta l_2$ , as follows:

$$\Delta l = \Delta l_1 + \Delta l_2 \quad (5.4)$$

$$\Delta l_1 = \tau_a \cdot \gamma(\tau) \quad (5.5)$$

$$l_2 = \frac{F \cdot l}{E \cdot A} = \frac{F \cdot l}{E \cdot b \cdot t} \quad (5.6)$$

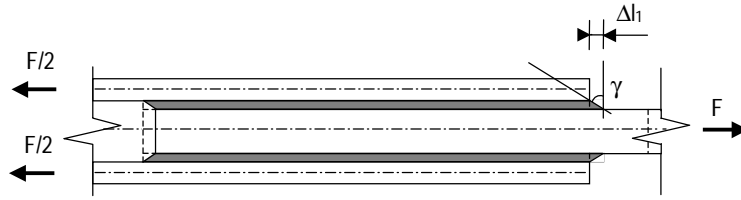


Figure 5.21 Joint elongation estimation for the ADP joints

Eq. 5.5 includes: the adhesive layer thickness,  $t_a = 2$  mm, and the shear strain of the adhesive  $\gamma(\tau)$ , defined by the measured shear stress-strain curve ( $\tau$ - $\gamma$ ). A constant shear stress distribution presumes a linear transfer of the axial load along the overlap. Thus, the global laminate elongation,  $\Delta l_2$ , was calculated as in Eq. 5.6. The denominator comprises: the laminate Young's modulus,  $E=30$  GPa, and the laminate cross-section area,  $A$ , defined by the width,  $b=100$  mm, and the thickness,  $t=10$  mm. An average value of both laminate Young's moduli (5 mm laminate: 32 GPa, 10 mm laminate: 28 GPa) is considered. From the global elongation,  $\Delta l$ , joint stiffness,  $k_{\text{joint}}$ , is estimated as follows:

$$k_{\text{joint}} = \frac{F}{\Delta l} \quad (5.7)$$

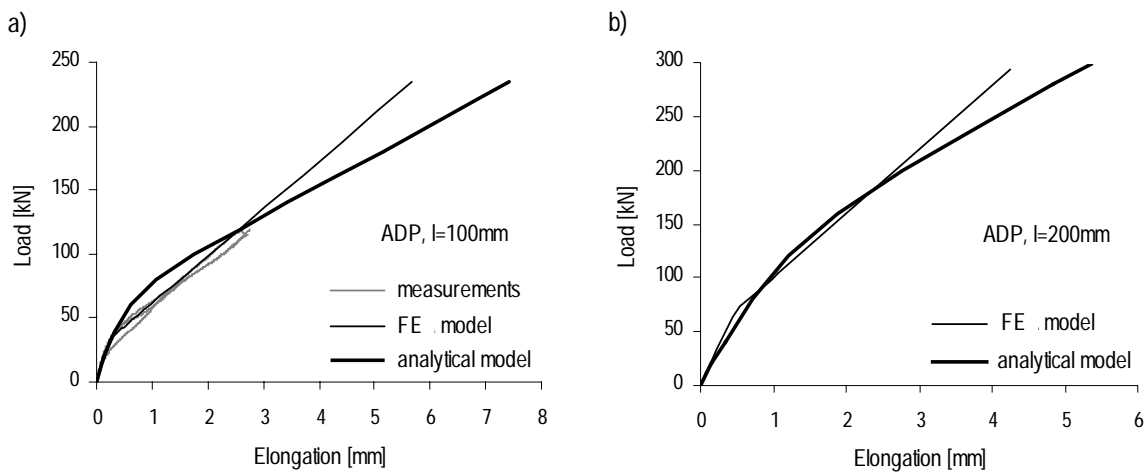


Figure 5.22: Load-elongation curves for ADP joints (a)  $l=100$  mm, (b)  $l=200$  mm, comparison of FE and analytical calculations and measurements

Figure 5.22(a) compares the measured joint elongation of specimens ADP.C7-9 with the FE and analytically calculated joint elongation and Figure 5.22(b) compares only calculated elongations. The FE model uses the bilinear shear stress-strain curve (characterized by two shear moduli  $G_e=33$  MPa and  $G_p=3$  MPa, yield shear stress,  $\tau_e=3$  MPa, and strain,  $\gamma_e=0.9\%$ ) while the analytical model refers directly to the measured shear stress-strain curve ( $\tau-\gamma$ ) (see Figure 4.5(c) page 59).

Table 5.7: Joint stiffness and failure load, comparison of FE and analytical calculations and measurements for ADP joints

Overlap length (mm)	Joint stiffness [kN/mm]						Failure load [kN]		
	(20 kN)		meas.	(100 kN)		meas.	FE		meas.
FE model	analytical model	FE model		analytical model	FE model		analytical model		
100	132	141	135±31	37	29	33±6	167-236	177-242	119±12 (202 <sup>1</sup> )
200	144	130	-	60	82	-	302-447	408-500	253±8

<sup>1</sup> Maximum strength of series with ADP adhesive and 100 mm overlap length (specimen ADP.B2.1)

### 5.2.6.2 Strength Prediction

The interlaminar failure criterion including the through-thickness and shear stress interaction described in Section 5.2.5 was used for strength prediction. The condition in Eq. 2.14 (page 45) should be satisfied along the failure line (Figure 5.23) where the factor  $\kappa_\tau = 1$  for constant shear stress distribution and the factor  $\kappa_\sigma = 1-1.5$  for linear through-thickness stress distribution. The assumed shear and through-thickness stress distributions are represented in Figure 5.23. The uniform shear stress distribution was derived from the distribution at the interface, calculated with Eq. 5.3, assuming a parabolic shear stress distribution through the 10 mm laminate (see Section 5.2.3). Then the almost constant shear stress was defined as:

$$\tau_{xy}(\text{failure line}) = \left( \frac{t - t_f}{t} \right)^2 \cdot \tau_{xy}(\text{adhesive}) \quad (5.8)$$

where  $t_f$  is the failure line depth (0.5 mm) and  $t$  is the 10 mm laminate thickness.

Due to the eccentricity of the 5 mm laminates, small secondary moments,  $M$ , were produced in these laminates, which caused through-thickness stresses. The through-thickness stress distribution is assumed to be zero at the middle of the overlap, 30 mm inwards from both edges, and bilinear towards the ends. FE calculations (for this double-lap joint geometry,  $l=100/150/200$  mm) enabled the stress distribution to be established and showed that maximum stress,  $\sigma_{y,1}$ , depends on stress  $\sigma_{y,2}$  as indicated in Eq. 5.9.

$$\sigma_{y,1}(\text{failure line}) = 2.5 \cdot \sigma_{y,2}(\text{failure line}) \quad (5.9)$$

These stresses at the edges were calculated from the bending moment,  $M$ , which resulted from the axial load,  $F/2$ , and its eccentricity,  $c=5$  mm, according to Eq. 5.10. The same bending moment should be obtained by summing the moments of forces  $F_1$  and  $F_2$  around the axis  $z$ , using the lever

arms  $x_1$  and  $x_2$ , as indicated in Eq. 5.11. The forces  $F_1$  and  $F_2$  are the resultants of stresses and are estimated with Eq. 5.12 where  $b$  is the joint width (100 mm).

$$M = \frac{F}{2} \cdot c \quad (5.10)$$

$$M = F_1 \cdot x_1 + F_2 \cdot x_2 \quad (5.11)$$

$$M = \left( \int_0^3 \sigma_y(x) \cdot b \cdot dx \right) \cdot x_1 + \left( \int_3^{30} \sigma_y(x) \cdot b \cdot dx \right) \cdot x_2 \quad (5.12)$$

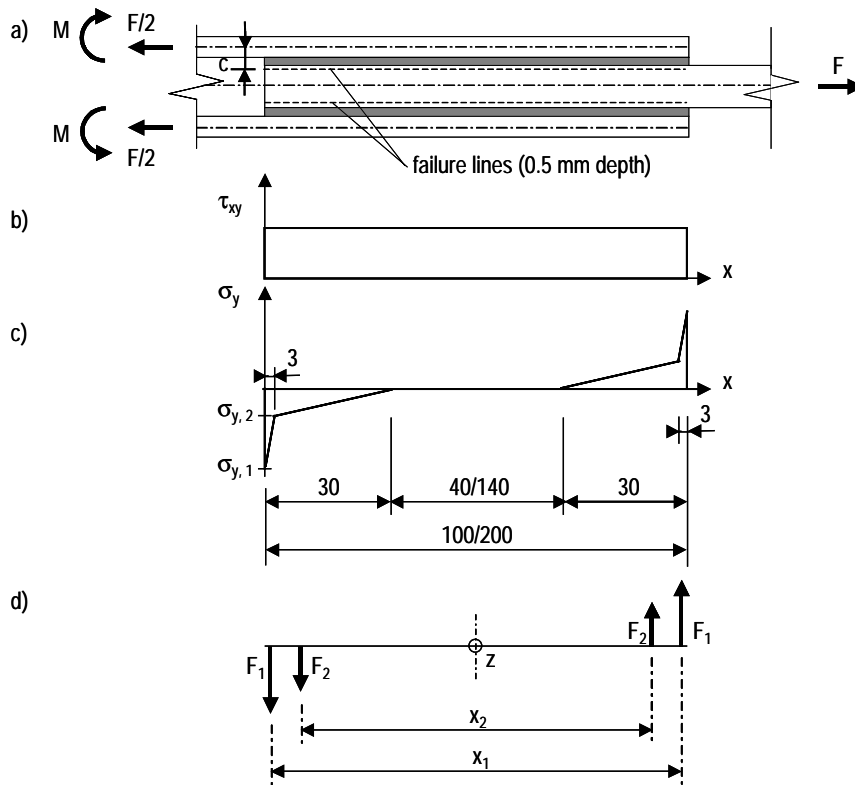


Figure 5.23: ADP joints (a) internal loads; (b) Shear and (c) through-thickness stress distribution along failure line; (d) Resultants of through-thickness stresses

The maximum values of the failure-criterion function,  $\eta$ , (at 100 kN), reached at the edges, were 0.32-0.17 ( $\kappa_\sigma=1-1.5$ ) for the 100 mm and 0.06-0.04 ( $\kappa_\sigma=1-1.5$ ) for the 200 mm overlap. Table 5.7 lists the corresponding analytically predicted strengths, FE predicted strength and experimental measurements. The analytically predicted strengths for the 100 mm overlap were similar to those of FE values while the analytically predicted strengths for the 200 mm overlap were higher than the FE values due to underestimation of the maximum through-thickness stresses.

### 5.3 Effects of Adhesive to Adherend Modulus Ratio

As seen in Section 5.2.2 and 5.2.3, the adhesive elastic modulus has a considerable effect on the joint stiffness and stress distribution along the overlap length and consequently the joint strength. It was

noticed, for instance, that PU joints exhibited a more suitable stress distribution than EP joints, leading to more uniform load transfer and reduced maximum stresses, while remaining as stiff as EP joints. Thus, adhesive elastic modulus has a non-linear effect on these two characteristics which vary in a different manner. For a better understanding of these phenomena, an investigation was carried out on the influence of adhesive to adherend modulus ratio,  $E_{\text{adhesive}}/E_{\text{adherend}}$ , on the two principal mechanical characteristics of joints: joint stiffness, related to joint serviceability state, and stress distribution, controlling failure load.

The double-lap joint FE model described in Section 5.2.1 and validated in Section 5.2.2 was used for this study. The studied joint had a 100 mm overlap length and 2 mm adhesive thickness. Adhesive behavior was linear elastic and characterized by an average elastic modulus, the average of the tension and compression values. Calculations were carried out for a series of sixteen elastic moduli (100%-0.1%). The reference value (100%) corresponds to 4 GPa, typical of structural epoxy adhesives commonly used for bonding applications (Flemming and Siegfried 2003, Michaeli et al. 1998) and similar to the EP adhesive tested in the experimental investigation (3.8 GPa).

### 5.3.1 Joint Stiffness

Figure 5.24(a) shows the joint load-elongation curves for six different adhesive elastic moduli. It can be seen that reducing the reference value (4 GPa) by a factor of 10 has little effect on joint elongation, which only increases 37%. Very flexible adhesives are required to develop large elongations. Figure 5.24(b) illustrates joint stiffness related to adhesive to adherend modulus ratio. Joint stiffness was calculated as defined in Eq. 5.7 (page 115). The adherend Young's modulus is an average value of both laminates Young's moduli (30 GPa). The two additional horizontal lines are the stiffness of the *rigid joint* and a continuous *laminated*. The *rigid joint* represents a theoretical double-lap joint without an adhesive layer connecting the laminates (Figure 5.25(a)), such as a welded joint. Its stiffness was also calculated with the FE model, just removing the adhesive layer. The rigid joint is obviously stiffer than bonded joints. The stiffness of the continuous inner *laminated* (the adherend to be connected) is calculated by Eq. 5.13 where  $E$  is the Young's modulus,  $A$  is the cross-section area and  $l$  is the length corresponding to joint overlap length (Figure 5.25(c)).

$$k_{\text{laminated}} = \frac{E \cdot A}{l} \quad (5.13)$$

The curve shape is logarithmic and located between two asymptotic lines: the vertical axis (joint stiffness) and the horizontal line corresponding to the *rigid joint*. Joints could be classified according to their stiffness as stiff or flexible. The area between *rigid joint* stiffness and continuous (inner) *laminated* stiffness delimits stiff joints and the area below defines flexible joints. Stiff joints create structural continuity as well as reinforcing the overlap area. The limit between the two behaviors occurs at an adhesive to adherend modulus ratio of 0.8%, corresponding to an adhesive modulus of 240 MPa for the configuration of the joint investigated. A bonded joint using an adhesive with this elastic modulus is as stiff as continuous laminated. As the joint and adhesive behaviors are linked,



adhesives are also classified as stiff or flexible; the limit is related to that of joint stiffness. The symbols located in the abscissa represent the adhesives used in the experimental study. The EP ( $E_{\text{adhesive}}/E_{\text{adherend}}=12.7\%$ ) and PU (1.7%) adhesives develop a stiff joint while the ADP adhesive (0.2% elastic behavior) generates a flexible joint. Thus, the EP and PU adhesives are stiff and the ADP adhesive is flexible.

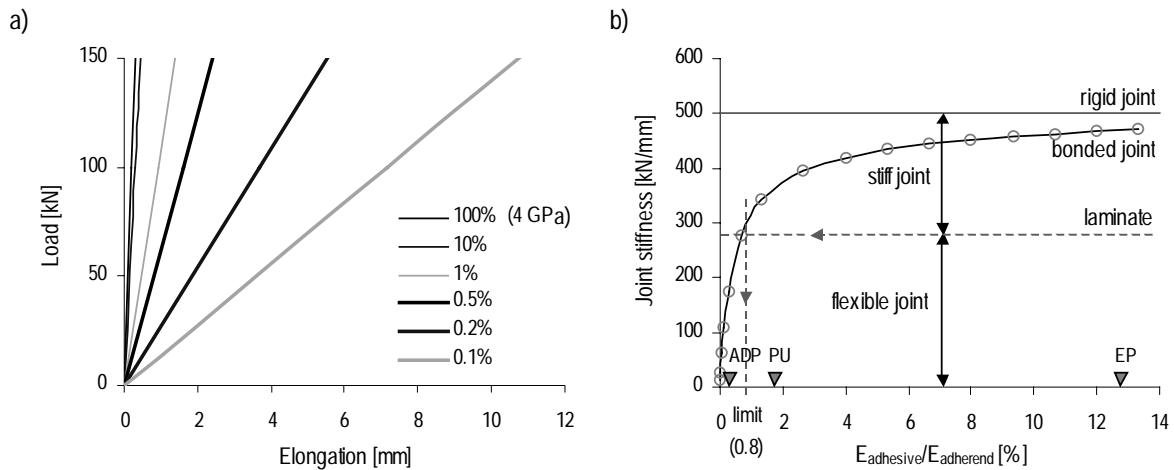


Figure 5.24: Effect of (a) adhesive elastic modulus on joint elongation, (b) adhesive to adherend modulus ratio on joint stiffness of 100 mm overlap length joints



Figure 5.25: (a) Rigid joint; (b) Adhesively-bonded joint; (c) Laminate

### 5.3.2 Stress Distribution

Figures 5.26(a) and (b) show the distribution of the shear and through-thickness stresses at 0.5 mm depth in the 10 mm laminate with a tensile load of 100 kN for four different adhesive elastic moduli. Reducing the reference value (4 GPa) by a factor of 10 leads to more uniform shear distribution and considerably reduces shear and through-thickness stresses while maintaining high joint stiffness as noted in the Section 5.3.1. The related maximum shear stresses at the *right edge* and in the *spew-fillet* are reduced to approximately 40% and 60% respectively (Figure 5.27(a)) and the maximum through-thickness stress is reduced to 60% (Figure 5.27(b)). No significant variations are observed when the elastic modulus is reduced from 1% (40 MPa) to 0.1% (4 MPa), both lead to almost constant shear distribution and low through-thickness stresses. The shear distribution is almost constant from an adhesive to adherend Young's modulus of 5% (200 MPa).

It is difficult to directly link the adhesive to adherend modulus ratio to its corresponding joint strength since failure criteria include not only the high stresses but also the two correction factors (see

Section 5.2.5). These depend on the stress-distribution shapes and are explicitly defined for extreme cases only (very stiff adhesives and very flexible adhesives, Vallée 2004). Nevertheless, to obtain some indication of the effect of the adhesive to adherend modulus ratio on the joint strength, different high stresses could be compared, particularly the maximum shear stress at the right edge and in the spew-fillet (Figure 5.26(a)) and the maximum through-thickness stress at the right edge (in tension) (Figure 5.26(b)). To facilitate comparison, these stresses were divided by the average shear stress value (5 MPa for a 100 kN load) calculated with Eq. 5.1. Figure 5.27 shows the maximum stress variation with the adhesive to adherend modulus ratio. As for joint stiffness, the symbols located on the abscissa represent the adhesives used in the experimental study. The EP adhesive layer ( $E_{\text{adhesive}}/E_{\text{adherend}}=12.7\%$ ) exhibits high stresses unlike the ADP adhesive (0.2%, elastic behavior).

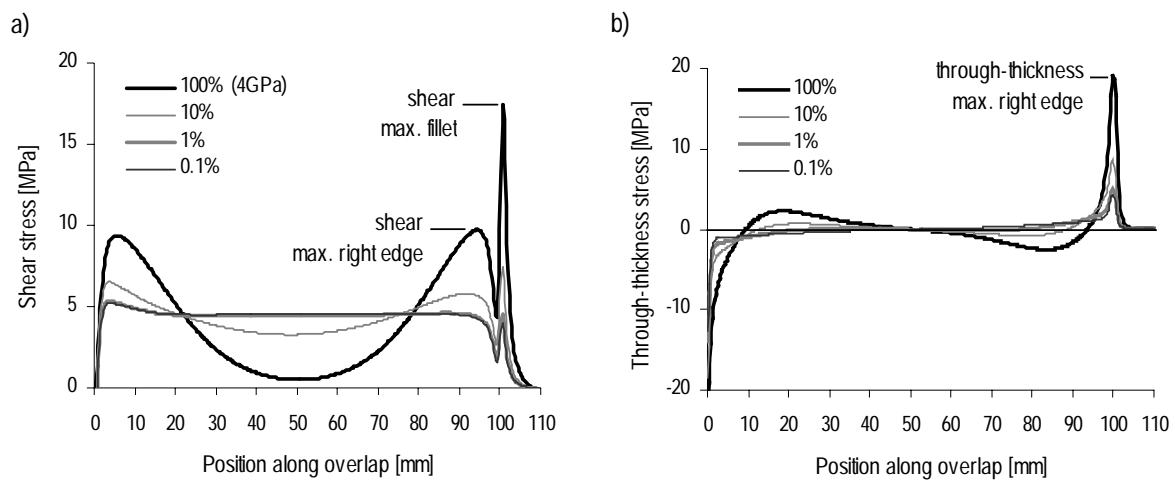


Figure 5.26: Effect of adhesive elastic modulus on (a) shear and (b) through-thickness stress distribution at failure line (0.5 mm inside 10 mm laminate) at 100 kN (100 mm overlap length joints)

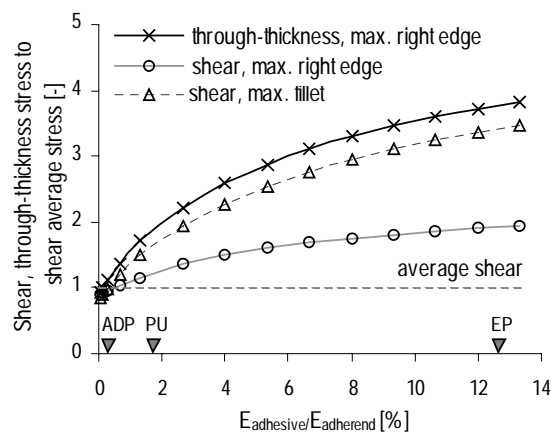


Figure 5.27: Effect of adhesive to adherend modulus ratio on maximum shear and through-thickness stresses to shear average stress at failure line (0.5 mm inside 10 mm laminate) (100 mm overlap length joints)

Another interesting point is the minimum to maximum shear stress ratio, which influences the creep deformation and thus the adhesive's long-term behavior (see Section 2.3.4.1). Hart-Smith's design philosophy (1987) claims that the joint should comprise a moderately-loaded adhesive region in the

middle to resist creep deformation. For this reason he recommended limiting the minimum adhesive shear strain. Nevertheless, no scientific basis exists for setting a minimum adhesive shear strain or stress and research must be undertaken to investigate this. When developing the PABST program (Primary Adhesively Bonded Structure Technology), Hart-Smith suggested limiting the minimum shear stress to 10% of the maximum shear stress at the ultimate load level.

An analysis of the minimum to maximum shear stress ratio with the adhesive to adherend modulus ratio was carried out but no limits were fixed. These depend on the adhesive's specific creep properties and the stress-state level. Figure 5.28 (a) shows the shear distribution at the adhesive centerline for a tensile load of 100 kN with four different adhesive elastic moduli. The two maximum stresses were located at the edges and the minimum stress at the center of the overlap. The average of the two minimum to maximum shear stress ratios was approximately 4% for the reference elastic modulus (4 GPa) and it increased to 49% when the elastic modulus was reduced by a factor of 10 (400 MPa). No significant variations were observed when the elastic modulus was reduced from 1% (40 MPa) to 0.1% (4 MPa); both led to an almost constant shear stress distribution and a minimum to maximum shear stress ratio close to 100%. Figure 5.28(b) illustrates the minimum to maximum shear stress ratio, taking both maximum values into account, as a function of the adhesive to adherend modulus ratio. The average of both ratios is also indicated. The curve decreases asymptotically towards zero. The symbols located on the abscissa represent the adhesives used in the experimental study. The dashed line indicates the Hart-Smith's recommendation.

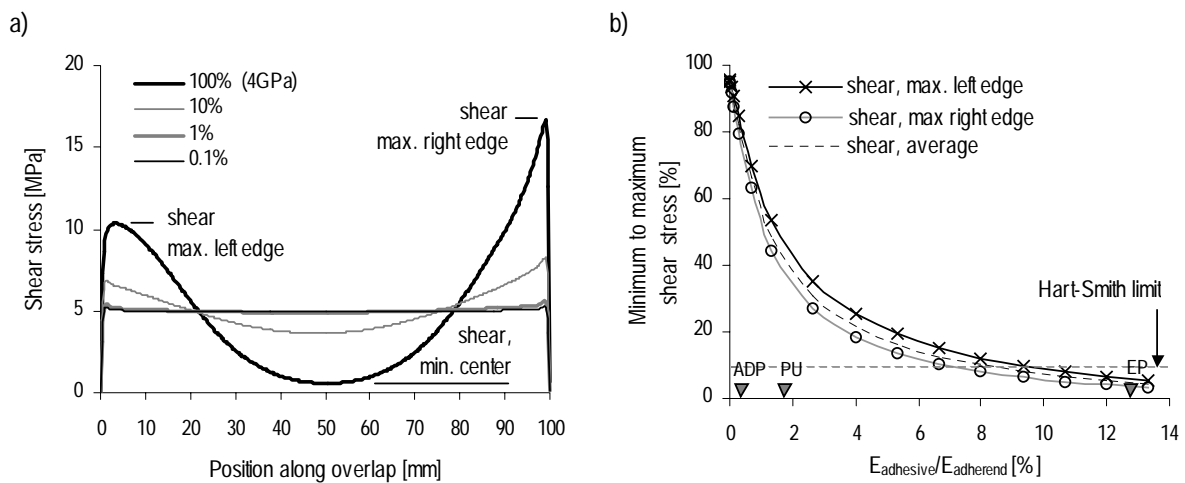


Figure 5.28: Effect of adhesive elastic modulus on (a) shear stress distribution at 100 kN, (b) minimum to maximum shear stress ratio at adhesive centerline (100 mm overlap length joints)

### 5.3.3 Behavior of Tailored Adhesive

Designing an appropriate bilinear adhesive behavior would be more advantageous than using a traditional structural and stiff epoxy adhesive. The bilinear behavior, illustrated in Figure 5.29, is defined by the elastic modulus,  $E_c$ , plastic modulus,  $E_p$ , elastic stress,  $f_c$ , and strain,  $\epsilon_c$ , and ultimate stress,  $f_u$ , and strain,  $\epsilon_u$ . Tailored adhesive design depends on the joint behavior required, which is

related to the required overall behavior of the structure to which the joint belongs. Nevertheless, some suggestions can be made concerning the adhesive moduli.

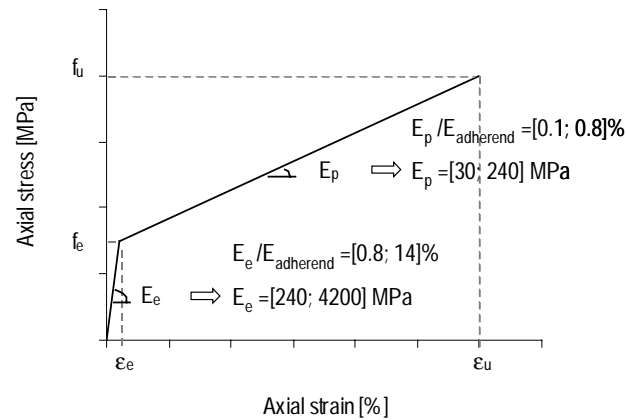


Figure 5.29: Adhesive bilinear behavior and moduli selection (100 mm overlap length joints)

The adhesive should produce a relatively stiff joint and limit creep deformation in the elastic phase ( $E_e$ ) governed by serviceability limit state (SLS). It should generate a flexible joint in the plastic phase ( $E_p$ ) to improve the failure limit state (FLS), increasing joint strength and ductility. Two intervals are recommended for each modulus, following results from Sections 5.3.1 and 5.3.2. Stiff joints are located between the *rigid joint* and the continuous *laminated* stiffness and flexible joints are located below the latter.

In the case of the double-lap with a 100 mm overlap length, the stiff-joint limit is reached for an adhesive to adherend modulus ratio of 0.8% (Figure 5.30(a)). Therefore, the adhesive to adherend modulus ratio should be situated in zone  $Z_e$ , within the range of 0.8% to 14%, corresponding to an elastic modulus within the range of 240 MPa to 4200 MPa. Additionally, creep deformation should be limited for long-term behavior. The adhesive to adherend modulus ratio should provide a lightly-loaded adhesive region in the middle of the overlap to regulate creep deformation. For this reason, a minimum to maximum shear stress ratio should be fixed according to adhesive's specific creep properties and stress state as indicated in Figure 5.31. This restriction would lead to an elastic modulus considerably higher than the minimum value (240 MPa) established in accordance with the joint stiffness.

Flexible joints are located below continuous *laminated* stiffness (Figure 5.24(b)). At this limit, the maximum through-thickness stress to average shear stress ratio is 1.5, and the maximum to average shear stress (right edge) ratio is approximately 1 (Figure 5.27); thus a constant shear distribution along the overlap length could be assumed. The adhesive to adherend modulus ratio should be located in zone  $Z_p$ , within the range of 0.1% to 0.8%, corresponding to a plastic modulus within the range of 30 MPa to 240 MPa. Figures 5.30(a) and (b) show the established limits of zones  $Z_e$  and  $Z_p$  and their effect on (a) joint stiffness and (b) maximum stresses. The tailored adhesive behavior is illustrated in Figure 5.29.

The elastic stress,  $f_e$ , defines the modulus transition and consequently the joint stiffness decrease. The initial joint stiffness should be reduced at the ultimate limit state (USL), and should not occur before the serviceability limit state (SLS). At this level, the maximum effective stress in the adhesive layer should be identical to the elastic stress. The ultimate stress,  $f_u$ , and strain,  $\epsilon_u$ , are defined by the required joint deformation. This is explained in detail in Chapter 6, which concerns the design of structures with ductile adhesive joints.

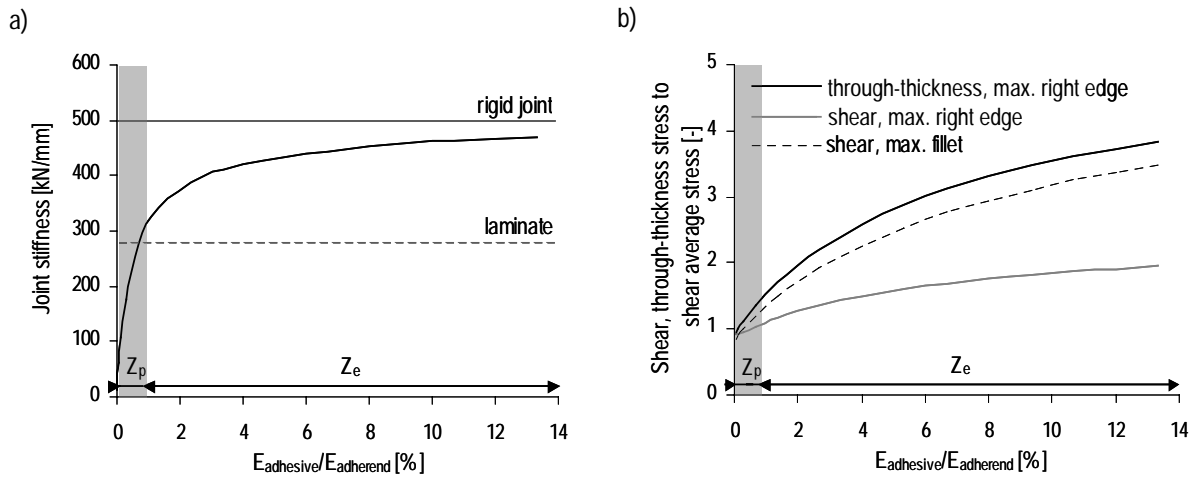


Figure 5.30: Adhesive to adherend modulus ratio choice (a) joint stiffness, (b) shear and through-thickness stress to average shear stress at failure line (0.5 mm inside 10 mm laminate) (100 mm overlap length joints)

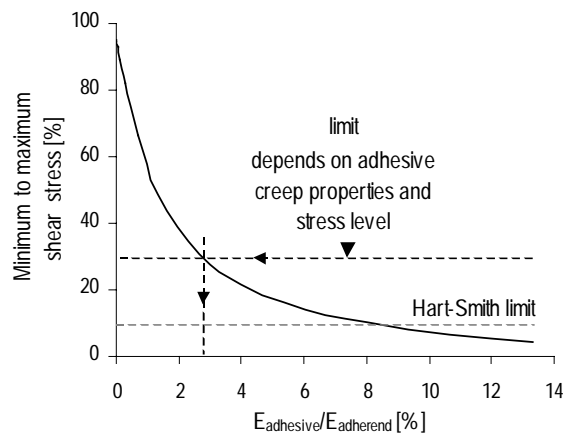


Figure 5.31: Adhesive elastic modulus choice - minimum to maximum shear stress ratio at adhesive centerline (average)

Increasing the laminate thickness and overlap length and maintaining the same adhesive thickness leads to the same curve shapes as illustrated in Figure 5.24 (see Section 6.4.1.1). The joint stiffness increases with the laminate thickness and overlap length increase. Thus the limit between the two zones would be lower than that proposed in the present study.

## 5.4 Concluding Remarks

This chapter includes the description and validation of the FE model developed for double-lap joints. The model was based on ANSYS plane elements and 2D non-linear analyses were performed. Validation of the FE model was carried out by comparison between the calculated results and experimental measurements of the specimen and joint elongations, axial stresses in laminate cross-sections and axial stresses along the overlap length. Subsequently the FE model was used for the calculation of shear and through-thickness stress distributions at the failure line and thus prediction of joint strength. Moreover the FE model was used to study the effect of the adhesive to adherend modulus ratio on joint stiffness and shear stress and through-thickness stress distributions at the bondline and failure line. The definition of stiff and flexible joints was presented in accordance with the joint stiffness. The following main conclusions can be drawn from this chapter:

- The developed numerical model, based on the finite element method, gives reliable predictions of joint stiffness and stress distributions along the failure line. The latter are needed to predict joint strength.
- The failure criterion for epoxy (EP) adhesive joints (Vallée 2004) is not accurate enough for predicting the joint strength with more flexible adhesives (PU and ADP) joint strength. Further investigations on correction factors need to be carried out.
- Joints are classified as stiff or flexible according to their stiffness, the limit corresponding to the continuous laminate (adherend to be connected) stiffness. The joint stiffnesses range between the rigid joint stiffness (theoretical double-lap joint without adhesive layer connecting adherends) and the continuous laminate stiffness. As the joint and adhesive behaviors are linked, adhesives are also classified as stiff or flexible.
- The use of an appropriate (well-designed) bilinear adhesive behavior is more advantageous than that of a traditional stiff structural epoxy adhesive. The adhesive should initially generate a relatively stiff joint and limit the creep deformation governed by serviceability limit state (elastic phase). Subsequently, it should develop into a flexible joint to improve the failure state, increasing joint strength and ductility (plastic phase). Upper and lower limits are proposed for the average modulus selection in both phases.
- An analytical method was developed for predicting joint elongation and stiffness when using ductile and soft adhesives (ADP) assuming that the adhesive deforms only and uniformly in shear and the adherends deform only in tension.

Further conclusions from the numerical calculations are:

- The results of stress calculations confirmed that the relatively stiff epoxy adhesive currently used led to high shear and through-thickness stress peaks at the edges of the overlap length. However, the flexible and highly non-linear ADP adhesive prevented the occurrence of high stress peaks. According to the FE calculated stress distributions and assuming an interlaminar

failure (excluding adhesion failure), the predicted strength of ADP joints with a 100 mm overlap length would be approximately 65% higher than that of EP joints.

- Adhesives behave differently in tension and compression. Nevertheless, a model including an identical behavior was developed for linear-elastic adhesives, considerably reducing the number of loading steps and calculation time. This simplification of average adhesive behavior is recommended for stiffness prediction. Adhesive tensile behavior is recommended for strength prediction since joint failure was initiated close to the adhesive-layer region loaded in shear and tension (positive through-thickness stresses).
- The effect of laminate Young's moduli was more significant on joint stiffness than on shear and through-thickness stress peaks.
- Meshing effects were greatest at the interface due to stress concentrations at the joint edges. However, since the location of the actual failure was inside the laminate and distant from the adhesive-layer edges, the failure line was less influenced by the discontinuity effects.
- The FE model's sensitivity to adhesive-layer geometry indicated that spew-fillets reduce peaks compared to the idealized joint. Nevertheless, the observed effect was much less than is indicated in the literature.





## 6 Design of FRP Structures with Ductile Adhesively-bonded Joints

The new concept of all-FRP structures achieves system ductility through the use of ductile adhesive joints and structural redundancy with statically indeterminate systems (see Section 3.1). The concept's feasibility was experimentally demonstrated on continuous beams with highly non-linear adhesively-bonded joints (see Section 4.3).

This chapter describes the design philosophy and explains the basis of adhesively-bonded joint design and appropriate adhesive selection. A design method is developed on the basis of both numerical and analytical model results for double-lap joints (see Sections 5.2 and 5.3). A case study is carried out on continuous beams with an adhesively-bonded joint at mid-support. The method for calculating the bonded connection behavior is finally validated through comparison with experimental results (see Section 4.3).

### 6.1 Design Philosophy

The widespread acceptance of all-FRP constructions by civil engineers is still hindered primarily by two material properties: the lack of ductility and difficulty in joining components. To overcome these two disadvantages of FRP structures, a new concept was developed for structures composed of brittle FRP components that provides system ductility through the use of ductile adhesive joints and system redundancy through statically indeterminate structures (see Section 3.2). Figure 6.1 illustrates the new FRP structure concept using the example of a continuous beam.

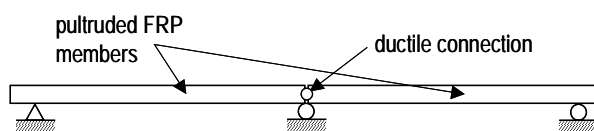


Figure 6.1: New concept of ductile and redundant FRP structure

Ductile joints are created by means of ductile adhesives. The actual non-linear behavior of adhesives can be characterized with an idealized elastoplastic or a bilinear model (see Section 2.3.5.1). The elastoplastic model is associated with ductility theory while the bilinear model is closer to the actual adhesive behavior. Figure 6.2(a) shows both adhesive models and the related behavior of the structure

illustrated in Figure 6.1, (b) hogging to sagging moment ratio-load ( $M^-/M^+-Q$ ), (c) load-deflection ( $Q-w$ ) and (d) hogging moment-rotation ( $M^--\theta$ ) curve. The subscripts (SLS, ULS, USS) indicate the corresponding state defined in Section 6.2. The proposed concept envisages adhesives with an initial elastic behavior sufficiently stiff to meet short- and long-term serviceability requirements. Beyond the service and ultimate loads, however, adhesive behavior should change and become plastic (elastoplastic model) or at least highly non-linear with a much lower stiffness (bilinear model). In the latter case, the behavior is hereafter designated as flexible and not ductile. Ductile or flexible joints can compensate for FRP components' lack of material ductility by providing ductility for the structural system (system ductility). The new concept entails creating elastoplastic connections similar to the plastic hinges developed in conventional ductile materials (steel and reinforced concrete).

Furthermore, elastoplastic or highly non-linear adhesive behavior prevents the occurrence of high stress peaks. Shear and through-thickness stresses are much more evenly distributed on the bonded surface, leading to less sensitive and more robust joints in relation to premature and unexpected failure.

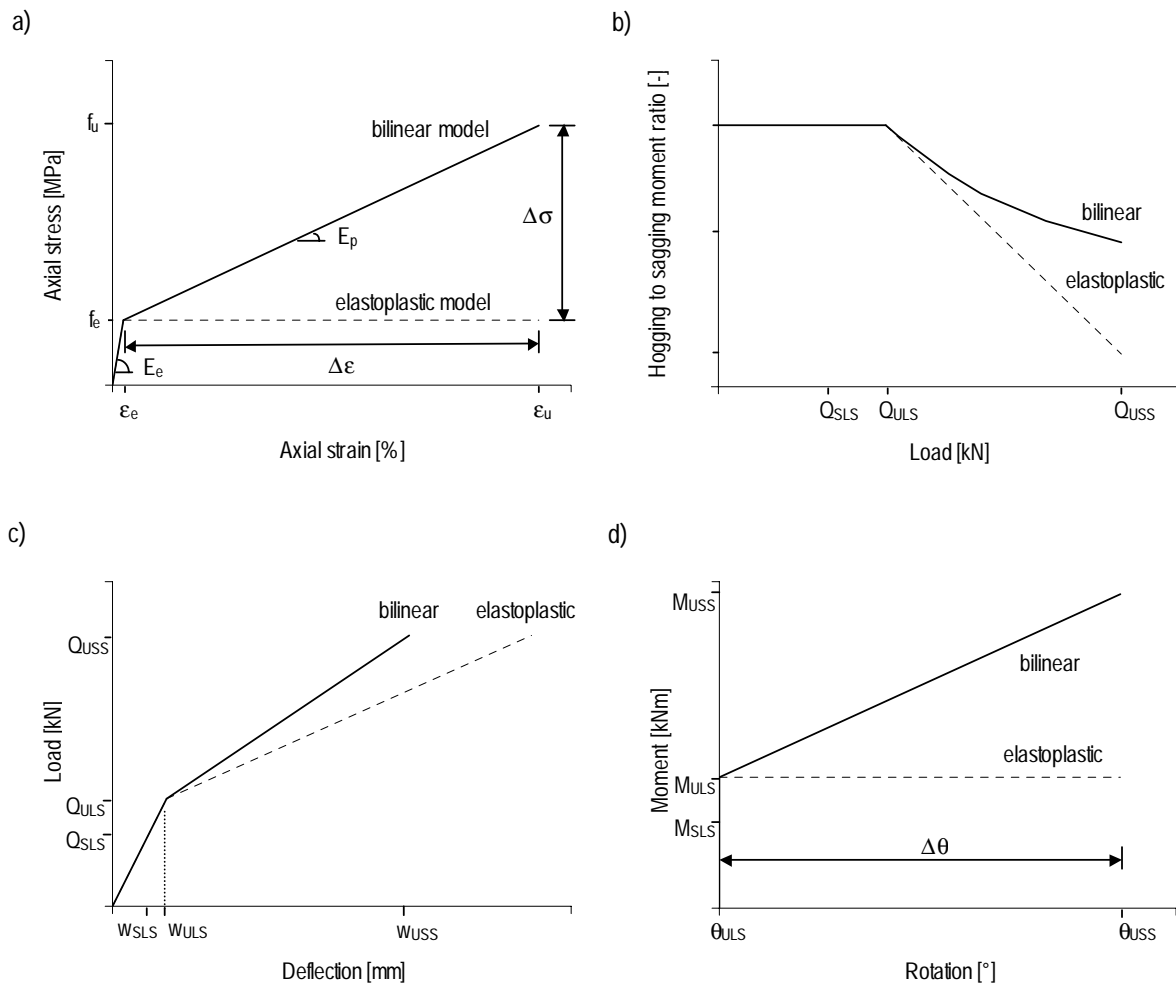


Figure 6.2: (a) Elastoplastic and bilinear adhesive models; Structural characteristics (b) hogging to sagging moment ratio-load, (c) load-deflection and (d) hogging moment-rotation curve

Since the surface preparation and adhesive application process are very demanding and no simple non-destructive quality control procedures exist, the unexpected failure of a bonded joint cannot be ruled out and must be considered in the structural concept. In the case of unexpected joint failure, the redundant system should provide alternative load paths to enable redistribution of section forces. Figure 6.3 illustrates bending moment distribution on two redundant systems before and after failure of the right joint. The static system modification and structure stiffness reduction lead to increased deflections and rotations, thus preventing structural collapse.

A procedure for designing the adhesively-bonded connection and selecting the appropriate adhesive to achieve the required structural behavior will be presented below. A concentrated load, as in experimental investigations (see Section 4.3), is considered in the present study.

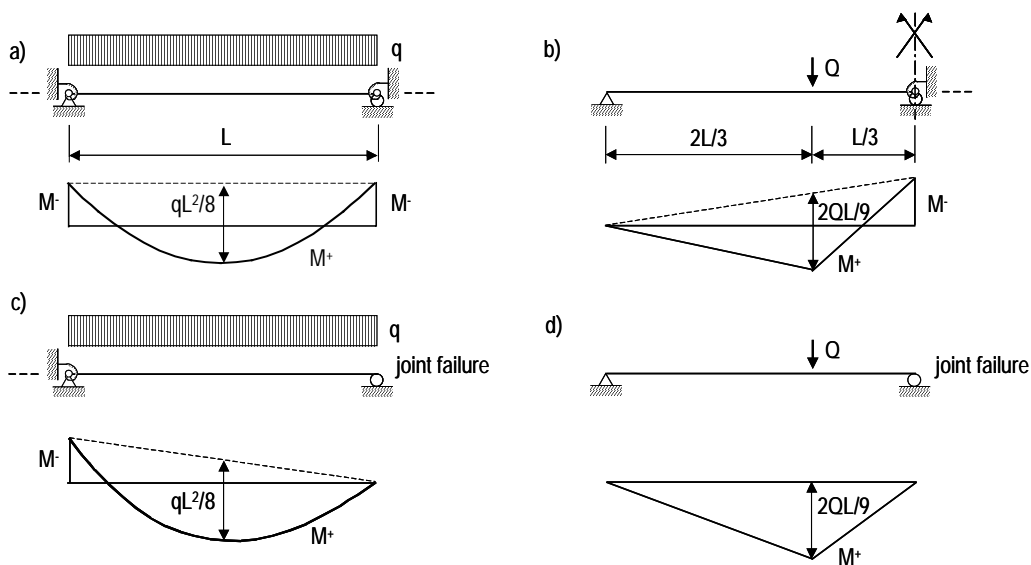


Figure 6.3: Multi-span beam or two-span beam with semi-rigid connection at mid-support before (a-b) and after (c-d) joint failure at the right connection

## 6.2 Limit States

Structural behavior is characterized by three limit states (Figure 6.2):

- serviceability limit state (SLS);
- ultimate limit state (ULS);
- ultimate strength state (USS).

### 6.2.1 Serviceability Limit State (SLS)

In the serviceability limit state, the designer must ensure that when everyday loads are imposed, the activities for which the structure was designed can still proceed. Serviceability limit states are

verifications that primarily ensure the “functioning of the structure or structural members under normal use” (Eurocode 0 (EN 1990 (2002))). To guarantee SLS, it is necessary to limit deformations, deflections, vibrations and oscillations. In this study, only deformations and deflections are discussed. A distinction should be made between:

- short-term deformations/deflections due to variable loads;
- long-term (time-dependent) deformations/deflections (creep) due to permanent loads.

The commonly used SLS criteria concern the vertical deflection limitation. Thus, the following conditions should be satisfied:

$$w_0 \leq w_{\text{lim,ST}} \quad (6.1)$$

$$w_\infty \leq w_{\text{lim,LT}} \quad (6.2)$$

where  $w_0$  and  $w_\infty$  are the calculated short- (variable actions) and long-term (permanent actions) deflections respectively and  $w_{\text{lim,ST}}$  and  $w_{\text{lim,LT}}$  are the short- and long-term deflection limits respectively. The SLS criteria are usually defined by the structure owner and established practice. Eurocode 1 (EN 1991 (2002)) concerning actions on structures recommend deflection limits which take into account the nature of the structure, finishes, partitions, fixings and function of the structure.

## 6.2.2 Ultimate Limit State (ULS)

In the ultimate limit state, the designer must ensure that the structure will not collapse under the most severe loading conditions that it can reasonably be expected to experience. Partial safety factors for actions and material properties are used to ensure that these loads can be carried safely. The structural design criteria to satisfy the ULS are based on the ultimate strength or stability limit in part of or the whole of the structure. The following condition should be satisfied:

$$S_d \leq R_d \quad (6.3)$$

where  $S_d$  is the design value of an applied internal force or bending moment and  $R_d$  is the corresponding design value of resistance. The former is determined for the relevant combination of actions. Nevertheless, only one concentrated load is considered in the present study (see Section 6.1), thus the design value of the applied internal force or bending moment is expressed according to Eq. 6.4, where  $Q_k$  is the characteristic concentrated action and  $\gamma_Q$  the corresponding partial safety factor. Eurocode 1 (EN 1991 (2002)) concerning actions on structures defines the actions and partial safety factors. The design value of the resistance related to an internal force or bending moment,  $R_d$ , is defined in the following section.

$$S_d = S(\gamma_Q \cdot Q_k) \quad (6.4)$$

### 6.2.3 Ultimate Strength State (USS)

As previously mentioned, the proposed structures consist of a series of FRP components and adhesively-bonded connections. Thus, structure failure could occur in either component. Design values of resistance are defined as follows:

$$R_{d,elem} = \frac{R_{k,elem}}{\gamma_{M,elem}} \quad (6.5)$$

$$R_{d,joint} = \frac{R_{k,joint}}{\gamma_{M,joint}} \quad (6.6)$$

where  $\gamma_{M,elem}$  and  $\gamma_{M,joint}$  are the partial safety factors of the FRP elements and joints and  $R_{k,elem}$  and  $R_{k,joint}$  are the characteristic values of FRP element resistance (corresponding to stability limit or ultimate strength) and joint resistance (corresponding to ultimate strength). The characteristic values of the resistance take the stochastic nature of the resistance into account; they are based on a normal probability distribution of the material property.

The required structure design should lead to an element failure and not a joint failure. Thus, the following condition linking FRP element and joint design resistances must be satisfied:

$$R_{d,joint} \geq R_{d,elem} \quad (6.7)$$

According to Eurocode 0 (EN 1990 (2002)), the partial safety factor,  $\gamma_M = \gamma_m \cdot \gamma_R$ , unites the partial safety factor of the material property,  $\gamma_m$ , and the resistance modeling,  $\gamma_R$ . The partial safety factor of the material,  $\gamma_m$ , considers the variability of material properties. In particular it does not consider variability caused by defects in the manufacture of the adhesive joint. The partial safety factor of the resistance modeling,  $\gamma_R$ , takes the design model reliability into account. According to Eurocomp (Clarke 1996), the partial safety factor  $\gamma_{M,elem}$  for composites materials depend on the derivation of the material properties, material production process, environmental effects and duration of loading. For pultruded elements, the partial factor  $\gamma_{M,joint}$  varies from 1.27 ( $=1.15 \times 1.1 \times 1.0 \times 1.0$ , for properties derived from tests) to 1.65 ( $=1.5 \times 1.1 \times 1.0 \times 1.0$ , for properties derived from theory) for short-term loading. Fiberline's manual (Anon 2003) indicates a value of 1.3 for short-term loading. Keller and Vallée (2005) estimated the partial factor corresponding to the pultruded element's strength in adhesively-bonded joints as  $\gamma_{M,joint}=1.34$ . For the partial factor of adhesives, Eurocomp (Clark 1996) takes into account the source of adhesive properties, adhesive application method, type of loading and environmental conditions. For short-term loading, it suggests  $\gamma_{M,adh}=1.56$  ( $=1.25 \times 1.25 \times 1.0 \times 1.0$ ) when properties are derived from tests at service conditions and 3.12 ( $=1.25 \times 1.25 \times 1.0 \times 2.0$ ) outwith service conditions.

### 6.3 Structural Behavior and Adhesive Choice

Figure 6.2(b-d) shows the behavior of a redundant structure with adhesively-bonded connections such as that illustrated in Figure 6.1. The structure can be classified according to its behavior as:

- phase I: a stiff structure, up to ULS;
- phase II: a flexible structure, from ULS to USS.

The structural behavior is related to joint stiffness. The latter is defined as stiff or flexible according to Figure 5.24(b) (page 119). Thus, a stiff adhesive joint characterizes stiff structural behavior and a flexible or ductile adhesive joint characterizes flexible structure behavior. The limit between these two joint stiffnesses is associated with the connected FRP member stiffness, assuming member continuity. As far as structural behavior is concerned, the transition from phase I to phase II should not occur before the SLS; nevertheless, for conservative reasons, an extension to ULS is recommended.

The structural behavior is mainly characterized by the bending-moment distribution. Thus, a certain distribution - a hogging to sagging moment ratio ( $M^-/M^+$ ) - must be defined in both phases. Figure 6.4 illustrates the bending-moment distribution of a two-span beam with an adhesively-bonded connection at mid-support in phase (a) I and (b) II. The hogging moment,  $M^-$ , is higher than the sagging moment,  $M^+$ , in phase I, while it becomes equal or lower in phase II. The choice of the bending-moment distribution will be explained below.

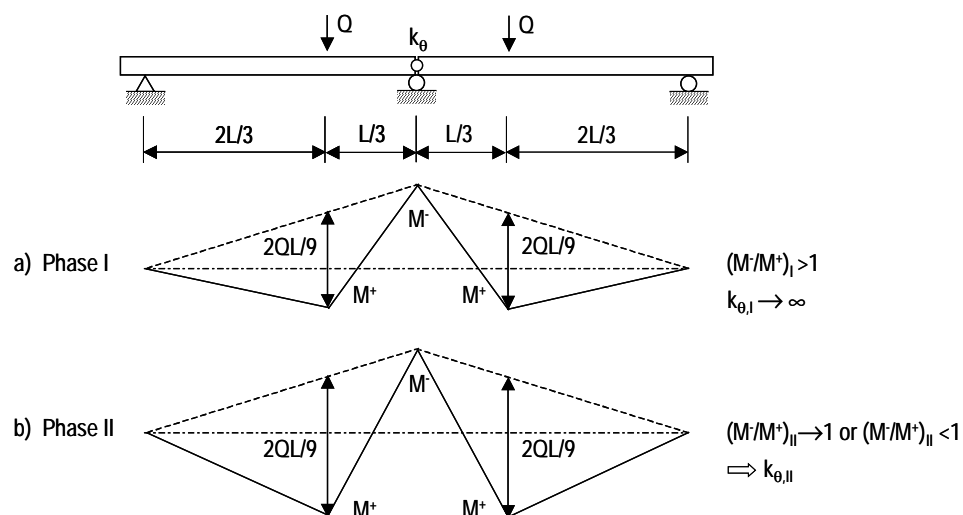


Figure 6.4: Bending-moment distribution (a) phase I: stiff behavior, (b) phase II: flexible behavior

Subsequently, a tailored adhesive behavior is designed according to the joint behavior required for the predefined overall structural behavior. Since a structure with a highly non-linear rather than an idealized elastoplastic behavior is preferred (see Section 2.2.4), an adhesive bilinear behavior is selected. The design procedure can be based on the adhesive tensile ( $\sigma$ - $\epsilon$ ) or shear ( $\tau$ - $\gamma$ ) bilinear behavior. The adhesive bilinear tensile behavior illustrated in Figure 6.2(a) is defined by the elastic modulus,  $E_e$ , plastic modulus,  $E_p$ , elastic stress,  $f_e$ , and strain,  $\epsilon_e$ , and ultimate strength,  $f_u$ , and strain,

$\epsilon_u$ . In the same way, the adhesive bilinear shear behavior is defined by the elastic shear modulus,  $G_e$ , plastic shear modulus,  $G_p$ , elastic shear stress,  $\tau_e$ , and strain,  $\gamma_e$ , and ultimate shear strength,  $\tau_u$ , and strain,  $\gamma_u$ . Both behaviors are related (see Section 6.3.2.3). For the following, the adhesive tensile bilinear behavior ( $\sigma$ - $\epsilon$ ) is chosen. The bilinear adhesive behavior is linked to the overall structural behavior. Figure 6.5 indicates the relationship between the structure and adhesive (tensile and shear) behaviors. The choice of the adhesive's characteristics will be described below.

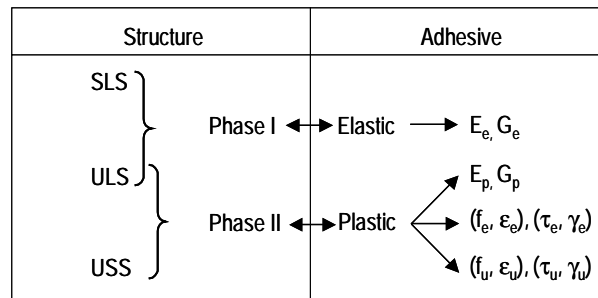


Figure 6.5: Relationship between structure and (tensile and shear) adhesive behavior

### 6.3.1 Phase I - Adhesive Choice

Phase I is governed by the SLS. As previously mentioned, vertical deflection limits are usually considered as SLS criteria. The conditions in Eqs. 6.1 and 6.2 should be satisfied for short- and long-term behavior respectively. Deflections are derived from shear deformation beam theory with semi-rigid connections (rotational stiffness,  $k_\theta$ , see Section 2.1.1). Shear deformations of FRP members are taken into account due to their low full-section shear modulus in the range of 3 to 5 GPa (Mottram 2004). Rotational stiffness ( $k_\theta$ ) depends on the joint configuration and the adhesive and adherend (connected and connecting elements) mechanical properties.

A stiff adhesively-bonded joint is required to limit rotations and deflections, creating a fixed (rigid) connection (rotational stiffness  $k_{\theta,1} \rightarrow \infty$ ) as well as local reinforcement of the structure, which means greatest stiffness than the FRP elements to be connected (see Section 5.3.1). Thus, the flexural ( $EI$ ) and shear ( $GKA$ ) stiffnesses along the reinforced length (joint-overlap length) increase compared to the connected members, especially the flexural stiffness (the components of flexural and shear stiffnesses are defined in Section 2.1.1). Nevertheless, the reinforcement effect on the bending-moment distribution is insignificant compared to the rigid-connection effect and can be ignored in the structural analyses (see Section 6.4.1.1). Thus in phase I, the connection is assumed to be rigid (fixed) (see Section 2.2.1). The beam illustrated in Figure 6.4, for instance, will be considered as a continuous beam in phase I.

The rigid-connection assumption must be guaranteed by the chosen adhesive. The adhesively-bonded joint is designed using a stiff adhesive in phase I. A similar investigation to that carried out on double-lap joints (see Section 5.3) can be conducted to evaluate the effect of adhesive to adherend modulus

ratio on the joint stiffness and adhesive shear-stress distribution. Subsequently, the adhesive elastic modulus,  $E_e$ , is selected according to the required joint stiffness (leading to a bending-moment distribution similar to that of a rigid connection) and creep deformation requirements (see Hart-Smith's recommendation in Section 5.3.2).

Long-term behavior includes the FRP element's and adhesive's creep deformations. The FRP elements (fibers and resin), consisting of relatively low-modulus glass fibers oriented in different directions, are expected to develop creep deformations that must be considered in the long-term behavior analysis. Normally the adhesive (resin) layer develops more significant creep deformations than the FRP elements. Few recommendations for adhesive creep deformation limits are available in literature. Hart-Smith's design philosophy (1987) claims that the joint should comprise a moderately loaded adhesive region in the middle to resist creep deformation. Thus, he recommended limiting the minimum adhesive shear stress and suggested a rather restrictive limit of 10% of maximum stress at ultimate load level. His recommendation has no scientific basis however and further investigation of creep deformation needs to be carried out and recommendations established.

Nevertheless, the creep effect on the type of adhesively-bonded joints considered here should not be a major problem for the following reasons:

- the adhesive layer is subjected to a low stress level due to permanent actions being normally very low compared to variable actions;
- the adhesive layer exhibits shear and through-thickness strain peaks at the edges and low strains in the middle since the selected adhesive elastic modulus should produce connections stiff enough to behave as rigid connections at SLS (agreeing with Hart-Smith's recommendations (1987)).

Experimental investigation of GFRP beams with flexible adhesively-bonded joints at mid-support (see Section 4.3.5) has shown that the stresses in the joints were small and creep deformations in the joints could be controlled due to the stiffness-governed design of GFRP beams.

Joint failure must be prevented in phases I and II (see Section 6.3.2.2). Stress distributions and correction factors included in the interlaminar failure criterion (Eq. 6.10 page 136) are different in the adhesive elastic and plastic phases. Thus, the stress level at the joint failure line must be verified at the ULS (corresponding to the adhesive elastic stress) and USS (corresponding to FRP element characteristic strength).

Using an idealized elastoplastic adhesive, the through-thickness and shear-stress distribution at the failure line exhibit peaks at joint edges in the elastic phase. Stress peaks are attenuated in the adhesive plastic phase with a more uniform stress distribution and the extension of plastic areas from the edges to the middle of the adhesive layer. Since the FRP element strength depends on the expansion of the stress surface (Figure 2.24(b) page 40), the correction factors used in the elastic-phase stress distribution are higher than those in the plastic phase. Thus joint failure in the adhesive elastic phase (structure phase I) is excluded when the joint remains intact at the FRP element characteristic



strength (structure phase II). The use of a bilinear adhesive leads to stress distributions in the plastic phase similar to an elastoplastic adhesive, with a slight stress increase at the joint edges. In the same way, joint failure in the adhesive elastic phase (structure phase I) is excluded.

### 6.3.2 Phase II - Adhesive Choice

Phase II is governed by a bending-moment distribution leading to failure in the FRP elements and the development of large deflections and rotations. From this bending-moment distribution, the adhesive plastic modulus,  $E_p$ , elastic stress and strain,  $f_e$  and  $\epsilon_e$ , and ultimate strength and strain,  $f_u$  and  $\epsilon_u$ , can be deduced. The procedure for selecting the adhesive mechanical properties is described below.

#### 6.3.2.1 Bending-moment Distribution

The bending-moment distribution in phase II should lead to large rotations and deflections, warning of failure. It is characterized by the hogging to sagging moment ratio,  $M^-/M^+$ , for the beam structure in Figure 6.4. A ratio close to 1 characterizes an equilibrated internal force distribution. The bending-moment distribution depends on the requirements concerning deformations and failure mode and is calculated for a static system consisting of members connected by non-linear rotational springs formed by the adhesively-bonded joints. The stiffness of the spring or connection rotational stiffness,  $k_{\theta,II}$ , of the beam structure in Figure 6.4 is calculated as follows:

$$k_{\theta,II} = \frac{M^-}{\theta(E_p)} \quad (6.8)$$

where the rotation at mid-support is estimated from the FRP element and adhesive layer deformations as illustrated in Section 6.4.1.2 and thus depends on the adhesive plastic modulus,  $E_p$ .

#### 6.3.2.2 Structural Strength Prediction

Structural failure could occur either in the FRP elements or the adhesively-bonded connections. FRP elements usually fail due to instability problems in thin-walled cross-sections (Barbero et al. 1991, Zureick and Shih 1998) and the adhesively-bonded joints usually exhibit an interlaminar failure (fiber-tear-failure) in the adherends (beam flanges or covering laminates), due to their low through-thickness strength. The required structural design should lead to an element failure and not a joint failure. Thus the condition in Eq. 6.7 linking the FRP element and joint design resistances (defined in Eqs. 6.5 and 6.6) must be satisfied. Since the partial safety factors for material resistances  $\gamma_{M,elem}$  and  $\gamma_{M,joint}$  are different, Eq. 6.7 becomes:

$$R_{k,joint} \geq \frac{\gamma_{M,joint}}{\gamma_{M,elem}} \cdot R_{k,elem} \quad (6.9)$$

The stress level at the joint failure line must be verified to ensure that joint remains intact (no failure). The stress level can be predicted using the interlaminar failure criterion developed by Vallée (2004) (see Section 2.3.6.2) integrating a shear and through-thickness stress interaction (Eq. 6.10). The shear and through-thickness strengths,  $\tau_{xy,u}$  and  $\sigma_{y,u}$ , included in Vallée's failure criterion, should be replaced by characteristic shear and through-thickness strengths,  $\tau_{xy,k}$  and  $\sigma_{y,k}$ , which are the 5% fractile of strength values. Nevertheless, to simplify the notation, the "k" subscript related to the FRP and adhesive "characteristic" values (moduli, stresses and strains) is not indicated. Thus, the stress level at the joint failure line remains:

$$f_{\text{joint}} = \left( \frac{\tau_{xy}}{\kappa_{\tau} \cdot \tau_{xy,u}} \right)^2 + \left( \frac{\sigma_y}{\kappa_{\sigma} \cdot \sigma_{y,u}} \right)^2 \leq 1 \quad (6.10)$$

### 6.3.2.3 Adhesive Choice

A flexible adhesively-bonded joint is required for the development of large rotations, increasing structural ductility and/or deformability (see Section 3.1). Moreover, an almost constant shear-stress distribution and low through-thickness stresses should develop at the overlap edges (see Section 5.3.2). The connection rotation depends on adherend axial and adhesive shear deformations. Assuming constant shear-stress distribution along the overlap length, joint elongation and thus connection rotation can be easily estimated (see Section 6.4.1.2). Thus, the choice of adhesive plastic modulus,  $E_p$ , depends on the required bending-moment distribution in phase II as expressed by Eq. 6.8.

The required rotation capacity of the connection,  $\Delta\theta$ , is defined at the USS, for the elements' characteristic resistance,  $R_{k,\text{elem}}$  (Figure 6.2(d)). The rotation in phase I is disregarded since the connection is assumed to be rigid. Subsequently, the corresponding tensile strain,  $\Delta\varepsilon$ , and stress,  $\Delta\sigma$ , can be estimated (Figure 6.2(a)). These depend on the adhesive plastic modulus,  $E_p$ , and the elements' characteristic resistance,  $R_{k,\text{elem}}$ . The adhesive elastic stress,  $f_e$ , reached at the ULS, linked to the design value of the applied internal force or bending moment,  $S_d$ , is related to ultimate strength,  $f_u$ , and stress variation,  $\Delta\sigma$ , as follows (Figure 6.2(a)):

$$f_u = f_e \cdot \max \left( \frac{R_{k,\text{elem}}}{S_d}, \gamma_{M,\text{adh}} \right) \quad (6.11)$$

$$f_u = f_e + \Delta\sigma \quad (6.12)$$

Since the tensile stress-strain ( $\sigma$ - $\varepsilon$ ) and shear ( $\tau$ - $\gamma$ ) curves are linked, an identical selection procedure could be applied for the latter. Various von-Mises modified functions, including the volumetric component of stresses characteristic of polymers, have been developed for adhesives (see Section 2.3.4.2) but they require various tensile, compressive and shear mechanical properties, which are usually unknown. Thus, when only the tensile or shear behavior is available, the von-Mises criterion, disregarding the volumetric component of stresses, can be employed, resulting in the

relationships expressed in Eqs. 2.6 and 2.7 (pages 36-37). The shear plastic modulus,  $G_p$ , and tensile plastic modulus,  $E_p$ , are linked according to Eq. (6.13) where  $\nu$  is the adhesive Poisson's ratio.

$$G_p = \frac{E_p}{2 \cdot (1 + \nu)} \quad (6.13)$$

### 6.3.2.4 Robustness and Energy Factors

As mentioned in Section 2.2.3.4, the structural safety analysis should include the strength and deformability capacities. Both characteristics are incorporated into the robustness factor,  $\mu_{\text{robustness}}$ , defined in Eq. 2.5 (van Erp (2001) see Section 2.2.3.4). In the present study, the ultimate strength state (USS) replaces the ultimate state, thus the robustness factor becomes the product of the USS to the SLS deflection ratio and the USS to SLS bending moment ratio (Eq. 6.14). At the SLS, the design value of the applied internal force or bending moment,  $S_d$ , is calculated for the design action,  $Q_d$ , which is identical to the characteristic value of the action,  $Q_k$ , since its partial safety factor is taken as  $\gamma_Q=1$ .

$$\mu_{\text{robustness}} = \frac{w_{\text{USS}}}{w_{\text{SLS}}} \cdot \frac{M_{\text{USS}}}{M_{\text{SLS}}} = \frac{w(R_{k,\text{elem}})}{w(S(Q_k))} \cdot \frac{M(R_{k,\text{elem}})}{M(S(Q_k))} \quad (6.14)$$

The robustness factor,  $\mu_{\text{robustness}}$ , should be higher than a certain limit. Van Erp (2001) indicated that the robustness factor of reinforced concrete and steel beams is approximately 20 and that of FRP is between 16 and 25. In traditional FRP beam structures such as simple and continuous beams, disregarding beam structures developed in the present study, strength and deformability factors (van Erp (2001) see Section 2.2.3.4) are identical due to the linear-elastic behavior of the material and thus the robustness factor can also be interpreted as the USS to SLS energy ratio.

A robustness and safety factor based on the absorbed energy seems more appropriate to all kinds of structural behavior and materials than deformability and strength capacities and follows the tendency of researchers when defining a ductility index (Naaman and Jeong (1995), Grace and Sayed (1998) see Section 2.2.3.2). Thus a new energy factor is proposed as follows:

$$\mu'_{\text{energy}} = \frac{E_{\text{USS}}}{E_{\text{SLS}}} = \frac{E(R_{k,\text{elem}})}{E(S(Q_k))} \quad (6.15)$$

## 6.4 Design Example: Bonded Pultruded Beams

A continuous beam over two spans with an adhesively-bonded connection at mid-support was analysed when subjected to concentrated loads at one third of the span length ( $L=3600$  mm) from mid-support (Figure 6.4). The static system is identical to that investigated experimentally in Section 4.3. The semi-rigid connection was composed of two adhesively-bonded strap joints in the top and bottom flanges. Firstly, different adhesive behaviors were defined in accordance with the

adhesively-bonded design previously developed and according to the overall structural behavior required. Secondly, measurements from the experimental investigation were compared to predictions made according to the adhesively-bonded design and ADP adhesive properties. The long-term behavior is not analyzed in this example although some remarks concerning creep deformation are made.

## 6.4.1 Adhesive Selection

### 6.4.1.1 Phase I

In phase I, the connection was assumed to behave like an ideal rigid connection (Figure 6.6), and the beam as a continuous beam. The beam behavior, especially the bending-moment distribution and deflections, was estimated using the beam theory including shear deformations and assuming a rigid connection. The beam was characterized by the flexural ( $EI$ ) and shear ( $GKA$ ) rigidities, which comprise the full-section elastic modulus ( $E=30$  GPa), moment of inertia ( $I=96.4 \times 10^6$  mm<sup>4</sup>), full-section shear modulus ( $G=3$  GPa), shear coefficient ( $K=0.38$ ) and cross-sectional area ( $A=11.0 \times 10^3$  mm<sup>2</sup>) (see Section 4.3.5.6). The established admissible short-term deflection to span ratio ( $w_{lim,ST}/L$ ) at the SLS was  $1/400$  ( $w_{lim,ST}=9$  mm). The condition in Eq. 6.1 was satisfied for a maximum load level of 58 kN. The hogging to sagging moment ratio was  $M^-/M^+=1.67$ .

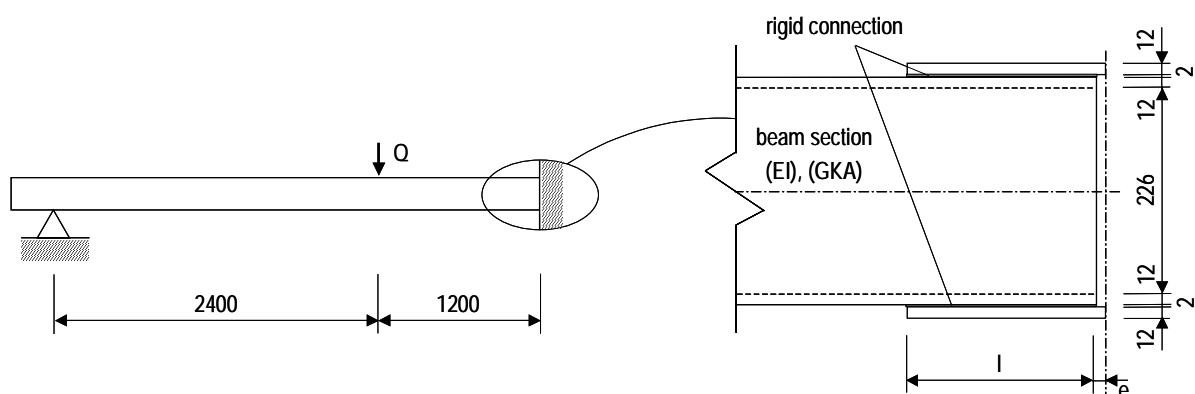


Figure 6.6: Semi-rigid simply-supported beam - phase I: rigid connection

The adhesive should develop a stiff connection, close to the assumed rigid connection, and limit creep deformations in the first phase. As in Section 5.3.1, an investigation was conducted to evaluate the influence of the adhesive to adherend modulus ratio,  $E_{adhesive}/E_{adherends}$ , on joint stiffness and bondline stress distribution in order to select the appropriate adhesive elastic modulus ( $E_{adhesive}=E_c$ ). The beam flanges were connected with two adhesively-bonded strap joints (cover-plates). The top and bottom strap joints exhibited similar behavior to double-lap joints loaded in tension and compression respectively. The cover-plate replaced the outer laminate and the beam flange, the inner laminate. The upper flange was loaded in tension while the cover-plate was also subjected to bending due to its

eccentricity. Thus, the FE double-lap joint model described in Section 5.2 could be used for this study, modifying the adherends' longitudinal Young's modulus ( $E_{\text{adherend}}=E_x=30$  GPa). The analyzed joint had a 100/200/300 mm overlap length,  $l$ , and a 2 mm adhesive thickness,  $t_a$ . The modeled adhesive was linear-elastic and characterized by an elastic modulus,  $E_e$ , since identical behavior in tension and compression was assumed. Calculations were carried out for a series of twelve elastic moduli (100%-0.1%). The elastic modulus reference value (100%) corresponds to 4 GPa, characterizing structural epoxy adhesives commonly used for bonded applications (Flemming and Siegfried 2003, Michaeli et al. 1998).

Figure 6.7 illustrates the strap-joint stiffness related to the adhesive to adherend modulus ratio for the three overlap lengths ( $l=100/200/300$ mm). The joint stiffness was calculated as defined in Eq. 4.6 (page 68). The two additional horizontal lines are the rigid joint and the adherends (beam flange and cover-plate) stiffnesses. The rigid joint represents a theoretical double-lap joint without an adhesive layer connecting adherends (Figure 5.25(a) page 119). Its stiffness was also calculated with the joint's FE model, by simply removing the adhesive layer. The rigid joint was obviously stiffer than bonded joints. The adherend stiffness was calculated as in Eq. 5.7 (page 115). The joint stiffness of the 100 mm overlap length was higher than that of the others, which seems to contradict the logical assumption that increasing overlap length leads to an increase in joint stiffness. This is due to the joint stiffness definition, the load per joint elongation. Calculating joint stiffness as the load per average axial strain along the overlap would lead to a stiffness increase when the overlap is increased.

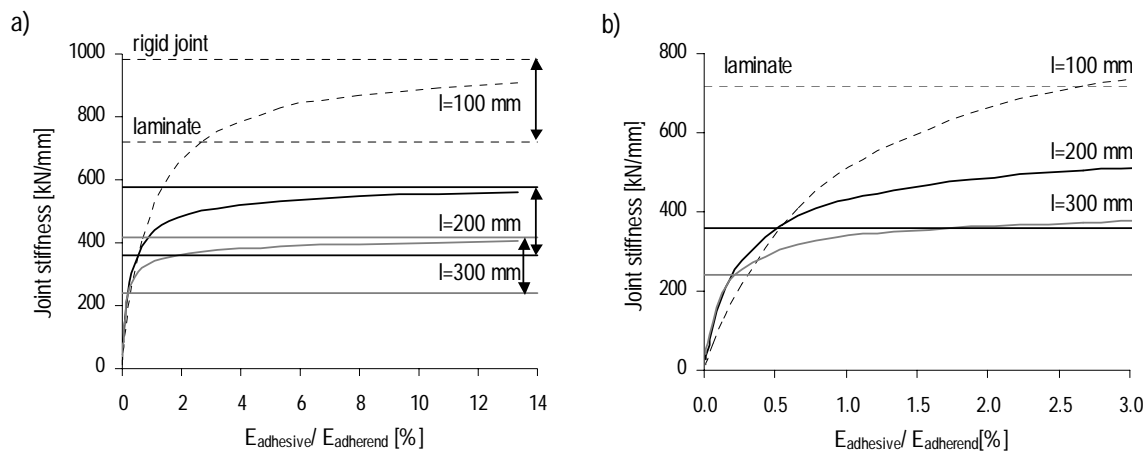


Figure 6.7: Adhesive to adherend modulus ratio effect on double-lap joint stiffness for 100/200/300 mm overlap lengths (a) global view including rigid joint and laminate stiffnesses, (b) zoom area including laminate stiffness

The curves indicating the variation of strap-joint stiffness according to the adhesive to adherend modulus ratio have a logarithmic shape. They are located between two asymptotic lines, the vertical axis (joint stiffness) and the horizontal line corresponding to the rigid joint. Joints can be classified according to their stiffness as stiff or flexible (see Section 5.3.1). The area between rigid joint stiffness and adherend stiffness delimits stiff joints and the area below defines flexible joints. Figure 6.7(b) focuses on the flexible joint limits (the intersection between the joint (curve) and the laminate

stiffness (straight line). The limit between the two behaviors occurs at the adhesive to adherend modulus ratios of 2.7%, 0.5% and 0.2% for the 100/200/300 mm overlap lengths respectively. Thus, the adhesive elastic modulus,  $E_e$ , must be selected within the range of 810 ( $=2.7\% \times 30$  GPa) to 4000 MPa ( $=13.3\% \times 30$  GPa), 150 to 4000 MPa and 60 to 4000 MPa. More flexible adhesives can be used when joint overlap length is increased. Nevertheless to guarantee SLS long-term requirements, creep deformations should be limited and thus higher elastic moduli than the minimum values previously established are recommended.

As mentioned in Section 6.3.1, a stiff connection creates a fixed connection (no rotation at mid-support) as well as local reinforcement of the structure. For the studied beam, the reinforcement effect of a rigid connection (the theoretical connection without an adhesive layer connecting adherends, assuring entire adherence between flanges and cover-plates) led to a hogging to sagging moment ratio increase from 8% ( $l=100$  mm) to 24% ( $l=300$  mm) compared to that of the continuous beam, inducing a deflection decrease from 4% ( $l=100$  mm) to 10% ( $l=300$  mm) at the loading point. Moreover, the actual adhesively-bonded connection stiffness was lower than that of a rigid connection and the reinforcement effect on bending-moment distribution and deflections was consequently lower. Thus the reinforcement effect on bending-moment distribution and deflections was insignificant compared to the fixed-connection effect and could be ignored in structural analyses.

#### 6.4.1.2 Phase II

Phase II is governed by a defined bending-moment distribution leading to failure in the FRP elements and the development of large deflections and rotations. The bending-moment distribution,  $M^-/M^+$ , defines the required adhesive tensile plastic modulus,  $E_p$ , and shear plastic modulus,  $G_p$ , according to Section 6.3.2.1 and tensile elastic stress and strain,  $f_e$  and  $\epsilon_e$ , and tensile ultimate strength and strain,  $f_u$  and  $\epsilon_u$ , according to Section 6.3.2.3. Afterward, it was verified that the joint had not failed. The strap-joint overlap length,  $l$ , is also selected according to the required structural behavior and adhesive plastic modulus,  $E_p$ .

##### Bending-moment distribution

The bending-moment distribution was calculated for a static system consisting of a simple beam with an elastic rotational spring at one support, formed by the adhesive joints, subjected to a concentrated load at one third of span length (Figure 6.8). The spring stiffness corresponds to the connection stiffness. The connection stiffness,  $k_{\theta,II}$ , depends on the mid-support rotation, which is related to adhesive shear plastic modulus,  $G_p$ , and thus tensile plastic modulus,  $E_p$ .

Based on the assumption of a constant shear-stress distribution in the adhesive bond, an estimate of the resulting angles of rotation,  $\theta$ , at mid-support at failure can be made. The constant shear stress,  $\tau_{xy}$ , was calculated from the axial force,  $F$ , in the beam flange while the axial force,  $F$ , resulting from the negative bending moment over the mid-support,  $M^-$ , in accordance with Eq. 6.16 (Figure 6.8).

$$\tau_{xy}(\text{adhesive}) = \frac{F}{l \cdot b} = \frac{M}{(h-t) \cdot l \cdot b} \quad (6.16)$$

Due to the eccentricity of the cover-plate, small secondary moments occurred in the cover-plate, which were however ignored in the elongation calculation. The maximum negative moment was used and any decrease along the length of the overlap was disregarded. The denominator in Eq. 6.16 comprises the section height,  $h=240$  mm, flange thickness of the beam,  $t=12$  mm, section width,  $b=240$  mm, and overlap length,  $l=100/200/300$  mm. The laminate thickness is identical to the beam flange thickness,  $t$ . The elongation of the upper overlap,  $\Delta l$ , is composed of the shear deformations of the adhesive layer,  $\Delta l_1$ , and the axial elongation of the cover plate and top flange,  $\Delta l_2$ , as follows:

$$\Delta l = \Delta l_1 + \Delta l_2 \quad (6.17)$$

$$\Delta l_1 = t_a \cdot \gamma(G_p) \quad (6.18)$$

$$\Delta l_2 = \frac{M \cdot l}{(h-t) \cdot t \cdot b \cdot E} \quad (6.19)$$

where  $t_a$  is the adhesive layer thickness (2 mm),  $\gamma$  is the shear strain of the adhesive depending on the shear plastic modulus,  $G_p$ , and  $E$  is the full-section elastic modulus (30 GPa). The adhesive shear plastic modulus,  $G_p$ , and tensile plastic modulus,  $E_p$ , are linked as in Eq. 6.13. From these elongations, the total rotation angle over the mid-support,  $\theta$  (Figure 6.8), was estimated as follows:

$$\theta = \arctan \frac{2 \cdot \Delta l}{h + t_a} \quad (6.20)$$

and the connection stiffness,  $k_{\theta,II}$ , according to Eq. 6.8. Subsequently, the bending-moment distribution of the beam structure was derived from the shear deformation beam theory, taking into account the connection stiffness.

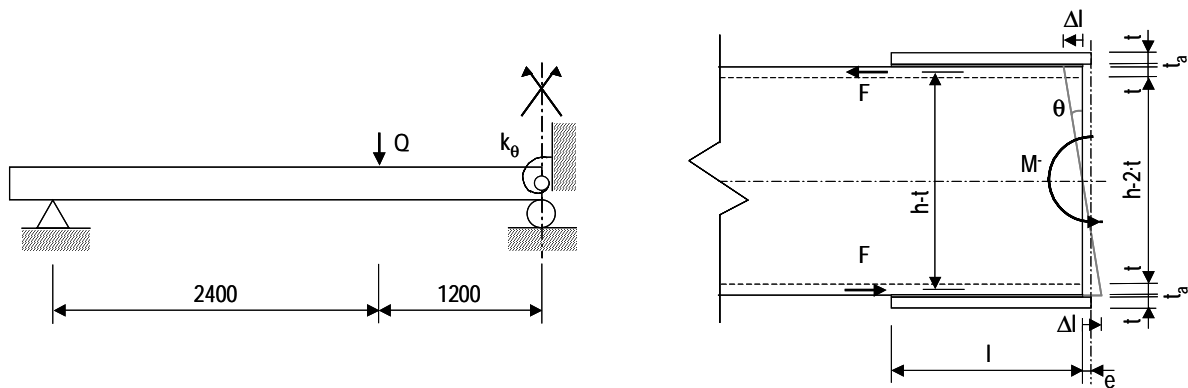


Figure 6.8: Semi-rigid simply-supported beam - phase II: elastic connection

### Structural strength prediction

The FRP element failure should occur before joint failure. Johnson (1985) proposed a simplified design analysis to predict failure loads of FRP thin-walled square-section beams under transverse loading. He considered five different failure modes: compression face buckling, tension material failure, compression material failure, shear material failure and shear buckling in the side wall. He assumed that since there is no interaction between bending and shear failures, beam strength would be the lower of the two. Mottram (1991) evaluated Johnson's simplified design analysis for different span lengths and section thicknesses and concluded that it was not applicable to short spans. Johnson's analysis was used to predict the failure of experimentally investigated bonded beams but the results were not conclusive for the following reasons:

- occurrence of actual interaction between bending and shear failures;
- lack of reliable material mechanical properties included in the failure prediction formulae;
- weak areas in the corners of the beam section – at the location of the overlap ends of the combined mats.

Due to the complexity of the phenomenon, beam strength prediction was not an integral part of the present study. The beam ultimate strength was therefore assumed to be the same as in the experimental investigation, approximately 180 kN (related to  $R_{k,elem}$ ). However, it must be noted that ultimate strength is related to bending-moment distribution and thus varies with connection stiffness.

As element failure should occur before joint failure, the joint stress level at the failure line must be verified at the load level indicated in Eq. 6.9. The failure line was assumed to be located at 0.5 mm depth in the flange as observed in the double-lap joint experimental investigations (see Section 4.2.4) with laminates similar to those of the beams and cover-plates (fiber architecture and material properties). The interlaminar failure criterion including the through-thickness and shear stress interaction described in Section 2.3.6.2 was used for this purpose. The condition in Eq. 6.10 must be satisfied along the overlap length, where the factor  $\kappa_t = 1$  for constant shear distribution and the factor  $\kappa_\sigma = 1.0-1.5$  for linear through-thickness distribution and low stress peaks (see Section 5.2.5). Two  $\kappa_\sigma$  values are considered since they are not accurately defined for the relevant stress distribution; thus two maximum interlaminar failure criterion values are calculated. The maximum interlaminar failure criterion value was reached at the edge subjected to tensile through-thickness stress (left edge).

Shear and through-thickness stress distributions are represented in Figure 6.9(b-c). A stress estimation similar to that used for the ADP double-lap joints was performed (see Section 5.2.6). The uniform shear-stress distribution was derived from the distribution at the interface, calculated with Eq. 6.16, assuming a parabolic shear stress distribution through the 12 mm beam flange (see Section 5.2.3). Thus the constant shear stress was defined as:

$$\tau_{xy}(\text{failure line}) = \left( \frac{t - t_f}{t} \right)^2 \cdot \tau_{xy}(\text{adhesive}) \quad (6.21)$$



where  $t_f$  is failure-line depth (0.5 mm) and  $t$  is twice beam-flange thickness (24 mm=2x12 mm).

Due to the eccentricity of the cover-plate, small secondary moments,  $M'$ , occurred, inducing through-thickness stresses. As for the ADP double-lap joints, the through-thickness stress distribution is assumed zero at the middle of the overlap, 30 mm inwards from both edges, and bilinear towards the ends (see Section 5.2.6). FE calculations (see Section 5.2.3) enabled the stress distribution to be established and showed that maximum stress,  $\sigma_{y,1}$ , depends on stress  $\sigma_{y,2}$  as indicated in Eq. 6.22.

$$\sigma_{y,1}(\text{failure line}) = 2.5 \cdot \sigma_{y,2}(\text{failure line}) \quad (6.22)$$

These edge stresses were calculated from the bending moment,  $M'$ , resulting from the axial load,  $F$ , and its eccentricity,  $c=8.5$  mm (=0.5+2+6 mm) (Figure 6.9(a)), according to Eq. 6.23. The same bending moment should be obtained by summing the moments of forces  $F_1$  and  $F_2$  about axis  $z$ , using the lever arms  $x_1$  and  $x_2$  (Figure 6.9(d)), as indicated in Eq. 6.24). The forces  $F_1$  and  $F_2$  are the resultants of stresses and are estimated using Eq. 6.25 where  $b$  is joint width (240 mm).

$$M' = F \cdot c \quad (6.23)$$

$$M' = F_1 \cdot x_1 + F_2 \cdot x_2 \quad (6.24)$$

$$M' = \left( \int_0^3 \sigma_y(x) \cdot b \cdot dx \right) \cdot x_1 + \left( \int_3^{30} \sigma_y(x) \cdot b \cdot dx \right) \cdot x_2 \quad (6.25)$$

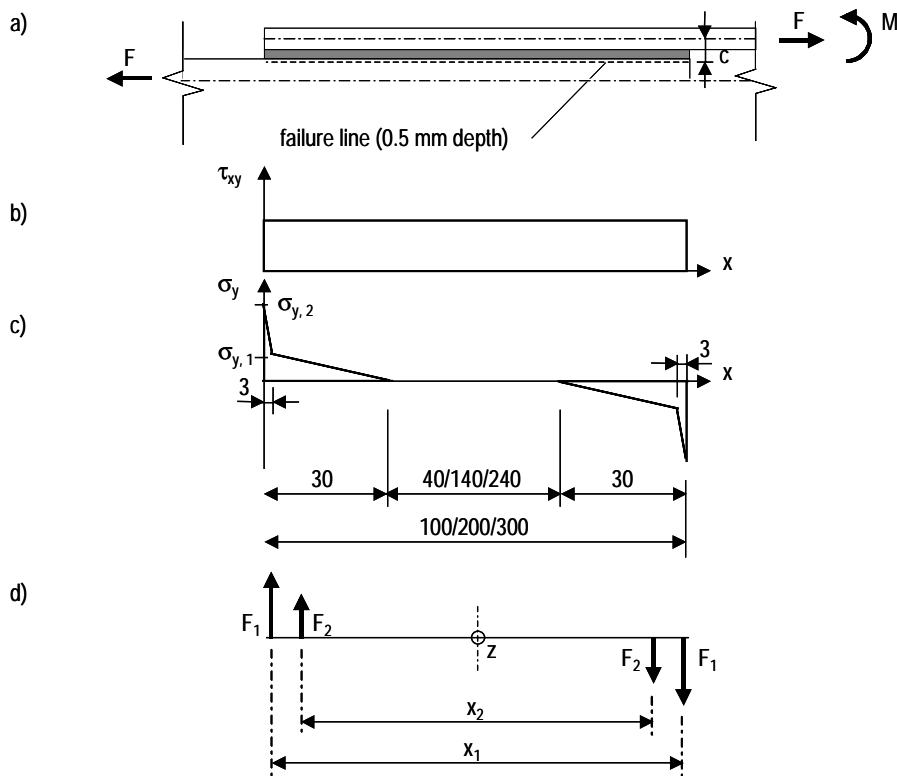


Figure 6.9: Strap joint (a) internal loads; (b) Shear and (c) through-thickness stress distribution along the adhesively-bonded failure line; (d) Resultants of through-thickness stresses

### Adhesive choice

Nine beams were analyzed, varying the strap-joint overlap length ( $l=100/200/300\text{mm}$ ) and adhesive tensile plastic modulus ( $E_p=10/15/20\text{ MPa}$ ). The related shear plastic modulus  $G_p$  was estimated from the plastic moduli,  $E_p$ , and the Poisson's ratio,  $\nu$ , as in Eq. 6.13, assuming  $\nu=0.40$  (average value for adhesives from the *Guide to the Structural Use of Adhesives* (Institution of Structural Engineers 1999)). As previously mentioned, the beam strength was reached at 180 kN (related to  $R_{k,elem}$ ). Assumptions concerning safety factors were made. The load safety factor was  $\gamma_k=1.5$ , according to Eurocode 0 (EN 1990 (2002)) concerning the basis of structural design, the material safety factors were  $\gamma_{M,elem}=1.27$ ,  $\gamma_{M,joint}=1.34$  and  $\gamma_{M,adh}=1.56$  (when properties are derived from tests at service conditions and 3.12 outwith service conditions) according to Eurocomp (Clarke 1996), Keller and Vallée (2005) and discussion in Section 6.2.3.

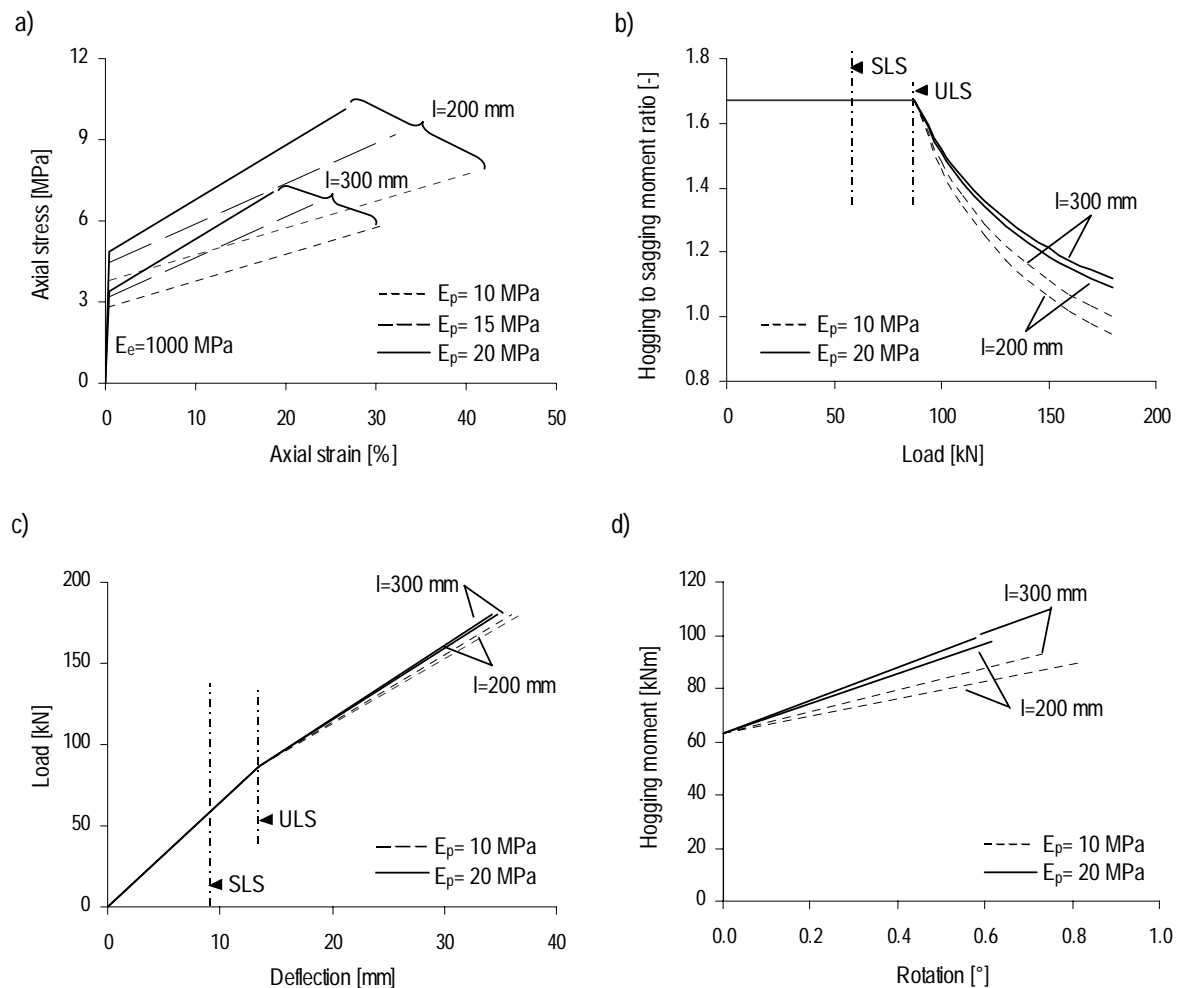


Figure 6.10: (a) Adhesive tensile behavior for different overlap lengths ( $l=200/300\text{ mm}$ ) and adhesive plastic moduli ( $E_p=10/15/20\text{ MPa}$ ); Estimation of (b) hogging to sagging moment ratio-load curve, (c) load-deflection curve and (d) hogging moment-rotation curve at mid-support for different overlap lengths ( $l=200/300\text{ mm}$ ) and adhesive plastic moduli ( $E_p=10/20\text{ MPa}$ )

Figure 6.10 (a) shows adhesive tensile behavior and Table 6.1 the resulting mechanical properties. Figure 6.10 illustrates the (b) hogging to sagging moment ratio-load ( $M^-/M^+-Q$ ) curve, (c) load-deflection ( $Q-w$ ) curve and (d) hogging moment-rotation ( $M^--\theta$ ) curve of beams with 200/300 mm overlap lengths. The initial rigid connection led to an identical hogging to sagging moment ratio and deflection to the continuous beam up to the ULS. No rotations were observed at mid-support up to ULS. Subsequently, the mid-support rotations developed leading to a decrease in the hogging to sagging moment ratio and an increase in the deflection.

The rotation capacity of the connection at the ultimate strength,  $\Delta\theta$ , is calculated following the procedure for estimating bending-moment distribution (Eqs. 6.16-6.19 and 6.20). Subsequently, the corresponding strain,  $\Delta\varepsilon$ , was estimated using Eq. 2.7 (page 37) where  $\Delta\gamma$  is defined by Eq. 6.18 and the corresponding stress,  $\Delta\sigma$ , by Eq. 6.26. Both depend on the adhesive plastic modulus ( $E_p$ ) and the element characteristic resistance,  $R_{k,elem}$ .

$$\Delta\sigma = E_p \cdot \Delta\varepsilon \quad (6.26)$$

The adhesive elastic stress,  $f_e$ , and ultimate strength,  $f_u$ , were defined according to Eqs. 6.11 and 6.12. An adhesive elastic modulus,  $E_e$ , of 1000 MPa was chosen from intervals based on numerical investigation of the adhesive to adherend modulus ratio's effect on joint stiffness ( $E_e > 810$  MPa for  $l=100$  mm,  $E_e > 150$  MPa for  $l=200$  mm,  $E_e > 60$  MPa for  $l=300$  mm, see Section 6.4.1.1). Table 6.1 lists these values for three overlap lengths ( $l=100/200/300$  mm) and three adhesive plastic moduli ( $E_p=10/15/20$  MPa). Cases where joint failure occurred before FRP element failure, as shown in the following, are also included.

Table 6.1: Ultimate rotation (at 180 kN) and tailored adhesive mechanical properties for different overlap lengths ( $l=100/200/300$  mm) and adhesive plastic moduli ( $E_p=10/15/20$  MPa)

Overlap length [mm]	Plastic modulus [MPa]	$\theta$ [°]	$\Delta\varepsilon$ [%]	$\Delta\sigma$ [MPa]	$f_e$ [MPa]	$f_u$ [MPa]
100	10	1.04	0.57	5.68	5.3	11.0
100	15	0.92	0.49	7.28	6.8	14.1
100	20	0.78	0.42	8.44	7.9	16.3
200	10	0.81	0.40	4.04	3.8	7.8
200	15	0.69	0.32	4.76	4.5	9.2
200	20	0.62	0.26	5.23	4.9	10.1
300	10	0.73	0.30	3.01	2.8	5.8
300	15	0.64	0.23	3.40	3.2	6.6
300	20	0.58	0.18	3.64	3.4	7.0

Table 6.2 lists the calculated ultimate hogging moment,  $M^-$ , its corresponding flange axial force,  $F$ , shear stress,  $\tau_{xy}$ , through-thickness stress,  $\sigma_y$ , and maximum value of stress interaction at failure line (Eq. 6.10),  $\eta = \max(f_{joint})$ , for three overlap lengths ( $l=100/200/300$  mm) and three adhesive plastic moduli ( $E_p=10/15/20$  MPa). Short adhesively-bonded joints ( $l=100$  mm) failed ( $\eta > 1$ ) while no failure was predicted in large joints (300 mm) at the loading point ( $\eta < 1$ ). Since the through-thickness correction factor,  $\kappa_\sigma$ , is not accurately defined, no conclusion concerning the 200 mm overlap length

joints could be drawn;  $\kappa_{\sigma}=1.5$  guaranteed that the joint would not fail while  $\kappa_{\sigma}=1$  indicated the opposite.

Table 6.2: *Ultimate hogging moment (at 180 kN) and its corresponding flange axial force, shear and through-thickness stresses and interaction formula at failure line for different overlap lengths ( $l=100/200/300$  mm) and adhesive plastic moduli ( $E_p=10/15/20$  MPa)*

Overlap length [mm]	Plastic modulus [MPa]	M [kNm]	F [kN]	$\tau_{xy}$ [MPa]	$\sigma_y$ [MPa]	$\eta$ [-]
100	10	74	323	12.9	18.6	5.9-2.9
100	15	79	346	13.8	19.9	6.7-3.3
100	20	83	363	14.5	20.9	7.4-3.6
200	10	81	357	7.1	9.3	1.5-0.7
200	15	86	378	7.6	9.8	1.7-0.8
200	20	89	392	7.8	10.2	1.8-0.9
300	10	85	371	4.9	6.2	0.7-0.3
300	15	88	388	5.2	6.5	0.7-0.4
300	20	91	398	5.3	6.7	0.8-0.4

Thus the longer overlap length ( $l=300$  mm) is required to assure FRP element failure before joint failure. As for the adhesive choice, the three plastic moduli ( $E_p=10/15/20$  MPa) are appropriate; the adhesive selection should also take into account the robustness and energy factors. Although, in practice, the defined adhesive behaviors are certainly not commercially available, they nonetheless facilitate appropriate adhesive selection.

### Robustness and energy factors

The robustness factor,  $\mu_{\text{robustness}}$ , was calculated according to Eq. 6.14. Table 6.3 summarizes the USS to SLS deflection ratio,  $w_{\text{USS}}/w_{\text{SLS}}$ , USS to SLS bending moment ratio,  $M_{\text{USS}}/M_{\text{SLS}}$ , and robustness factor,  $\mu_{\text{robustness}}$ , for different overlap lengths ( $l=100/200/300$  mm) and adhesive plastic moduli ( $E_p=10/15/20$  MPa). Cases where the overlap lengths induced joint failure before FRP element failure are also included. Figure 6.11 shows the hogging moment-deflection curve for different overlap lengths ( $l=200/300$  mm) and adhesive plastic moduli ( $E_p=10/20$  MPa). The robustness factor varies between 8.7 and 9.4 and increases when the overlap length and the adhesive plastic modulus increase, since the bending-moment increase is higher than the deflection decrease when connection stiffness is increased (via  $l$  or  $E_p$ ). Nevertheless, the variations are not pronounced (within one order of magnitude). The robustness factor values are lower than those indicated by van Erp (2001) for FRP simple beams (16-25).

The new energy factor,  $\mu'_{\text{energy}}$ , was calculated according to Eq. 6.15. Table 6.3 summarizes the SLS energy,  $E_{\text{SLS}}$ , USS energy,  $E_{\text{USS}}$ , and energy factor,  $\mu'_{\text{energy}}$ . As previously mentioned, the energy and robustness factors are identical in structures with linear behavior. Due to the non-linear behavior of the structure, the energy and robustness factors are different, the former varying between 11.4 and 12.2 and being higher than the latter. Nevertheless, as with the robustness factor, variations of the energy factor are not pronounced. The energy factor, contrary to the robustness factor, decreases

when the overlap length and the adhesive plastic modulus increase, since the USS energy decreases and the SLS energy remains constant when the connection stiffness is increased (via  $l$  or  $E_p$ ). It must be noted that an identical GFRP-element characteristic resistance ( $R_{k,elem}$ ) was assumed for all cases due to the lack of strength prediction. Thus, the improved characteristic resistance that accompanies increased connection stiffness (sagging moment decreases) was not taken into account in the calculation of the robustness and energy factors, which led to an underestimation of them both.

Concerning the adhesive choice, the three plastic moduli ( $E_p=10/15/20$  MPa) are appropriate since their corresponding robustness and energy factors are similar.

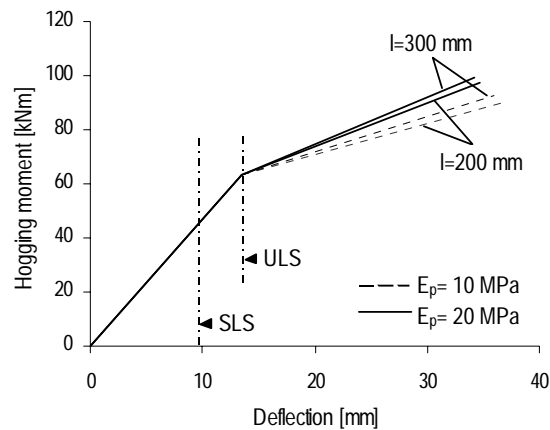


Figure 6.11: Estimation of hogging moment-deflection curve for different overlap lengths ( $l=200/300$  mm) and adhesive plastic moduli ( $E_p=10/20$  MPa)

Table 6.3: USS to SLS deflection ratio, USS to SLS bending moment ratio, robustness factor, energy at USS, energy at SLS, and USS to SLS energy ratio for different overlap lengths ( $l=100/200/300$  mm) and plastic moduli ( $E_p=10/15/20$  MPa)

Overlap length [mm]	Plastic modulus [MPa]	$w_{USS}/w_{SLS}$ [-]	$M_{USS}/M_{SLS}$ [-]	$\mu_{robustness}$ [-]	$E_{SLS}$ [kNmm]	$E_{USS}$ [kNmm]	$\mu^{energy}$ [-]
100	10	4.3	2.0	8.7	165	2012	12.2
100	15	4.2	2.1	9.0	165	1985	12.0
100	20	4.1	2.3	9.1	165	1954	11.8
200	10	4.1	2.2	9.1	165	1966	11.9
200	15	3.9	2.3	9.3	165	1929	11.7
200	20	3.9	2.4	9.4	165	1902	11.5
300	10	4.0	2.3	9.2	165	1937	11.7
300	15	3.9	2.4	9.3	165	1907	11.5
300	20	3.8	2.5	9.4	165	1884	11.4

## 6.4.2 Application to Experimental Beams

Measurements from the experimental investigation of two-span beams (see Section 4.3.5) were compared to estimations made according to the adhesively-bonded design procedure developed in Section 6.3 and incorporating the ADP adhesive properties (see Section 4.1.4) for validation. The measured material properties (moduli, stresses and strains) are used instead of the characteristic

material properties included in the design procedure. No partial safety factor was applied to load and resistance values. The static system consists of a continuous beam over two spans with an adhesively-bonded connection at mid-support subjected to a concentrated load at one third of span ( $L/3=1200$  mm) from mid-support (Figure 6.4). The tested beams were connected with two adhesively-bonded strap joints on the top and bottom flanges using the ADP adhesive. The strap joints had different overlap lengths,  $l$ :  $2 \times 100$  mm (PH3),  $2 \times 200$  mm (PH1 and PH2) and  $2 \times 300$  mm (PH4).

Axial strains measured in the joints showed a linear distribution along the overlap length during the loading, with the exception of small areas at the beginning and end (each approximately 5% of joint length, see Figure 4.30 (page 85)). Therefore, shear stresses in the adhesive layer were constant in the region of linear strain distribution for the ADP adhesive elastic and plastic phases. This was due to the low ADP adhesive's moduli ( $E_c=101$  MPa and  $E_p=14$  MPa, see Table 4.2 (page 60) compared to the adherends' modulus ( $E=30$  GPa, see Table 4.7 page 74). This agrees with the experimental (see Section 4.2.4.3) and numerical (see Section 5.2.2.4) results on ADP double-lap joints. Thus, the joint elongation could be estimated, assuming constant shear deformation in the adhesive elastic and plastic phases in accordance with Eq. 6.17 (page 141). Consequently, the rotation at mid-support (Eq. 6.20) and joint stiffness (Eq. 6.8) were calculated and the bending-moment distribution and deflections were estimated using Timoshenko's beam theory (including shear deformations).

The beam behavior was calculated directly from the adhesive's measured shear stress-strain curve. The ultimate strength was not estimated; it was assumed identical to measured ultimate strength. Figure 6.12 shows (a) the measured shear stress-strain curve of the ADP adhesive and the (b) calculated and measured hogging to sagging moment ratio-load ( $M^-/M^+-Q$ ), (c) load-deflection ( $Q-w$ ) and (d) hogging moment-rotation ( $M^--\theta$ ) curves of beams PH3 ( $l=100$  mm) and PH4 ( $l=300$  mm). The following remarks are also valid for beams PH1,2 ( $l=200$  mm).

The calculated and measured load-deflection curves match well until the stiffness decrease due to local buckling in the loading points observed during the experiments (see Section 4.3.5.3-5), whereas the calculated and measured moment-rotation curves differ. The connection rotational stiffnesses (curve slopes) are in agreement, while the reduction in connection rotational stiffness occurred at a higher load level with the calculated model than in experiments. This curve shift is the result of assumptions in the calculation method. The adhesive at the joint edges was also subjected to through-thickness stresses that were disregarded in the calculation method. Thus, the adhesive was not loaded in pure shear and plastified (it attained the elastic equivalent stress) before reaching the elastic shear strain. A similar shift was observed when comparing the analytical method for predicting the ADP double-lap joint behavior with FE-model calculations and experimental results (see Section 5.2.6.1). The differences were especially observed in beam PH3, with a short-overlap length ( $l=100$  mm), which experimentally exhibited a flexible behavior without the initial stiff behavior since the adhesive plastic phase was reached at low load levels.

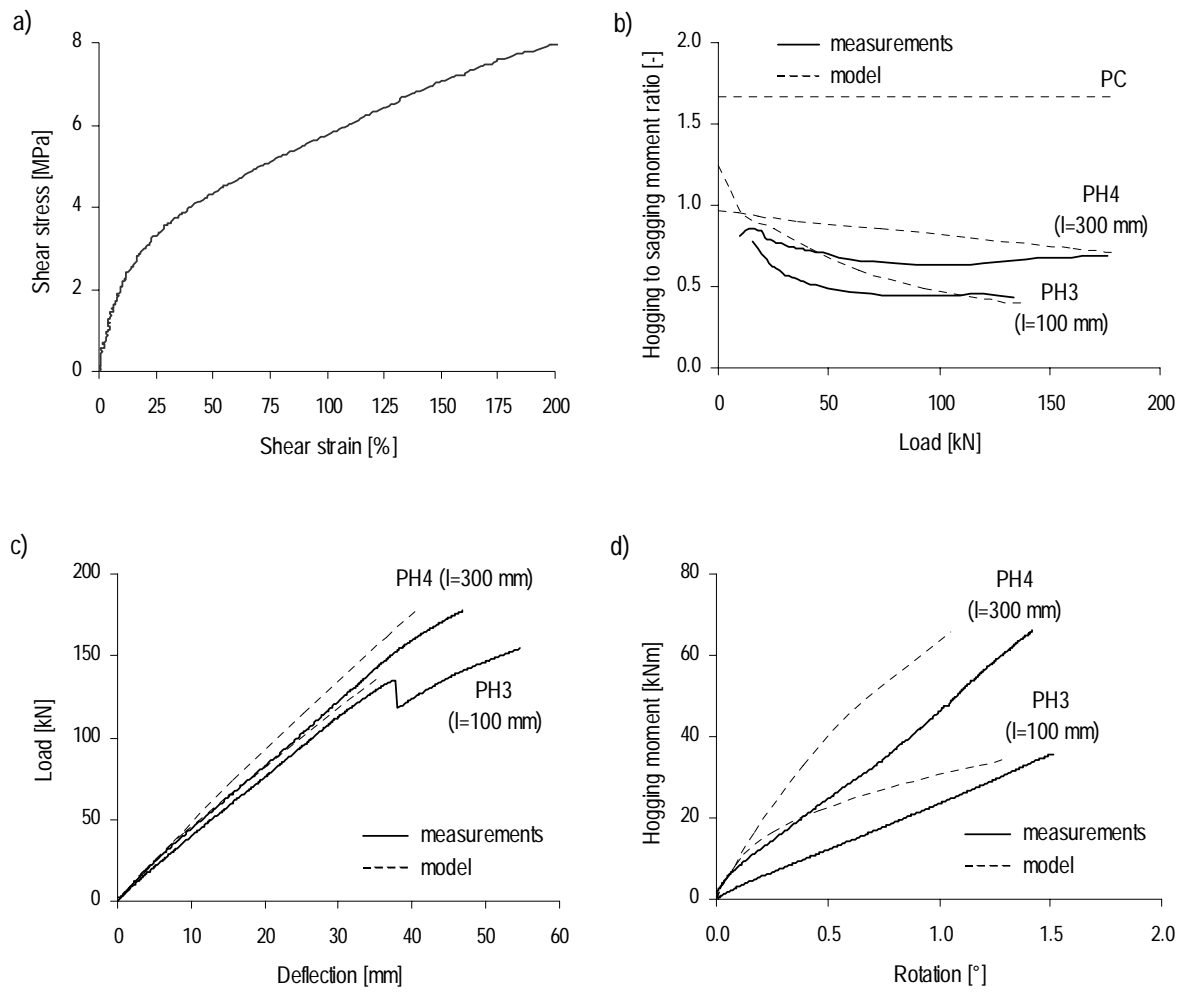


Figure 6.12: (a) ADP shear behavior; (b) Hogging to sagging moment ratio-load curve, (c) load-deflection curve and (d) hogging moment-rotation at mid-support; comparison of model calculations and measurements of beams PH3 ( $l=100$  mm) and PH4 ( $l=300$  mm)

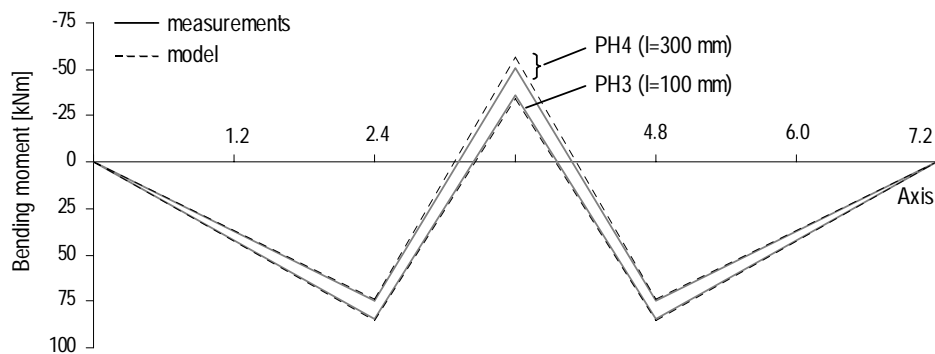


Figure 6.13: Bending-moment distributions (at 136 kN load per jack), comparison of model calculations and measurements for beams PH3 ( $l=100$  mm) and PH4 ( $l=300$  mm)

Redistribution of the moments from the support,  $M^-$ , to the loading-point regions,  $M^+$ , occurred in beams PH1-4 due to the non-linear behavior of the adhesive joint (Figure 4.32 page 86). The calculated and measured hogging to sagging moment ratio-load curves exhibited similar tendencies, particularly at higher load. Figure 6.13 compares the bending moment diagram based on model calculations with measurements of beams PH3 ( $l=100$  mm) and PH4 ( $l=300$  mm) at 136 kN per jack, corresponding to the lowest failure load of the experimental beams, and indicates their good agreement.

The redistribution effect was smaller than required since the ADP adhesive was initially too flexible. Figure 6.14(a) compares the ADP (continuous line) and tailored adhesive bilinear shear stress-strain for different overlap lengths ( $l=100/200/300$  mm) defined in Section 6.4.1, with an elastic modulus  $E_e=1000$  MPa and  $E_p=10$  MPa (dashed line, see Section 6.4.1). The shear behavior was derived from tensile behavior in accordance with Eqs. 2.6 and 2.7 (pages 36 and 37). Figure 6.14(b) shows their corresponding hogging to sagging moment ratio,  $M/M^+$ , evolution with load. Ideally (dashed line), the moment ratio should be constant up to the ULS load ( $1.5 \times 58$  kN=87 kN, SLS load: 58 kN), and then start to decrease.

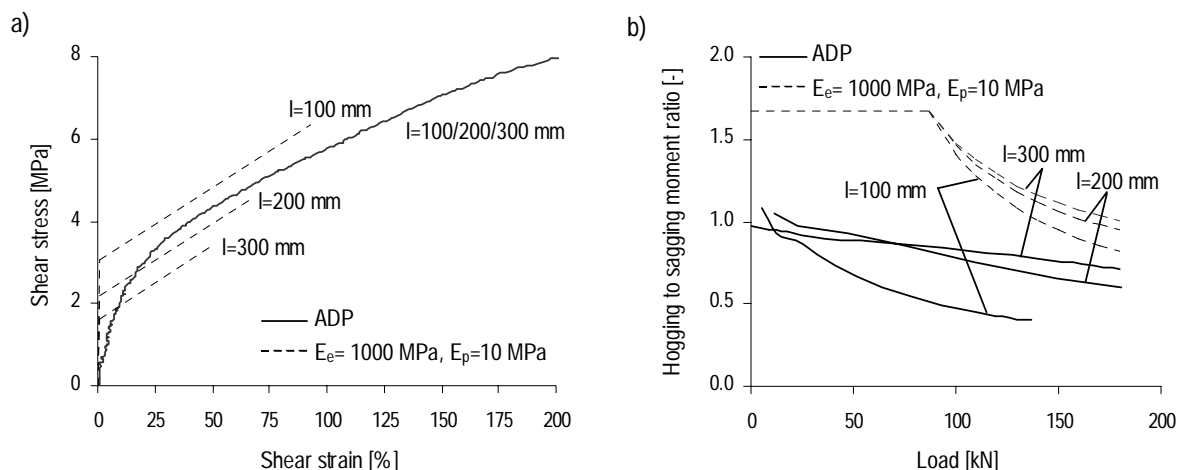


Figure 6.14: (a) ADP and tailored adhesive shear stress-strain for  $l=100/200/300$  mm, (b) calculated hogging to sagging moment ratio-load curve

The calculated rotation and hogging moment at mid-support at failure load (corresponding to FRP element resistance ( $l=200/300$  mm) or joint resistance ( $l=100$  mm)) are shown in Table 6.4, and are compared to measured values (Table 4.6 page 73). Calculated rotations are lower than measured rotations by between 13% and 28%. Despite the shift observed in the calculated and measured hogging moment-rotation curves, the calculated and measured rotations at failure are of the same magnitude. The variations from the “measured” moments at mid-support, calculated from the measured support reactions, are between -5% and +15%. The largest deviations from the calculated values were observed in beam PH2, which was tested at an elevated temperature, and beam PH4, with the longest overlap length. Beams PH1 and PH3 showed much better results (-5%, +6%).



Table 6.4: Estimation of the rotation angles and moments at mid-support at failure

Beams	$\tau$ [MPa]	$\gamma$ [%]	$\theta_{\text{calc}}$ [°]	$\theta_{\text{meas}}$ [°]	$\Delta\theta$ [%]	$M_{\text{calc}}$ [kNm]	$M_{\text{meas}}$ [kNm]	$\Delta M$ [%]
PH1 (l=200 mm)	5.7	1.0	1.3	1.5	-13	62	67	-5
PH2 (l=200 mm)	5.7	1.0	1.3	1.8	-28	62	53	+15
PH3 (l=100 mm)	6.2	1.2	1.2	1.5	-20	34	36	-6
PH4 (l=300 mm)	4.3	0.5	1.1	1.4	-21	71	66	+8

Table 6.5 shows the calculated ultimate moments at mid-support,  $M$ , and their corresponding flange axial force (Eq. 6.16),  $F$ , shear (Eq. 6.21),  $\tau_{xy}$ , and through-thickness stress (Eqs. 6.22-6.25),  $\sigma_y$ , and the maximum stress interaction value at the failure line (Eq. 6.10),  $\eta = \max(f_{\text{joint}})$ , for beams PH1-4. The characteristic shear and through-thickness strengths included in the interaction criterion are replaced by the shear and through-thickness strengths,  $\tau_{xy,u}$  and  $\sigma_{y,u}$ . The correction factors are  $\kappa_\tau = 1.0$  for constant shear distribution and factor  $\kappa_\sigma = 1.0-1.5$  for linear through-thickness distribution (see Section 5.2.5). Two values of  $\kappa_\sigma$  are considered since no value is accurately defined for the relevant stress distribution (see Section 5.2.5); thus two maximum interlaminar failure criterion values are calculated. The maximum value of the interlaminar failure criterion was reached at the edge subjected to the tensile through-thickness stress.

Table 6.5: Calculated ultimate moment at mid-support and its corresponding flange axial force, shear and through-thickness stresses and the maximum value of interaction formula at the failure line for beams PH1-4

Beams	$M_{\text{calc}}$ [kNm]	$F$ [kN]	$\tau_{xy}$ [MPa]	$\sigma_y$ [MPa]	$\eta$ [-]
PH1,2 (l=200 mm)	62	272	5.43	7.06	0.9-0.4
PH3 (l=100 mm)	34	149	5.96	8.59	1.3-0.6
PH4 (l=300 mm)	71	311	4.15	5.22	0.5-0.2

The long adhesively-bonded joints (l=200/300 mm) did not fail before the FRP elements ( $\eta < 1$ ), corresponding with experimental results, while short adhesively-bonded joints (l=100 mm) failed ( $\eta > 1$ ) when a through-thickness correction factor  $\kappa_\sigma = 1$  was assumed but did not fail with  $\kappa_\sigma = 1.5$ . The estimated joint failure agreed with experimental results on beam PH3, where joint failure occurred before final collapse. Nevertheless, as explained in Section 4.3.5.5, the experimental joint exhibited a mixed failure combining “light-fiber-tear” and “adhesion promoter to substrate” failure, due to inappropriate surface treatment or physical/chemical incompatibility, and did not exhibit the “fiber-tear” (interlaminar) failure assumed in joint-strength prediction. Thus no conclusion concerning the 100-mm overlap length joints could be drawn. Solving the adhesion problem could guarantee that the joint will not fail before the FRP beam as indicated in the calculations with  $\kappa_\sigma = 1.5$ . Use of the ADP adhesive leads to lower hogging moments than continuous beams and thus a lower stress level at the joint failure line, which explains why 200 mm strap joints do not fail in contrast to cases studied in Section 6.4.1. The robustness and energy factors of experimental beams

are not calculated since the initial phase (phase I) is too flexible compared to SLS requirements, and the transition phase (from phase I to II) occurs at a lower load level than expected, because the ADP was slightly too soft at the beginning.

## 6.5 Concluding Remarks

This chapter introduces the design philosophy of the developed all-FRP structure concept including system ductility through the use of ductile adhesive joints and structural redundancy with statically indeterminate systems. It includes the adhesively-bonded joint design procedure and adhesive mechanical properties selection based on the serviceability limit state and ultimate strength requirements. The procedure was initially illustrated by a case study of continuous beams with ductile adhesive joints and subsequently validated by an experimental investigation results on continuous beams with flexible adhesive joints. The following conclusions can be drawn from this chapter:

- The proposed concept envisages ductile and redundant structures with an initially stiff behavior to meet short- and long-term serviceability requirements and a flexible behavior exceeding the service and ultimate limit states. Since the structure's behavior is related to adhesively-bonded connection stiffness and consequently adhesive behavior, a ductile or at least highly non-linear adhesive behavior is appropriate.
- The flexible joints with ductile or highly non-linear adhesive characteristics brought about a favorable redistribution of internal and external forces in the redundant system.
- The required structure design must lead to FRP element failure rather than joint failure. Nevertheless, the unexpected failure of a bonded joint must be considered in the structural concept. When this occurs, the redundant system should provide alternative load paths to enable redistribution of section forces.
- The proposed concept provides both ductile (when FRP elements fail) and pseudo-ductile (when adhesively-bonded joints unexpectedly fail) structural behavior.
- The structure behavior is derived from Timoshenko's beam theory and the connections' rotational stiffness. Connections are assumed to be rigid (fixed) during the structure's stiffness phase while they exhibit low rotational stiffness in the structure's flexible phase. The rotational stiffness of the connection is estimated from the joint elongation assuming that the adhesive deforms only in shear and the adherends deform only in tension.
- The appropriate adhesive bilinear behavior is designed according to required structure behavior. The adhesive elastic modulus ( $E_c$ ) is selected according to the high joint stiffness and creep deformation requirements. The bending-moment distribution, leading to the pre-established failure mode and the development of large deflections and rotations, defines the adhesive plastic modulus ( $E_p$ ) and the ultimate state defines the adhesive elastic stress and strain ( $f_c, \epsilon_c$ ) and ultimate strength and strain ( $f_u, \epsilon_u$ ).

- 
- An energy factor defined as the ultimate strength to serviceability limit state energy ratio is proposed to quantify and compare the behavior of structures built from both ductile and brittle materials. Nevertheless, no limits have been established and thus further investigation should be carried out.
  - The stress level at the joint failure line is verified to ensure that joints remain intact up to FRP element failure. The stress level predicted using an interlaminar failure criterion for adhesively-bonded joints with epoxy (stiff adhesive) (Vallée 2005) is not currently sufficiently accurate to predict joint strength with highly non-linear adhesives. Further investigation of the correction factors to be included in the failure criterion needs to be carried out.
  - The elastoplastic or highly non-linear behavior of adhesives prevents the occurrence of high stress peaks. Shear and through-thickness stresses are much more evenly distributed on the bonded surface, leading to less sensitive and more robust joints with regard to premature and unexpected failure.
  - The comparison of model predictions and experimental measurements indicates that the calculated rotations underestimate the measured rotations by 13% to 28% and the variations from the “measured” hogging moments are between -5% and +15%.
  - The model predictions show, like the experimental investigations, that the bending-moment redistribution effect was low since the ADP adhesive was initially too flexible compared to a tailored adhesive leading to higher and constant connection stiffness up to ultimate limit state.
  - Recommendations concerning creep deformation limits are not available in the literature (Hart-Smith’s recommendation (1987) are too restrictive and have no scientific basis) and have not been established in the present study. Further investigation of creep deformation needs to be carried out and recommendations established. It must nonetheless be noted that the adhesive layer is subjected to a low stress level at the serviceability limit state and thus is only slightly influenced by creep.



## **7 Conclusions and Future Work**

This chapter focuses on the principal conclusions and recommendations for future work. The conclusions may be considered as “answers” to the question “How may ductile structures be developed using brittle all-FRP materials?” posed in Section 1.3 and are linked with the objectives of this thesis (also summarized in Section 1.3).

### **7.1 Conclusions**

#### **7.1.1 Structural Concept**

The results of this thesis confirm the feasibility of a new concept for structures composed of brittle all-FRP components. The concept proposes the use of redundant structural systems and ductile adhesively-bonded joints to provide system ductility compensating for the lack of FRP material ductility. The concept envisages ductile and redundant structures based on:

- initially stiff behavior to meet short- and long-term serviceability requirements;
- flexible behavior exceeding serviceability and ultimate limit states.

Since structure behavior is related to adhesively-bonded connection stiffness and consequently adhesive behavior, ductile – or at least highly non-linear – adhesive behavior is appropriate. The flexible joints with ductile adhesive characteristics bring about a favorable redistribution of internal and external forces in the redundant system in the same way as plastic hinges in statically indeterminate systems with ductile materials.

The structure design must lead to FRP element failure rather than joint failure. Nevertheless, the unexpected failure of a bonded joint must be considered in the structural concept. When this occurs, the redundant system should allow the creation of alternative load paths and redistribution of section forces resulting in pseudo-ductile behavior and the prevention of structural collapse. Thus, the new structural concept provides both ductile (failure of FRP elements) and pseudo-ductile structural behavior (unexpected failure of adhesively-bonded joints).

### **7.1.2 Ductile Joints and Adhesives**

The FE model developed is reliable for determining the joint stiffness and strain and stress distributions along the failure plane in order to predict joint strength. The FE study of the effect on the joint behavior of the adhesive to adherend modulus ratio gives rise to the following concluding remarks:

- Joints are classified as stiff or flexible according to their stiffness. The limit corresponds to the continuous laminate (adherend to be connected) stiffness. Stiff joint stiffnesses range between rigid joint stiffness (theoretical double-lap joint without adhesive layer connecting the adherends) and continuous laminate stiffness. As the joint and adhesive behaviors are linked, adhesives are also classified as stiff or flexible.
- Appropriate adhesive bilinear behavior is designed according to the predefined joint behavior. The adhesive must initially generate a relatively stiff joint and limit creep deformation governed by the serviceability limit state (elastic phase). Subsequently, it must develop a flexible joint assuring joint ductility and the required strength (plastic phase). The definition of two adhesive to adherend modulus ratio intervals is proposed for elastic and plastic modulus selection.
- The use of an appropriate (well-designed) bilinear adhesive behavior is more advantageous than that of a traditional structural and stiff epoxy adhesive.

The previous FE results have been validated by experimental investigations:

- Ductile adhesively-bonded joint efficiency (ADP-acrylic adhesive: 76%) is greater than mechanical joint efficiency (50% according to Matthews (1987)) and stiff and brittle adhesively-bonded joint efficiency (EP-epoxy adhesive: approx. 50%).
- Ductile adhesives exhibit a linear strain distribution and therefore constant shear stress distribution along the overlap.
- All ductile adhesive could not achieve ductile joint behavior. The use of an appropriate ductile adhesive (ADP-acrylic) creates ductile joint behavior, while that of an inappropriate ductile adhesive (PU-polyurethane) results in joint failure before plastic deformations develop.

The developed analytical model, based on numerical and experimental results, is reliable for predicting joint elongation and stiffness when using ductile and flexible adhesives, assuming that the adhesive deforms only and uniformly in shear and that adherends deform only in tension.

### **7.1.3 Design Method**

The design method was developed in accordance with the new structural concept and Eurocode design philosophy based on limit states and partial safety factors.

The structure behavior exhibits an initially stiff phase governed by the serviceability limit state and a flexible phase, exceeding serviceability and ultimate limit states, governed by a bending-moment distribution leading to failure in FRP elements and the development of large deflections and rotations.

The structure behavior is derived from Timoshenko's beam theory and the connection's rotational stiffness. Connections are assumed to be rigid in the structure stiffness phase, up to serviceability limit state, while they exhibit low rotational stiffness in the flexible phase, exceeding the serviceability and ultimate limit states. Connection rotational stiffness is estimated from joint elongation, assuming that the adhesive deforms only in shear and that adherends deform only in tension; these assumptions are based on the results of numerical and analytical models of adhesively-bonded double-lap joints.

An energy factor, defined as the ultimate strength to serviceability limit state energy ratio, is proposed to quantify and compare the behavior of structures built from both ductile and brittle materials. No limits have been established and thus further investigation should be carried out.

### **7.1.4 Guidelines for Ductile Adhesive Selection**

The appropriate adhesive bilinear behavior is designed according to predefined structure behavior. The adhesive elastic modulus is selected according to high joint stiffness and creep deformation requirements. The structure bending-moment distribution, related to the structure's flexible phase, leading to failure in FRP elements and the development of large deflections and rotations, defines adhesive plastic modulus, while the structure failure limit state (FRP element characteristic resistance) defines adhesive elastic stress and strain and ultimate strength and strain.

## **7.2 Future Work**

This section introduces research that should be carried out in the future. It concerns the numerical and experimental investigation and the further development stages of new all-FRP structure concepts.

## **7.2.1 Experimental and Numerical Investigation**

### **7.2.1.1 Adhesive Characterization**

The adhesive stress-strain curve varies according to the operating environment. An increased loading rate has an effect equivalent to temperature reduction and both increase the elastic modulus and stress, maintaining identical strain energy. Thus, estimations based on adhesive properties can differ from the actual behavior of the adhesive layer between the FRP adherends, due to differences in the operating environment. Adhesive characterization must take into account these property variations and thus the temperature and loading rate for adhesive tests must be defined to correspond with the operating environment of adhesively-bonded joints.

### **7.2.1.2 Long-term Behavior**

Since this thesis limits itself to numerical and experimental investigations for quasi-static and short-term conditions, the long-term behavior of adhesively-bonded joints must be investigated. Moreover, investigations are limited to laboratory environmental conditions, thus research on environmental action effects on joints must also be carried out.

#### **Creep**

Since no recommendations concerning creep deformation limits are available in literature (Hart-Smith's recommendation (1987) is too restrictive and without scientific basis), further investigation must be carried out on this subject and recommendations established. It should nonetheless be noted that the adhesive layer is subjected to a low stress level at the serviceability limit state and thus should be only slightly influenced by creep.

#### **Fatigue**

Investigation of the fatigue behavior of adhesively-bonded joints - especially for bridge construction - must be carried out. Since GFRP structures are very light and subjected to low permanent actions compared to repetitive traffic actions, the question of the fatigue resistance of GFRP bridges, especially their connections, arises. Fatigue studies concerning adhesively-bonded double-lap joints with epoxy (EP) and acrylic (ADP) adhesives are currently in progress in the CCLab (Composite Construction Laboratory) at the EPFL (Keller and Tirelli 2003, Keller et al. 2005).

#### **Environmental actions**

Environmental actions can have a significant influence on the performance of adhesively-bonded joints. Ageing of the adhesive layer leads to mechanical property degradation and in some cases to joint failure. Ageing studies concerning the effect of high temperature and humidity on adhesively-bonded double-lap joints with epoxy (EP) and acrylic (ADP) adhesives are planned in the CCLab (Composite Construction Laboratory) at the EPFL.



### 7.2.1.3 Strength Prediction

#### GFRP beam

GFRP thin-walled section beams exhibit instability failure modes at concentrated loading-points or supports. Due to the complexity of the buckling phenomena, beam strength prediction has not formed an integral part of the present study. The experimental investigation indicated weak areas at the beam section corners – the location of the overlap ends of the combined mats. Improving fiber architecture increases FRP member, and thus the developed beam structure, performance. Investigations of GFRP thin-walled section beams, especially the interaction between buckling modes, should be carried out.

#### Adhesively-bonded joint

The interlaminar failure criterion used for joint-strength prediction includes through-thickness and shear strengths and two correction factors, taking into account through-thickness and shear stress distributions at the failure line (Vallée 2004). These factors were established for two extreme cases – uniformly distributed stresses and high stress peaks developed with stiff adhesives (EP) – and were not accurately defined for intermediate stress distributions developed with more flexible adhesives (PU and ADP). Thus, the interlaminar failure criterion is not sufficiently accurate to predict joint strength with highly non-linear adhesives and further investigations on correction factors need to be carried out.

## 7.2.2 Structural Concept

The new all-FRP structure concepts introduced in the present study achieve system and component ductility through the use of ductile adhesively-bonded joints and redundant systems. The first concept-development stage consists of designing system ductility through ductile connections (at system level) and structural redundancy (statically indeterminate system) (see Chapter 3 and 6) and the second stage consists of designing component ductility through ductile connections (at system level) and cross-sectional redundancy (see Chapter 3).

Girders composed of pultruded elements (Figure 2.4(b) page 14) or pultruded and translucent sandwich elements (Figure 7.1) assembled using ductile adhesively-bonded connections can generate component ductility (see Section 3.1).

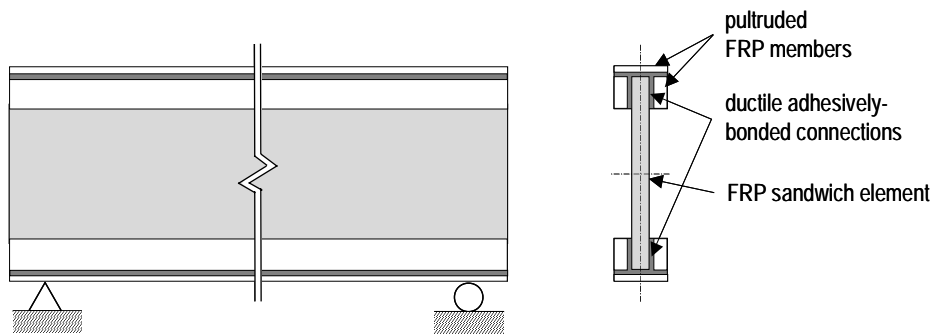


Figure 7.1: Second new structure concept (component ductility)

At the serviceability limit state, the adhesive and girder behavior remain linear elastic. At the ultimate limit state, the adhesive starts to plastify just before brittle component failure. The use of ductile adhesives limits stress transfer from low-stressed to high-stressed components, leading to favorable stress distribution across the redundant cross-section and increasing load-carrying capacity and structural safety. Single cross-sectional components, or the adhesive bond between single components, can fail without the whole section failing, avoiding brittle failure and warning of structure collapse. Internal stress redistribution operates in the cross-section in the same way as internal force redistribution in ductile statically indeterminate structures.

An experimental investigation had been carried out previously to analyze the structural behavior of adhesively-bonded sandwich girders connected with a stiff and elastic epoxy adhesive (Figure 7.2) (Keller et al. 2004). The girders were composed of double sandwich-element webs and pultruded-member flanges. They were subjected to quasi-static, four-point bending experiments. The experimental investigation verified the load-carrying capacity of the sandwich elements in their plane. The sandwich girders exhibited an almost linear behavior up to failure, with a slight loss of stiffness due to the sandwich element progressively debonding between the sandwich face sheets and trapezoidal cores under the jacks. The following conclusions were drawn:

- The shear load, relatively small compared with the bending load, carried by slender girders allows the use of very economical GFRP-sandwich elements as the web.
- The large adhesive surfaces between the sandwich webs and flanges are loaded in a highly favorable manner: shear stresses are very small and through-thickness stresses arise only in the vicinity of the supports (areas of high transversal compression).
- Despite the complex load-carrying and failure behavior, simple beam theory can be applied for the girder design. Deflection behavior and failure loads can be predicted.

Additionally, the translucent sandwich elements can combine different functions: architectural (transparency, translucency, lighting, color), building physical (thermal insulation) and load-carrying, reducing the number of building components and simplifying the construction process.

This work could be extended by the integration of ductility through the use of ductile adhesives and improvement of the compressive strength of sandwich elements (adherence between face sheets and core).

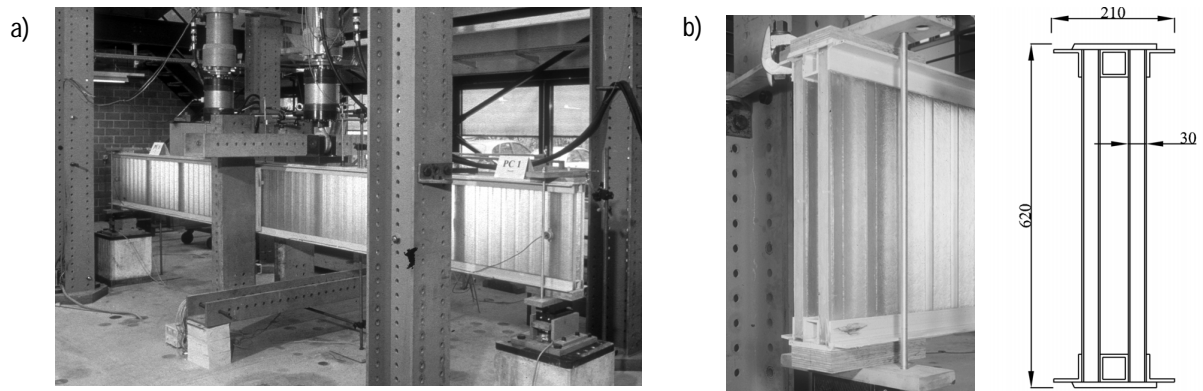


Figure 7.2: Translucent sandwich girder (a) experimental set-up, (b) cross-section (CCLab)



---

## References

- ABDELRAHMAN A.A., TADROS G., RIZKALLA S.H. (1995), Test Model for the First Canadian Smart Highway Bridge, *ACI Structural Journal*, Vol. 92, No. 4, pp 451-458.
- ADAMS R.D., PEPIATT N.A. (1974), Stress Analysis of Adhesive-Bonded Lap-Joints, *Journal of Strain Analysis*, Vol. 9, No. 3, pp 185-196.
- ADAMS R.D., COPPENDALE J. (1977), The Elastic Moduli of Structural Adhesives, *Adhesion*, Allen K.W. ed., Applied Science Publishers, London, United Kingdom, pp 1-17.
- ADAMS R.D., COPPENDALE J. (1979), The Stress-Strain Behaviour of Axially-Loaded Butt Joints, *Journal Adhesion*, Vol.10, No. 1, pp 49-62.
- ADAMS R.D., HARRIS J.A. (1987), The Influence of Local Geometry on the Strength of Adhesive Joints, *International Journal of Adhesion and Adhesives*, Vol. 7, No. 2, pp 69-80.
- ADAMS R.D., COMYN J., WAKE W.C (1997), The Nature and Magnitude of Stresses in Adhesive Joints, *Structural Adhesive Joints in Engineering*, Second Edition, Chapman & Hall, Chapter 2.
- ALTHOF W., BROCKMANN W. (1976), New Test Methods for the Prediction of Environmental Resistance of Adhesive Bonded Joints, *Science of Advanced Materials and Process Engineering Series*, Vol. 21, pp 581-591.
- AMERICAN CONCRETE INSTITUTE (2001), Guide for Design and Construction of Reinforced Concrete with FRP Bars, *ACI440 IR-01*, Detroit.
- ANDRUET R.H., DILLARD D.A., HOLZER S.M. (2001), Two- and Three-Dimensional Geometrical Nonlinear Finite Elements for Analysis of Adhesive Joints, *International Journal of Adhesion and Adhesives*, Vol. 21, No. 1, pp 17-34.
- ANON (2000 a), *Extren Design Manual*, Strongwell Corp. Bristol, Virginia, United States of America.
- ANON (2000 b), *The New and Improved Pultex Pultrusion Global Design Manual of Pultex Standard and Custom Fiber Reinforced Polymer Structural Profiles*, Revision 3, Creative Pultrusions Inc., Alum Bank, Pennsylvania, United States of America.
- ANON (2003), *Fiberline Design Manual*, Internet -<http://www.fiberline.com/gb/home/index.asp>
- ANSYS (2004), Homepage of Ansys Incorporated. Internet -<http://www.ansys.com>

ASHBY M.F. (1991), Materials and Shapes, *Acta Metallurgica et Materialia*, Vol. 39, No. 6, pp 1025-1039.

ASTM D 695M-96 (1996), Standard Test Method for Compressive Properties of Rigid Plastics [Metric]<sup>1</sup>, *Annual Book of ASTM Standards*, Vol. 08.01, United States of America.

ASTM D907-96a (1996), Standard Terminology of Adhesives, *Annual Book of ASTM Standards*, Vol. 15.06, United States of America.

ASTM D2093-03 (1984), Standard Practice for Preparation of Surfaces of Plastics Prior to Adhesive Bonding, American Society for Testing and Materials. *Annual Book of ASTM Standards*, Vol. 15.06, United States of America.

ASTM 3983-98 (2000), Standard Test Method for Measuring Strength and Shear Modulus of Nonrigid Adhesives by the Thick-Adherend Tensile-Lap Specimen, *Annual Book of ASTM Standards*, United States of America.

ASTM D5573-99 (1999), Standard Practice for Classifying Failure Modes in Fiber-Reinforced-Plastic (FRP) Joints, *Annual Book of ASTM Standards*, Vol. 15.06, United States of America.

BAKHT B., AL-BAZI G., BANTHIA N., CHUNG M., ERKI M.-A., FAORO M., MACHIDA A., MUFTI A., NEALE K.W., TADROS G. (2000), Canadian Bridge Design Code Provisions for Fiber-Reinforced Structures, *Journal of Composites for Construction*, Vol. 4, No. 1, pp 3-15

BRAESTRUP M.W. (1999), Footbridge Constructed from Glass-Fibre-reinforced Profiles, Denmark, *Structural Engineering International*, Vol. 9, No. 4, pp 256-258.

BAKIS C.E., NANNI A., TEROSKY J.A., KOEHLER S.W. (2001), Self-Monitoring, Pseudo-Ductile, Hybrid FRP Reinforcement Rods for Concrete Applications, *Composites Science and Technology*, Vol. 61, No. 6, pp 815-823.

BAKIS C.E., BANK L.C., BROWN V.L., COSENZA E., DAVALOS J.F., LESKO J.J., MACHIDA A., RIZKALLA S.H., TRIANTAFILLOU T.C. (2002), Fiber-Reinforced Polymer Composites for Construction – State-of-the-Art Review, *Journal of Composite for Construction*, Vol.6, No. 2, pp 73-87.

BANK L.C. (1987), Shear Coefficient for Thin-Walled Composite Beams, *Composite Structures*, Vol. 8, No. 1, pp 47-61.

BANK L.C., MOSALLAM A.S, GONSIOR H.E. (1990), Beam-to-Column Connections for Pultruded FRP Structures, *Serviceability and Durability of Construction Materials*, Proc. of the First Materials Engineering Congress, Denver, Colorado, pp 804-813.

BANK L.C., MOSALLAM A.S (1991), Linear and Nonlinear Response of Pultruded FRP Frames Subjected to Static Loads, *Proc. of the Symposium on Plastics and Plastic Composite: Material Properties*, ASME Winter Annual Meeting, Atlanta, Georgia, pp 1-6.

- BANK L.C., MOSALLAM A.S, MCCOY G.T. (1992), Design and Performance of Connections for Pultruded Frame Structures, *Technical Sessions of the 49<sup>th</sup> Annual Conference, Composites Institute of The Society of the Plastics Industry*, Cincinnati, Ohio, Session 2-B.
- BANK L.C., GENTRY T.R., NADIPELLI M. (1994), Local Buckling of Pultruded FRP Beams-Analysis and Design, *Technical Sessions of the 49<sup>th</sup> Annual Conference, Composites Institute of The Society of the Plastics Industry*, Cincinnati, Ohio, Session 8-D.
- BANK L.C., YIN J., NADIPELLI M. (1995), Local Buckling of Pultruded FRP Beams – Nonlinearity, Anisotropy and Inhomogeneity, *Construction and Building Materials*, Vol. 9, No. 6, pp 325-331.
- BANKS W.M., RHODES J.R. (1980), The Buckling Behaviour of Reinforced Plastic Box Sections, *The Reinforced Plastics Congress'80*, Brighton, United Kingdom, pp 85-88.
- BARBERO E.J., FU S.H. (1990), Local Buckling as Failure Initiation on Pultruded Composite Beams, *Impact and Buckling of Structures*, American Society of Mechanical Engineers, Aerospace Division, Vol. 20, pp 41-45.
- BARBERO E.J., FU S.H., RAFTOYIANNIS I. (1991), Ultimate Bending Strength of Composite Beams, *Journal of Materials in Civil Engineering*, Vol. 3, No. 4, pp 292-306.
- BASS A.J., MOTTRAM J.T. (1994), Behaviour of Connections in Frames of Fiber-Reinforced-Polymer Sections, *The Structural Engineer*, Vol. 72, No. 17, pp 280-285.
- BASSETTI A. (2001), *Lamelles précontraintes en fibres carbone pour le renforcement de ponts rivetés endommagés par fatigue*, Dissertation ETH No. 2440, ETH Lausanne, Switzerland.
- BAYLOR J.S, SANCAKTAR E. (1995), A Comparison of Adhesively Bonded Single Lap, Scarf and Butt Joints, Reliability, Stress Analysis, and Failure Prevention Issues in Emerging Technologies and Materials, *ASME International Mechanical Engineering Congress and Exposition*, New York, United States of America, pp 41-48
- BELINGARDI G., GOGLIO L., TARDITI A. (2002), Investigating the Effect of Spew and Chamfer Size on Stresses in Metal/Plastics Adhesive Joints, *International Journal of Adhesion and Adhesives*, Vol. 22, No. 4, pp 273-282.
- BILLINGTON D.P. (1997), *Robert Maillart: Builder, Designer, and Artist*, Cambridge University Press, Cambridge, United Kingdom.
- BOSC J.-L., CHAUVEAU J.-M., CLEMENT J., DEGENNE J., MARREY B. (2001), *Joseph Monier et la naissance du ciment armé*, Editions du Linteau, Paris, France.
- BURGOYNE C.J. (2001), Ductility and Deformability in Beams Prestressed with FRP Tendons, *FRP Composites in Civil Engineering*, The Hong Kong Institution of Engineers, Teng J.G. ed., Elsevier, Amsterdam, The Netherlands, pp 15-25.

CANADIAN HIGHWAY BRIDGE DESIGN CODE (DRAFT) (1998), Canadian Standards Association, Rexdale, Ontario, Canada.

CANNING L., HOLLAWAY L., THORNE A.M. (1999), Manufacture, Testing and Numerical Analysis of an Innovative Polymer Composite/Concrete Structural Unit, *Poc. Inst. Civ. Eng. Structures and Buildings*, Vol. 134, pp 231-241.

CHAMBERS R.E. (1997), ASCE Design Standard for Pultruded Fibre-Reinforced-Plastics (FRP) Structures, *Journal of Composites for Construction*, Vol. 1, No. 1, pp 26-38.

CHEN W.F. (1987), *Joint Flexibility in Steel Frames*, Elsevier Applied Science, London, United Kingdom.

CHILTON J. (2000), *Heinz Isler*, Thomas Telford, London, United Kingdom.

CLARKE J.L. (1996), *Structural Design of Polymer Composites Eurocomp Design Code and Handbook*, The European Structural Polymeric Composites Group, E & FN Spon, London, United Kingdom.

COGNARD J.(2000), *Science et technologie du collage*, Presses Polytechniques et Universitaires Romandes, Lausanne, Switzerland.

COWPER G.R. (1966), The shear Coefficient in Timoshenko's Beam Theory, *Journal of Applied Mechanics*, Transactions of the ASME, Vol. 33, pp 335-340.

CROCOMBE A .D., RICHARDSON G, SMITH P.A. (1993), Measuring Hydro-Static Dependent Constitutive Behaviour of Adhesives Using a Bend Specimen, *Journal Adhesion*, Vol. 42, No. 3, pp 209-223.

DAVIS G. (1997), Performance of Adhesive Systems for Structural Timbers, *International Journal of Adhesion and Adhesives*, Vol. 17, No. 3 , pp 247-255.

DE BRUYNE N.A. (1951), *Adhesion and Adhesives*, De Bruyne N.A. and Houwink R. ed., Elsevier, Amsterdam, The Netherlands, pp 92.

DE BRUYNE N.A. (1957), Fundamentals of Adhesion, *Proc. of Conference on Bonded Aircraft Structures*, pp 1-9.

DESKOVIC N., TRIANTAFILLOU T.C., MEIER U. (1995), Innovative Design of FRP Combined with Concrete : Short-Term Behavior, *Journal of Structural Engineering*, Vol. 121, No. 7, pp 1069-1078.

DHARMARAJAN S., MCCUTCHEN JR.H. (1973), Shear Coefficients for Orthotropic Beams, *Journal of Composite Materials*, Vol. 7, pp 530-535.

DOLEV G., ISHAI O. (1981), Mechanical Characterization of Adhesive Layer "In Situ" and as Bulk Material, *Journal Adhesion*, Vol. 12, No. 4, pp 283-294.

DOOLEY S.C. (2004), *The Development of Material-Adapted Structural Form*, Dissertation EPF No. 2986, EPF Lausanne, Switzerland.



- EN ISO 527-1 (1996), Determination of Tensile Properties - Part 1: General Principles, *European Standard*, Brussels, Belgium.
- EN ISO 527-2 (1996), Determination of Tensile Properties - Part 2: Test Conditions for Moulding and Extrusion Plastics, *European Standard*, Brussels, Belgium.
- EN 923 (1998), Adhesives – Terms and Definitions, *British Standards Institute*, London, United Kingdom.
- EN ISO 11003-1 (1993), Adhesives - Determination of Shear Behaviour of Structural Bonds - Part 1: Torsion Test Method Using Butt-Bonded Hollow Cylinders, *European Standard*, Brussels, Belgium.
- EN 1990 (2002), *Eurocode: Basis of Structural Design*, European Committee for Standardisation, Brussels, Belgium.
- EN 1991 (2002), *Eurocode 1: Actions on Structures*, European Committee for Standardisation, Brussels, Belgium.
- EN 1992 (2002), *Eurocode 2: Design of Concrete Structures*, European Committee for Standardisation, Brussels, Belgium.
- EN 1993 (2002), *Eurocode 3: Design of Steel Structures*, European Committee for Standardisation, Brussels, Belgium.
- FARDIS M.N., KHALILI H. (1981), Concrete Encased in Fiberglass-Reinforced Plastics, *Journal of the American Concrete Institute*, Vol. 78, No. 6, pp 440-446.
- FARLEY G.L. (1986), Effect of Specimen Geometry on the Energy Absorption Capability of Composite Materials, *Journal of Composite Materials*, Vol. 20, pp 390-400.
- FISCHER M., PASQUIER M.(1989), Shear Behaviour of Structural Adhesives in the Bondline, *Construction & Building Materials*, Vol. 3, No. 1, pp 31-34.
- FLEMMING M., SIEGFRIED R. (2003), *Faserverbundbauweisen Eigenschaften*, Springer, Berlin, Germany.
- FREY F. (1994), *Analyse des structures et milieux continus : mécanique des structures*, Traité de Génie Civil Vol. 2, Presses polytechniques et universitaires romandes, Lausanne, Switzerland.
- GALI S., DOLEV G., ISHAI O. (1981), An effective Stress/Strain Concept in the Mechanical Characterization of Structural Adhesive Bonding, *International Journal of Adhesion and Adhesives*, Vol. 1, No. 3, pp 135-140.
- GOLAND M., REISSNER E. (1944), The Stress in Cemented Joints, *Journal of Applied Mechanics*, Vol. 66, No. 7, A17-27.
- GRACE N.F., SAYED G.A. (1998), Ductility of Prestressed Bridges Using CFRP Strands, *Concrete International*, Vol. 20, No. 6, pp 25-30.

- HABEL K. (2004), Structural Behavior of Elements Combining Ultra-High Performance Fiber Reinforced Concretes (UHPFRC) and Reinforced Concrete, Dissertation EPF No. 3036, EPF Lausanne, Switzerland.
- HARRIS H.G., SOMBOONSONG W., KO F.K. (1998), New Ductile Hybrid FRP Reinforcing Bar for Concrete Structures, *Journal of Composites for Construction*, Vol. 2, No. 1, pp 28-37.
- HART-SMITH L.J. (1973), *Adhesive-bonded Double Lap Joints*, NASA CR-112235, United States of America.
- HART-SMITH L.J. (1974), Advances in the Analysis and Design of Adhesive-Bonded Joints in Composite Aerospace Structures, *New Industries and Applications for Advanced Materials Technology, 19<sup>th</sup> National SAMPE Symposium and Exhibition*, Azusa, California, United States of America, pp 722-737.
- HART-SMITH L.J. (1987), Design of Adhesively Bonded Joints, *Joining Fibre-Reinforced Plastics*, Matthews F.L. ed., Elsevier, London, United Kingdom, Chapter 7.
- HART-SMITH L.J. (1990), Joining, Mechanical Fastening, *International Encyclopedia of Composites*, Stuart M.L. ed., VCH Publisher, New York, Vol. 2, pp 438-460.
- HEGER F.J., CHAMBERS R.E., DIETZ A.G.H. (1984), *Structural Plastic Design Manual*, ASCE Manuals and Reports on Engineering Practice No. 63, ASCE, New York, United States of America.
- HESLEHURST R.B., HART-SMITH L.J. (2002), The Science and Art of Structural Adhesive Bonding, *SAMPE Journal*, Vol. 38, No. 2, pp 60-71.
- HOLLOWAY L. (1994), *Handbook of Polymer Composites for Engineers*, Woodhead Publishing Limited, Cambridge, United Kingdom.
- HOLLOWAY L., HEAD P.R (2001), *Advanced Polymer Composites and Polymers in the Civil Structures*, Elsevier, Oxford, United Kingdom.
- HULATT J., HOLLOWAY L., THORNE A.M. (2003), The Use of Advanced Polymer Composites to Form an Economic Structural Unit, *Construction and Building Materials*, Vol. 17, No. 1, pp 55-68.
- HUTCHINSON A. (1997), *Joining of Fiber-Reinforced Polymer Composite Materials*, Project Report 46, Construction Industry Research and Information Association, London, United Kingdom.
- HUTCHINSON A. (1999), Adhesive-Bonded Joints Involving Fiber-Reinforced Polymer Composites, *Composites and Plastics in Construction*, Rapra Technology Limited, Shawbury, United Kingdom, paper 9.
- IKEGAMI K., KAJIYAMA M., KANIKO S., SHIRATORI E. (1979), Experimental Studies of the Strength of an Adhesive Joint in a State of Combined Stress, *Journal Adhesion*, Vol. 10, No. 1, pp 25-38.
- INSTITUTION OF STRUCTURAL ENGINEERS (1999), *Guide to the Use of Structural Adhesives*, SETO, The Institution of Structural Engineers, London, United Kingdom.

- ISHAI O., DOLEV G. (1981), Mechanical Characterization of Bonded and Bulk Adhesive Specimens as Affected by Temperature and Moisture, *26<sup>th</sup> National SAMPE Symposium*, Los Angeles, United States of America, pp 630-641.
- JAEGER L.G., TADROS G., MUFTI A.A. (1995), *Balanced Section, Ductility and Deformability in Concrete with FRP Reinforcement*, Research Report submitted to Joint US - Canadian Meeting at West Virginia University, United States of America.
- JAEGER L.G., MUFTI A.A., TADROS G. (1997), The Concept of the Overall Performance Factor in Rectangular Sections Reinforced Concrete Beams, *Proc. 3<sup>rd</sup> Int. Symp. on Nonmetallic (FRP) Reinforcements for Concrete Structures*, Japan Concrete Institute, Tokyo, Japan, Vol. 2, pp 551-558.
- JEANDRAU J.P., GROLADE D. (1985), Méthodes de calculs des assemblages collés, *Colloquium on Tendances actuelles en calcul des structures*, DRET, Bastia, France, pp 873-890.
- JEANDRAU J.P. (1986), Intrinsic Mechanical Characterization of Structural Adhesives, *International Journal of Adhesion and Adhesives*, Vol. 6, No. 4, pp 229-231.
- JEANDRAU J.P. (1991), Analysis and Design Data for Adhesively Bonded Joints, *International Journal of Adhesion and Adhesives*, Vol. 11, No. 2, pp 71-79.
- JONES R.M. (1975), *Mechanics of Composite Materials*, McGraw-Hill Book Co., New York, United States of America.
- JOHNSON A.F. (1985), Simplified Buckling Analysis for RP Beams and Columns, *1<sup>st</sup> European Conference on Composite Materials*, Bordeaux, France, pp 541-549.
- KADIOGLU F., OZEL A., SADELER R. (2003), The Strength in the Weakness, *Journal of Advanced Materials*, Vol. 35, No. 3, pp 47-51.
- KARBHARI V.M., HALLER J.E (1998), Rate and Architecture Effects on Progressive Crush of Braided Tubes, *Composite Structures*, Vol. 43, No. 2, pp 93-108.
- KARBHARI V.M., SEIBLE F. (1999), Fiber-Reinforced Polymer Civil Infrastructure in the USA, *Structural Engineering International*, Vol. 9, No. 4, pp 184-287.
- KASSAPOGLOU C., ADELMANN J.C. (1991), KGR-1 Thick Adherend Specimen Evaluation for the Determination of the Adhesive Mechanical Properties, *23<sup>th</sup> International SAMPE Technical Conference*, Carri R.L., Poveromo L.M. and Gauland J. eds, Vol. 23, pp 162-176.
- KELLER T. (1998), Struktur und Form: Zur Entstehung materialgerechter Strukturformen, *Schweizer Ingenieur und Architekt*, No. 12, Zurich, Switzerland.
- KELLER T. (1999), Towards Structural Forms for Composite Fiber Materials, *Structural Engineering International*, Vol. 9, No. 4, pp 297-300.
- KELLER T., DE CASTRO J., DOOLEY S., DUBOIS V. (2001), Use of Fiber Reinforced Polymers in Bridge Construction, State-of-the-Art Report with Application and Research Recommendations, Swiss Federal Roads Authority, Report No. 555, Zurich, Switzerland.

- KELLER T., DE CASTRO J., SCHOLLMAYER M. (2004), Adhesively Bonded and Translucent Glass Fiber Reinforced Polymer Sandwich Girders, *Journal of Composites for Constructions*, Vol. 8, No. 5, pp 461-470.
- KELLER T., GUERTLER H. (in press, a) Quasi-static and Fatigue Performance of a Cellular FRP Bridge Deck Adhesively Bonded to Steel Girders, *Composite Structures*, in press, available online 19 November 2004.
- KELLER T., GUERTLER H. (in press, b) In-plane Compression and Shear Performance of FRP Bridge Decks Acting as Top Chord of Bridge Girders, *Composite Structures*, in press, available online 18 December 2004.
- KELLER T., GUERTLER H. (under review), Composite action and adhesive bond between FRP bridge decks and main girders, *Journal of Composites for Construction*, *Journal of Composites for Construction*, Manuscript number CC/2003/022477, under review.
- KELLER T., TIRELLI T. (2003), Fatigue Behavior of Adhesively Connected Pultruded GFRP Profiles, *Composites Structures*, Vol. 65, No. 1, pp 55-64.
- KELLER T., TIRELLI T., ZHOU A. (2005) Tensile fatigue performance of pultruded glass fiber reinforced polymer profiles, *Composites Structures*, Vol. 68 No. 2, pp 235-245.
- KELLER T., VALLEE T. (2005), Adhesively Bonded Lap Joints from Pultuded GFRP Profiles Part II: Joint Strength Prediction, *Composites part B: Engineering*, Vol. 36 No. 4, pp 341-350.
- KINLOCH A.J (1983), *Durability of Structural Adhesives*, Applied Science Publishers, United Kingdom.
- KINLOCH A.J (1987), *Adhesion and Adhesives*, Chapman and Hall, London, United Kingdom.
- KOLAKOWSKI Z., KUBIAK T. (2005), Load-Carrying Capacity of Thin-Walled Composite Structures, *Journal of Composite for Construction*, Vol. 67, No. 4, pp 417-426.
- LANG T.P., MALLICK P.K. (1998), Effect of Spew Geometry on Stresses in Single-Lap Joints, *International Journal of Adhesion and Adhesives*, Vol. 18, No. 3, pp 167-177.
- LAUFS W., LUIBLE A. (2003), *Introduction on Use of Glass in Modern Buildings*, Report ICOM 462, ICOM-EPFL, Lausanne, Switzerland.
- LEES W. A. (1989), *Adhesives and the Engineers*, Mechanical Engineering Publications Limited, London, United Kingdom.
- LI G., LEE-SULLIVAN P. (2001), Finite Element and Experimental Studies on Single-Lap Balanced Joints in Tension, *International Journal of Adhesion and Adhesives*, Vol. 21, No. 3, pp 211-220.
- LONG R.S. (1991), Static Strength of Adhesively Bonded ARALL-1 Joints, *Journal of Composite Materials*, Vol. 25, No. 4, pp 391-415.

- LOPEZ ANIDO R., FALKER E., MITTELSTADT B., TROUTMAN D. (1997), Shear Tests of FRP Pultruded Beam-to-Column Connection with Clip Angles, *Materials and Construction: Exploring the Connection*, Proc. of the Fifth ASCE Materials Engineering Congress, Cincinnati, Ohio, pp 92-99.
- MAISSEN A. (1997), Concrete Beams Prestressed with CFRP Strands, *Structural Engineering International*, Vol .7, No. 4, pp 284-287.
- MAISSEN A. (2000), Concrete Beams Prestressed with CFRP Cables, *Structural Engineering International*, Vol. 10, No. 2, pp 117-120.
- MARLEY M.J. (1982), *Analysis and Tests of Flexibly-Connected Steel Frames*, Report to AISI, University of Colorado, Unites States of America.
- MATTHEWS F.L., KILTY P.F., GODWIN E.W. (1982), A Review of the Strength of Fiber-Reinforced Plastics, Part 2: Adhesively Bonded Joints, *Composites*, Vol. 13, No. 1, pp 29-37.
- MATTHEWS F.L. (1987), *Joining Fiber-Reinforced Plastics*, Elsevier, London, United Kingdom, Chapter 3.
- MAYS G.C., HUTCHINSON A.R. (1992), *Adhesives in Civil Engineering*, Cambridge University Press, Cambridge, United Kingdom.
- MEIER U. (1987), Réparation de ponts avec des matériaux composites hautes performances, *Material und Technik*, No. 4, pp 125-128.
- MELLAART J. (1971), Çatal Hüyük: une des premières cités du monde, Jardin des Arts, Tallandier, Nouveaux aspects de l'archéologie.
- MEYER J.F. (1990), Joining Polymeric Composites, Adhesives, *International Encyclopedia of Composites*, Lee S.M. ed., VCH, New York, United States of America, Vol. 2, pp 509-524.
- MICHAELI W., GRIEF H., WOLTERS L., VOSSEBUERGER F.-J. (1998), *Technologie der Kunststoffe*, 2. Auflage, Hanser Verlag, Munich, Germany.
- MORAIS M., BURGOYNE C.J. (2001), Energy Dissipation in Sections Prestressed with FRP Tendons, *Composites in Construction*, Proc. of the International Conference in Composites in Construction, Swets & Zeitlinger, Figueras J., Juvandes L., Faria R. ed., Balkema Publishers, Lisse, The Netherlands, pp 421-426.
- MOSALLAM A. S. (1993), Stiffness and Strength Characteristics of PFRP UC/Beam-to-Column Connections, *Composite Material Technology*, Proc. of the 16<sup>th</sup> Annual Energy Sources Technology Conference and Exhibition, Houston, United States of America, pp 275-283.
- MOSALLAM A. S., ABDELHAMID M.K. (1993), Dynamic Behavior of FRP Structural Sections, Composite Material Technology, *Composite Material Technology*, Proc. of the 16<sup>th</sup> Annual Energy Sources Technology Conference and Exhibition, Houston, United States of America, pp 37-44.

- MOSALLAM A. S. (1995), Connection and Reinforcement Design Details for Pultruded Fiber Reinforced Plastic (PFRP) Composite Structures, *Journal of Reinforced Plastics and Composites*, Vol. 14, pp 752-784.
- MOTTRAM J.T. (1991 a), Structural Properties of a Pultruded E-Glass Fibre-Reinforced Polymeric I-Beam, *Composite Structures*, Elsevier, London, United Kingdom, Vol. 6, pp 1-28.
- MOTTRAM J.T. (1991 b), Evaluation of Design Analysis for Pultruded Fibre-Reinforced Polymeric Box Beams, *The Structural Engineer*, Vol. 69, No. 11, pp 211-220.
- MOTTRAM J.T. (1993), Recommendations for the Optimum Design of Pultruded Frameworks, *Mekhanika Kompozitnykh Materialov*, Vol. 29, No. 5, pp 675-682.
- MOTTRAM J.T., TURVEY G.J. (1998), *State-of-the-Art Review on Design, Testing, Analysis and Applications of polymeric Composite Connections*, EC COST C1 Initiative on the Semi-rigid Behaviour of Civil Engineering Structural Connections, European Commission.
- MOTTRAM J.T. (2004), Shear Modulus of Standard Pultruded Fiber Reinforced Plastic Material, *Journal of Composites for Construction*, Vol. 8, No. 2, pp 141-147.
- MUFTI A.A., NEWHOOK J.P., TADROS G. (1996), Deformability versus Ductility in Concrete Beams with FRP Reinforcement, *Advanced Composite Materials in Bridges and Structures*, El-Badry M.M. ed., Canadian Society for Civil Engineering, Montréal, Canada, pp 189-199.
- NAAMAN A.E., HARAJLI M.H., WIGHT J.K. (1986), Analysis of Ductility in Partially Prestressed Concrete Flexural Members, *PCI Journal*, Vol. 31, No. 3, pp 64-87.
- NAAMAN A.E., JEONG S.M. (1995), Structural Ductility of Concrete Beams Prestressed with FRP Tendons, *Non-metallic (FRP) Reinforcement for Concrete Structures*, Proc. of the Second International RILEM Symposium (FRPRCS-2), pp 379-386.
- NAHAS M.N. (1986), Survey of Failure and Post-Failure Theories of Laminated Fiber-Reinforced Composites, *Journal of Composites Technology and Research*, Vol. 8, No. 4, pp 138-153.
- OMIDVAR B. (1998), Shear Coefficient in Orthotropic Thin-Walled Composite Beams, *Journal of Composites for Construction*, Vol. 2, No. 1, pp 46-55.
- OSNES H., ANDERSEN A. (2003), Computational Analysis of Geometric Nonlinear Effects in Adhesively Bonded Single Lap Composite Joints, *Composites: Part B*, Vol. 34, No. 5, pp 417-427.
- PARK K.T, HWANG Y.K., KIM H.Y., LEE Y.H., KIM S.M. (2004), Deck-to-girder Connections for GFRP Bridge Decks, *Advanced Composite Materials in Bridges and Structures*, Calgary, Canada, paper 137.
- PARK R., PAULAY T. (1975), *Reinforced Concrete Structures*, John Wiley and Sons, New York, United States of America.

- PENADO F.E., DROPECK R.K. (1990), Numerical Design and Analysis, *Engineered Materials Handbook: Adhesives and Sealants*, ASM International Handbook Committee, Ohio, United State of America, Vol. 3, pp 477-500.
- PEPPIATT N.A. (1976), *Some Aspects of the Paraboloidal Yield Surface*, University of Bristol Internal Report.
- RAGHAHA R.S., CADDELL R.M. (1973), The Macroscopic Yield Behaviour of Polymers, *Journal of Material Science*, Vol. 8, No. 2, pp 225-232.
- RAZAQPUR A.G., ALI M.M. (1996), Ductility and Strength of Concrete Beams Externally Reinforced with CFRP Sheets, *Advanced Composite Materials in Bridges and Structures*, M.M. El-Badry, ed. Canadian Society for Civil Engineering, Montréal, Canada, pp 505-512.
- REINHART T.J. (1987), *Engineered Materials Handbook*, ASM International Handbook Committee, Ohio, United States of America, Vol. 1.
- RENTON W.J., VINSON J.R. (1975 a), The Efficient Design of Adhesive-bonded Joints, *Journal of Adhesion*, Vol. 7, No. 3, pp 175-193.
- RENTON W.J., VINSON J.R. (1975 b), On the Behaviour of Bonded Joints in Composite Material Structures, *Engineering Fracture Mechanics*, Vol. 7, No. 1, pp 41-60.
- RICHARDSON G., CROCOMBE A.D., SMITH P.A. (1993), A Comparison of Two- and Three-Dimensional Finite Element Analyses of Adhesive Joints, *International Journal Adhesion and Adhesives*, Vol. 13, No. 3, pp 193-200.
- SCHINDEL-BIDINELLI E. H. AND GUTHERZ W. (1988), *Konstruktives Kleben*, VCH-Verlagsgesellschaft mbH, Germany.
- SANCAKTAR E., NARAYAN K. (1999), Substrate Volume and Stress Gradient Concepts in Mechanical Adhesion: Analysis of Single Straight Sections, *Journal of Adhesion Science and Technology*, Vol. 13, No. 2, pp 237-271.
- SCHMID M., KIESELBACH R. (2001), Adhesive Bonding - a Challenge for Design, *Journal of the Engineering Integrity Society*, Vol. 10, pp 24-33.
- SEIBLE F., KARBHARI V.M., BURGUEÑO R. (1999), Kings Stormwater Channel and I-5/Gilman Bridges, USA, *Structural Engineering International*, Vol. 9, No. 4, pp. 250-253.
- SMITH S.J., PARSONS I.D., HJELMSTAD K.D. (1998), An Experimental Study of the Behavior of Connections for Pultruded GFRP I-Beams and Rectangular Tubes, *Composite Structures*, Vol. 42, No. 3, pp 281-290.
- SOBRINO J. A., PULIDO M. D. G. (2002), Towards Advanced Composite Materials Footbridges, *Structural Engineering International*, Vol. 12, No. 2, pp 84-86.
- SOLOMON G., GODWIN G. (2002), Expanded Use of Composite Deck Project in USA, *Structural Engineering International*, Vol. 9, No. 4, pp 102-104.

- SOTIROPOULOS S.N., GANGARAO H.V.S., ALLISON R.W. (1994), Structural Efficiency of the Pultruded FRP Bolted and Adhesive Connections, *Composite Institute's 49<sup>th</sup> Annual Conference*, The Society of the Plastics Industry, New York, Session 8-A.
- STILLER W.B., GERGELY J., ROCHELLE R. (2004), In-situ Testing of an FRP Bridge Deck, *Advanced Composite Materials in Bridges and Structures*, Calgary, Canada, paper 43.
- STRUTT J.G. (1852), Tallis's History and Description of the Crystal Palace and the Exhibition of the World's Industry in 1851, Tallis, London, United Kingdom.
- THORNTON P.H., EDWARDS P.J. (1982), Energy Absorption on Composite Tubes, *Journal of Composite Materials*, Vol. 16, No. 6, pp 521-545.
- TIERNEY J.J., GILLESPIE J.W., BOURBAN P.-E. (2000), Joining of Composites, *Comprehensive Composite Materials*, Vol. 2, Elsevier Science Ltd, Oxford, United Kingdom.
- TIMOSHENKO S.P. (1921), On the Correction for Shear of the Differential Equation for Transverse Vibrations of Prismatic Bars, *Philosophical Magazine*, Vol. 41, pp 744-746.
- TIRELLI T. (2003), *Static and Fatigue Behavior of Pultruded GFRP Laminates*, Technical Report CCLab2000.1c/2, CCLab-EPFL, Lausanne, Switzerland.
- TOLF G., CLARIN P. (1984), Comparison Between Flexural and Tensile Modulus of Fibre Composites, *Fibre Science and Technology*, Vol. 21, pp 319-326
- TONG L. (1997), An Assessment of Failure Criteria to Predict the Strength of Adhesively Bonded Composites Double-Lap Joints, *Journal of Reinforced Plastics and Composites*, Vol. 16, No. 8, pp 698-713.
- TONG L., STEVEN G.P. (1999), *Analysis and Design of Structural Bonded Joints*, Kluwer Academic Publishers, Norwell, Massachusetts, United States of America.
- TORROJA E. (1957), *Razón y ser de los tipos estructurales*, Instituto Técnico de la Construcción y del Cemento, Madrid, Spain.
- TRIANAFILLOU T.C., MEIER U. (1992), Innovative Design of FRP Combined with Concrete, *Proc. 1<sup>st</sup> International Conference on Advanced Composite Materials for Bridges and Structures (ACMBS)*, Sherbrooke Quebec, pp 491-499.
- TSAI M.Y., MORTON J. (1995), The Effect of a Spew Fillet on Adhesive Stress Distribution in Laminated Composite Single-Lap Joints, *Composite Structures*, Vol. 32, No. 1-4, pp 123-131.
- TSUNO S. (2003), Selection of Sika Primer for Adhesion to FRP by SikaFAst-5221, Technical Report, Sika Technology AG, Tüffenwies, Switzerland.
- TURVEY G.J. (1997), Analysis of Pultruded Glass Reinforced Plastic Beams with Semi-Rigid End Connections, *Composite Structures*, Vol. 38, No. 1-3, pp 3-16.



- VALLEE T. (2004), *Adhesively Bonded Lap Joints of Pultruded GFRP Shape*, Dissertation ETH No. 2964, ETH Lausanne, Switzerland.
- VAN ERP G.M. (2001), Robustness of Fibre Composite Structures Loaded in Flexure, *FRP Composites in Civil Engineering*, Elsevier, Amsterdam, pp 1421-1426.
- VAN ERP G.M., CARTER D., HELDT T., TRANBERG C., MCCORMICK L. (2002), Development of an Innovative Fibre Composite Deck Unit Bridge, Towards a Better Built Environment – Innovation, Sustainability, Information Technology, IABSE Report Vol. 86, pp 1-13.
- VENETZ V. (2004), personal communication, Sika AG, Tüffenwies, Switzerland.
- VIJAY P.V., KUMAR S.V., GANGARAO H.V.S. (1996), Shear and Ductility Behavior of Concrete Beams Reinforced with GFRP Rebars, *Advanced Composite Materials in Bridges and Structures*, El-Badry M.M. ed., Canadian Society for Civil Engineering, Montréal, Canada, pp 217-226.
- VOLKERSEN O. (1938), Die Nietkraft verteilung in Zugbeanspruchten mit Konstanten laschen querschnitten, *Luftfahrtforsch*, Vol. 15, pp 41-47.
- WISNOM M.R., ATKINSON J.W. (1997), Reduction in Tensile and Flexural Strength of unidirectional Glass Fibre-Epoxy with increasing Specimen Size, *Composite Structures*, Vol. 38, No. 1-4, pp 405-123.
- YOUNG W.C. (1989), *Roark's Formulas for Stress and Strain*, sixth edition, McGraw-Hill, New York, United States of America.
- ZETTERBERG T, ASTROM B.T., BAECKLUND J., BURMAN M. (2001), On Design of Joints Between Composite Profiles for Bridge Deck Applications, *Composite Structures*, Vol. 51, No. 1, pp 83-91.
- ZHOU A., KELLER T. (in press), Joining Techniques for Fiber Reinforced Polymer Composite Bridge Deck Systems, *Composite Structures*, available online 27 August 2004.
- ZOU P.X.W. (2003), Flexural Behavior and Deformability of Fiber Reinforced Polymer Prestressed Concrete Beams, *Journal of Composites for Construction*, Vol. 7, No. 4, pp 275-284.
- ZUREICK A., KAHN L.F., BANDY B.J. (1994), Test on deep I-Shapes Pultruded Beams, *Composites Institute's 49<sup>th</sup> Annual Conference*, The Society of the Plastic Industry, New York, Session 8-C.
- ZUREICK A., SHIH B. (1998), Local Buckling of Fiber-Reinforced Polymeric Structural Members under Linearly-Varying Edge Loading – Part 1: Theoretical Formulation, *Composite Structures*, Vol. 41, No. 1, pp 79-86.
- ZWEBEN C., SMITH W.S., WARDLE M.W. (1979), Test Methods for Fibre Tensile Strength, Composite Flexural Modulus and Properties of Fabric-Reinforced Laminates, *Composite Materials: Testing and Design (Fifth Conference)*, S. W. Tsai ed., ASTM, Philadelphia, United States of America, pp 228-262.



## List of Figures

Figure 1.1:	<i>Thesis methodology and organization</i>	6
Figure 2.1:	<i>Beam with various end supports: Configuration 1 (a) simply-supported, (b) fixed, (c) semi-rigid fixed; Configuration 2 (d) simply-supported, (e) fixed, (f) semi-rigid</i>	10
Figure 2.2:	<i>(a) Semi-rigid connection; (b) Moment-rotation curves (Mosallam 1993)</i>	12
Figure 2.3:	<i>Universal Connector – UC (Mosallam 1993, Mosallam and Abdelhamid 1993)</i>	13
Figure 2.4:	<i>(a) Standard pultruded shapes (Fiberline Composite A/S, DK); (b) Eyecatcher building – adhesively-bonded components (CCLab)</i>	14
Figure 2.5:	<i>(a) Idealized elastic (GFRP) and elastoplastic (steel) models; (b) Elastoplastic model showing unloading response and energy dissipation (plastic energy)</i>	18
Figure 2.6:	<i>Component or material ductility – simply-supported beam subjected to uniformly distributed load (a) static system, (b) moment-curvature curve, (c) bending strain and (d) stress distributions across the mid-span section</i>	18
Figure 2.7:	<i>System ductility – fixed beam subjected to uniformly distributed load (a) elastic, (b) elastoplastic (two plastic hinges) and (c) plastic behavior (three plastic hinges); (d) Load-deflection curve</i>	20
Figure 2.8:	<i>Ductility of structural members based on energy (a) general case, (b) elastoplastic case</i>	21
Figure 2.9:	<i>Moment-rotation curve for (a) unbonded prestressed slab (example from Burgoyne 2001), (b) non-linear brittle behavior</i>	23
Figure 2.10:	<i>Load-deflection curve (a) idealized ductility and (b) appropriate ductility</i>	24
Figure 2.11:	<i>Static system and failure mechanism of concrete beams with (a) steel strands: first plastic hinge forms over the mid-support and second in the right-hand span (b) CFRP strands: an elastic hinge forms over the mid-support (Maissen 2000)</i>	25
Figure 2.12:	<i>Hybrid GFRP and steel girder (a) cross-section, (b) deflection at the onset of failure, plastic hinge between the jacks (CCLab)</i>	26
Figure 2.13:	<i>Pseudo-ductile behavior</i>	27
Figure 2.14:	<i>Redundant system – structural redundancy: Pontresina bridge (CCLab)</i>	27

- Figure 2.15: Redundant system – cross-sectional redundancy: (a) hybrid GFRP/CFRP and concrete section (Triantafyllou and Meier 1992), (b) modular bridge system incorporating GFRP/CFRP girders and fiber-reinforced concrete deck (Karbhari and Seible 1999), (c) hybrid girder with GFRP sandwich panels and pultruded profiles adhesively-bonded (Keller et al. 2004) 28
- Figure 2.16: Mechanical connection (a) partial view and (b) detail of pedestrian bridge in Strandhude, DK (Braestrup 1999), (c) failure modes (CCLab); (d) Advanced Composite Construction System (Maunsell Structural Plastics, UK) 30
- Figure 2.17: Parameters of adhesively-bonded double-lap joints 31
- Figure 2.18: Eyecatcher building (a) open cross-section, (b) closed cross-section manufacture (CCLab) 32
- Figure 2.19: Typical structural adhesive joint configurations (Hart-Smith 1987) 33
- Figure 2.20: Typical elastic stress distribution along the overlap length at the adhesive centerline in a single-lap joint, made with adhesives with low and high modulus (a) shear, (b) through-thickness 34
- Figure 2.21: (a) Effect of temperature on adhesive behavior (Hart-Smith 1987); (b) Polymer state dependency on temperature 35
- Figure 2.22: Hydrostatic and deviatoric stress components and associated material changes 36
- Figure 2.23: Single-lap joint (a) rigid adherends and shear stress distribution, (b) elastic adherends and shear stress distribution (Volkersen 1938), (c) Goland and Reissner's bending moment and through-thickness stress distribution (1944); (d) Double-lap joint 39
- Figure 2.24: (a) Adhesive non-linear behavior; (b) Shear stress distribution at the bondline (Hart-Smith 1973) 41
- Figure 2.25: 3D FEM analysis of single-lap joint (a) through-thickness, (b) shear stress distributions (Andruet et al. 2001). 41
- Figure 2.26: (a) Possible failure modes of adhesively-bonded joints with composite materials loaded in shear (Hollaway 1994); (b) Interlaminar tensile mode of failure (Heslehurst and Hart-Smith 2002) 42
- Figure 2.27: Failure modes of adhesively-bonded joints in composite materials according to ASTM D5573-99 classification 43
- Figure 2.28: (a) Longitudinal section through STI-device; (b) Shear-tensile criterion for 10 mm thick coupons (Vallée 2004) 45
- Figure 3.1: System ductility: (a) ductility, (b) pseudo-ductility; (c) Deformability 50
- Figure 3.2: Ductility and deformability features 50
- Figure 3.3: New ductile and redundant FRP structure concept, stage 1: statically indeterminate structure with ductile connections (a) static system, (b) cross-section; stage 2: statically determinate hybrid structure with ductile connections (c) static system, (d) cross-section 52
- Figure 4.1: Dimensions of tensile test specimen according to EN ISO 527-2 (1996) (a) specimen 1A (EP, PU), (b) specimen 5A (ADP) (dimensions in mm); (c) Tensile testing device (Sika) 55

Figure 4.2:	(a) Dimensions of compression test specimen according to ASTM D 695M-96 (1996) (dimensions in mm); (b) Compression testing device (Sika)	56
Figure 4.3:	(a) Napkin-ring specimen (Schmid and Kieselbach 2003); (b) Napkin-ring specimen dimensions (mm) (Bassetti 2001); (c) Shear testing device (Department of Strength and Technology, EMPA)	56
Figure 4.4:	(a) Displacements on surface of bonded cylinders (Fischer and Pasquier 1989); (b) Area parameters for torque calculation	59
Figure 4.5:	True average stress-strain curves for (a) EP, (b) PU and (c) ADP adhesives	60
Figure 4.6:	(a) Tensile true average stress-strain curves for ADP (5,10,50,100 mm/min; (b) and (c) Tensile nominal load-unload-reload stress-strain curves for ADP (0,5,30 min and 12 h), (d) Time-dependent creep to instantaneous strain ratio	62
Figure 4.7:	(a) Specimen with 100 mm overlap length and gage positioning; (b) Tensile testing device	63
Figure 4.8:	10 mm GFRP laminate (a) fiber architecture after resin burn-off (without surface veil), (b) microscopic section through thickness (Tirelli 2003)	63
Figure 4.9:	(a) Local axis; (b) Schematic drawing of laminate section (not to scale)	64
Figure 4.10:	Internal strain gage positioning: (a) configuration 1 and (b) configuration 2	65
Figure 4.11:	(a) Positioning of video-extensometer measurement points; (b) Fully-instrumented specimen	66
Figure 4.12:	Load-elongation curves for specimens (a) EP.A4, PU.B1 and ADP.C3 ( $l=100$ mm), (b) EP.D1 and ADP.D1 ( $l=200$ mm)	67
Figure 4.13:	Failure modes (a) and (b) EP specimens: fiber-tear, (c) PU specimens: light-fiber-tear, (d) ADP specimens: adhesion promoter to substrate failure and light-fiber-tear failure (mixed), surface failure indication	68
Figure 4.14:	(a) Load-joint elongation of specimens EP.A8, PU.B7 and ADP.C9; (b) Load-elongation of global specimen and joint of specimen ADP.C9	69
Figure 4.15:	Axial strain distribution across joint width of series EP.A at 50 kN, measurements and parabolic and linear fit curves	70
Figure 4.16:	Axial strain distribution along overlap length at 50 kN for series (a) EP.A, (b) PU.B, (c) ADP.C, measurements and linear regression, (d) linear regression comparison	71
Figure 4.17:	(a) Loading test set-up for bonded beam PH2; (b) Bonded joint over mid-support of beam PH1 with strain gages and clinometers	72
Figure 4.18:	Loading positions: (a) and (b) simple beams PS, (c) continuous beams PC, (d) bonded beams PH (dimensions in mm); (e) Idealized beam section; (f) Joint detail	73
Figure 4.19:	Fiber architecture of a 240x240x12 mm profile after resin burn-off test	74
Figure 4.20:	Arrangement of displacement transducers, clinometers and strain gages in beam PH2 (dimensions in mm)	75
Figure 4.21:	Strain gage arrangement in upper and lower adhesive joints of beam PH2 with 200 mm overlap (grey label: lower flange; black label: upper flange)	76

Figure 4.22:	<i>Loading procedure for beam PH2</i>	77
Figure 4.23:	<i>Load-deflection curves at loading section</i>	78
Figure 4.24:	<i>(a) Strain distribution across tension and compression flanges of beam PS2 (dimensions in mm); (b) Failure of beam PS1 near patch load</i>	78
Figure 4.25:	<i>Load-rotation curves at (a) mid-support for beams PS1-3, PC1-3 (not measured) and PH1-4, (b) edge-support for beams PS1-3 and PC1-3</i>	78
Figure 4.26:	<i>(a) Buckling of beam PC2 at mid-support; (b) Failure of beam PC3 at mid-support</i>	79
Figure 4.27:	<i>(a) Deformation of bonded beam PH1 at onset of failure; (b) Failure of beam PH1 below patching load</i>	80
Figure 4.28:	<i>Creep deformation of bonded beam PH2 during first hour</i>	81
Figure 4.29:	<i>(a) First failure of bonded beam PH3 at mid-support (strain gages staggered in the 100 mm overlap); Widening of upper part of bonded joint of beam PH3 (b) initial position, (c) deformation at 118 kN</i>	82
Figure 4.30:	<i>Axial strain distribution (symbols) on upper flanges in adhesive joints of beams PH1-4 at load of 50 kN per jack and linear regression (line)</i>	85
Figure 4.31:	<i>Bending moment distributions (at 136 kN load per jack)</i>	86
Figure 4.32:	<i>Redistribution of bending moments from mid-support (<math>M^-</math>) to loading point sections (<math>M^+</math>)</i>	86
Figure 5.1:	<i>Singularity points (A, C, E and G), average stress location in the adhesive (line BF), and failure location (line DH)</i>	92
Figure 5.2:	<i>(a) Specimen and machine loading-grips; (b) 2D double-lap joint geometry, materials and boundary conditions.</i>	92
Figure 5.3:	<i>Adhesive spew-fillet geometry (a) no spew-fillet (ideal), (b) a curved spew-fillet with 2 mm radius, (c) a 45° spew-fillet; (d) Studied spew-fillet geometries: 1mm radius, half of adhesive thickness, 2 mm radius and a 45° spew-fillet in half of adhesive thickness</i>	93
Figure 5.4:	<i>Tensile and compressive model stress-strain curves (a) EP, (b) PU, (c) ADP (partially see page 59)</i>	94
Figure 5.5:	<i>Element Plane183 and its variation (Ansys 2004)</i>	95
Figure 5.6:	<i>Mesh used in FE model of double-lap joint</i>	96
Figure 5.7:	<i>Load-elongation curves of global specimen for series (a) EP.A (<math>l=100</math> mm), (b) EP.D (<math>l=200</math> mm); (c) PU.B (<math>l=100</math> mm), (d) ADP.C (<math>l=100</math> mm), (e) ADP.D (<math>l=200</math> mm), comparison of FE calculations and measurements</i>	97
Figure 5.8:	<i>Load-elongation curves for joint of series (<math>l=100</math> mm) (a) EP.A, (b) PU.B, (c) ADP, comparison of FE calculations and measurements, (d) FE calculations</i>	98
Figure 5.9:	<i>Displacement-position curves along the joint for series (<math>l=100</math> mm) (a) EP.A at 50 kN, (b) PU.B at 50 kN, ADP.C (c) at 20 kN and (d) at 50 kN, comparison of FE calculations and measurements; (e) Point positioning in the joint</i>	99

- 
- Figure 5.10: Axial strain distribution along overlap length at 50 kN for series (a) EP.A, (b) PU.B, (c) ADP.C, comparison of FE calculations and measurements, (d) FE calculations; (e) 10 mm laminate interface (dotted line) 101
- Figure 5.11: Shear stress distribution (a)  $l=100\text{mm}$ , (b)  $l=200\text{ mm}$  and through-thickness stress distribution (c)  $l=100\text{mm}$ , (d)  $l=200\text{ mm}$  along overlap length at 10 mm laminate interface at 100 kN; (e) 10 mm laminate interface (dotted line) 103
- Figure 5.12: Shear stress distribution (a)  $l=100\text{mm}$ , (b)  $l=200\text{ mm}$  and through-thickness stress distribution, (c)  $l=100\text{mm}$ , (d)  $l=200\text{ mm}$  along overlap length at failure line at 100 kN; (e) 10 mm laminate failure line (0.5 mm depth) (dotted line) 103
- Figure 5.13: (a) Shear stress to average shear stress distribution and (b) through-thickness to average shear stress distribution along overlap length at failure line at 20 kN and 100 kN 105
- Figure 5.14: (a) EP, (b) ADP shear stress distribution and (c) EP, (d) ADP through-thickness stress distribution along joint thickness at six distances from right edge (0/0.5/1/2/5/25) for joints with 100 mm overlap length at 100 kN; (e) Path position 106
- Figure 5.15: Effect of meshing (number of elements through adhesive layer) on stress distribution at 0.5 mm inside the 10 mm laminate of EP joint at 100 kN (a) shear stress, (b) through-thickness stress 107
- Figure 5.16: Effect of adhesive-layer geometry on stress distribution at 0.5 mm inside 10 mm laminate of EP joint at 100 kN, (a) shear stress, (b) through-thickness stress 108
- Figure 5.17: Effect of EP adhesive model on stress distribution at 0.5 mm inside 10 mm laminate at 100 kN (a) shear stress, (b) through-thickness stress 109
- Figure 5.18: Effect of laminate Young's moduli on stress distribution at 0.5 mm inside 10 mm laminate of EP joint at 100 kN (a) shear stress, (b) through-thickness stress 110
- Figure 5.19: Shear and through-thickness stress distributions at failure line and related correction factors of STI-device and EP.A, ADP.C and PU.B ( $l=100\text{ mm}$ ) series 112
- Figure 5.20: Failure surface of specimens and types of failure (a) ADP.B2.1, (b) ADP.B3.1, (c) ADP.B4.2 114
- Figure 5.21 Joint elongation estimation for the ADP joints 115
- Figure 5.22: Load-elongation curves for ADP joints (a)  $l=100\text{ mm}$ , (b)  $l=200\text{ mm}$ , comparison of FE and analytical calculations and measurements 116
- Figure 5.23: ADP joints (a) internal loads; (b) Shear and (c) through-thickness stress distribution along failure line; (d) Resultants of through-thickness stresses 117
- Figure 5.24: Effect of (a) adhesive elastic modulus on joint elongation, (b) adhesive to adherend modulus ratio on joint stiffness of 100 mm overlap length joints 119
- Figure 5.25: (a) Rigid joint; (b) Adhesively-bonded joint; (c) Laminate 119
- Figure 5.26: Effect of adhesive elastic modulus on (a) shear and (b) through-thickness stress distribution at failure line (0.5 mm inside 10 mm laminate) at 100 kN (100 mm overlap length joints) 120

Figure 5.27:	Effect of adhesive to adherend modulus ratio on maximum shear and through-thickness stresses to shear average stress at failure line (0.5 mm inside 10 mm laminate) (100 mm overlap length joints)	120
Figure 5.28:	Effect of adhesive elastic modulus on (a) shear stress distribution at 100 kN, (b) minimum to maximum shear stress ratio at adhesive centerline (100 mm overlap length joints)	121
Figure 5.29:	Adhesive bilinear behavior and moduli selection (100 mm overlap length joints)	122
Figure 5.30:	Adhesive to adherend modulus ratio choice (a) joint stiffness, (b) shear and through-thickness stress to average shear stress at failure line (0.5 mm inside 10 mm laminate) (100 mm overlap length joints)	123
Figure 5.31:	Adhesive elastic modulus choice - minimum to maximum shear stress ratio at adhesive centerline (average)	123
Figure 6.1:	New concept of ductile and redundant FRP structure	127
Figure 6.2:	(a) Elastoplastic and bilinear adhesive models; Structural characteristics (b) hogging to sagging moment ratio-load, (c) load-deflection and (d) hogging moment-rotation curve	129
Figure 6.3:	Multi-span beam or two-span beam with semi-rigid connection at mid-support before (a-b) and after (c-d) joint failure at the right connection	129
Figure 6.4:	Bending-moment distribution (a) phase I: stiff behavior, (b) phase II: flexible behavior	132
Figure 6.5:	Relationship between structure and (tensile and shear) adhesive behavior	133
Figure 6.6:	Semi-rigid simply-supported beam - phase I: rigid connection	138
Figure 6.7:	Adhesive to adherend modulus ratio effect on double-lap joint stiffness for 100/200/300 mm overlap lengths (a) global view including rigid joint and laminate stiffnesses, (b) zoom area including laminate stiffness	139
Figure 6.8:	Semi-rigid simply-supported beam - phase II: elastic connection	141
Figure 6.9:	Strap joint (a) internal loads; (b) Shear and (c) through-thickness stress distribution along the adhesively-bonded failure line; (d) Resultants of through-thickness stresses	143
Figure 6.10:	(a) Adhesive tensile behavior for different overlap lengths ( $l=200/300$ mm) and adhesive plastic moduli ( $E_p=10/15/20$ MPa); Estimation of (b) hogging to sagging moment ratio-load curve, (c) load-deflection curve and (d) hogging moment-rotation curve at mid-support for different overlap lengths ( $l=200/300$ mm) and adhesive plastic moduli ( $E_p=10/20$ MPa)	145
Figure 6.11:	Estimation of hogging moment-deflection curve for different overlap lengths ( $l=200/300$ mm) and adhesive plastic moduli ( $E_p=10/20$ MPa)	147
Figure 6.12:	(a) ADP shear behavior; (b) Hogging to sagging moment ratio-load curve, (c) load-deflection curve and (d) hogging moment-rotation at mid-support; comparison of model calculations and measurements of beams PH3 ( $l=100$ mm) and PH4 ( $l=300$ mm)	149
Figure 6.13:	Bending-moment distributions (at 136 kN load per jack), comparison of model calculations and measurements for beams PH3 ( $l=100$ mm) and PH4 ( $l=300$ mm)	149



---

<i>Figure 6.14:</i>	<i>(a) ADP and tailored adhesive shear stress-strain for <math>l=100/200/300</math> mm, (b) calculated hogging to sagging moment ratio-load curve</i>	<i>150</i>
<i>Figure 7.1:</i>	<i>Second new structure concept (component ductility)</i>	<i>160</i>
<i>Figure 7.2:</i>	<i>Translucent sandwich girder (a) experimental set-up, (b) cross-section (CCLab)</i>	<i>161</i>



## List of Tables

Table 2.1:	<i>Moment, rotations and displacements for different end connections</i>	11
Table 2.2:	<i>Advantages and disadvantages of adhesively-bonded joints (Hutchinson 1999, The Institution of Structural Engineers 1999)</i>	31
Table 2.3:	<i>Typical properties and characteristics of some structural adhesives (The Institution of Structural Engineers 1999)</i>	35
Table 3.1:	<i>System Ductility and Redundancy - Overview</i>	51
Table 4.1:	<i>Adhesive technical characteristics</i>	54
Table 4.2:	<i>Tensile and compressive mechanical properties of adhesives EP, PU and ADP</i>	60
Table 4.3:	<i>Shear mechanical properties of adhesives PU and ADP</i>	60
Table 4.4:	<i>Overview: experimental double-lap joints and results at failure (see Appendix B)</i>	66
Table 4.5:	<i>Measured joint stiffness and joint elongation to specimen elongation ratio of joint series EP.A, PU.B and ADP.C (three specimens per series)</i>	69
Table 4.6:	<i>Overview: experimental beams and results at failure</i>	73
Table 4.7:	<i>Material Properties of GFRP Beams</i>	74
Table 4.8:	<i>Beam shear coefficient K determined with different approaches</i>	83
Table 4.9:	<i>Comparison of beams with adhesive joints and simple/continuous beams</i>	84
Table 5.1:	<i>GFRP laminate mechanical properties for FE model</i>	93
Table 5.2:	<i>Adhesive mechanical properties for FE model</i>	94
Table 5.3:	<i>Joint stiffness and ratio of joint elongation to specimen elongation of series EP.A, PU.B and ADP.C</i>	99
Table 5.4:	<i>Shear and through-thickness strengths of GFRP laminate coupons (Keller and Vallée 2005)</i>	111
Table 5.5:	<i>Correction factors, maximum value of failure-criterion function, calculated and measured failure loads and calculated and measured failure load ratio of EP.A, PU.B, ADP.C, EP.D, ADP.D series</i>	113
Table 5.6:	<i>Strength of specimens ADP.B2.1, ADP.B3.1 and ADP.B4.2, measured, processed, predicted and predicted to processed strength ratio</i>	114

---

Table 5.7:	<i>Joint stiffness and failure load, comparison of FE and analytical calculations and measurements for ADP joints</i>	116
Table 6.1:	<i>Ultimate rotation (at 180 kN) and tailored adhesive mechanical properties for different overlap lengths (<math>l=100/200/300</math> mm) and adhesive plastic moduli (<math>E_p=10/15/20</math> MPa)</i>	145
Table 6.2:	<i>Ultimate hogging moment (at 180 kN) and its corresponding flange axial force, shear and through-thickness stresses and interaction formula at failure line for different overlap lengths (<math>l=100/200/300</math> mm) and adhesive plastic moduli (<math>E_p=10/15/20</math> MPa)</i>	146
Table 6.3:	<i>USS to SLS deflection ratio, USS to SLS bending moment ratio, robustness factor, energy at USS, energy at SLS, and USS to SLS energy ratio for different overlap lengths (<math>l=100/200/300</math> mm) and plastic moduli (<math>E_p=10/15/20</math> MPa)</i>	147
Table 6.4:	<i>Estimation of the rotation angles and moments at mid-support at failure</i>	151
Table 6.5:	<i>Calculated ultimate moment at mid-support and its corresponding flange axial force, shear and through-thickness stresses and the maximum value of interaction formula at the failure line for beams PH1-4</i>	151

# Curriculum Vitae

## Julia de Castro San Román

julia.decastro@a3.epfl.ch

Nationality: Spanish

Date of birth: June 14<sup>th</sup>, 1974

### Academic Qualifications

---

<b>Phd. candidate at CCLab-EPFL</b>	2001-2005
Swiss Federal Institute of Technology, Lausanne, (EPFL), Switzerland	
<b>M.Sc. in Civil Engineering</b>	1993-1999
Swiss Federal Institute of Technology, Lausanne, (EPFL), Switzerland	
Title of the diploma thesis: « La réhabilitation du Casino de Morges (CH) »	
Hennebique Reinforced Concrete Construction System	
<b>Baccalauréat scientifique</b> section internationale, Saint-Germain-en-Laye, France	1993

### Languages

---

**Spanish and French:** mother tongue

**English:** good knowledge

**Italian:** basic knowledge

### Work Experience

---

<b>Research engineer</b> at the CCLab (Composite Construction Laboratory, prof. T. Keller), EPFL	since July 2000
GFRP structures, adhesively-bonded connections	
<b>Research Assistant</b> at the IBAP (Institut de Béton Armé et Précontraint, prof. R. Favre and prof. A. Muttoni), EPFL	1999 (May)- 2000 (Dec.)
Assistance in lectures and exercises “Reinforced concrete”	
Responsibility for diploma projects in the domain of reinforced concrete	
<b>Trainee</b> in the Structures Laboratories of the Civil Engineering Department, Imperial College of Science, Technology & Medicine, London, GB (Dr. M. Chryssanthopoulos)	1997 (Aug.-Sept.)
Buckling tests on of GFRP cylinders	
<b>Student assistant</b> at the IMAC (Institut de Mesure et Analyse des Contraintes, prof. Pflug), EPFL	1997 (March)- 1998 (March)
“Structure and Solid Mechanics” exercises	

## Publications

---

KELLER T., DE CASTRO J., System Ductility and Redundancy of FRP Beam Structures with Ductile Adhesive Joints, *Composites Part B*, Manuscript CC/2004/022480, under review.

DE CASTRO J., KELLER T. (2005), System Ductility and Redundancy of FRP Beam Structures with Ductile Adhesive Joints, *3<sup>rd</sup> International Conference on Composites in Construction (CCC2005)*, Hamelin P. et al. eds, Lyon, CD-Rom.

DE CASTRO J. (2005), *Experiments on Epoxy, Polyurethane and Acrylic Adhesives*, Technical Report CCLab2000.1b/1, CCLab-EPFL, Lausanne, Switzerland.

DE CASTRO J. (2005), *Experiments on Double-lap Joints with Epoxy, Polyurethane and Acrylic Adhesives*, Technical Report CCLab2000.1b/2, CCLab-EPFL, Lausanne, Switzerland.

DE CASTRO J. (2005), *Experiments on Simple, Continuous and Bonded GFRP Beams*, Technical Report CCLab2000.1b/3, CCLab-EPFL, Lausanne, Switzerland.

KELLER T., DE CASTRO J., SCHOLLMAYER M. (2004), Adhesively Bonded and Translucent Glass Fiber Reinforced Polymer Sandwich Girders, *Journal of Composites for Constructions*, Vol. 8, No. 5, pp 461-470.

KELLER T., DE CASTRO J., ZHOU A. (2004), Concept of System Ductility and Redundancy for FRP Beam Systems with Adhesive Joint, *4<sup>th</sup> International Conference on Advanced Composite Materials in Bridges and Structures (ACMBS IV)*, El-Badry M. and Dunaszegi L. eds, Calgary, CD-Rom.

DE CASTRO J. (2002), Concepts of Adapted GFRP Structures with Redundancy and Ductility, *Fourth International Ph.D. Symposium in Civil Engineering*, Fédération Internationale du Béton (FIB), Munich, Germany, pp 86-91.

KELLER T., DE CASTRO J., DOOLEY S., DUBOIS V. (2001), Use of Fiber Reinforced Polymers in Bridge Construction, State-of-the-Art Report with Application and Research Recommendations, Swiss Federal Roads Authority, Report No. 555, Zurich, Switzerland.

KELLER T., DE CASTRO J. (2001), Structural Applications of Advanced Composite Materials for Bridges and Buildings, *Symposium on Theory, Design and Realization of Shell and Spatial Structures*, International Association for Shell and Spatial Structures IASS, Nagoya, Japan, CD-Rom.

FAVRE R., DE CASTRO J. (2001), The Arch: Enduring and Endearing, *Structural Concrete*, Vol. 2, No. 4, pp 187-200.

FAVRE R., DE CASTRO J. (2000), La pérennité de l'arc dans le construction, *Ingénieurs et architectes suisses, Bulletin technique de la Suisse romande*, No. 13, Lausanne, Switzerland, pp. 268-280.

BURDET O., DE CASTRO J. (2000), *Pont sur la Mentue – côté Jura (VD) Rapport d'essai de charge statique*, EPFL-ISS-IBAP 99.10, Lausanne, Switzerland.

ADEY B., DE CASTRO J., BRUEHWILER E. (1998), *Carbon Fibre Shear Strengthening of Rectangular Concrete Beams*, EPFL-MCS 97.02, Lausanne, Switzerland.